COUPLING OF REPETITIVE MULTIBEAM SURVEYS AND HYDRODYNAMIC MODELLING TO UNDERSTAND BEDFORM MIGRATION AND DELTA EVOLUTION

DANAR GURUH PRATOMO

June 2016

COUPLING OF REPETITIVE MULTIBEAM SURVEYS AND HYDRODYNAMIC MODELLING TO UNDERSTAND BEDFORM MIGRATION AND DELTA EVOLUTION

Danar Guruh Pratomo

Department of Geodesy and Geomatics Engineering
University of New Brunswick
P.O. Box 4400
Fredericton, N.B.
Canada
E3B 5A3

June 2016

PREFACE

This technical report is a reproduction of a dissertation submitted in partial fulfillment of the requirements for the degree of Doctor of Philosophy in the Department of Geodesy and Geomatics Engineering, June 2016. The research was supervised by Dr. John Hughes Clarke, and funding was provided by the Natural Sciences and Engineering Research Council of Canada (NSERC) Strategic Grants for Projects and Discovery Grants Programs.

As with any copyrighted material, permission to reprint or quote extensively from this report must be received from the author. The citation to this work should appear as follows:

Pratomo, Danar Guruh (2016). *Coupling of Repetitive Multibeam Surveys and Hydrodynamic Modelling to Understand Bedform Migration and Delta Evolution*. Ph.D. dissertation, Department of Geodesy and Geomatics Engineering, Technical Report No. 303, University of New Brunswick, Fredericton, New Brunswick, Canada, 233 pp.

ABSTRACT

This study addresses channelized delta top sediment transport on the Squamish estuary in Howe Sound, British Columbia. The mechanism of bedform migration and delta evolution is affected by the manner in which the available sediment flux from the feeder fluvial system is distributed. The present study is complementary to a parallel project looking at the sediment migrating on the delta slope as landslides or turbidity currents.

The termination of the Squamish River consists of a single channel that flows between flanking intertidal sand bars and over a mouth bar at the lip of the delta. The delta front is growing rapidly with about 1 million m^3 of sediment being input from the river system annually. There is a 3 to 5 m tidal range that strongly modulates the flow in the channel and over the adjacent intertidal sand banks.

In 2011, the delta top channel was surveyed every 3 to 4 day at high water, over a period of 4 months during which the river discharge waxed and waned and the tides ranged from springs to neaps. In 2012 and again in 2013, the channel was surveyed daily over a week while the tides increased from neaps to springs.

In order to understand the sediment transport mechanism in this estuary, this research parameterized the short wavelength bedform morphology and the long wavelength channel shape on the delta top, extracted the shape of the delta lip, and used volumetric

characterization of the sediment on the delta top and the delta lip vicinity. A three dimensional hydrodynamic model was also built to predict the flow within the river, the delta top, and adjacent fjord over the complete tidal cycle so that the bed shear stress associated with tide modulation and river discharge could be quantified.

This research shows that the short wavelength bedform characteristics and long wavelength channel shape are primarily a result of the low water period when the off-delta flows are strongest. The flow fields of the research area are dominated by the tidal modulation. However the river surge also plays a role during the high flow regime.

Good correlation was demonstrated between flow conditions (parameterized by the Froude number) and all of: the bedform roughness, the bedform mobility, the 1D bedform roughness spectra and the off-delta sediment flux. These relationships indicate that a single snapshot of the riverbed morphology could potentially be used to estimate sediment transport conditions.

ACKNOWLEDGEMENTS

Table of Contents

Curriculum Vitae

List of Tables

List of Figures

List of Abbreviations

1D   One Dimensional

2D   Two Dimensional

3D   Three Dimensional

ACEnet   Atlantic Computational Excellence Network

ASME   American Society of Mechanical Engineers

BOT   Brooke Ocean Technology

CSL   Canadian Survey Launch

CW   Continuous Wave

DoY   Day of Year

DTM   Digital Terrain Model

EGM   Earth Gravitational Model

ERS   Ellipsoidally Referenced Survey

FFT   Fast Fourier Transform

FM   Frequency Modulated

FVCOM   Finite Volume Coastal Ocean Model

GcGPS   Globally Corrected GPS

GIS   Geographical Information System

GPS   Global Positioning System

GNSS   Global Navigation Satellite System

IMU   Inertial Measurement Unit

ITRF	International Terrestrial Reference Frame
JD	Julian Date
MPI	Message Paring Interface
MVP	Moving Vessel Profiler
MWI	Mass Wasting Index
OBS	Optical Backscatter
OMG	Ocean Mapping Group
PPK	Post-Processing Kinematic
PPP	Precise Point Positioning
QGIS	Quantum GIS
RTG	Real Time Gypsy
RTK	Real Time Kinematic
SFI	Sediment Flux Index
TIN	Triangular Irregular Network
TSS	Total Suspended Sediment
WHOI	Wood Hole Oceanographic Institution

Chapter 1: Introduction

A multi-year project looking at the fate of the fluvial sediments moving from the estuary into its adjacent fjord has been conducted in the Squamish River, British Columbia. The underlying goal of this project is to provide a better understanding of the sediment transport processes on the delta top that influence the mass wasting on the delta slope. This project is complementary to a parallel project looking at the adjacent mass wasting processes [Hughes Clarke et al., 2011; Hughes Clarke et al., 2012]. More than 100 mass wasting events and 30 turbidity currents were identified during summer 2011 [Hughes Clarke et al., 2012].

This research focuses on the delta top as, during the summer freshet period, several thousand cubic meters of sediment are passing through and depositing on the delta lip every day [Hughes Clarke et al., 2012]. The changes of the bedform on the delta top represent a potential indicator of the amount of transport of sediment to the lip of the delta. The rate at which the sediment arrives appears to be modulated by tides and river discharge. This project attempts to understand that modulation. To assess this, repetitive mutibeam surveys were performed to monitor the changing bedforms on the delta top in the years 2011, 2012, and 2013.

The primary focus area of this research is on the delta top, from the delta edge, extending approximately 1500 m upstream into the estuary. Examining the delta top over time provides an indication of the extent of variation in the delta top morphology. It becomes apparent that significant variations in the riverbed morphology are present in the delta top area. These variations include both short wavelength bedform field changes and long wavelength channel shape evolutions. The variations of riverbed morphology might reflect the sediment flux on the delta top which controls the mass wasting process in the adjacent slope.

Nowadays, multibeam sonar systems are commonly used to examine subaqueous geomorphology. These systems provide seafloor bathymetry with 100% coverage and provide quantitative 2D roughness information about previously unrecognized bedform morphologies [Duffy & Hughes Clarke, 2005; Hughes Clarke, 2012; Nittrouer, Allison, & Campanella, 2008]. These systems also provides acoustic backscatter data to reveal significant information for indirect seafloor characterization. and sediment attributes [Mayer et al., 1991; Mitchell & Hughes Clarke, 1994; Medialdea et al., 2008; Preston et al., 2001].

Following the approach of those previous studies, this research utilized the Heron, the Ocean Mapping Group (OMG)'s research vessel, to collect precise bathymetry, backscatter, oceanographic and sedimentologic samples over this area. The data presented in this thesis represent the most frequent set of repetitive surveys, to date, used to examine changing seabed morphology. During summer 2011, the delta top area was surveyed two times a week for four months. In order to more intensely monitor the

bedform changes, in the years 2012 and 2013, the area of interest was surveyed on a daily basis to achieve a better temporal resolution than the three to four day sampling cycle used in summer 2011. To understand the extent of estuarine circulation, an underway profiler was used to measure water temperature, salinity as well as optical backscatter of suspended sediment in the river. Data acquisition that has been conducted for this research is discussed in Chapter 3.

In order to monitor the changing of the bedform over time, Digital Terrain Models (DTMs) of the delta top were built from the time series of bathymetric data. While terrain models can be used for qualitative interpretation of bedform populations, to better quantify the bedform morphological changes as well as the shape of the channel changes, several automated methods have been used in this research.

Most previous studies which attempted to quantify the characteristic of a bedform used single beam echo sounding profile to extract one dimensional (1D) depth profile. From that they measure the wavelength, height and ratio between wavelength and height of the bedform [Simons & Richardson, 1966; Guy et al., 1966; Allen, 1982; van Rijn, 1993]. Most recent study is using a two dimensional (2D) spectral analysis to investigate the dominant wavelength and orientation of the bedform [Cazenave, Lambkin, & Dix, 2008; Lefebvre, 2009] and wavelet transform to characterized the bedform [Nyander et al., 2003; Singh et al., 2011]. Another approach by Duffy & Hughes Clarke (2005) used spatial cross correlation to investigate the bedform migration and relate it with the sediment flux rate in a headland-associated bank near Saint John, New Brunswick using

3

repetitive multibeam surveys. They related that sediment flux to direct current observations using Acoustic Doppler Current Profiler (ADCP).

Building on these previous studies, this research extends the approach by using more frequent multibeam repetitive surveys to more precisely characterize the evolving bedforms. This research applied 1D and 2D spectral analyses and roughness characterization adopted from American Society of Mechanical Engineers (ASME) to characterize the short wavelength bedform morphology and monitor the bedform evolution using repetitive multibeam surveys. The long wavelength channel (the depth along and across the channel) change was investigated using depth and volumetric analyses. These methods were used to quantitatively monitor both the evolution of the bedform morphology and the channel shape over time. The methods to quantitatively analyze these evolutions are provided in Chapter 4.

The tremendous variability in both short wavelength bedform morphology and long wavelength channel shape was related to the spatial and temporal flow field in this area. The river flow clearly peaks at low water and this is when sediment transport is expected to be the most active. However, for logistical reasons, a direct current observation was not possible for a long period. To address the lack of observation, a hydrodynamic model has been developed as a means to predict the flow field spatially and temporally. The model was optimized to address the tide and river discharge modulations over the delta top during the experimental sampling periods.

Assessments in hydrodynamic conditions are important to understand the sediment migration. Hydrodynamic models have been routinely used to understand ocean and estuarine circulation. Many previous studies using a hydrodynamic model had been conduct in order to simulate the variation of the flow in space and time in estuaries. A hydrodynamic model can be used to improve an understanding of sediment dynamic in an estuary which is critical for understanding the source of sedimentation and prediction of dredge requirements [Hu et al., 2009; Church, 2014]. Yang et al. (2014) shows the ability of hydrodynamic model to be used for investigating the estuarine hydrodynamic response to sea-level rise and change in river flow due to the effect of future climate and land-used/land-cover changes in the Snohomish River estuary, Washington, USA.

Although both repetitive multibeam surveying and hydrodynamic modelling have previously been used separately to investigate sediment transport in an estuarine/deltaic environment, as far as the author is aware, this is the first time they have been applied simultaneously. In this research hydrodynamic model is used to relate the bedform morphology and the flow condition in the area of interest. The boundary of the hydrodynamic model for this research starts from the north, approximately 7 km upstream within the estuary, and extends down at about 5 km south of Woodfibre (Figure 1.1).
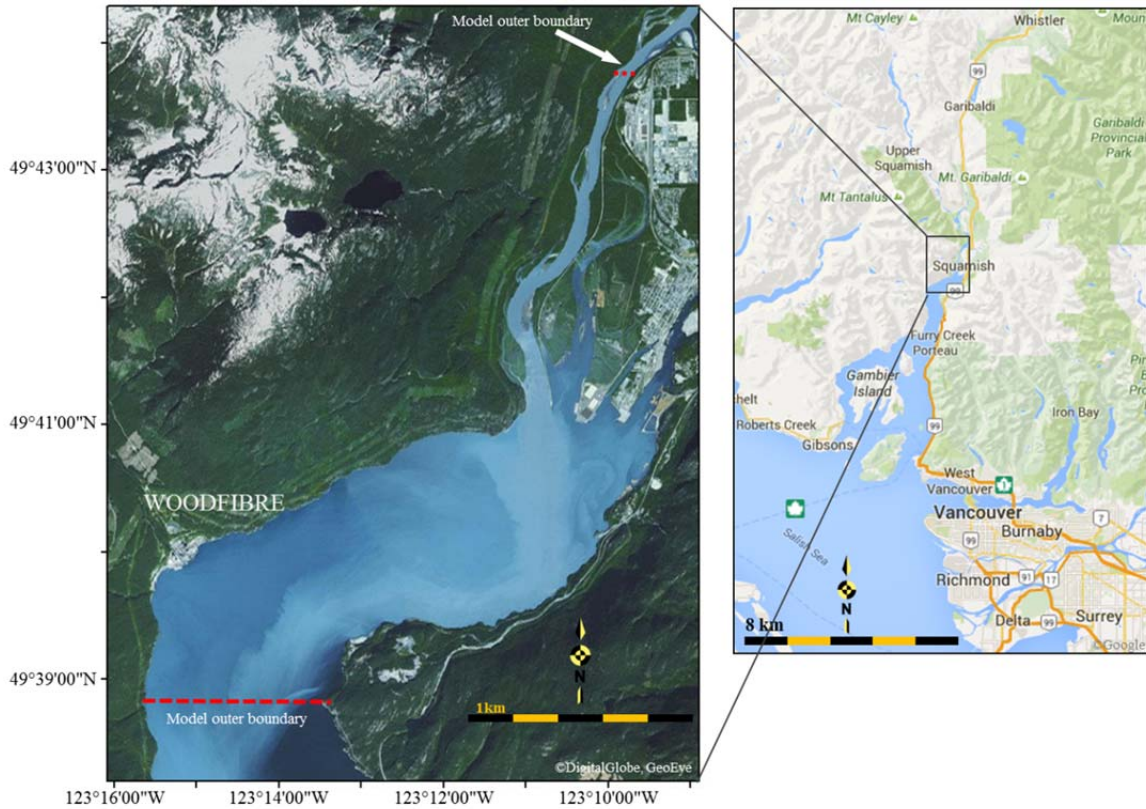
Figure 1.1: Outer boundaries of the hydrodynamic model developed in this research.

Higher resolution of triangular irregular elements was applied in the area of interest to get better flow field solutions. This model provides the spatial and temporal prediction of three dimensional (3D) varying current velocities. The development of the hydrodynamic model for the research is described in Chapter 5.

In order to monitor the evolution of short wavelength bedform morphology and long wavelength channel shape over time, a comprehensive analysis of combined repetitive multibeam surveys and hydrodynamic model is presented in Chapter 6. A repetitive multibeam survey provides snapshots of bedforms population and the hydrodynamic

model contributes in providing a characterization of the flow regime in this area at the same time. Combined these two will give a better understanding of sediment transport processes on the delta top which may affect the mass wasting event on the adjacent delta slope. Final conclusions of the works that have been done in this research, recommendations and suggestions for the future work are provided in Chapter 7.

Three primary objectives are accomplished in this research: [1] elaboration of quantitative analysis methods to assess the evolution of both short wavelength and long wavelength bedform morphology from repetitive multibeam surveys, [2] development of a three dimensional hydrodynamic model to predict the temporal and spatial flow in the research area, and [3] development of an understanding of the sediment transport processes on the delta top that may contribute to mass wasting process on the prodelta slope beyond the river mouth.

The contribution to knowledge made in this research is a detailed study of the application of coupled repetitive multibeam survey and hydrodynamic model to reveal the evolution of the bedform and channel morphology in the Squamish River. The particular focus at this location is to better understand regions which are affected both by net down stream flow as well as superimposed modulation due to the tidal currents. As far as the author aware, this is the first application of combined repetitive multibeam survey and hydrodynamic model to address sediment transport issue.

Chapter 2: Research Area

The Squamish River is located in the District of Squamish at the head of Howe Sound, approximately 50 km northwest of Vancouver, British Columbia. The delta of the Squamish River is classified as a bayhead delta [Bell, 1975]. This river drains a watershed encompassing all land from the Pemberton ice field down to the head of Howe Sound. Approximately 3589 km^2 of coastal rain forest in southern British Columbia is drained by this glacial-fed river system [*Squamish Estuary Management Plan*, 1999]. The Squamish River watershed (the area inside the black dashed line in Figure 2.1) comprises four main rivers: [1] Squamish River, [2] Elaho River, [3] Mamquam River, and [4] Cheakamus River.

The Squamish River provides by far the largest flux both of water and sediment of all four rivers. The flux is strongly modulated by seasonal precipitation and snow melt. This represents a potential flood hazard to its vicinity. To mitigate this, the river mouth was extensively modified in 1971 by establishing a training dyke. This impacted the associated estuary, reducing its capacity as a productive habitat for fish and wildlife. After the modification of the river mouth, there was an effort by the federal and provincial governments to implement an estuary management plan. The main aim of this plan is to accommodate the conflict between the industrial development and conservation of estuarine habitat [*Squamish Estuary Management Plan*, 1999].
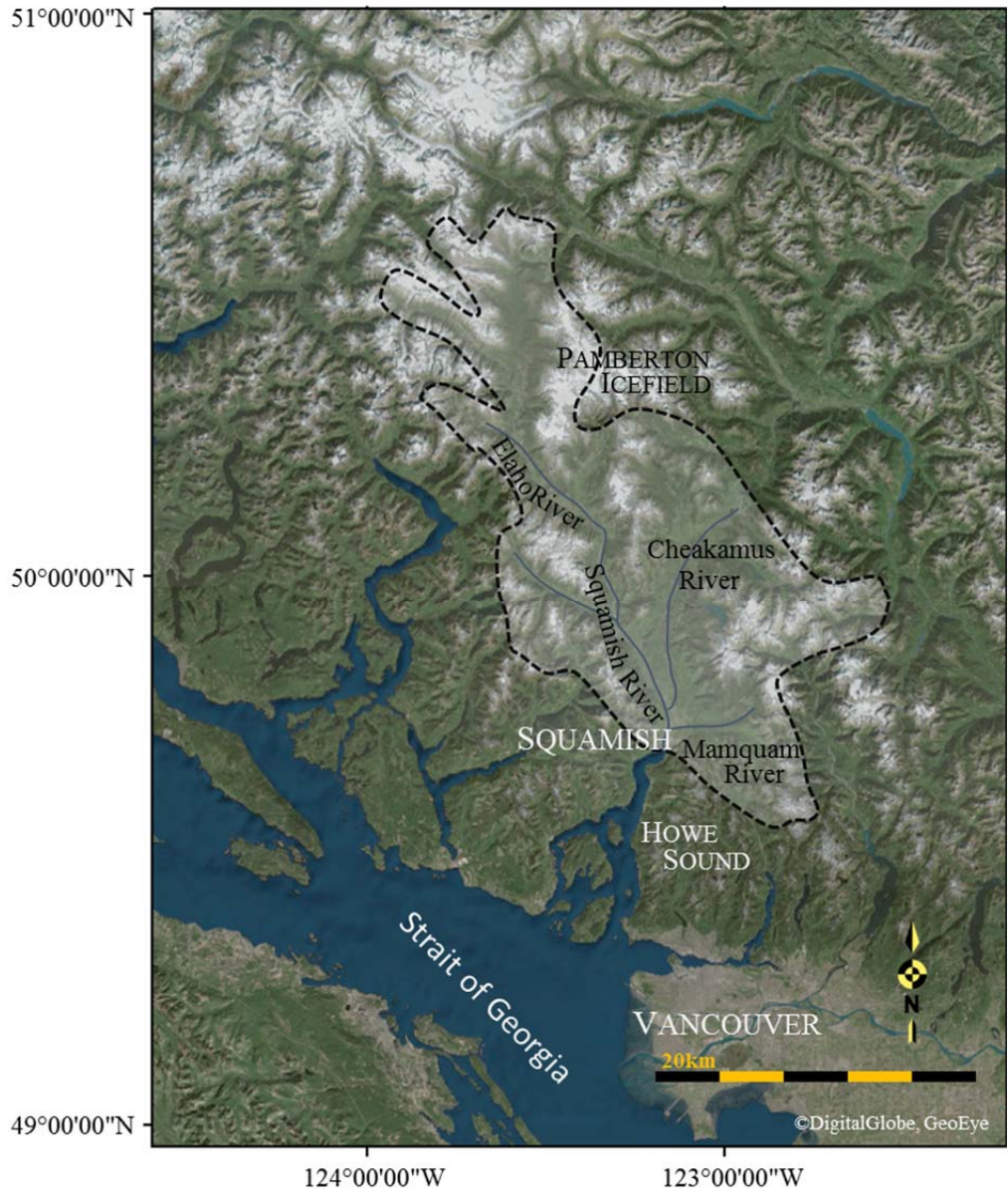
Figure 2.1: The Squamish River watershed and its four main tributaries. The area inside the black dashed line represents the watershed of the Squamish River.

The focus area of this research falls within a subset of the management plan area (Figure 2.2). It specifically targets this region into which the whole Squamish discharge has been compressed; as such the sedimentary processes (flux, deposition, and mass wasting) are artificially enhanced by the training dyke.
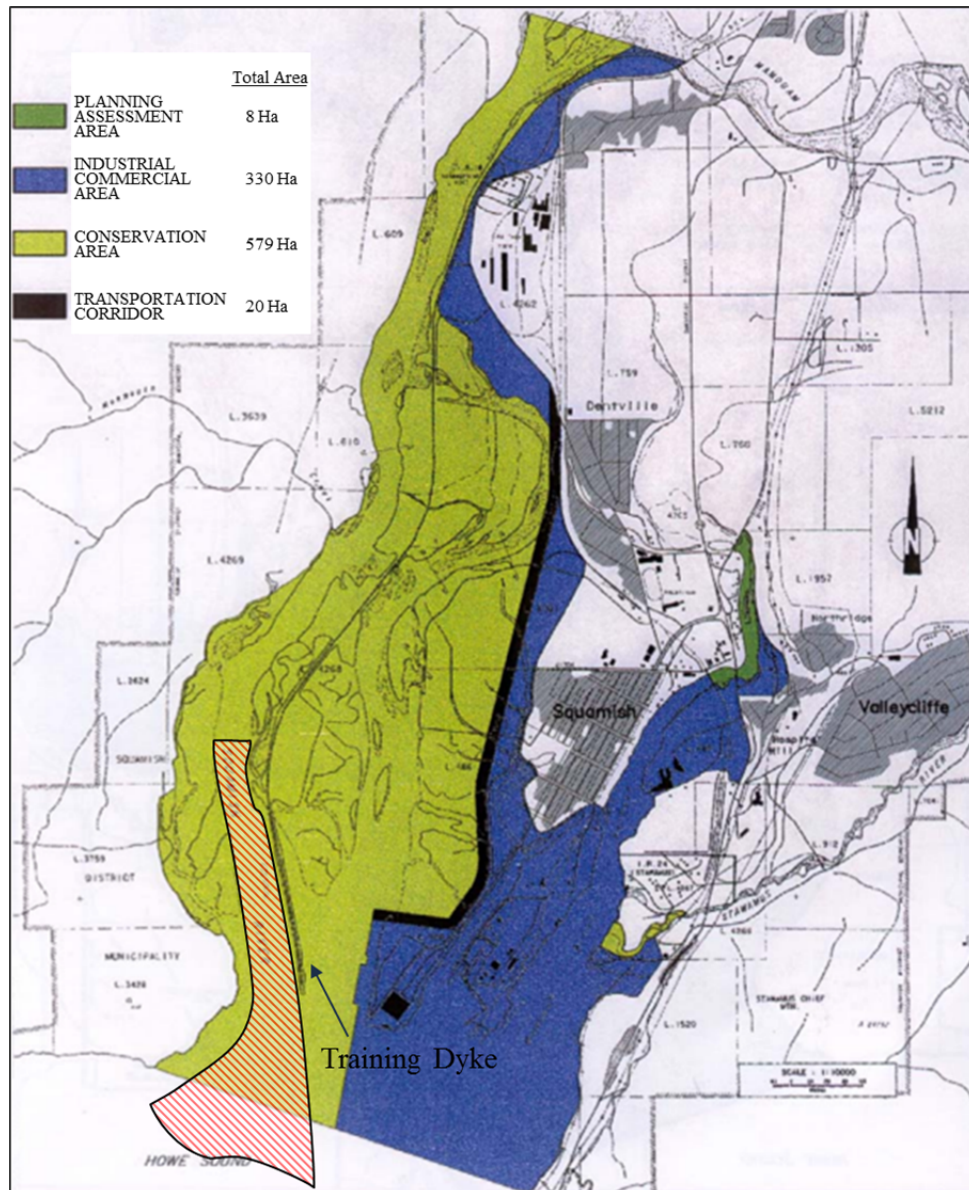
Figure 2.2: The research area (dashed area) overlaid with 1999 area designations for the Squamish Estuary (modified from Williams and Langer, 2002).

2.1. Geographical Location of the Research Area

The research area covers the transition from the active river to the fjord (Howe Sound). While the research area is referred to as a river; strictly it is a seasonal estuary. The delta top can be divided into three zones: [1] intertidal zone, [2] subtidal shoal zone, and [3] river channel.

The intertidal zone includes the western and eastern intertidal shoal. The western intertidal zone is bounded between Squamish valley bedrock and the river channel. The eastern intertidal shoal extends from the east side of the training dyke to the eastern limits of the Squamish terminal (Figure 2.3). The subtidal shoal includes the mouth bar and the actively changing delta lip. It is notably shallower than the main river channel, extending to 0.5 m below Chart Datum.

The river channel is located between the western intertidal shoal and the training dyke. The channel has deeper bathymetry (up to 3 m below Chart Datum) and becomes more shallow as it goes towards the delta front where it forms a mouth bar. Figure 2.3 shows an oblique aerial photo of the research area with the illustration of the zonation on the delta top.
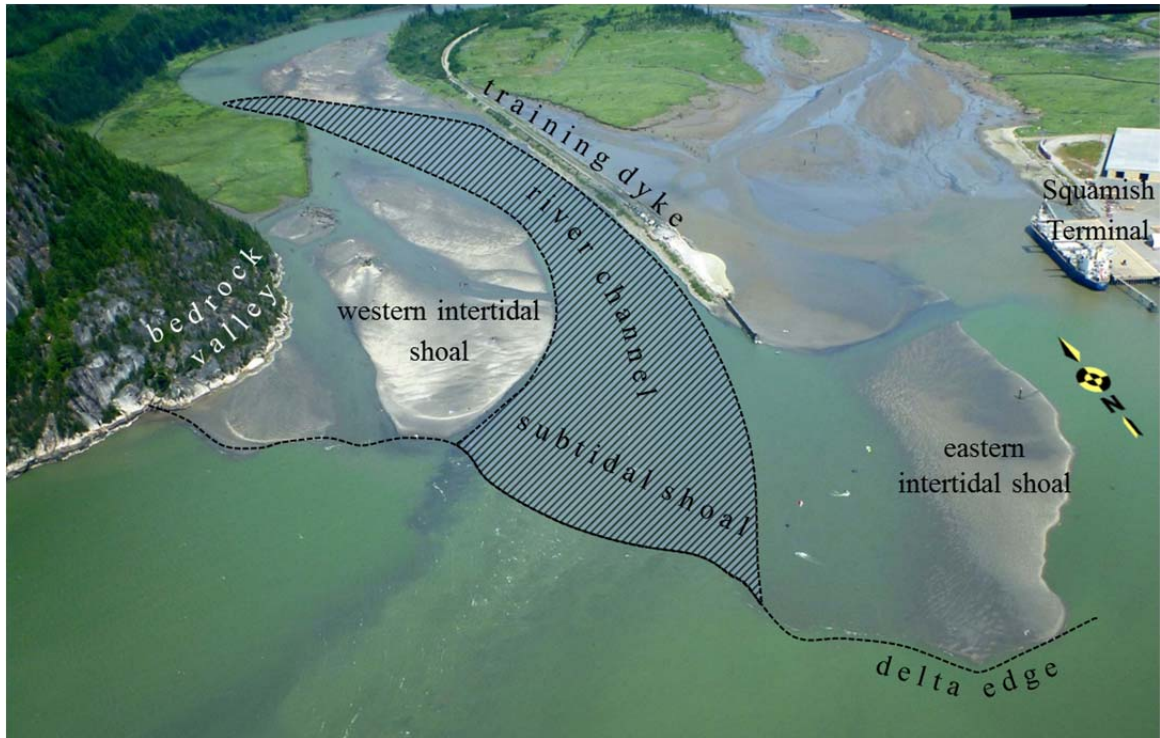
Figure 2.3: An oblique aerial photo of the research area. The photo was taken at low-water spring tide and reveals the intertidal sand banks. The shaded area indicates a 1500 m long subtidal stretch of the mouth of the river which was repeatedly surveyed to provide the data for this research.

2.2. The River and Delta Morphology

The morphology of the Squamish River has been changing very rapidly over the last century [Bell, 1975; Friele, Ekes, & Hickin, 2000; Hickin, 1989]. Before 1921, it flowed into the present Mamquam Blind Channel forming the Mamquam estuary. After a major flood in 1921, the flow to the Squamish River altered its course from a southerly to a westerly direction. According to Bell (1975), a major flood in 1945 cut a new channel through the delta. In order to protect the area from the flood, and to allow for the development of the Squamish terminal, in early 1970, the flood control facilities

12

restricted the flow of the Mamquam River to the Squamish River by building the existing dykes and floodgates [*Squamish Estuary Management Plan*, 1981].

The dykes were designed to protect the area against a 1 in 50 year flood, but subsequent analyses of the peak flows of the Squamish River indicate that the dykes provide protection against 1 in 200 year flood [*Squamish Estuary Management Plan*, 1981]. From the point of view of this research, the construction of the training dyke resulted in a concentration of the discharge into a much smaller cross-section. This has accelerated the rates of sedimentation in the research area.

According to Syvitski & Macdonald (1982), the sediments in the delta range from muddy sands in the estuary, sandy silt on the delta top, silt on the delta slope, and mud at the foot of the slope and along the basin floor. The gradient and decrease in grain-size down fjord indicate that the basin is primarily fed by gravity driven sedimentation from the delta of the Squamish River. The Squamish Delta is a particularly rapidly growing wedge of sediment that is prograding into a more than 200 m deep fjord.

Analysis of the floodplain sediments upstream of the delta [Gibson & Hickin, 1997] and buried alluvial fans within the floodplain [Friele et al., 2000] indicate that, since the end of the last glaciation (~12000 years ago), the delta has been prograding and has infilled an approximately 20 km section of the fjord. Bell (1975) calculated the delta front of the Squamish River to be advancing at a rate of about 6 m per year based on a comparison of bathymetric surveys made in 1930 and 1973. That research successfully revealed the morphology, but lacked the positioning confidence to resolve short term changes.

13

Gibson and Hickin (1997) suggested an average horizontal progradation rate of the delta is about 4.0 m per year. On a year to year basis, this study has been examining the position of the edge of the delta from 2011 to 2013. The inter year variation has been both positive and negative with horizontal local change of more than 10 m (will be discussed in Chapter 6).

The sediment activity on the delta is critically important as it controls the navigational access to the Squamish terminal. Any catastrophic slope instability on the delta front could adversely affect the recent urban development in the town of Squamish. The delta has been the focus of previous surveys including single beam hydrographic surveys in 1973 and 1990 and a side scan survey in the early 1980s [Prior & Bornhold, 1984].

The first multibeam survey of prodelta was in 2004; subsequent surveys in 2005, 2006, and 2009 were used to demonstrate the activity of mass wasting on the prodelta. There are 9 multibeam surveys of the prodelta which have been conducted at intervals either of 2 years, 1 year or 6 months between 2004 to 2009 [Brucker et al., 2007; Hughes Clarke & Brucker, 2009]. Although geomorphically, the delta appears to extend across the full width of the fjord, the modern active delta has been altered by a training dyke that now constricts almost all the flow to the western side [Brucker et al., 2007].

Hughes Clarke et al. (2011) established a locally based multibeam system and confirmed that there were over 100 turbidity currents in a 4 month summer period caused by slope failure on the delta edge. The results indicate that the delta slope has intense mass-wasting activity and it is apparent that by far the majority of the delta morphological

evolution takes place during the summer freshet [Hughes Clarke et al., 2012]. The surveys by Brucker et al. (2007) and Hughes Clarke et al. (2009, 2011, and 2012) confirm that, away from the modern channel, the delta is inactive. During the 2011 Squamish Program, the first delta top surveys were performed. These form the main observations for this research.

2.3. Local Oceanographic Conditions in the Research Area

The sediment transport on the delta top is affected by the local oceanographic conditions in this area. This section briefly describes the oceanographic conditions on the research area. These oceanographic features includes: [1] tide, [2] river discharge, [3] current, [4] wave, and [5] estuarine circulation. The detailed descriptions of oceanographic features in the Squamish delta are given by many researchers [Bell, 1975; Buckley, 1977; Gibson & Hickin, 1997; Hickin, 1989; Hickin, 1978].

The tidal regime in the Squamish River can be categorized as a mixed semidiurnal tide, typical of the Pacific coast. The tide in the area can be classified as a macrotidal due to an average tidal range of 3.2 m and a maximum tidal range of 5.1 m [Gibson & Hickin, 1997]. At high tides the water covers the whole intertidal areas (western and eastern intertidal shoals) and these areas are exposed at lower low tides.

The mean discharge of the Squamish River is approximately 300 m^3s^{-1}. The river discharge during summer months is supplied largely by glacial meltwater with the average of approximately 550 m^3s^{-1}. The peak discharges during summer months usually

occur in June with the amplitude of more than 800 m^3s^{-1}. During winter months the river discharge is low with an average of approximately 70 m^3s^{-1}. A second discharge peak in the Squamish River commonly occurs between September and February resulting from increased precipitation in combination with sudden snow melt. These yield flows that are larger but of shorter duration then summer freshet flood [Gibson & Hickin, 1997].

Figure 2.4 shows the historical data of daily average river discharge from year 2000 to 2013 and the daily average river discharge from 2011 to 2013 in which the observation was conducted. The highest discharge peak in the last 10 years was in late fall 2003 which peaked at more than 2500 m^3s^{-1} of fresh water delivered to the delta. It was this event that was the reason for the first multibeam investigation in 2004.

The current in the Squamish estuary are modulated by the tide and seasonally affected by the river discharge. The fresh and less dense water enter the estuary on top of the incoming more denser seawater. The result of the unidirectional flow is to decrease the speed of flood tide and increase the speed of ebb tide.

The surface current (top 2 m) in the vicinity of the Squamish delta is approximately 0.8 ms^{-1} to 1.0 ms^{-1} [Buckley, 1977]. Current velocities range from less than 0.5 ms^{-1} in the winter to high of about 1.5 ms^{-1} during spring freshet [Bell, 1975]. Flash floods during the winter month and autumn can also produce high velocities. This then could be an important factor when assessing the net movement of sediment on the delta.
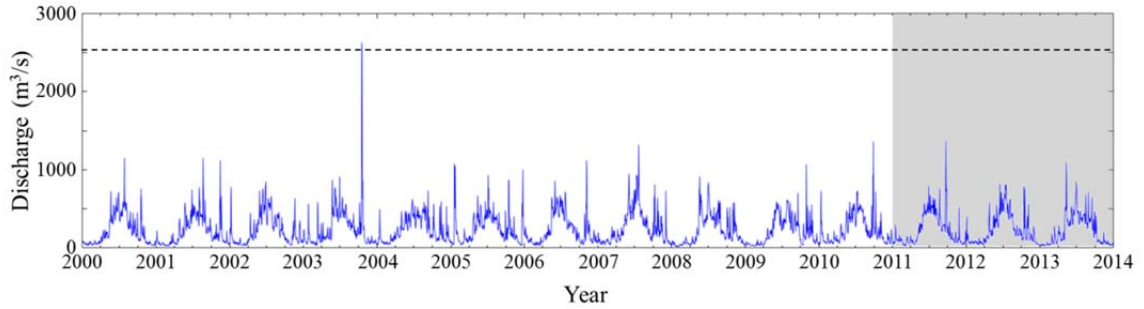
a. Historical daily river discharges of the Squamish River from 2000-2011.
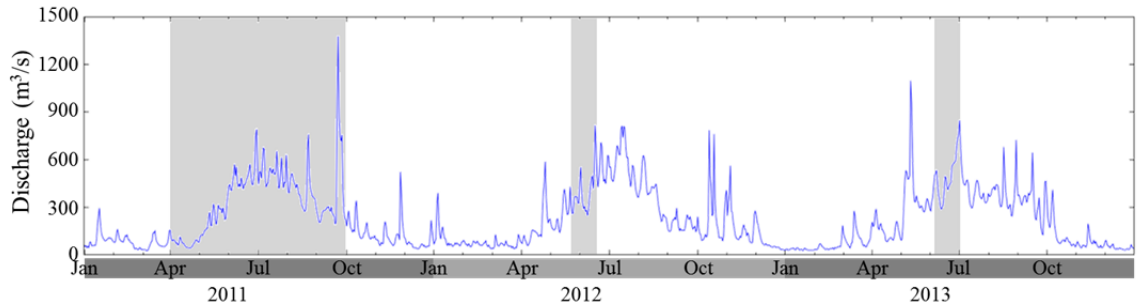
b. Daily river discharges from 2011-2013. Shaded areas are the time of observations in the research.

Figure 2.4: River discharge of the Squamish River.

Wave may be divided into two categories; wind generated surface waves and internal waves. The surface wave plays more important role than the internal wave in the distribution and redistribution of the sediment building the delta [Bell, 1975]. The internal wave may occur in the vicinity of the Squamish delta, but their effect on sediment transport is not known and is probably quite low when compared to the effect generated by the surface waves [Bell, 1975].

The estuarine circulation in the research area is driven by a combination of tidal modulations, katabatic winds, and river discharge which produces the major residual flow [Syvitski, Burrel & Skei, 1987]. The length of the riverine estuary and the degree of tidal influence vary seasonally. During winter months, the estuary extends 5500 m up stream

17

to the confluence of Squamish and Mamquam Rivers and salt wedge may extend 1500 m

upstream [Gibson & Hickin, 1997]. During summer months, tides are less able to modify

river flows because high river discharge caused by melting snow and freshet flow

effectively suppresses the tidal influence on the estuary. During this time, when the river

discharge is high (more than 500 m^3s^{-1}), the current flow never reverses and the salt

wedge is pushed out of the river [Gibson & Hickin, 1997].

Chapter 3: Data Acquisition

Most of the datasets used in this research were collected using the OMG vessel launch, CSL Heron. This research platform is equipped with: a Kongsberg EM 710 (70 to100 kHz) multibeam system, Knudsen 320R 3.5 kHz and 28 kHz sub-bottom profiler, C&C Technologies C-Nav2050 differential GPS receiver, Applanix POS MV V4 inertial navigation system, ODIM Brooke Ocean Technology (BOT) MVP 30 moving vessel profiler, and Applied Microsystems surface sound speed probe. The Heron also brings a US BMH60 bed sediment sampler and a Kemmerer water bottle sampler on board to collect the sedimentary data needed for this research.

This research also utilized a Boston-Whaler, approximately 3 m survey platform, to collect bathymetric data in the area in which the Heron cannot reach because of its draft limitation. This boat was equipped with a Trimble 5700 GPS system and a Humminbird 898c single beam system. The data collected using this small boat is for additional bathymetry data used in developing the hydrodynamic model and for validating the results of the hydrodynamic model. Details of data acquisition for this research and their results are explained in the following sections.

3.1. Horizontal and Vertical Positioning

In order to achieve a high accuracy in horizontal and vertical positioning, the Heron uses two sources of real-time positioning system: [1] C-Nav Real-Time Gypsy (RTG) and [2] POS MV systems. C-Nav is a positioning system built by C&C Technologies. This system is capable of receiving the L_1 and L_2 GPS frequencies as well as the StarFire (Globally corrected GPS) GcGPS corrections transmitted over the Inmarsat L-Band frequency. Computation of GcGPS corrections is facilitated by measurements from the globally distributed International Terrestrial Reference Frame (ITRF) network of reference and transmitted throughout the geo-stationary communication satellite.

C-Nav provides two real-time corrections to improve the GPS positioning accuracy: [1] Clock corrections for each active GPS satellite, which are computed every few seconds and [2] Orbit corrections for each active GPS satellite, which are computed every few minutes. These corrections are based on refraction corrected measurements ["C&C Technologies," 2014].

The second real-time positioning system on the Heron is POS MV from Applanix. This system computes a real-time position (latitude, longitude, and altitude) as well as orientation (roll, pitch, and heading) solution continuously using a Kalman Filter based aided inertial navigation algorithm. The inertial sensor component compromises a self-contained Inertial Measurement Unit (IMU). Three gyros and three accelerometers are mounted inside IMU in orthogonal axes. The positioning solution given by this system is derived by blending the inertial data from accelerometers and gyros with position and velocity data from an aiding navigation sensor (in this case, differential GPS receivers).

Then the algorithm combines inertial navigation with GPS navigation to generate a
blended navigation solution that retains the best characteristics of inertial and GPS
navigation ["Applanix - A Trimble Company," 2014]. Applanix (2014) claimed the
angular resolution for roll, pitch and heading provided by POS MV are within 0.02° of
standard deviation (σ).

Most of the area on the delta top is shallower than 15 m. In shallow water, the alignment
between three axes of IMU and Ship Reference Frame (SRF) plays an important role in
depth accuracy. The position of the vessel should be maintained within the dimension of
the projected beam footprint. In depths less than 10.0 m, the beam footprint of the
multibeam used in this research will be smaller than 0.17 m for a 1° nadir beam-width of
the EM710.

According to Hughes Clarke (2003), the realistically accuracy of the alignment between
MRU and SRF is within 0.05° for pitch and roll and half of beam-width (0.5°) for yaw.
With swath angle ± 75° and the depth shallower than 10 m, error from misalignment will
contribute less than 0.27 m in horizontal and less than 0.03 m in vertical. However, the
terrain model used in this research was built with 0.25 m resolution, thus resolutions
provided by POS MV and misalignment are acceptable for this research.

In order to confirm the horizontal and vertical accuracy of POS MV, the solutions from
POS MV are compared with other GPS solutions which are from: [1] C-Nav RTG, [2]
Precise Point Positioning (PPP), and [3] Post Processed Kinematic (PPK). PPP and PPK
solutions were processed from raw C-Nav data using GrafNav 8.10, a GPS processing

software packages from NovAtel's Waypoint Products group. Raw data from C-Nav must be converted to the format that can be accepted by this software to get PPP and PPK solutions.

PPP is a GPS post processing technique using precise satellite ephemeris and clocks corrections to determine horizontal and vertical position. It utilizes a single receiver and does not require local base stations. These corrections can be automatically downloaded in GrafNav from http://www.ngs.noaa.gov. The advantage of using PPP over the RTG is that PPP technique uses actual observed satellite and clock errors while RTG uses predicted or estimated errors based on the previous satellite history. The actual correction of the satellite and clock errors is more accurate than the predicted or the estimated ones, therefore PPP is expected to provide better positioning solution over RTG.

Slightly different from PPP solution, PPK technique requires multiple receivers, with one at a known fixed location as a base station, observing the same satellites at the same time as the roving receiver. This processing method essentially eliminates the satellite ephemeris and clock errors as well as receiver clock errors by differencing them to eliminate a major component of the tropospheric error.

This research used SQMS.115, a Cansel Can-Net base station to get PPK solutions. This base station is located at WGS84 latitude 49° 43' 30.78516" N, longitude 123° 8' 30.25032" W and height 0.980 m above ellipsoid reference. The difference in horizontal trajectories between POS, RTG, PPP, and PPK solutions can be graphically visualized in

Figure 3.1. All solutions were translated with respect to the ship reference point in order to appreciate the relative horizontal differences among them.
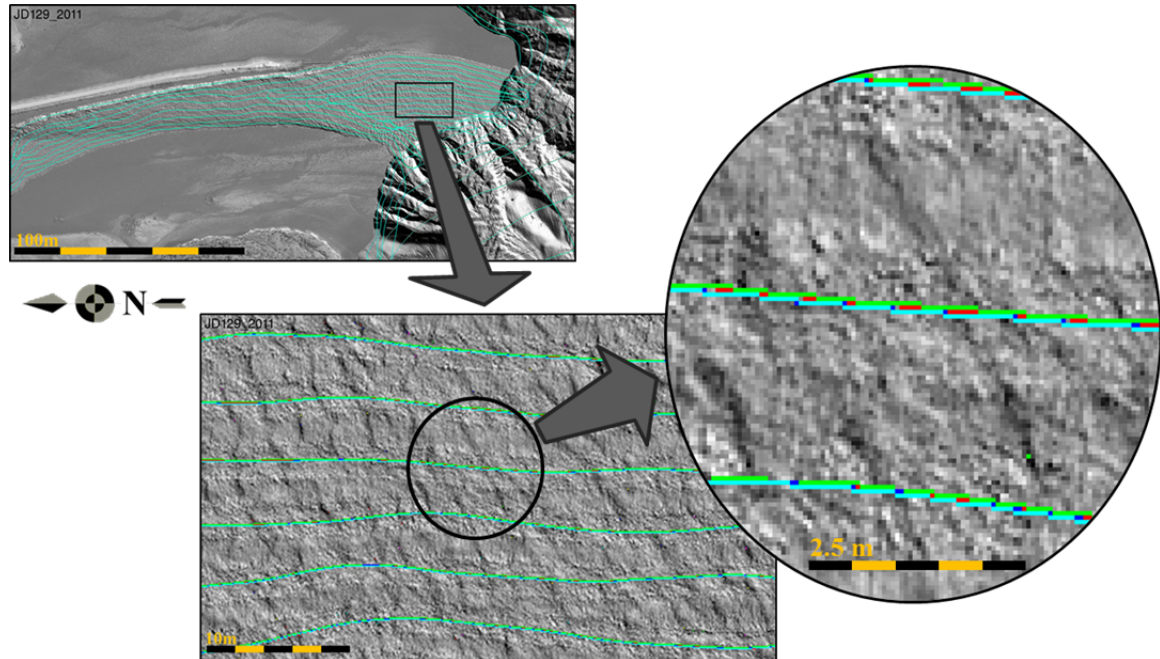
Figure 3.1: Different zoom level of horizontal tracks from POS (red), RTG (green), PPP (blue), and PPK (magenta) overlaid on bathymetry map of the research area.

Trajectories among these solutions vary over time. Their average difference is small: less than 0.254 m and 0.336 m in easting and northing directions respectively (RTG vs PPP, Figure 3.2c). Horizontal difference between POS and PPP is less than 0.218 m and between POS and RTG is less than 0.232 m. The horizontal difference between PPP and PPK has the smallest average which is 0.001 m for easting and 0.017 m for northing (Figure 3.2a).
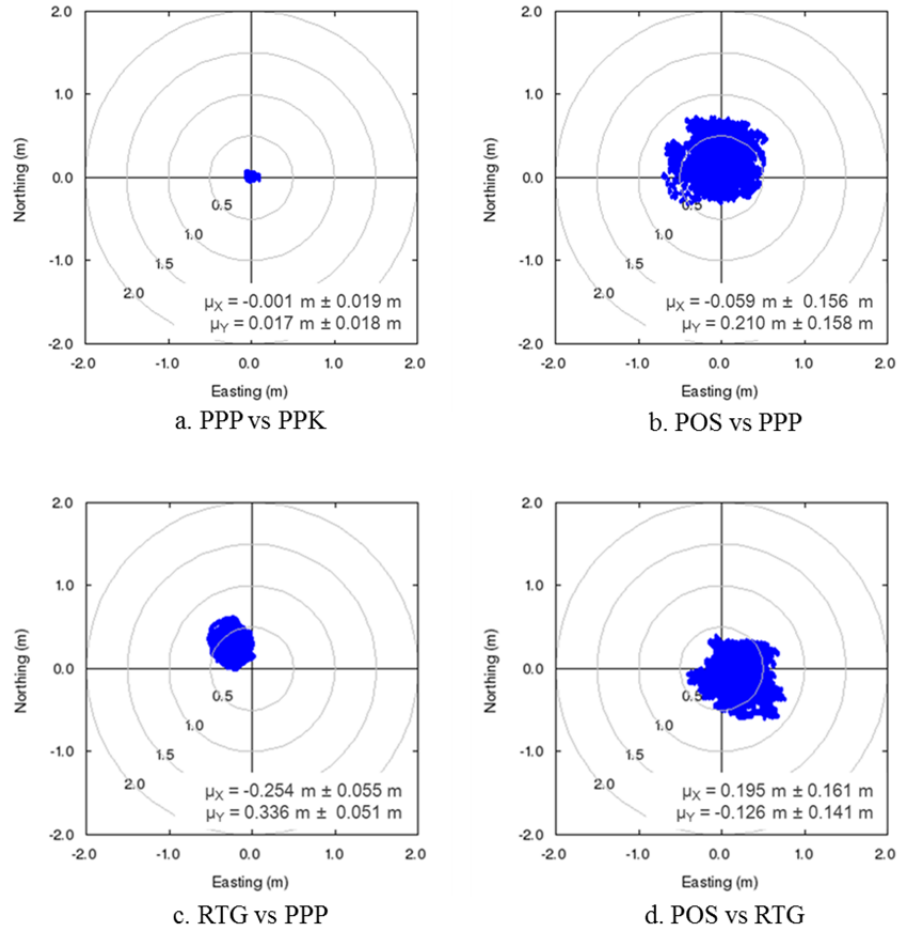
Figure 3.2: The horizontal differences between POS, RTG, PPP, and PPK solutions on one of the

observation epoch (JD129 2011).

Although PPP and PPK solutions are clearly superior when compared with the other

solutions, these solutions cannot be reliably achieved without any data gaps. During the 4

month period of observation in 2011, there were several days without any precise

ephemeris and clock corrections that can be downloaded for PPP processing. This also

happened for PPK processing, as there are data gaps at the base point so that it is not

possible to use PPK solution for all the datasets. Therefore this research adopted POS

24

MV solutions as a complete position as well as orientation solutions for multibeam motion compensation and geocoding of the multibeam data.

The horizontal uncertainty of the POS MV is ± 0.218 m (1σ). By using this solution as a horizontal position for the multibeam data, it would matter a lot in investigating bedform evolution if the bedform has small horizontal displacement from one to the next observation (less than half wavelength of the bedform). However, in hindsight, the bedform in the Squamish River varies significantly from one to the next observation, the bedform moves more than half wavelength, thus the horizontal position solution from POS MV is adequate to characterize the bedform.

The research also used volumetric characterizations to robustly investigate the sediment deposit onto or removed from the area of interest. The horizontal uncertainty of POS MV brings consequences in volumetric analysis. On a near-level surface, the consequences are small, but on steeper surfaces, including the bedform lee slopes and particularly the delta lip, the effect of a horizontal displacement is greater.

As a part of this research, the possibility of using Ellipsoidally Referenced Surveying (ERS) as a vertical reference was also examined. ERS uses the GPS height solution as the prime vertical reference. This contrasts with a conventional tide based approach which uses water level as a reference. The ERS solution can also catch dynamic draft issues due to squat and loading. In order to compare the GPS ellipsoid height solutions with observed water level, a separation model needs to be selected [Hughes Clarke et al.,

2011]. This separation model links chart datum to ellipsoid. This research adopted the EGM 2008 model as a separation model.

Figure 3.3 shows the vertical difference between GPS solutions and tide observation from Point Atkinson. The offset between them is contributed from imperfect separation model superimposed with the difference of local tide and tide in Point Atkinson (discussed in section 3.4.1). The local fluctuation in GPS solutions is the dynamic draft of the vessel because of squat and loading (Figure 3.3 inset).
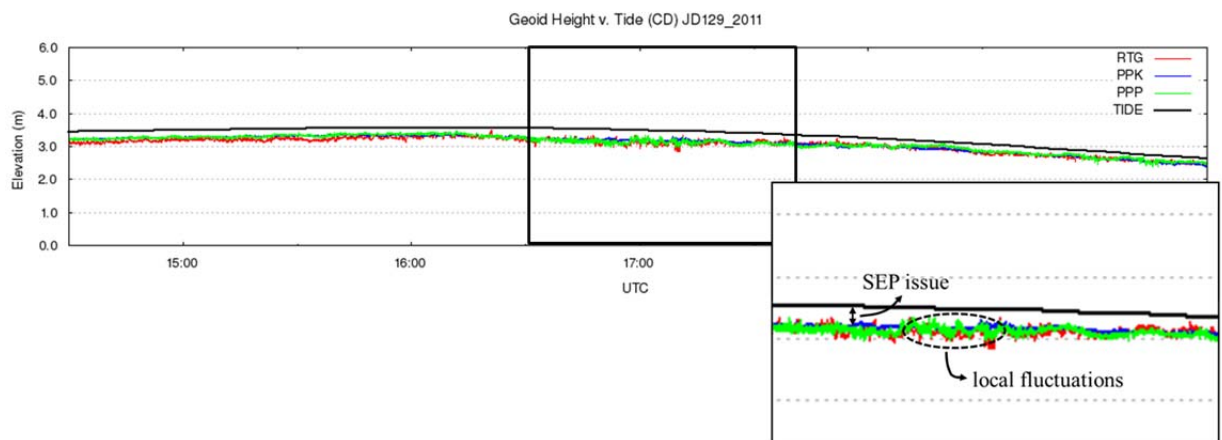
Figure 3.3: Vertical difference between GPS solutions and observed tide.

The three GPS height solutions differ in accuracy and reliability, but all these GPS solutions can capture the vertical variation when the vessel is moving. As expected, accuracy increases from RTG to PPP to PPK, but inversely the reliability drops. Sometimes, raw GPS data from RTG cannot be processed using PPP because of the lack of availability in precise clock and ephemeris corrections (area A in Figure 3.4).

26

The same situation also happens in PPK processing, if there is a lack of available observed data, the raw data cannot be processed (area B in Figure 3.4). While tide and heave based solutions have imperfections due to zoning, squat, and loading errors, here tide solutions are much more reliable. Therefore, for this research, the vertical reference for the bathymetric map is using tide observation because of the reliability of the data.
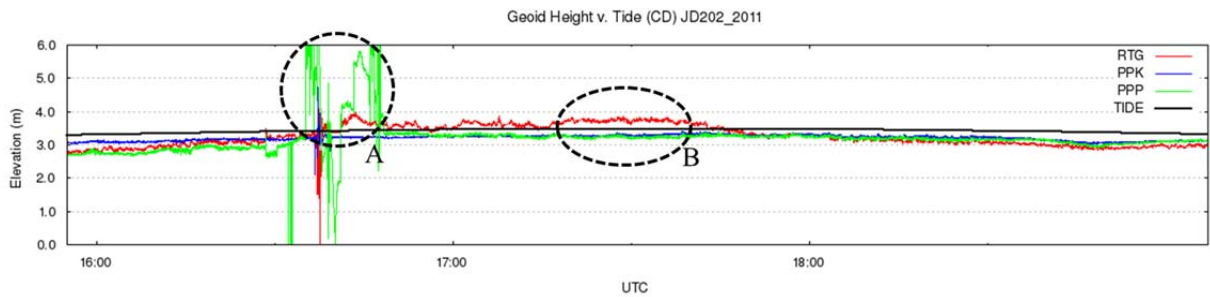
Figure 3.4: Erroneous in GPS vertical solutions. The lack of availability data corrections are represented inside dashed lines area A and B.

Although using ERS would eliminates the vertical uncertainty because of the tide, heave, and squat, unfortunately this solution could not give a continuous solution for entire four summer period in 2011. On the other hand, even though the tide has a potential large source of error because of the extreme tidal range, it does provides a continuous observations for the whole summer period. By using the tide observation, rather than ERS to correct the depth solution throughout each survey will increase the total vertical uncertainty.

27

When using tide-based vertical referencing, additional vertical perturbations due to the vessel dynamics have to be accounted for separately through a squat model. In this case however, as all the surveys were run with a common slow survey speed (typically 3 to 5 knots), the consequences of ignoring this extra effect is minor. This is because the squat is both small (approximately 3 to 5cm) and more importantly it is an almost constant bias for all the surveys. As the volume calculations represent differences, as long as the bias is near constant, the effect is minimal.

3.2. Bathymetry Dataset

Terrain models for this research were built using bathymetric data collected with a Kongsberg EM710 multibeam. Data acquisition was performed two times a week over 4 months during summer 2011. In order to improve temporal resolution, daily surveys were undertaken over an eight-day period in summer 2012 and in summer 2013. On one occasion in June 2013, a bathymetric dataset in the Squamish River was collected with a Kongsberg M3 in parallel with the EM710. Note that all multibeam data was collected only during high tide or at least 3 m above Chart Datum, because of the draft limitation of the Heron which is approximately 1.15 m.

In order to build a hydrodynamic model, bathymetric data should cover the area inside the model domain (Figure 1.1). However, not all the area in model domain can be surveyed with the Heron, thus this research also used a Boston-Whaler which was

equipped with a low-cost single beam system (Humminbird 898c) to survey the particular area that the Heron cannot reach.

3.2.1. Multibeam performance

A Kongsberg EM710 multibeam system is claimed to provide high resolution seabed mapping capability with a minimum acquisition depth of 3 m below its transducers, and a maximum acquisition depth of up to 2000 m. This system has frequency encoded, multi-sector multi swaths and is set up with roll, pitch, and yaw stabilization to maintain a nearly constant sounding spacing and density on the seafloor.

The EM710 operates at sonar frequencies within 70 to 100 kHz range (30 kHz bandwidth). The system aboard the Heron has a 1° transmit beam-width and a 2° receive beam-width, yielding seafloor sounding resolution on the order as small as 1.7% of oblique range.

As the survey area is shallow, the multibeam system uses dual swaths and three sectors in CW mode. The pulse length of each sector is 0.16 ms. Using the same pulse length, it is not possible to achieve 6 unique centre frequencies separated by 6.25 kHz within the available transducer bandwidth. Therefore, the outer sectors of each swath share the same centre frequency. As a result only 4 distinct centre frequencies need to be utilized.

In shallow water, the centre frequencies are set at 73, 81, 89, and 97 kHz. The two highest frequencies (89 and 97 kHz) are used for the middle sectors for each swath. The

outer port and the outer starboard of the first and second swath use centre frequency 73 kHz and 81 kHz respectively (Figure 3.5).

a. EM710 dual swath - 3 sectors   b. M3 single swath - single sector
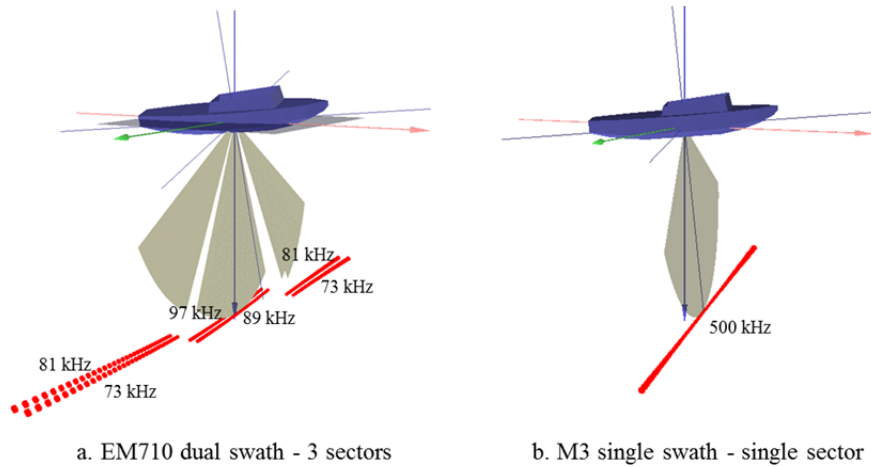
Figure 3.5: Illustrations of a dual swaths multibeam system in the EM710 (a) and a single swath multibeam system in the M3 (b) [Hughes Clarke, 2015].

A cartoon illustrating the utilization of 4 distinct centre frequencies in three different depths (shallow, medium, and deep) which are used in EM710 system is shown in Figure 3.6. Figure 3.6a illustrates that, in shallow water, this system uses all available bandwidth for 4 distinct centre frequencies each of which has a 5 kHz bandwidth (0.2 ms pulse length). In medium water, this system utilizes lower centre frequencies than in shallow water. Each sector uses 0.5 ms CW pulse (2 kHz bandwidth) and the separation between each centre frequency is 4 kHz (Figure 3.6b). In deep water, this system only uses a small part of the available transducer bandwidth. The highest centre frequency in this mode is 79 kHz. Each sector has 2.0 ms CW pulse (0.5 kHz) and between them there is 2 kHz frequency separation (Figure 3.6c).
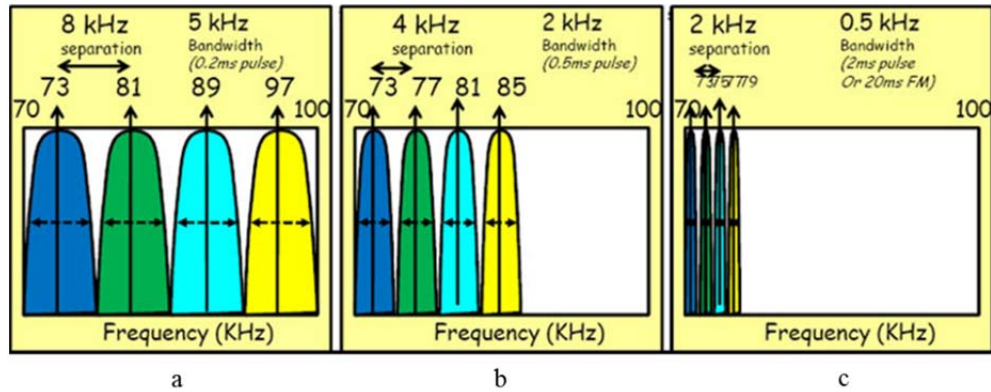
Figure 3.6: a Kongsberg EM710 frequency encoding in dual swath mode for shallow water (a), medium depth water (b), and deep water (c) [Hughes Clarke, 2010].

This frequency encoding permits transmit steering for the outer sectors because they do not overlap. The frequency encoding used in this system also accommodates individual transmit focusing for each sector to retain the angular resolution in the near field. This is of particular importance at the short ranges used in this research.

EM710 multibeam system utilizes 128 beams and in a high density beam processing mode provides up to 200 soundings per swath. This system adopts a combination phase and amplitude bottom detection algorithms, in order to provide soundings with the best possible accuracy across the entire swath [Hammerstad, 2000].

With a frequency span 73 to 97 kHz, EM710 works optimal in the depth between approximately 100.0 – 300.0 m [Beaudoin, 2012]. However, the depth average in the research area is less than 10.0 m. Thus this system suffered from mistracking in the nadir region because of its relatively low operating frequency as well as the soft bedform sediment on the delta top.

31

On one day in summer 2013, the EM710 was run in parallel with a M3 multibeam system to evaluate the resolution of EM710 in shallow water. The EM710 transducers were mounted on the gondola and the M3 was mounted using a retractable pole mount on the port side of the Heron (Figure 3.7).

Figure 3.7: A gondola on the Heron where the EM710 is mounted (a) and retractable mount pole for the M3 (b).

The M3 system has a relatively higher frequency (500 kHz) than the EM710. This means the M3 has more available bandwidth than the EM710. Thus, the M3 has better range resolution than EM710. For example, in the shallow mode, the EM710 uses a 0.2 ms pulse which provides approximately 0.150 m range resolution, whereas the M3 uses a 0.02 ms that affords 0.015 m. As a result, seafloors appear better defined when using the M3. Additionally this system works optimally in the depth of the research area, as it does not penetrate to subsurface.

The M3 utilizes 3° × 1.8° beam-width on the transmit and receive beam respectively whereas, as it is stated before, the EM710 has 1° × 2° beam-width on the transmit and receive beam. This makes the M3 has slightly lower angular resolution than the EM710. The M3 does not have dual swath capability and it only has one sector with opening angle ± 60°. Thus, the system also does not have capability to maintain across and along track sounding density as there is no electronic stabilization in the system. However, this system is ideal with slow speed and without a lot of motion of the vessel during data acquisition. Furthermore, with a narrow sector, the allowable ping rate is higher, resulting in better along track-density.

Figure 3.8a and 3.8b present terrain models of a single survey line built using the EM710 and the M3 bathymetric data, respectively. Between the dune crests, the seabed definition of the EM710 is smoother using the M3 system. Additionally, at lower grazing angles, the M3 is less prone to mistracking over the dune crests. The difference of terrain models between the EM710 and M3 is shown in Figure 3.8c; the average difference is -0.125 m and the standard deviation is 0.097 m.
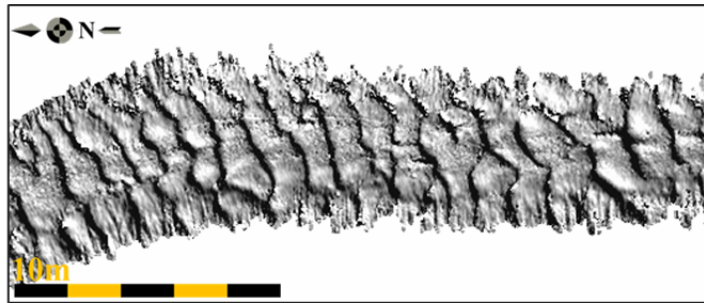
a. A sun-illuminated terrain model was built using the EM710 data.

b. A sun-illuminated terrain model was built using the M3 data.
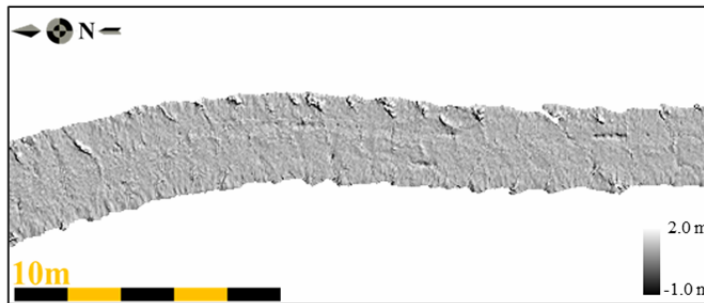
c. A different terrain model between the terrain model of EM710 and M3.

Figure 3.8: One line terrain model of the EM710 (a), one line terrain model of the M3 data (b), and

their surface difference (c).

As explained in the navigation section, the research used tidal observation as a vertical correction for the bathymetric data. However, during data acquisition, a predicted tide was used to correct the real-time depth result. The predicted tide was derived using Xtide, a tide and current predictions package from http://www.flaterco.com/xtide/files.html, with the command-line interface (*tide* command).

Tidal correction is essential in shallow water and predicted tides only measures the astronomical contributions to tide. Thus an observed tide data can differ considerably from predicted tides due to weather surges, geographical position, density changes, and currents. Figure 3.9a illustrates observed and predicted tide at the same epoch and the vertical difference between predicted tide and observed tide is shown in Figure 3.9b.

Figure 3.9c displays a histogram as statistical information of the difference between observed and predicted tides. The mean difference between observed and predicted tide in 2011 is 0.039 m with standard deviation of ± 0.147 m. The maximum and minimum differences are 0.793 m and -0.714 cm respectively. Therefore, an observed tide can improve the quality data especially for navigational purpose.
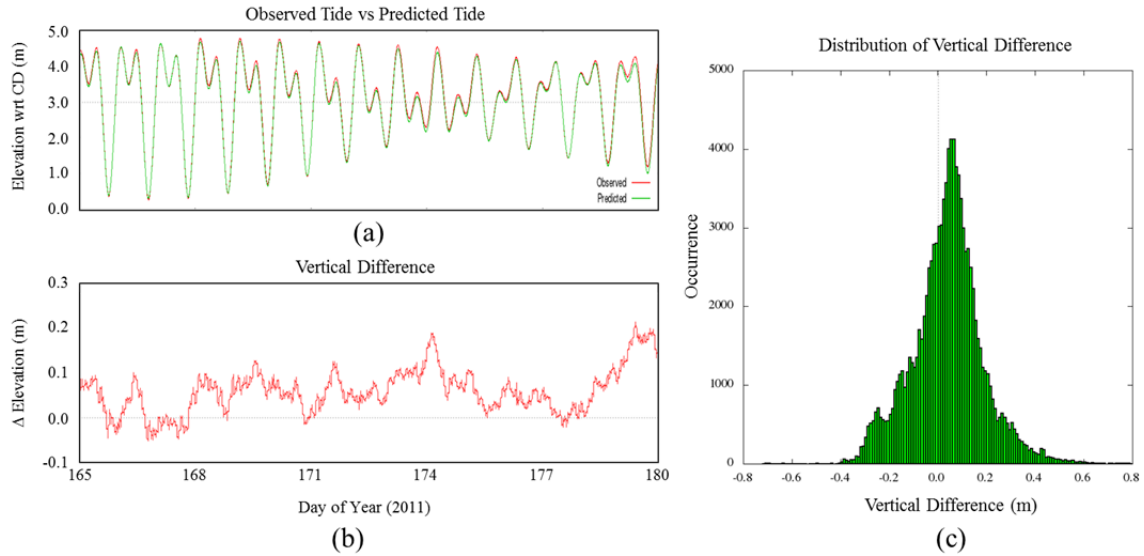
Figure 3.9: Observed and predicted tide modulations of Point Atkinson (a), the vertical differences between observed and predicted tides (b), and the distribution of the vertical differences (c).

Two bathymetric components were analyzed, the bedform morphological characteristic and the long wavelength channel shape. The bedform morphological characteristic is less affected by errors in tide level as the focus is the bottom topography relative shape. However, the long wavelength topography will be strongly affected by errors in the tide. Naturally, observed tides at Point Atkinson were used for all analysis in this research. The remaining errors due to using observed tides at Point Atkinson are a result in uncertainty in the difference between the tides along the length of Howe Sound.

36

3.2.2. Bottom tracking issue

In order to quantify the dominant wavelength using a spectral analysis tool, the terrain model has to be free from roughness artifacts that exceeds a pixel dimension, in this case is 0.25 m. Terrain models for the year 2013 contain along track artifacts that may affect the short wavelength bedform. This artifact may come as a result of a dropping in transmit beam pattern at sector boundaries and/or the presence of the receiver sidelobes which contaminate the quality of bottom tracking in multibeam data.

Almost all line arrays are constructed of discrete transducers elements positioned at equally spaced distance along the long axis of the array. These elements can both transmit and receive independently and they have their own inherent beam pattern based on their individual dimension [Hughes Clarke, 2012]. Ideally, the combined sum of the transmitter elements projects with a constant source level across swath. In reality, however, the absolute source level may vary across swath.

Another complication is the fact that multi-sector multibeam has different source level with respect to its sectors' frequency. The source level has a tendency to get weaker away from the centre of each sector. The illustration of transmit beam pattern because of this effect can be seen in Figure 3.10. The solid line is the ideal condition of the source level across the swath and the dashed line is where the source level is weaker as it goes away from the centre of each sector.

The other possibility of the appearance of these artifacts is from degradation in transducer elements in the receiver. The resultant receiver beam pattern is the complex summation of all signals at each of the elements which vary in elevation and azimuth angle. Ideally all elements in the receiver have the same receiving sensitivity and sidelobe suppression. However, if one or more elements are degraded, the sum beam pattern may not have the same sidelobe suppression.

Figure 3.10 illustrates that the outer transmit sectors does not point at nadir, but the inner transmit sector does point at nadir. At the location of A in Figure 3.10, where the transmit is weaker, the receivers pointed there will tend to track their inboard sidelobe. This may contribute to false topographic signature in bottom detections. This problem has been getting worse since 2012 on the EM710 onboard the Heron.
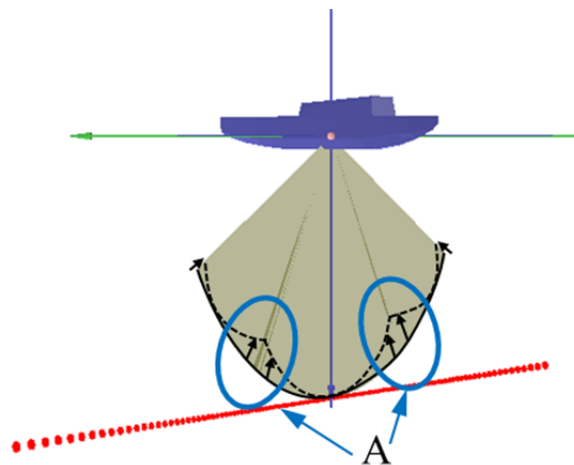
Figure 3.10: Transmit beam patterns that may cause the artifact.

Figure 3.11 shows across track profile which has the horn like artifact caused by the issues discussed above. These severely impacted the quality of the definition of the bedforms. In order to remove this artifact, a filtering algorithm was developed and implemented in this research. The algorithm examines observed depths across each swath. This filter uses an iterated standard deviation to remove the depth outliers from the isolated observed depths around the inboard edge of the central sector boundaries where the weaker beam pattern is located.
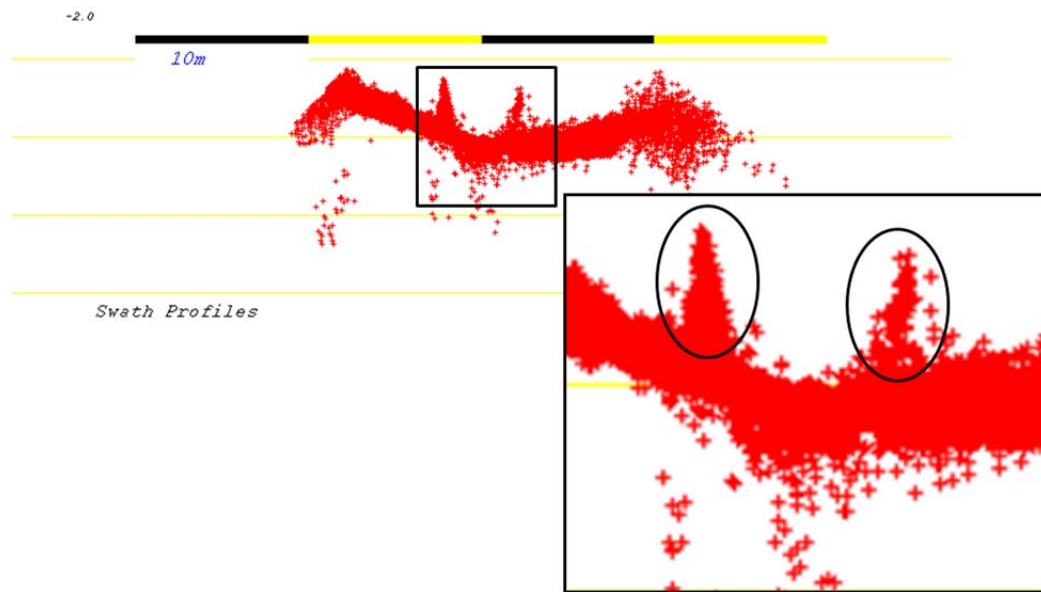
Figure 3.11: False topographic signatures at the sector boundaries. Inset figure is the exaggeration of the area inside the black box. Areas inside the black ellipses are false depths which occur due to reducing performance of the EM710.

This thesis focuses on the short wavelength roughness due to the bedforms, thus this false topographic signature would interfere with the results. Figure 3.12 shows the difference of terrain models before and after applying the filter developed in this research.
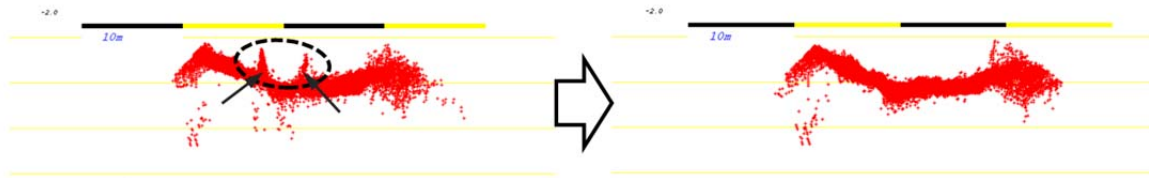
a. Across track depth profiles before (left-side image) and after (right side image) applying the filter.
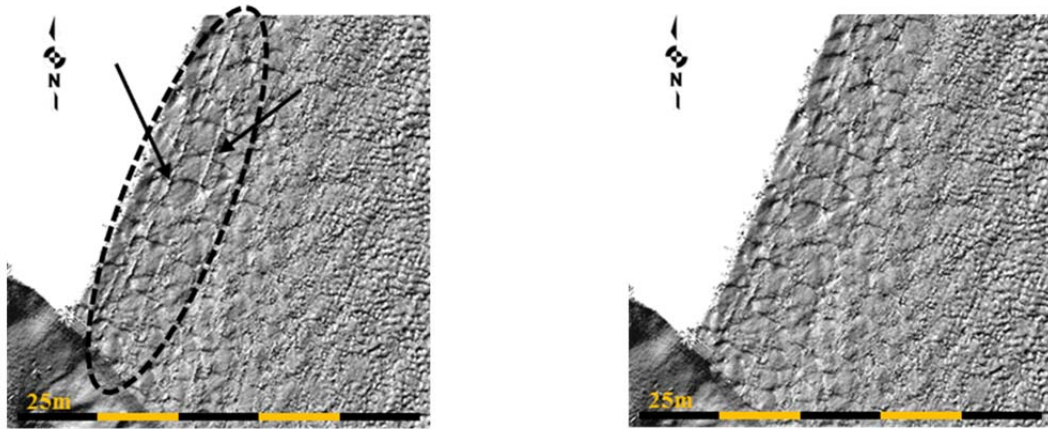
b. Sun-illuminated terrain models before (left-side image) and after (right side image) applying the filter.

Figure 3.12: The across track depth profiles and sun-illuminated terrain model before and after applying the filter to remove sector boundaries artifact (black arrows inside the black dashed ellipses).

3.3. Sediment and Backscatter Data

The sediment and backscatter data acquired as part of this research are used to understand the sediment distribution on the delta top. Three methods were used to collect the sedimentology data: [1] using grab sampler, [2] using water sampler, and [3] derived from multibeam backscatter data.

3.3.1. Grain-size analysis

In order to investigate the physical properties of the sediment on the research area, the research performed grain-size analysis of the sediment samples. 29 sediment samples were taken from the research area from June to July 2012. These samples were taken from different locations (Figure 3.13). These locations were chosen based on the multibeam backscatter image collected on the same day. The information of the sediment grain-size was used to understand the dynamic conditions of the sediment deposition and erosion on the delta top.
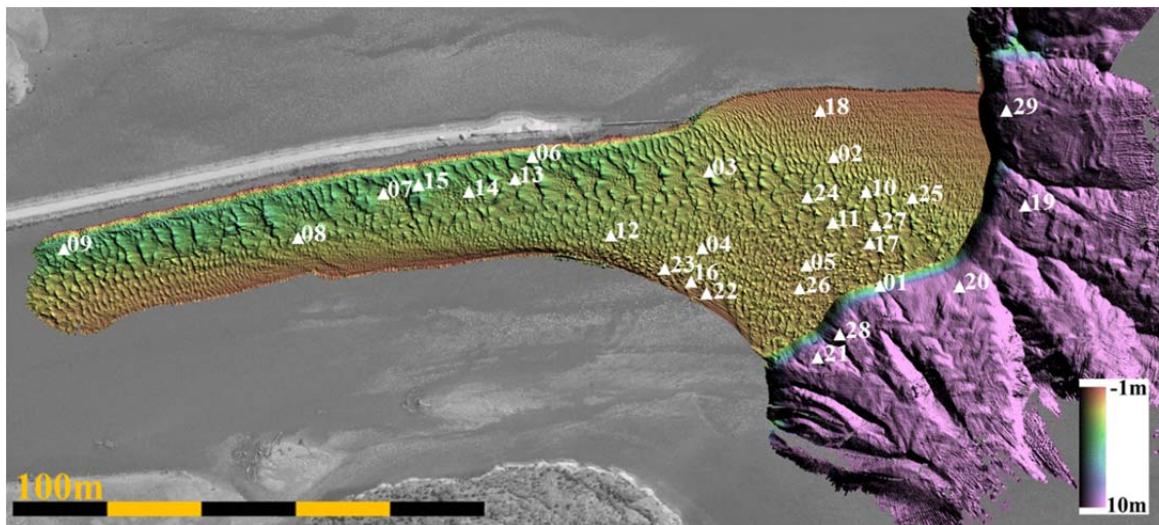
Figure 3.13: Sediment sample locations on the delta top and delta lip.

The accuracy of grain-size analysis is limited by sampling techniques, storage conditions analytical methods, equipment, and the capability of the operator [Poppe et al., 2000]. Sediment samples for this research were collected using a US BMH 60 bed sampler. This 13.6 kg bed sampler has penetration of the bed material of approximately 4.4 cm. The

sampling bucket of this sampler can accommodate approximately 175 cc of material

["Hoskin Scientific: Bed Material Samplers - US BMH-60," 2012]. After collecting the

sample, the sediments then were kept in clean and contamination free plastic bags.

The sieve analysis was performed on the collected samples to determine the sediment

size and its distribution over the research area. The aggregate of the sediment from the

largest to the smallest can be revealed using the analysis. The smallest mesh that was

used for the grain-size analysis was No. 200 (75 μm). Thus, an accurate determination of

sediment smaller than 75 μm cannot be performed. In order to robustly determine the

sediment smaller than 75 μm, the sample was washed through a No. 200 sieve. The

amount of the material passing this sieve was determined by comparing dry sample

masses before and after the washing process.

The sieving and weighting processes was performed by pouring the dry sample of each

measurement into the column of sieves, with the largest screen openings at the top. Each

lower sieve in the column has smaller openings than the one above. After sieve No. 200,

at the base, was round pan, called the receiver. The column of sieves was placed and

shook using a mechanical shaker for 15 minutes. After the shaking is complete, the

material on each sieve is weighed. The weight of the sample of each sieve is then divided

by the total weight to give a percentage retained on each sieve. These also include any

material finer than 75 μm that was washed out. More detail of sieve analysis method that

was used in this research can be seen in

http://www.wsdot.wa.gov/Publications/Manuals/M46-01.htm.

The statistics of the sediment size and distribution can be represented in metric (mm) or

phi (ϕ) scale. The phi scale is a logarithmic transformation of metric scale based on the

negative logarithm to the base 2 of the particle size. Phi scales are calculated from

particle size measures in millimeters as follows:

$$\phi = -log_2 d(mm) \qquad\qquad 3.1$$

where ϕ is the sediment size in phi scale and d is the particle size in mm. The negative

sign is affixed so that commonly encounter sand sized sediment can be described using

positive ϕ value [Pfannkuch & Rick Paulson, 2015].

The parameters used to describe a grain-size distribution in the research are in metric

scale. These parameters fall into four principal groups: those measuring [1] the average

size, [2] the spread (sorting) of the sizes around the average, [3] the symmetry or

preferential spread (skewness) to one side of the average, and [4] the degree of

concentration of the grains relative to the average (kurtosis). Formulas to calculate

aforementioned parameters are shown as follows [Blott & Pye, 2001]:

$$\bar{x}_s = \exp\frac{\Sigma f \ln d_{50}}{100}$$

$$3.2$$

$$\sigma_s = \exp\sqrt{\frac{\Sigma f\,(\ln d_{50} - \ln \bar{x}_s)^2}{100}}$$

$$3.3$$

$$S_s = \frac{\Sigma f\,(\ln d_{50} - \ln \bar{x}_s)^3}{100 \ln \sigma_s{}^3}$$

$$3.4$$

43

$$K_S = \frac{\sum f \, (\ln d_{50} - \ln \bar{x}_s)^4}{100 \ln {\sigma_s}^4}$$

3.5

where:

f is the frequency in per cent;

d_{50} is the median size of the sediment cumulative distribution in mm;

$\bar{x}_s$ is the mean of the sediment distribution;

σ_s is the sorting (standard deviation);

S_s is the skewness;

K_s is the kurtosis.

The sediment classification based on the average size of sediment distribution can be seen in Table 3.1 and the classification for sorting, skewness, and kurtosis of the sediment distribution is shown in Table 3.2 [Blott & Pye, 2001].

Table 3.1: Size scale and descriptive terminology of sediment.

Grain size		Descriptive terminology	
phi	mm/μm		
−6	64 mm	———————	
−5	32		
−4	16	Pebbles	Gravel
−3	8		
−2	4	——————	
		Granules	
−1	2	——————	
		Very coarse sand	
0	1	Coarse sand	
1	500 μm	Medium sand	Sand
2	250	Fine sand	
3	125	Very fine sand	
4	63	———————	

Table 3.2: Classification of sediment sorting, skewness, and kurtosis.

Sorting (σ_g)		Skewness (Sk_g)		Kurtosis (K_g)	
Very well sorted	<1·27	Very fine skewed	$<^-1\cdot30$	Very platykurtic	<1·70
Well sorted	1·27–1·41	Fine skewed	$^-1\cdot30$ to $^-0\cdot43$	Platykurtic	1·70–2·55
Moderately well sorted	1·41–1·62	Symmetrical	$^-0\cdot43$ to $^+0\cdot43$	Mesokurtic	2·55–3·70
Moderately sorted	1·62–2·00	Coarse skewed	$^+0\cdot43$ to $^+1\cdot30$	Leptokurtic	3·70–7·40
Poorly sorted	2·00–4·00	Very coarse skewed	$>^+1\cdot30$	Very leptokurtic	>7·40
Very poorly sorted	4·00–16·00				
Extremely poorly sorted	>16·00				

The result of grain-size analysis can be seen in Table 3.3. The result shows that the sediment on the delta top ranges from fine sand to granule (very fine pebbles). Based on the grain-size analysis results, the delta top is dominated by coarse sand and the sediment becomes finer at the edge.

Table 3.3: Grain-size analysis results and sediment samples location

Sample Number	Sample Id	Latitude (° ' ")	Longitude (° ' ")	$\bar{x}_s$ (mm)	σ_s (mm)	Sediment description
01	180_01	49°40'57.71"	-123°10'50.17"	0.705	1.770	Coarse sand
02	182_01	49°40'59.24"	-123°10'43.48"	0.880	1.948	Coarse sand
03	182_02	49°41'03.61"	-123°10'44.31"	0.713	1.442	Coarse sand
04	182_03	49°41'03.85"	-123°10'48.31"	0.607	1.493	Coarse sand
05	182_04	49°41'00.28"	-123°10'49.10"	0.487	1.554	Medium sand
06	182_05	49°41'09.75"	-123°10'43.38"	0.774	1.846	Coarse sand
07	182_06	49°41'14.92"	-123°10'45.27"	0.752	2.591	Coarse sand
08	182_07	49°41'17.85"	-123°10'47.69"	0.931	2.329	Coarse sand
09	182_08	49°41'25.97"	-123°10'48.34"	0.603	1.692	Coarse sand
10	183_01	49°40'58.22"	-123°10'45.35"	0.671	1.694	Coarse sand
11	183_02	49°40'59.34"	-123°10'46.80"	0.390	1.693	Medium sand
12	183_03	49°41'07.00"	-123°10'47.56"	0.774	1.846	Coarse sand
13	183_04	49°41'10.42"	-123°10'44.58"	0.465	1.438	Medium sand
14	183_05	49°41'11.97"	-123°10'45.29"	0.551	1.676	Coarse sand
15	183_06	49°41'13.68"	-123°10'44.98"	0.794	1.636	Coarse sand
16	184_01	49°41'04.24"	-123°10'50.00"	0.686	2.229	Coarse sand
17	184_02	49°40'58.07"	-123°10'47.72"	0.345	1.506	Medium sand
18	184_03	49°40'59.85"	-123°10'41.00"	1.063	1.815	Very coarse sand
19	188_01	49°40'52.68"	-123°10'45.99"	0.211	1.873	Fine sand
20	188_02	49°40'54.95"	-123°10'50.32"	0.468	1.972	Medium sand
21	188_03	49°40'59.84"	-123°10'54.06"	0.349	1.940	Medium sand
22	188_04	49°41'03.71"	-123°10'50.65"	0.190	1.594	Fine sand
23	188_05	49°41'05.14"	-123°10'49.32"	0.316	1.559	Medium sand
24	188_06	49°41'00.23"	-123°10'45.46"	0.476	1.553	Medium sand
25	188_07	49°40'56.56"	-123°10'45.59"	2.010	3.694	Granules
26	188_08	49°41'00.40"	-123°10'50.41"	0.862	3.031	Coarse sand
27	188_09	49°40'57.87"	-123°10'46.90"	0.572	1.529	Coarse sand
28	188_10	49°40'59.13"	-123°10'52.81"	0.293	1.887	Medium sand
29	188_11	49°40'53.30"	-123°10'41.04"	0.331	2.223	Medium sand

Figure 3.14 shows the representatives of the dominant grain-size collected for the research. Complete results of sediment analysis including the sediment sample images can be seen in Appendix A.
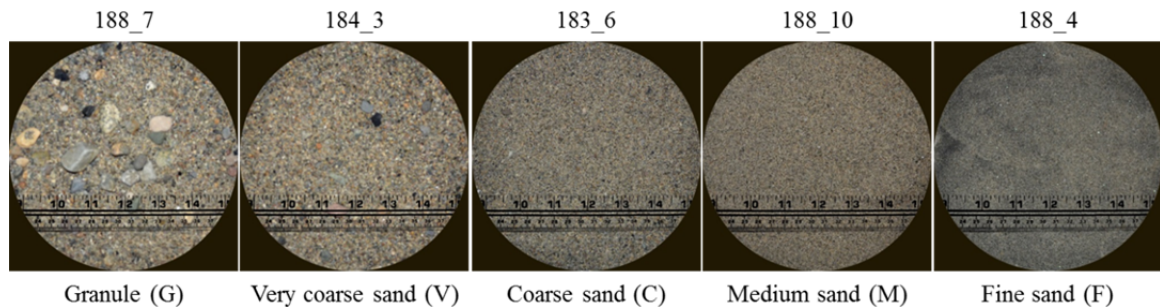
Figure 3.14: Representatives of sediment types collected from the delta top of the Squamish River vary from granules to fine sand.

3.3.2. Multibeam backscatter

As this research only sampled the sediment for a small subset of the observation times, the backscatter data provided by the EM710 multibeam system is used as a proxy for a sediment measurement. The backscatter imagery provides a representation of the seafloor which is a mixture of both bathymetric and sedimentological signatures. The acoustic response of seabed varies as the sediment type, roughness, grain-size, compaction and slope spatially change.

In addition, however, returned backscatter energy depends not just on the seafloor physical properties but also on the sonar configuration, water column propagation, and measurement geometry. Thus the geometric and radiometric corrections are necessary to get backscatter data which represent an inherent property of seabed that reflects its

physical properties. In this case, to a first order, the geometric and radiometric corrections

have been applied by the manufacturer [Hammerstad, 2000]. Figure 3.15 shows the

location of the samples overlaid with the delta top's backscatter imagery.
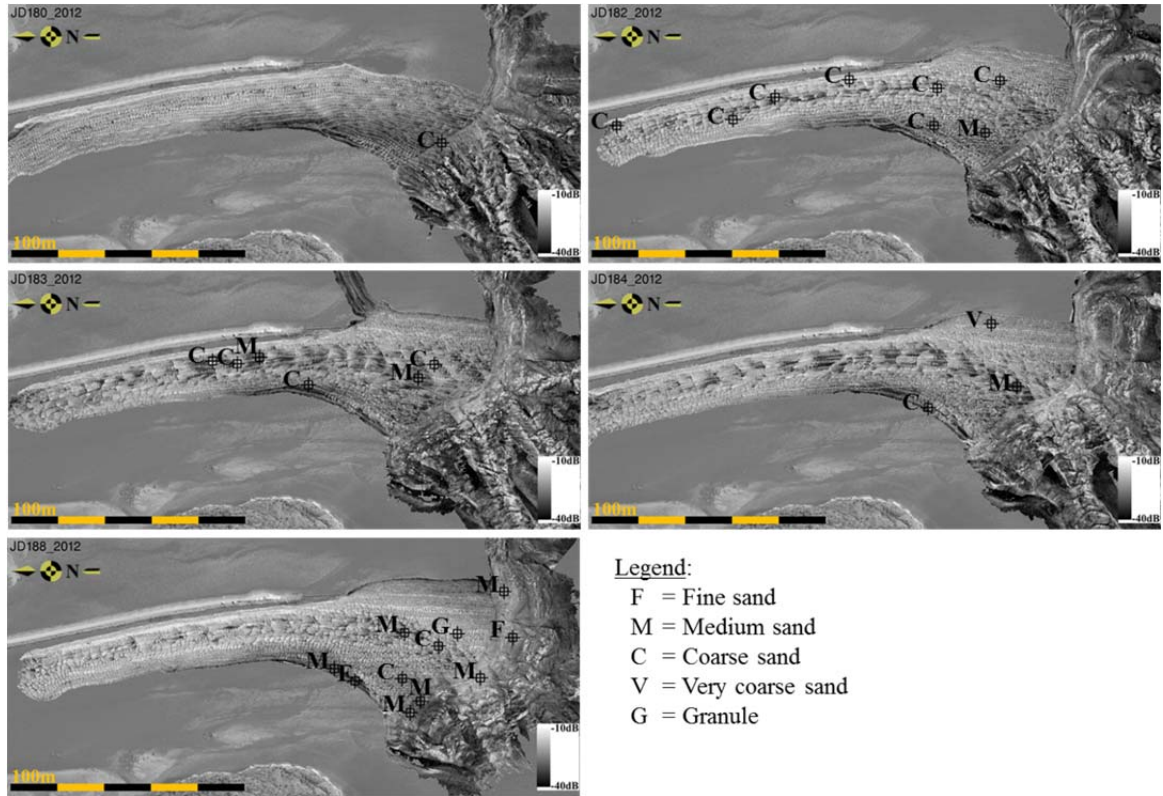
Figure 3.15: Multibeam backscatter image and the location of sediment samples.

The repetitive backscatter mosaics were utilized in this research to infer spatial and

temporal changes in seabed sediment grain-size. The empirical correlations between the

mean grain-size and mean backscatter strength in where the sediment was taken, was

calculated. The association of these quantitative variables can be determined from their

coefficient correlation (Figure 3.16).
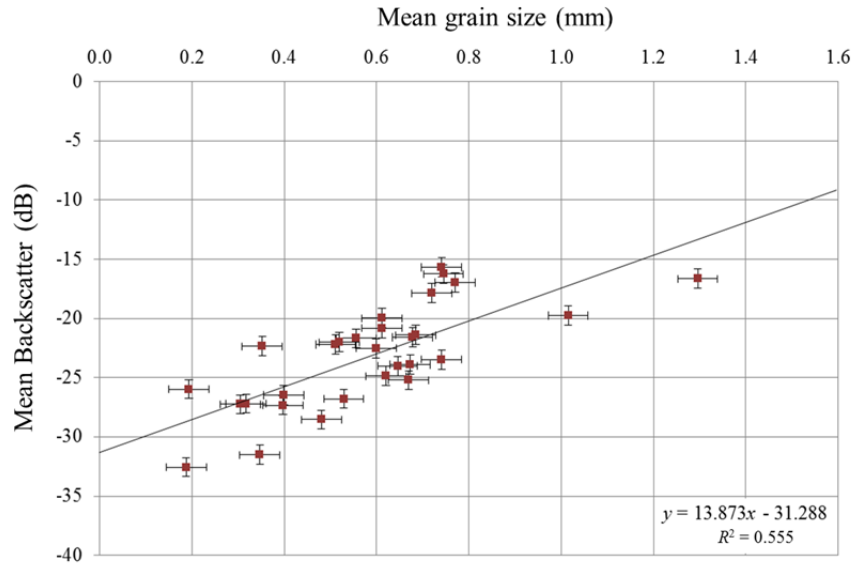
Figure 3.16: Correlation between mean grain-size and mean backscatter strength. The black line represents the trend of the relationship between the mean grain-size and the mean backscatter strength.

Based on the correlation analysis between the mean grain-size and the mean intensity from the data from backscatter image, these variables have moderate relation with the coefficient correlation is 0.555. This is because the grain-size is not the only controlling factor of the backscatter. The size of the grab sampler can also be a controlling factor. The size of the grab sampler may not be representative for the very rapid change of the sediment grain-size on the seabed (Figure 3.17).

The seabed backscatter maps reveal that the sediment type changes rapidly over a distance of just few meters from the stoss to the lee side of the bedform. The positioning accuracy of the grabs is only approximately 2.0 to 4.0 m due to cable angle and timing uncertainly between grab closure and vessel position.

The other factor that may affect the relation between the grain-size and the backscatter is the use of relatively low frequency sonar for this depth. This might penetrate to sub layer of the seabed, thus the backscatter does not come from the sediment and water boundary, but from sublayer. Another possibility is that the backscatter map is derived by mosaicking several overlapping lines from the neighboring swaths. The backscatter from one survey line to the other may not collect the same bedform properties as in this case the bedforms change rapidly.
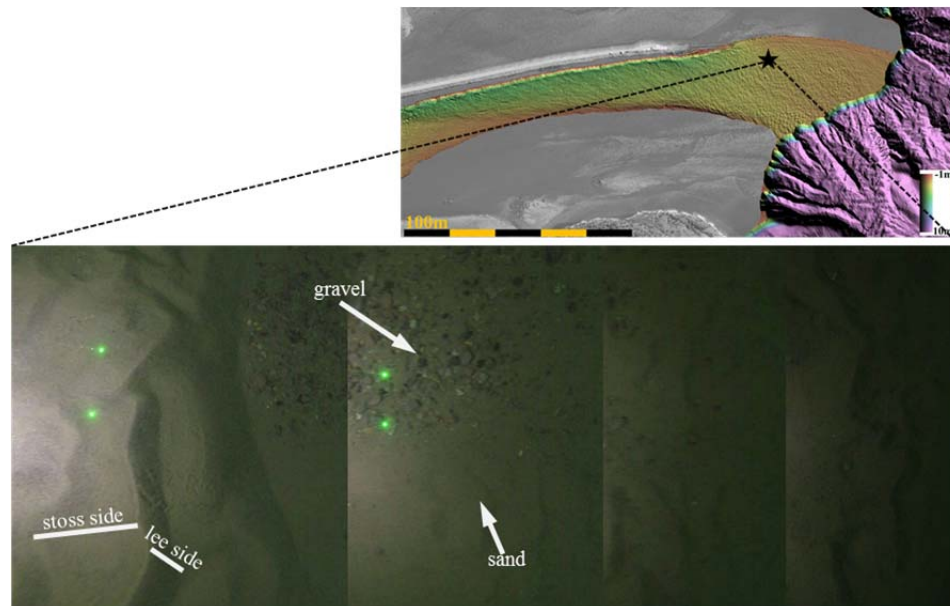
Figure 3.17: The unregistered mosaic of underwater photos shows the spatial variation of the sediment distribution on the delta top.

3.3.3. Total Suspended Sediment analysis

In order to characterize the washload sediment in this area, a Kemmerer bottle was used to collect water samples. The mass of washload sediment retained on the filter per unit volume of the water sample was then compared with data from optical backscatter probe attached in the underway profiler.

Using the observed correlation between optical backscatter and physical sampling of suspended solids, the optical backscatter data can be used to rapidly map spatial and temporal variation of suspended solids. The empirical calibration between the optical backscatter data and TSS analysis can be seen in Figure 3.18. These data are strongly correlated with the coefficient correlation is 0.827.

$$y = 701.95x - 1.504$$
$$R^2 = 0.827$$
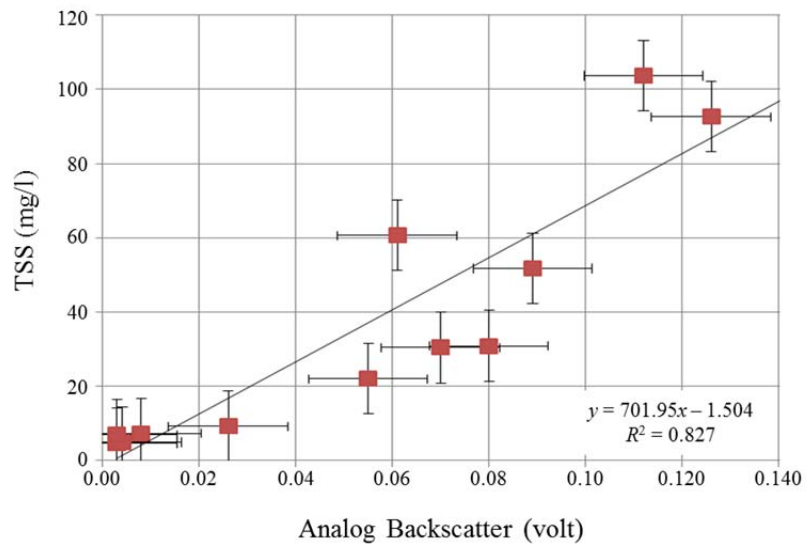
Figure 3.18: The relation between total suspended sediment and analog backscatter data.

The optical backscatter data collected in this research provides the suspended sediment in the river during high tide. However, the suspended sediment load off the delta lip was also taken at low water. Figure 3.19 shows transects of underway profiler where the samples were taken. The time when the samples were taken overlaid with the average river discharges during the observation period is shown on the bottom of this figure. The small vertical lines are all available data and the long vertical lines are the samples data used as representatives.
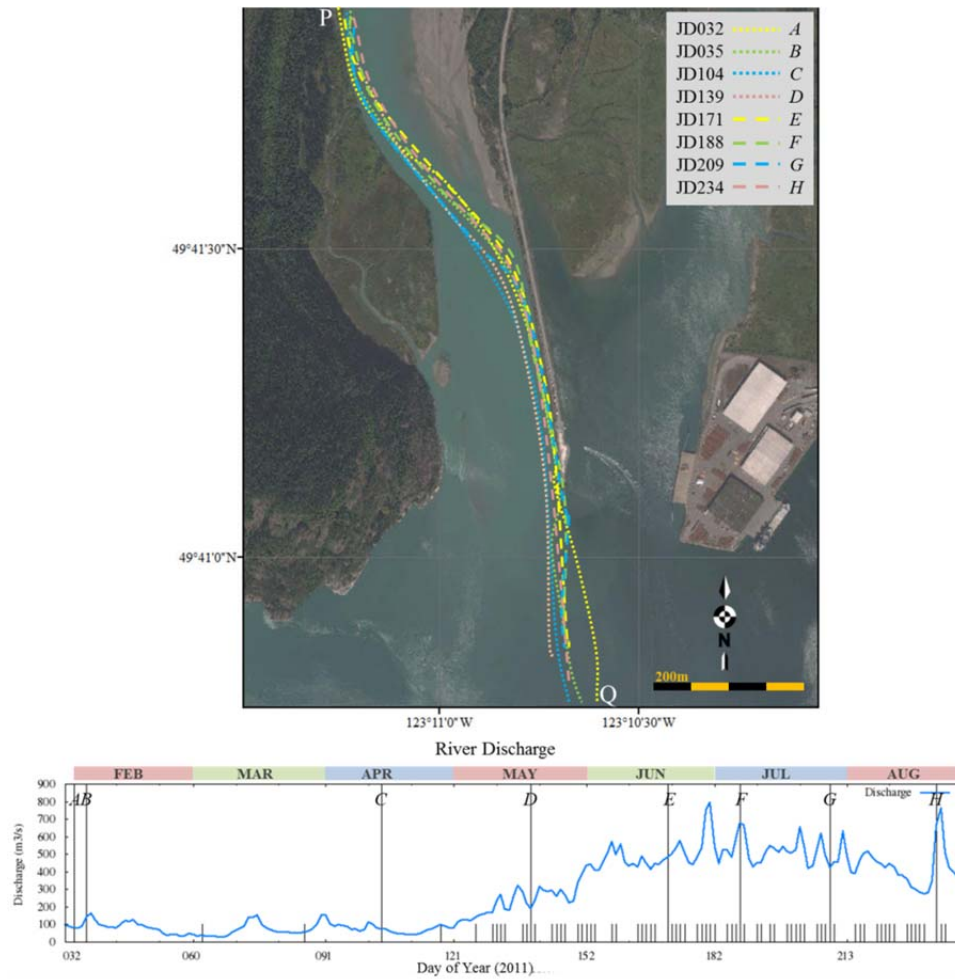
Figure 3.19: Transects of underway profiler (top) and the river discharge condition during the observations time (bottom).

The optical backscatter profiles shown in Figure 3.20 indicates that suspended sediment becomes much more pronounced in summer (*E*, *F*, *G*, *H*) than in winter (*A*, *B*), as high discharge happens during summer.
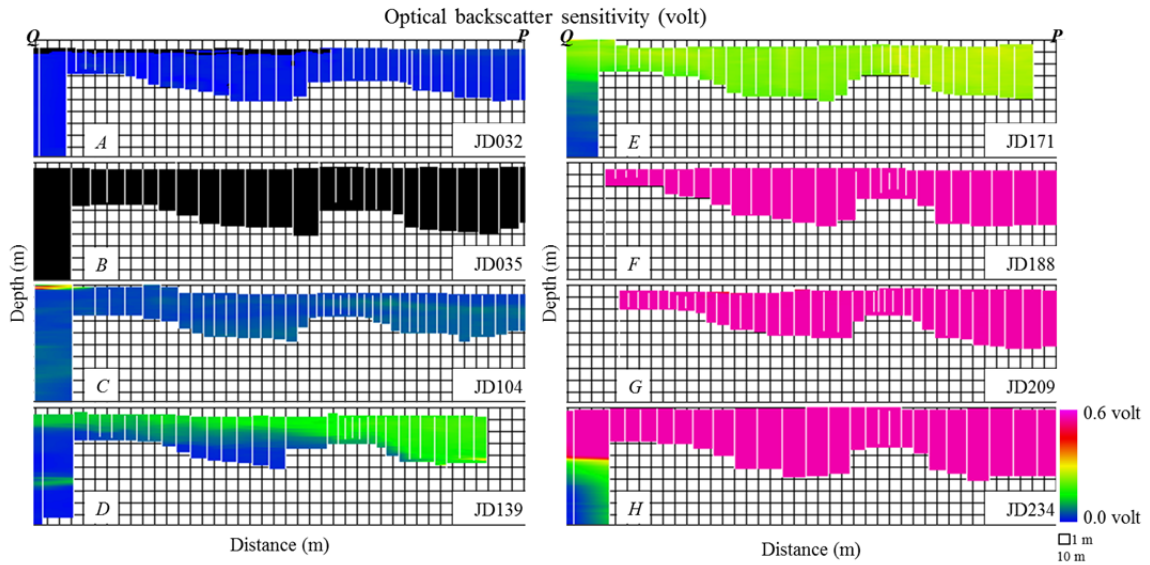
Figure 3.20: Optical backscatter data collected from underway profiler [Taylor, 2012].

3.4. Oceanography Dataset

3.4.1. Tide observation

The tidal modulation of the river is a major control on the focus of this thesis. Furthermore the operational implementation of the field program depends on the tides. As stated earlier, the PPK height solution was not reliable for this research because its lacking sufficient data observations.

In this research, the tide observation was used for vertical correction of the bathymetric data as well as a forcing condition for the hydrodynamic model. The research used tide observation at Point Atkinson which was downloaded from Fisheries and Oceans Canada website. This permanent tide gauge station is maintained by Fisheries and Oceans Canada and it has been operating since 1897 ["Fisheries and Oceans Canada: Tides, Currents, and Water Levels," 2008]. The approximate location of this gauge is at latitude 49° 20' 24" N and longitude 123° 15' 00" W (Figure 3.21).
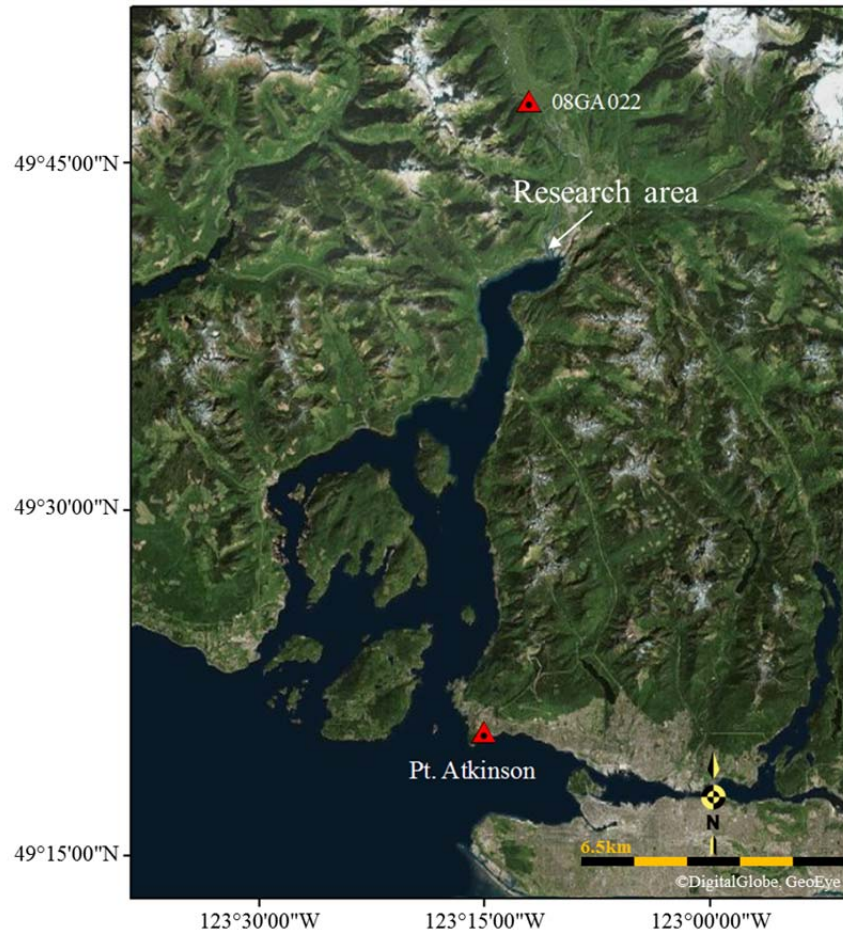
Figure 3.21: The location of permanent tidal station at Point Atkinson and river discharge station 08GA022 (Squamish near Brackendale)

54

Point Atkinson is a major reference port which has similar tidal constituents'

characteristics as the Squamish delta top. While this lies at the mouth of Howe Sound,

which is approximately 40.0 km south of the research area, the deep water means that

there is less than a 5 minute phase lag between Point Atkinson and the Squamish River

without discernible amplification (less than 5.0 cm). The amplitude and phase of the tidal

constituents at the Squamish River and Point Atkinson are given in Table 3.4.

Table 3.4: Major tidal constituents of Point Atkinson and the Squamish River (Fisheries and Oceans
Canada)

Name of Partial Tides	Symbol	Point Atkinson		Squamish	
		Amplitude (mm)	Phase (degree)	Amplitude (mm)	Phase (degree)
Mean Tide	Z_0	3090	0.0	3139	0.0
Diurnal Components					
Lunisolar diurnal	K_1	862	165.8	874	166.5
Principal lunar diurnal	O_1	483	151.7	492	152.7
Principal solar diurnal	P_1	268	163.4	271	164.4
Semidiurnal Components					
Principal lunar	M_2	918	159.3	942	159.3
Principal solar	S_2	229	179.9	232	180.1
Large lunar elliptic	N_2	184	135.4	194	136.4
Lunisolar semidiurnal	K_2	62	179.2	63	186.3

All the constituent phases are within 1° and the highest rate of tide change is

approximately 3cm/minute and thus up to 6 - 12 cm of error could be present during the

peak flood or ebb tide. All the surveys, however, were done very close to high water when the rate of change of tide is a minimum.

The average differences of the amplitudes of all the constituents are about 1 to 2% higher in the Squamish River. Thus during a 5 m tide, the high water could be off by 5 to 10 cm. However, as again, all the surveys were run at high water, the relative differences between surveys are much smaller.

The tide in the Squamish River has a pronounced diurnal inequality (Figure 3.22). This tide characteristic has a large impact on the flow field in this area. Between the two high waters and the high low water, the current velocities do not change significantly. Yet between highest water and lowest water, the current velocity changes significantly. This is important, as the peak of the current which is sufficient to move the sediment only happens once a day and to capture this event using multibeam is not possible. The only possibility of taking a bedform snapshot using multibeam is during high water. At this time the bedform population is inherited from the previous high velocity event which was the last lower low water.
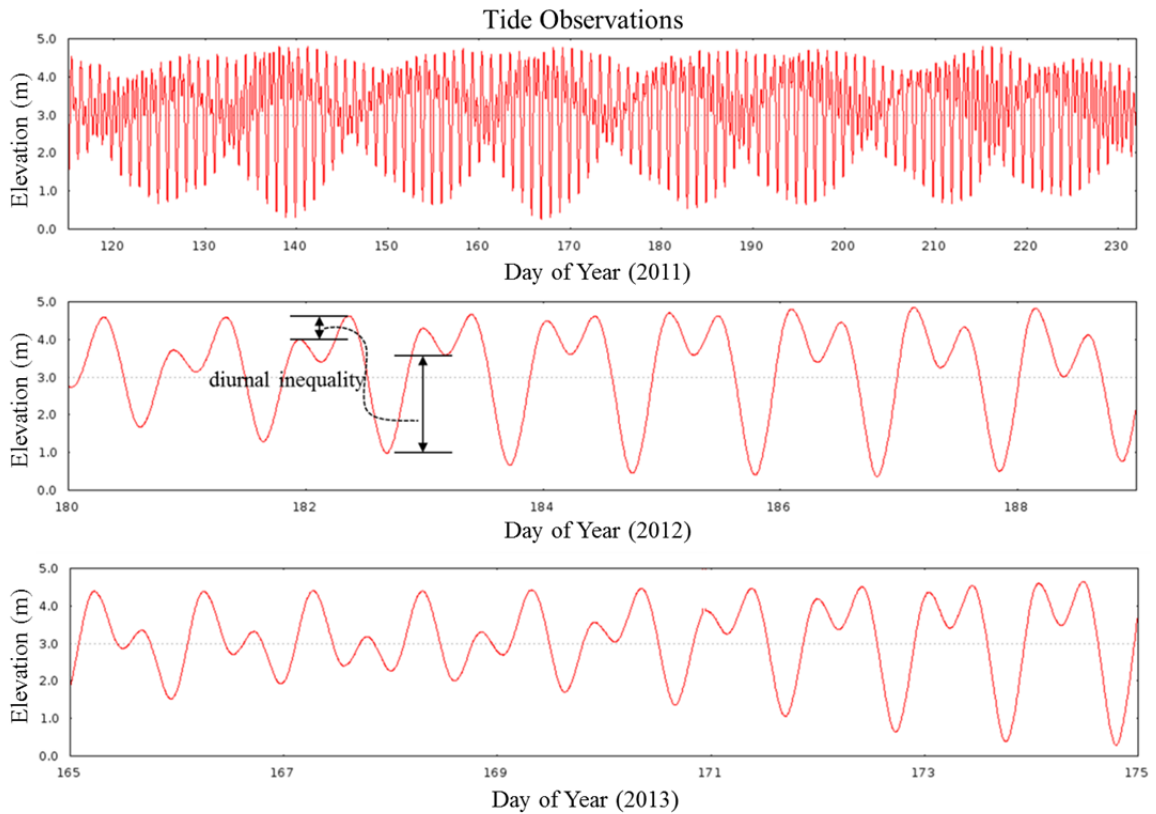
Figure 3.22: Tide observations during the time of observations. The tides show the diurnal inequality.

At high tide the current velocities are expected to be relatively slow compared to those at lower low water. When the tide is high, the water covers the intertidal zone. In this situation, the flows diverge toward the fjord (Figure 3.23a). But when the tide drops, it exposes the western and eastern intertidal zones and only the subtidal area is covered by water. Therefore, the flows are expected to be focused within this area. This focusing creates the jet at the river mouth (Figure 3.23b) and is responsible for most of the sediment transport.
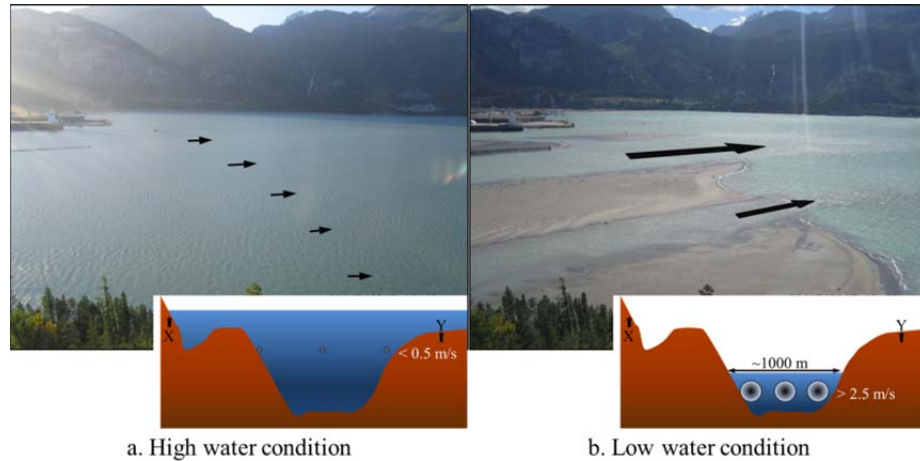
Figure 3.23: The flow is weaker during high tide (a) and the flow is focusing at the lowest tide (b). The black arrows represent the current flow. The bigger arrow shows the larger current magnitude.

3.4.2. River discharge

In addition to the tide modulation, the current velocities and the sediment migration on the delta top are also affected by the variation of the river discharge. The research used daily river discharge data which was downloaded from Environment Canada [https://wateroffice.ec.gc.ca]. The river discharge is recorded from station 08GA022 (Squamish River near Brackendale). This river gauge station has recorded the discharge and elevation of the Squamish River since 1920 ["Water Office - Environment Canada," 2011]. The geographical location of this station which is approximately at latitude 49° 47' 39.984" N and longitude 123° 12' 00" W (see Figure 3.21).

The average discharge during summer 2011 observation was 403 m^3s^{-1} with minimum and maximum discharges of 79 m^3s^{-1} and 793 m^3s^{-1}, respectively. The minimum discharge occurred on JD120 (April 30, 2011) and the maximum discharge was on JD181

(June 30, 2011). Throughout the summer 2012 observation period, the mean discharge

was 526 m^{3}s^{-1}; the lowest was 446 m^{3}s^{-1} on JD180 (June 29, 2012) and the highest was

627 m^{3}s^{-1} on JD182 (June 30, 2012). Within the summer 2013 period, the mean discharge

was 418 m^{3}s^{-1}, slightly lower than 2012, with minimum and maximum discharges of 300

m^{3}s^{-1} on JD165 (June 14, 2013) and 494 m^{3}s^{-1} on JD168 (June 17, 2013). The daily

average of the discharge data for the year 2011, 2012 and 2013 can be seen in Figure

3.24. The shadowed areas are the discharge when the surveys were undertaken.
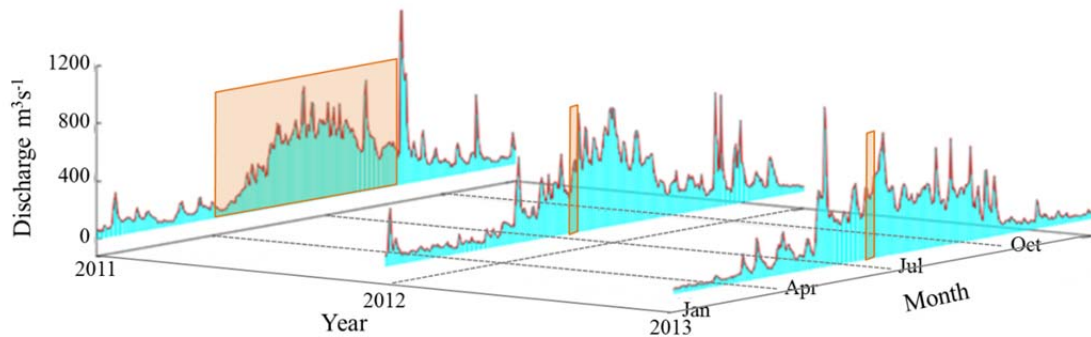
Figure 3.24: River discharge data in the year 2011, 2012, and 2013.

3.4.3. Sound speed

Working in an estuarine fjord environment and in the proximity of a river plume, the

spatial and temporal variability in sound speed is an obvious source of bathymetric

measurement uncertainty [Hughes Clarke et al., 2011]. In order to minimize this

uncertainty, an underway profiling system (BOT MVP-30) is utilized for measuring

sound speed. It does not directly measure the sound speed, rather derives it from

observation of conductivity, temperature, and pressure.

59

This sound speed was applied directly to the multibeam acquisition software in order to mitigate the sound refraction effects. Representative sound speed sections along the river up to just beyond the lip of the delta were undertaken for most surveys. To get more frequent data of sound speed near the surface, a sound speed probe is mounted directly beside the multibeam system.

Figure 3.25 displays the sound speed variability for the same 8 periods shown in Figure 3.20. During the summer months, sound velocity on the delta top does not vary significantly as it is all fresh water (*E*, *F*, *G*, and *H*).
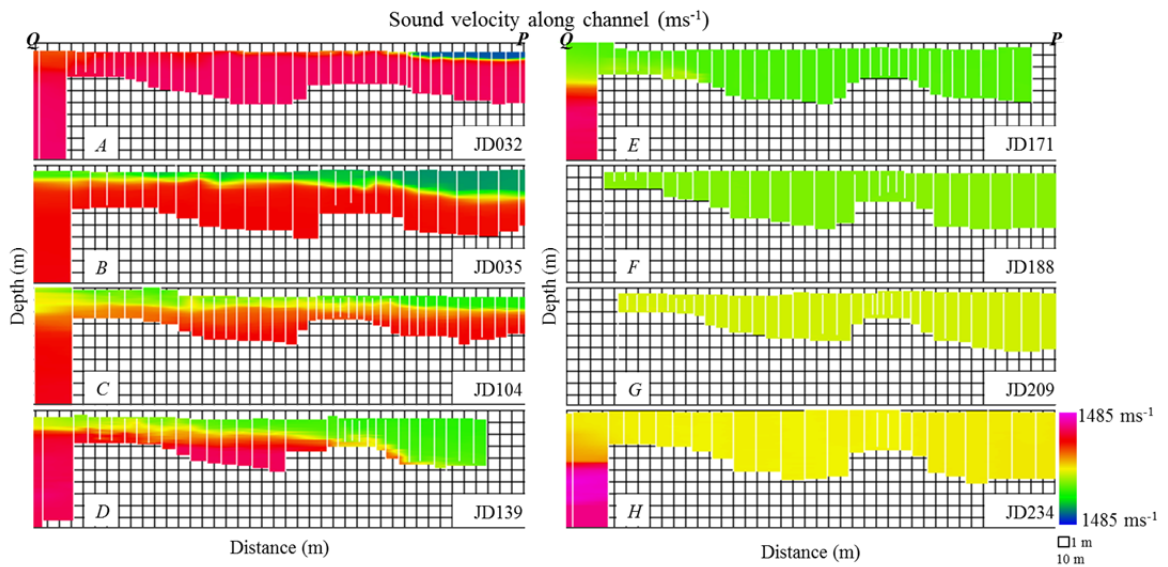
Figure 3.25: Sound velocity profile of the Squamish River [Taylor, 2012].

3.4.4. Salinity and temperature

The temperature and salinity output from the MVP was used to describe the oceanography on the delta top. This allows one to see the extent of penetration of the salt wedge into the estuary in the summer. The temperature and salinity information were used to confirm that salt water penetration does not take place during summer discharge periods.

Figure 3.26 and 3.27 show the variation of salinity and temperature respectively for the same 8 periods as in Figure 3.20 and Figure 3.25. The evidence that the salt water does not penetrate up the river during summer can be seen in Figure 3.26 (*E*, *F*, *G*, and *H*).
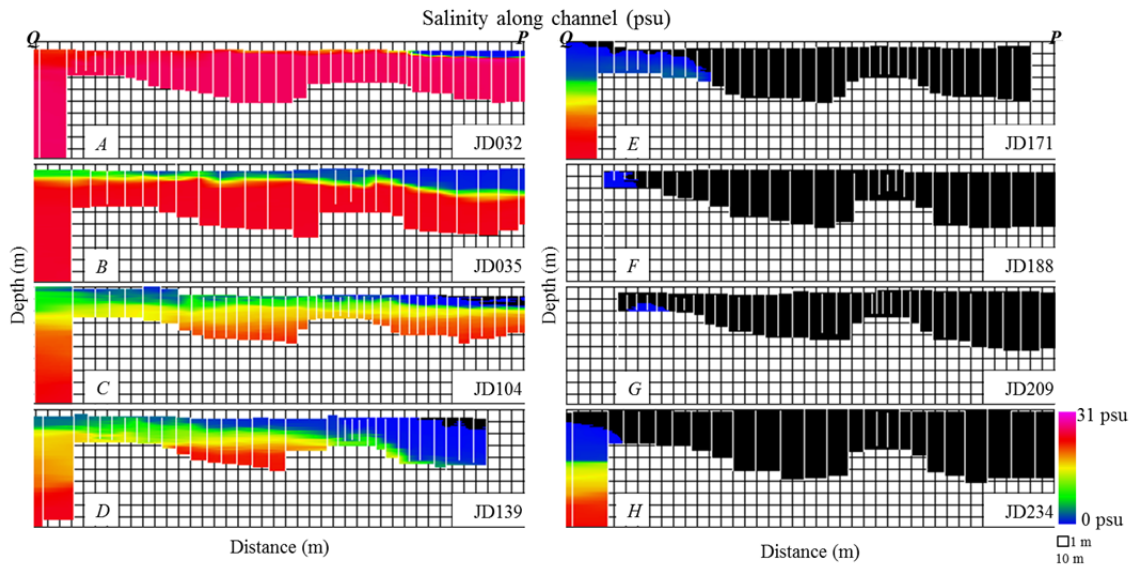
Figure 3.26: Salinity profile of the Squamish River [Taylor, 2012].
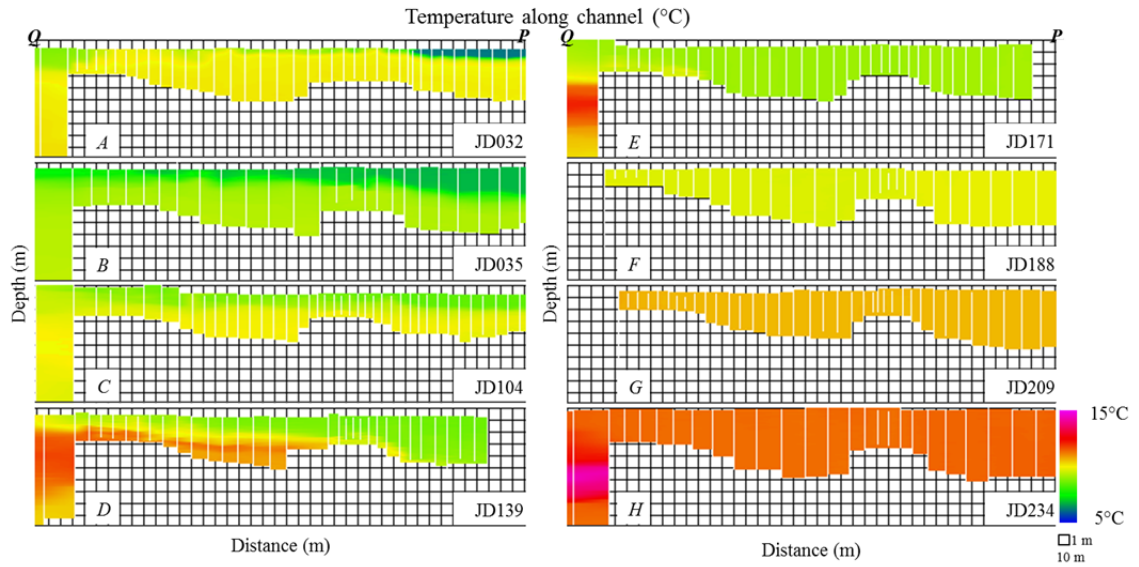
Figure 3.27: Temperature profile collected using underway profiler [Taylor, 2012].

Chapter 4: Parameterization of the Delta Top Geomorphology

Bedforms are ubiquitous features in sand-bed rivers and estuaries. They can be represented as dunes and ripples. It is assumed that the dimensions of the bedforms are controlled by the bedload transport [van Rijn, 1985]. The change of bedform roughness affects the spatial and temporal variability in flow fields and vice versa.

Much research in developing relationships between bedform and their controlling environment have been established in laboratory flumes with unidirectional steady and uniform currents. However, that ideal, steady, and uniform relation can be rarely achieved in a tidal setting as the flow is not unidirectional and it is dynamic [Kostaschuk & Best, 2005].

4.1. Bedform Characteristics and Flow Regimes

One of focuses in the research is to characterize the bedform morphology associated with flow conditions in the research area. The bedform morphology in a channel is related to how the sediment is transported by the flow. The movement of the sediment in a channel depends on the grain settling rate and the shear stress at the boundary layer. The settling rate describes the tendency for sediment particles to fall out of suspension, and the

boundary layer shear stress describes the tendency for moving fluid to bring sediment particles into suspension (or moving along the bottom) [Lemke, 2015].

The movement of the bed material in a unidirectional flow channel was extensively studied by Simons & Richardson (1966). They classified the geometry of the bedforms based on flow regimes under which the bedform is developed. This concept is widely accepted and used by sedimentologists.

Based on the Simons & Richardson (1966) concept, the roughness of the bedform in an alluvial channel can form over a variety of discrete stages. Those stages are: [1] a plane bed without sediment movement, [2] ripples, [3] ripples on dunes, [4] dunes, [5] plane bed with sediment movement, [6] anti-dunes, and [7] chutes and pools. These bed configurations are listed in their order of occurrence with increasing value of stream power for bed material having a median diameter, d_{50}, less than 0.6 mm. For bed material coarser than 0.6 mm, dunes form instead of ripples after the beginning of motion at small values of stream power. Notably the Froude number was chosen as the parameter best suitable for characterizing the flow that is associated with the bedform sequence.

The concept of bedform sequence is useful in describing bedforms because it provides a basis for a qualitative appreciation of the relative flow strengths that are required to form them. Not all of the bedforms described in this sequence will develop on a bed of any one size of sediment; some bedforms are limited to coarse bed material while others are limited to fine bed material. This sequence is hypothetical, but is one that provides valuable insight into the interpretation of bedforms and their stratification [Cheel, 2005].

In order to characterize the flow derived from the hydrodynamic model, a representative metric was needed to correlate with observed bedform populations and sediment volume changes. Two choices were considered: the bed shear stress and the Froude number. The bed shear stress is clearly the driving factor controlling sediment transport. However, for this study, the primary morphologic indicator extracted was the bedform morphology rather than the sediment grain size. The bed shear stress can be derived from the depth-averaged flow and the bed roughness. In this case, however, the bed roughness was seen to be another variable that was hard to define (see discussion in hydrodynamic modelling) as it changed with the bedforms. As a result the Froude number was preferred. In reality, both of these are strongly linked to the depth averaged flow and thus are probably nearly equivalent.

In order to understand the development of the bedform on the delta top, this research used the Froude number (F) to represent the flow regime in the area. The Froude number is a dimensionless parameter that describes the flow regime of an open channel flow. This flow competence provides a way of classifying flow conditions based on the relationship between flow velocity and depth.

The Froude number is a ratio of inertial forces to gravitational forces. This parameter reflects the energy condition of water flow and the likelihood of sediment entrainment and erosion. The formula to calculate the Froude number is given in Equation 4.1:

$$F = \frac{U}{\sqrt{gD}}$$

4.1

where U is mean flow velocity, g is acceleration due to gravity and D is hydraulic depth. The mean flow velocity in this research was derived from the hydrodynamic model.

The Froude number classifies deep slow flow as subcritical, and this occurs when F is less than 1.0. Subcritical flow produces a low energy state. Critical flow occurs when F is equal to 1.0; there is a perfect balance between the gravitational and inertial forces. Supercritical flow is shallow and fast, and occurs when F is more than 1.0, when the river is in a high energy state.

Table 4.1 shows the relationship between the type of current (lower or upper flow regime) and bedform classification. This relationship is partly based on the bedform that are produced under unidirectional steady state flows. The relationships between bedform characteristics and flow conditions were adapted to the strongly tidal and discharge modulated bedform populations in the Squamish River. These should reflect the sediment flux available for the mass wasting processes on its adjacent prodelta slope.

Table 4.1: Definition of the flow regime concept based on Simons and Richardson (1966)

Flow Regime	Bedforms	Characteristics
Lower flow regime	Lower plane bed, Ripples, Dunes	• $F<1.0$ • low rate of sediment transport, dominated by contact load; • bedforms out-of-phase with the water surface.
Upper flow regime	Upper plane bed, Chutes and pools	• $F>1.0$ • high rates of sediment transport, high suspended load; • bedforms in-phase with the water surface.

Simons and Richardson (1966) noted that the bed configuration at a smaller discharge will be a remnant of the bed configuration formed when sediment was moving. Thus, as part of this thesis, when trying to correlate stream power with bedform population, relict populations may be present which do not reflect the most recent measure of stream power. In the context of the Squamish River, the observed bedform population is expected to be a proxy for the recent flow conditions, which are represented by the Froude number.

The work undertaken as part of this thesis provides an opportunity to quantitatively assess bedform characteristics and investigate if a related metric can be extracted that correlates with flow regime. On a riverbed dominated by coarse sand, just as the flow strength exceeds the threshold required for sediment movement, the first bed configuration should be a flat, planar surface. The lower plane bed will only form on beds of sediment coarser than 0.7 mm and is characterized by its planar surface and relatively low rates of sediment transport. The limitation of lower plane beds to relatively coarse sand indicates that this bed configuration will only form under dynamically rough turbulent boundaries [Cheel, 2005]. This might be of concern in the Squamish River as the grain-sizes extend up to coarse sand.

The occurrence of a particular bedform type is not exclusive in a natural river or a plume. The type usually varies spatially and temporally. The bedform morphology may vary over multiple roughness scales and may form in sequence related to variation in shear stress, stream power or reaction of bed material to a given stream power [Simons & Richardson, 1966].

The bedform morphology on the delta top qualitatively varies in time and space. Figure 4.1a shows the terrain model JD181 2011 as an example bedform morphological variation in the delta top. The observation on this epoch was taken immediately after the mass wasting event (will be discussed in Chapter 6). This figure shows that the bedforms on the delta top vary from smaller to relatively longer wavelength over this area. The depth variability along the river thalweg (segment L_1L_2 in Figure 4.1a) is represented in Figure 4.1b. The depth along this line has the tendency to get shallower after the training dyke until it crosses the mouth bar at the lip of the delta. The depth drops abruptly on the delta slope.

The typical depth across the channel can be seen from the depth profiles of crosswise segments (A_1A_2, B_1B_2, and C_1C_2 in Figure 4.1a). Figure 4.1c illustrates that the depth on segment A_1A_2 abruptly changes as it approaches the wall of the training dyke. The depth on segment B_1B_2 gradually changes from western intertidal zone to the training dyke. Across the broad mouth bar there are only small depth variations on segment C_1C_2.
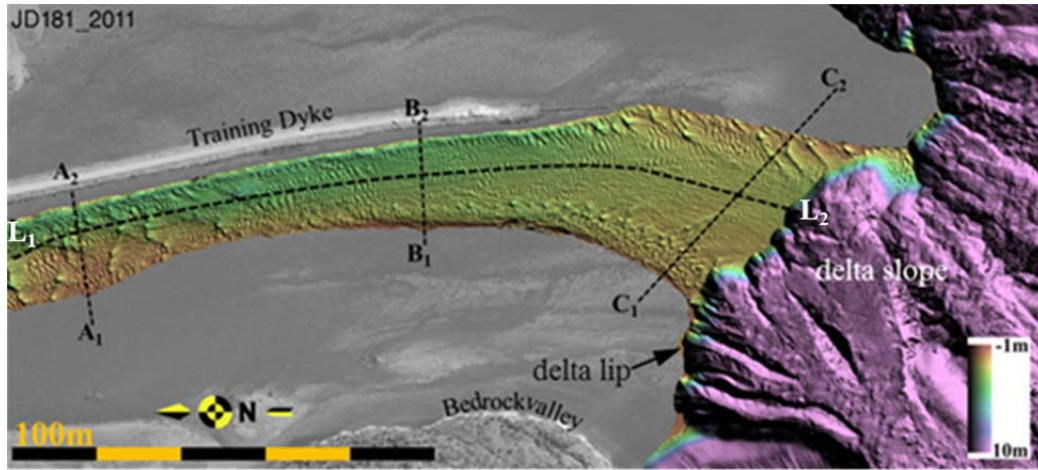
a. A segment along the channel (L_1L_2) and segments across the channel (A_1A_2, B_1B_2, and C_1C_2).
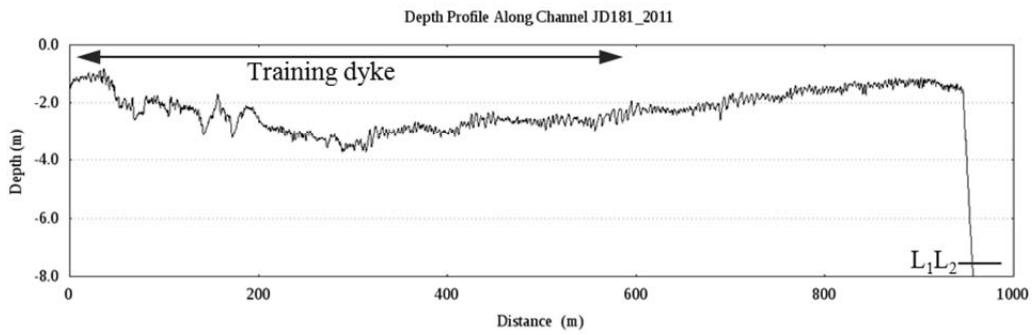
b. Depth profile along the channel.
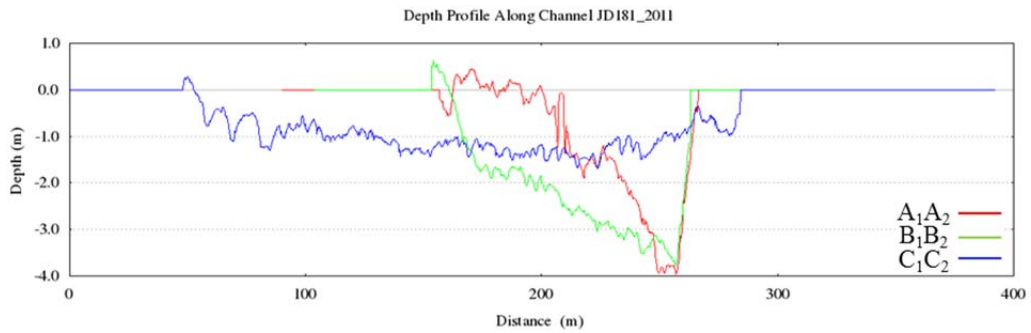
c. Depth profiles across the channel.

Figure 4.1: Depth profile along and across the channel.

69

The ratio between width and depth of a channel affects the probability of spatial variability in bed shear stress, stream power, and bed material. The greater the width-depth ratio of a stream, the greater the probability of spatial variations [Lemke, 2015]. Thus, the occurrence of multiple roughness values is closely related to the width-depth ratio of the stream. In this case, the heterogeneity of bedforms is also related to the width-depth ratio, which varies with tide modulation and river discharge.

Figure 4.2 shows magnified areas around the cross sections shown in Figure 4.1a. This figure shows how the bedforms vary at those localities. Figure 4.2a and 4.2b are in the vicinity area of segments A_1A_2 and B_1B_2 which are constricted with the training dyke. Figure 4.2c is the locality of segment C_1C_2 which has no man made constriction.
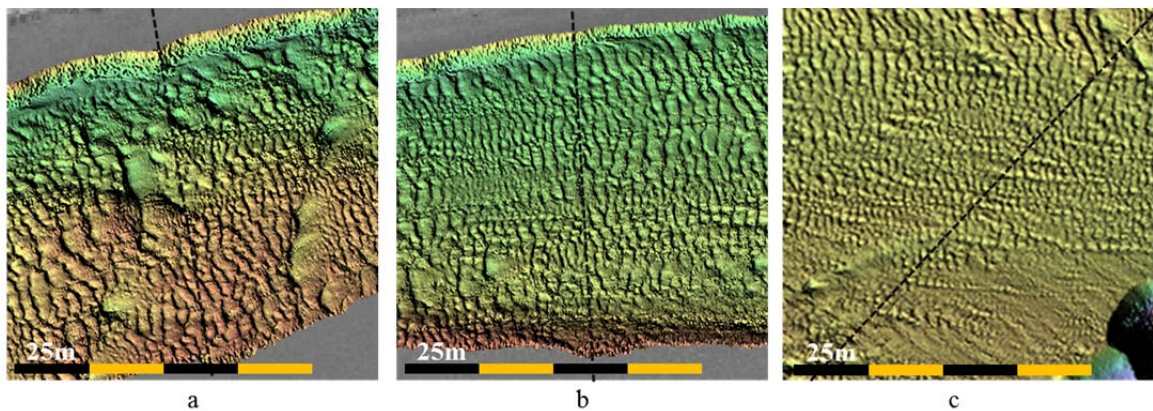
Figure 4.2: Bedforms distribution in the Squamish River based on width-depth ratio. The variation of the bedforms on the proximity area of segment A_1A_2 (a), B_1B_2 (b), and C_1C_2 (c).

In order to understand the evolution of the bedforms on the delta top as well as on the delta edge, several approaches were undertaken in this research. These approaches

parameterize both the short wavelength bedform population as well as the long wavelength channel relief on delta top. The parameterization of the delta top combined with the flow parameter, was used to understand sediment transport on the Squamish delta top. That transport is expected to be a primary control on turbidity currents and mass wasting events on the delta slope.

This research used several approaches in order to parameterize the bedform characteristics and channel shape on the delta top: 1D and 2D spectral analysis, surface roughness characterization adopted from ASME, and depth analysis along and across the channel. The progradation and retrogradation of the delta lip were also monitored in this research in order to see whether changes in the delta lip shape affect both the short wavelength bedform characteristics and long wavelength channel shape on the delta top.

The sediment volume changes on the delta top and at the vicinity of the delta lip were also examined in order to robustly monitor the day to day sediment fluxes on these areas. The aforementioned methods will be discussed in more detail in the next sections.

In order to parameterize the short wavelength bedform characteristics and long wavelength channel shape, the research used area A (Figure 4.3) as representative of the delta top. This area covers an evolution of bed and channel morphologies from the constricted to unconstricted zone. This area is the transition from constrained channel flow to lateral expansion over the mouth bar.

Area B (Figure 4.3) is a rotated map that has approximately the same orientation as the delta lip. This area is used to monitor the evolution of the delta lip over time as well as the changing sediment volume due to off lip deposition and collapse. Both area A and area B illustrated in Figure 4.3 are important in controlling the flux of fluvial sediment that feeds turbidity currents and mass wasting events on the adjacent prodelta slope.

Figure 4.3: The area on the delta top for examining bedform roughness distribution and volumetric characterization. The area A is from constricted with the training dyke and intertidal wall to unconstructed area. The area B is the delta lip area.

4.2. Spectral Analysis of Bedform Morphology

Traditionally, geologists would qualitatively interpret sidescan images or sun-illuminated terrain models to decide what type of bedforms are represented in an area of interest. This research attempted to utilize spectral analysis using the Fourier algorithm [Cazenave, Lambkin, & Dix, 2008; Lefebvre & Lyons, 2011] to quantify the dominant wavelength of the bathymetry maps of area A in Figure 4.3. The area A was used to represent bedform roughness on the delta top as the most obvious feature.

Both 2D and 1D spectral analyses are used in this research. While usually this area is dominated by bedforms with 2.0 to 10.0 m wavelength, which can be solved using a 2D spectral analysis of a window narrower than the channel width (discussed in section 4.2.1), sometimes longer wavelength dunes exist extending over distances greater than the channel width (approximately 50.0 m). To address the spatial variability of these larger bedforms, a 1D spectral analysis was used along the channel axis (discussed in section 4.2.2).

4.2.1. 2D spectral analysis

A three dimensional bathymetry model of area A, represented as a Digital Terrain Model (DTM), was constructed for each survey epoch. These DTMs were quantitatively analyzed using 2D spectral analysis to examine the roughness spectrum. To perform this analysis, the DTM acts as a two dimensional object. The formula of Fourier transform algorithm used in this research is given in Equation 4.2:

$$F(u,v) = \frac{1}{N} \sum_{x=0}^{N-1} \sum_{y=0}^{N-1} f(x,y)\, e^{-2\pi j(xu+yv)/N}$$

<div align="right">4.2</div>

where $f(x,y)$ is the spatial signal (the DTM dimensions $N{\times}N$) as a function of the x and y

direction and $F(u,v)$ is the amplitude as a function of the u and v frequencies and j is

$\sqrt{-1}$.

A custom 2D Fourier transform tool was developed in this research to automatically

assess the roughness characteristics of a bedform. This tool is embedded in the OMG

multibeam processing software, and is an addition to the terrain model viewing tool

(jview). The window of this tool can be seen in Figure 4.4. The terrain model to be

analyzed is shown in area 8. This terrain model can be scanned interactively using a 256

$\times$ 256 pixels movable window (9) to get bedform characteristics.

The DTM within the movable window (area 1 in Figure 4.4) is prepared using a series of

procedures which will be explained in the next section, after which is ready to be

analyzed using 2D spectral analysis to get the dominant wavelength and orientation of the

area within the movable window. However, this tool does not store the bedform

characteristic result, it is only for viewing and it used for examining and determining the

appropriate global parameters on 2D spectral analysis to be subsequently extracted in a

command line program.
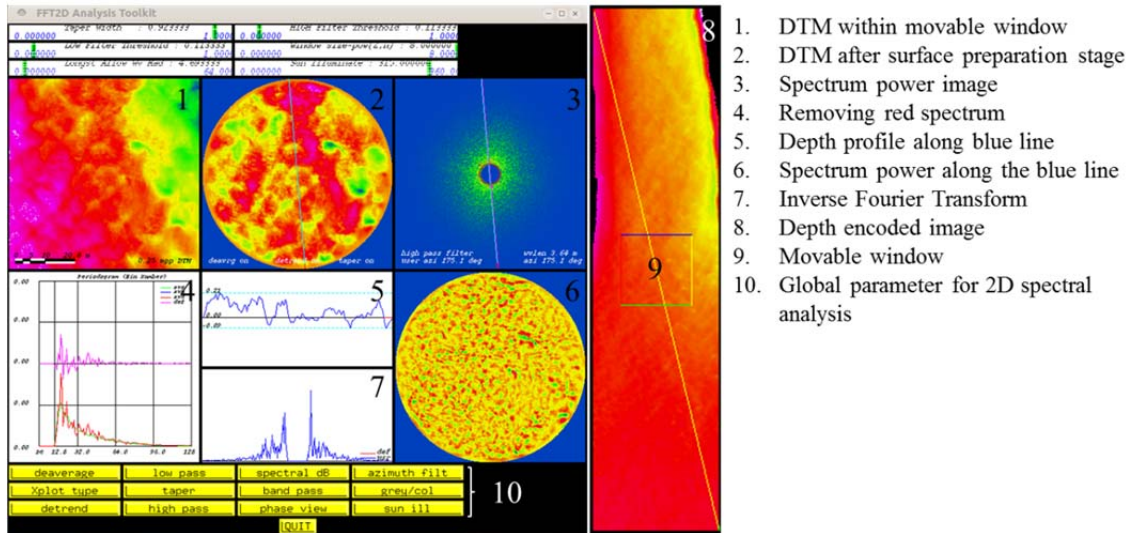
Figure 4.4: Spectral analysis tool used for examining and determining global parameters on 2D spectral analysis in a command line program.

Both the 2D spectral analysis tool and the command line program used the same algorithms. There are three stages implemented on these programs: [1] surface preparation, [2] wavelength extraction and [3] spectral peak selection.

4.2.1.1. Surface preparation

For each window viewed, there are three steps automatically computed before the dataset is processed in order to achieve a better highlight of dominant peaks in the spectrum. First, the mean depth was removed to minimize the energy in the centre of a spectrum image (the static bias component). In the terms of Fourier transform, if the dataset has a

static bias (i.e. the average is not 0), there will be a lot of energy in the first (zero wavenumber) bin. Removing the static bias will improve the Fourier transform solution.

The second step is removing the mean slope (de-trending). A two dimensional dataset still has a surface trend, even if the mean depth has already been removed. It also affects the bias term. Thus removing the mean slope will provide a better solution for the 2D spectrum. In this case, removing the mean slope is performed using the first order linear trend.

The third step in surface preparation is tapering the edges of the DTM. Tapering will remove a spectral leakage which is caused by using a rectangular window [Cazanave, 2008, Lefebvre & Lyons, 2011]. A non-zero value at the edge of the surface window will result in a step in presumed infinitely repeating pattern. Applying a symmetric tapering function to the dataset removes spectral leakage associated with the finite dataset. These spectral analysis programs have cosine tapered window type with the width specified as a fraction of the window width from 0.0 to 0.5.

4.2.1.2. Extracting the dominant wavelength

After surface preparation, the 2D spectral power of the DTM is then calculated using formula 4.2. The 2D spectral power can be represented in linear or logarithmic unit. The relation between linear and logarithmic units as follows:

$$Fp = 20 \log_{10}|F| \qquad\qquad 4.3$$

where *F* is the amplitude of spectral power in linier unit and *Fp* is the spectral power amplitude in logarithmic unit.

The spectral power comprises positive and negative frequency components hence the spectrum has two peaks which mirror each other. In this case, only half the spectrum (0º - 180º) was considered for further analysis, therefore all the orientations are given in modulo 180º.

As with most natural terrains, the roughness is represented as a "red spectrum" with more power in the longer wavelength. That is true for all azimuths and the average of the spectrums in all directions reflects the isotropic roughness spectrum (azimuth invariant). To remove this isotropic component, the average variation in spectral power with wave number is calculated for all azimuths from 0º to 180º in one degree steps and then averaged. This averaged roll off in power (logarithmic units) is then fitted with a linear regression. In order to obtain the residual spectrum, the observation spectrum is subtracted using the linear fit. The result is a residual spectrum that should reflect just anomalous local spectral peaks (and dips) relative to the mean red spectrum (Figure 4.5).
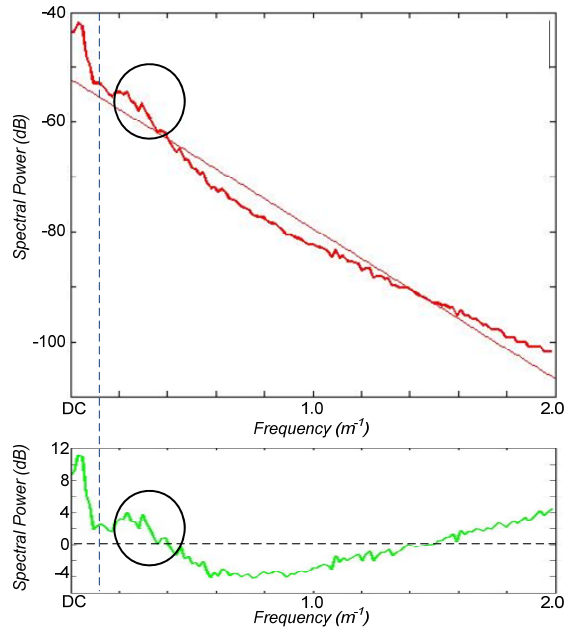
Figure 4.5: The average slice (red line) as a "red spectrum" and its linear fit (magenta). The residual plot of the red spectrum is shown in a green line. The area to the left side of the dash blue line is the truncated wavelength which is very long wavelength bedform. The wavelengths of interest are in the circle.

4.2.1.3. Selection of residual spectral peak

The last stage of the algorithms used in the 2D spectral analysis is selecting a residual spectral peak. Figure 4.6a shows a 0.25 m resolution DTM of riverbed. Figure 4.6b shows the original spectrum of Figure 4.6a. Figure 4.6c shows the extracted/residual spectrum of Figure 4.6b. The dominant peak in a residual spectrum is highlighted better than in its original spectrum.

78

Figure 4.6c shows that the residual spectrum of the bedform of interest looks sparse, except in the vicinity of the zero wavenumber (DC bias) area. This means the low frequency components (long wavelength features) are still present. To address this issue, a maximum wavelength of interest, which is specified by user, was applied as a threshold (the red circle line in Figure 4.6c) to mask the presence of the large scale features (low frequencies). The principal peak is determined from the highest spectral power in the region outside the radius of wavelength interest. This is effectively excluding longer wavelength bedform from the analysis, as they present as an artifact and affect the result of 2D spectral analysis.

The dominant orientation (shown as a cyan line in Figure 4.6b and 4.6c) and the dominant residual wavelength are calculated subsequently based on the position of the principal peak. Additionally the magnitude of the peak is recorded in two ways, absolute and residual. Even if there are no clearly preferred dominant wavelengths, this algorithm will still select a peak. Thus it is necessary to use the residual magnitude as a measure of peak significance.
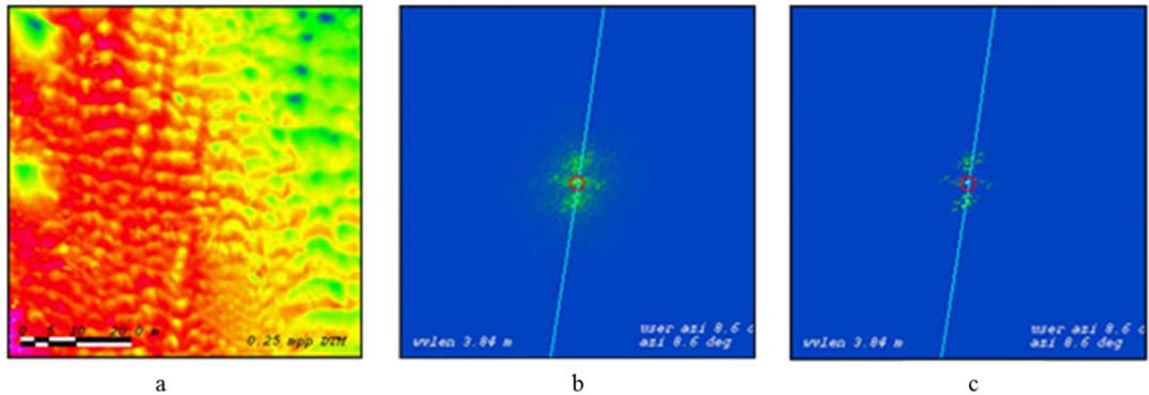
Figure 4.6: A terrain model with 0.25m in resolution (a), a 2D spectrum of the DTM (b), and the residual 2D spectrum (c). The red circle in b and c indicates the threshold for the user wavelength interest and the cyan line in b and c indicates the dominant orientation of the bedform of the terrain model (a).

The aforementioned stages are also implemented in the command line program. The parameters used in this command are based on the 2D spectral analysis tool. A Set of 32 × 32 m windows with an 8 m interval between adjacent boxes was used to perform an automated scan sequentially over area A (Figure 4.7a). The size of the box for scanning was chosen by considering the width of the channel. The boxes are scanned through the mapping region to determine spatial variability of bedform characteristics. The scanning path covers the whole terrain model area reading from north to south and progressing eastward, as shown in Figure 4.7a.

Figure 4.7b shows the dominant wavelength and orientation of the bedform (red arrows). Each arrow represents the roughness properties of a 32 × 32 m window area within a terrain model. The length of the arrow represents the length of the dominant wavelength

and the direction of the arrow represents the orientation of the dominant bedform which is respected to the north. The vectors in this are scaled by 0.25 of the DTM scale for the purpose of visualization. The dominant wavelength and the orientation distribution on the area of interest are represented in Figure 4.7c and Figure 4.7d respectively.
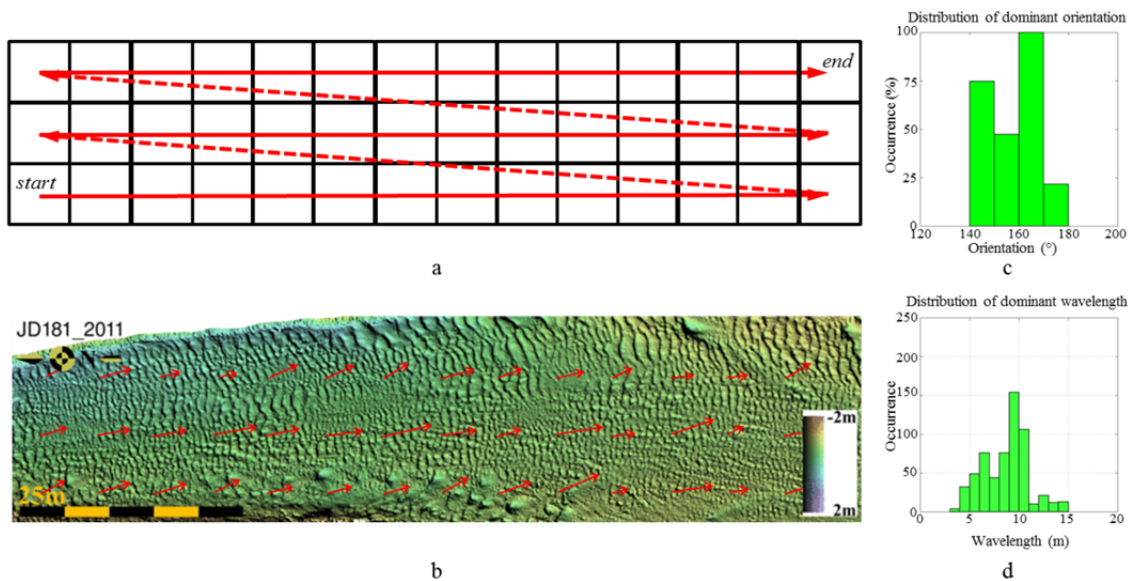
Figure 4.7: The automated 2D spectral analysis of the bedform within the area of interest. The scanning sequential (a), the dominant wavelength roughness represented by black arrows overlaid on the DTM (b), the distribution of dominant orientation (c), and the distribution of the dominant wavelength (d).

This 2D spectral analysis is limited by the window size. It has to be a square size and a power of 2 (2^n). This research used a 32×32 m window size on the terrain model. This means the maximum wavelength that can be solved is 16 m. Additionally, depending on the taper length used, wavelengths shorter than this and approaching 8m can be

81

artificially attenuated. This may be one of the reasons why the dominant wavelength results tended to always peak at ~10m irrespective of the flow conditions.

The reason that the extraction of dominant wavelength was so intensively investigated herein was that it was the preferred method of several previous researchers [Cazenave et al., 2008; Lefebvre, Ernstsen, & Winter, 2013].. In this thesis, this method is used and the results presented in Chapter 6. Based on that analysis, however, it is not clear that those dominant wavelength distributions are providing a useful discrimination of the observed populations. This is believed to be the result of too small a window. In order to look at the full spectrum of roughness, including wavelengths longer than the channel width, a 1D FFT approach was therefore preferred.

4.2.2. 1D spectral analysis

Many researchers have previously used 1D profiles from a single beam echo sounder to characterize bedform wavelength, height, the ratio between the two and the asymmetric of the bedform [Simons & Richardson, 1966; Guy et al., 1966; Allen, 1982; van Rijn, 1993]. They measure from crest to crest to determine these parameters. As the bedform is unidirectional, this research also utilizes 1D spectral analysis to characterize the bedform by using the power spectrum of the roughness to deal with the limitations in 2D spectral analysis.

The width of the river channel is approximately 100 m. This becomes one of restrictions of using this 2D spectral analysis. The maximum window that can be used for this case is

32×32 m ($2^4 \times 2^4$ m). The next size larger window is 64×64 m ($2^5 \times 2^5$ m). Using this window size, wavelengths less than 32 m can be resolved. However, only 1 line can be used for automatic scanning using this window, which is along the centre of the channel (Figure 4.3).

Another restriction of using the 2D spectral analysis with the 32×32 m window is that it does not identify bedforms more than 16 m long, which do occur at certain flow stages in several cases. To address this limitation, this research also utilizes a 1D spectral analysis, using FFT algorithm as an additional approach to parameterize the bedform morphology.

There are 2 independent variables used in 2D spectral analysis (x,y), but there is only 1 independent variable (x) in 1D spectral analysis. This research used this analysis to determine the dominant wavelength in the area of interest by looking at the depth profile of segment A_1A_2 (Figure 4.3). The basic formula for 1D FFT is given in Equation 4.4:

$$F(u) = \frac{1}{N} \sum_{x=0}^{N-1} f(x)e^{-2\pi jxu/N}$$

4.4

The same prefiltering approach used in the 2D spectral analysis is applied in the 1D spectral analysis. Before performing the 1D spectral analysis, the mean depth and trend should be removed from the observed depth. The depth which is free from mean and trend, is then tapered on the edges to minimize the static bias component and spectral leakage. The depth preparation step can be seen in Figure 4.8a. The original depth is shown as a black line and the blue line represents the remove-averaged depth. The

detrended depth is represented by the yellow line and the final depth that has been tapered is represented by the green line.

Figure 4.8b shows an example of the 1D spectrum of segment A_1A_2 with the 1D spectrum power as the blue line and its trend as the red line. The trend of the 1D power spectra was calculated using the kernel smoothing regression method. The details of this regression method can be seen in Rodriguez (2001) and Irizarry & Bravo (2010).

The length of this segment is 470 m, thus it can resolve a maximum 235 m of wavelength. As the sampling depth is every 0.25 m, the minimum wavelength that can be solved is 0.50 m. The change of power spectrum between two consecutive observations can be seen in Figure 4.8c. The red line represents the power spectra trend of the most recent observation and the green line represents the power spectra trend of the previous observation. The green area in Figure 4.8c shows that the spectrum power of one observation increases from the spectrum power of the previous observation. The red area in Figure 4.8c shows that the spectrum power of one observation decreases from the spectrum power of the previous observation.
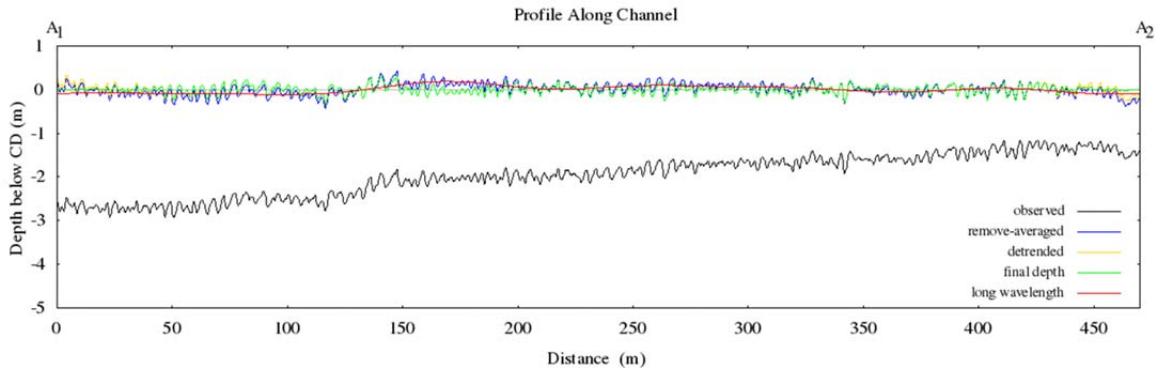
a. Depth preparation before 1D spectral analysis
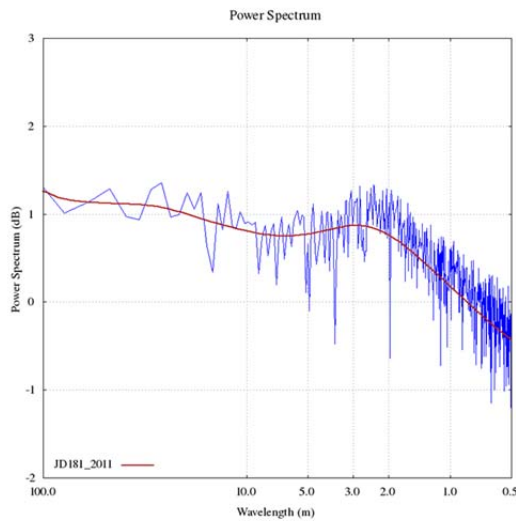
b. 1D power spectrum power (blue line) and its trend (red line)
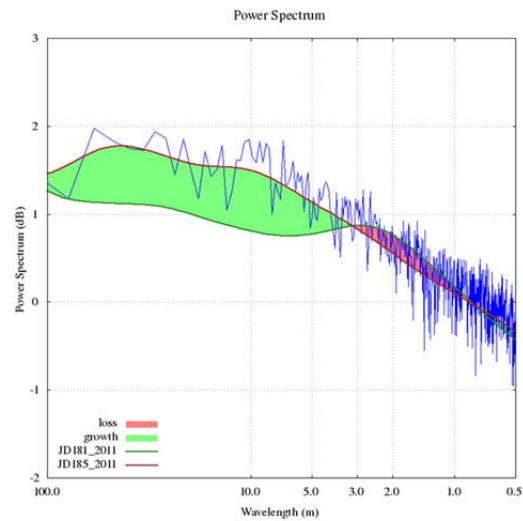
c. The spectrum trend difference between one to the next observation

Figure 4.8: Depth preparation before 1D spectral analysis (a), 1D power spectrum and its trend (b), and the differences in spectrum trend between two consecutive observation (c).

4.3. Surface Roughness Characterization

This research also implements a method from ASME to determine surface roughness characteristics. In order to extract the roughness properties of a bedform, a terrain model should be free from any long wavelength depth components. The long wavelength

component was extracted using a moving average method with a window size of 12.5 × 12.5 m. By subtracting long wavelength depth component from the original depths, a terrain model only contains short wavelength roughness components.

Figure 4.9a and b show the terrain model before and after it was detrended. Notice that not every depth is detrended. The wall of the training dyke intrudes into this surface and will result in a non-natural roughness element, unrelated to the bedforms. Thus, this surface was masked so that depths on the training dyke's wall are not included for surface analysis (Figure 4.9b). Figure 4.9c presents the final result of the roughness amplitude histogram from the original bedform in Figure 4.9a.

a. Terrain model of area in Figure 4.3

b. Detrended depth within masking area (black line)

c. Histogram of detrended depth
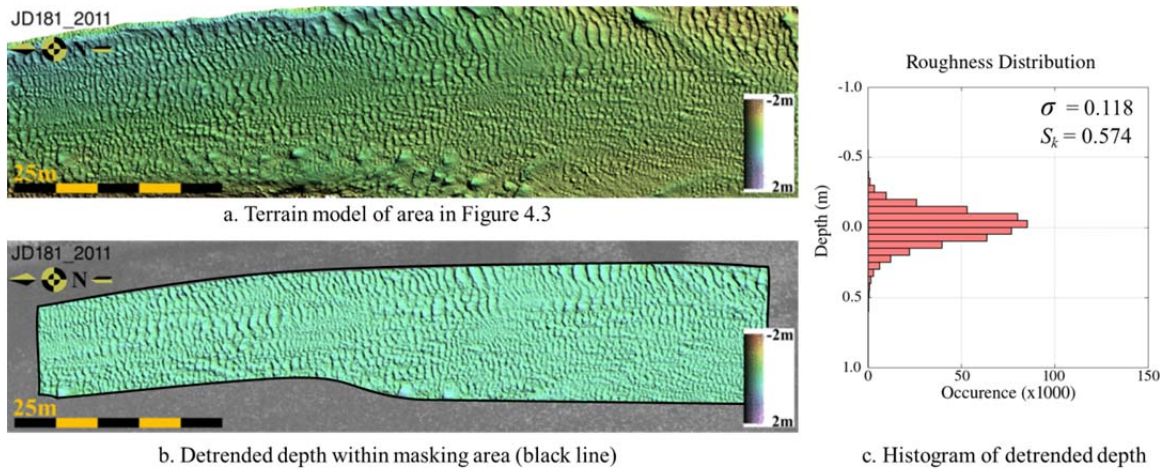
Figure 4.9: Terrain model before it was detrended (a) and after it was detrended (b), and the histogram of the detrended terrain model (c).

There are 4 surface parameters used for surface characterization analysis in this research: [1] roughness average, [2] roughness standard deviation, [3] skewness, and [4] kurtosis. The average roughness of the bedform can be calculated using Equation 4.5 (Image Metrology, 2014):

$$Sa = \frac{1}{MN} \sum_{k=0}^{M-1} \sum_{l=0}^{N-1} |z(x_k, y_l)|$$

4.5

where is Sa is the surface roughness, M and N are the dimensions of the terrain model and z is the depth at each pixel coordinate (x_k, y_l) in the terrain model. Standard deviation (Sq) of the surface can be calculated using Equation 4.6:

$$Sq = \sqrt{\frac{1}{MN} \sum_{k=0}^{M-1} \sum_{l=0}^{N-1} [z(x_k, y_l)]^2}$$

4.6

Other important parameters of roughness characterization are skewness and kurtosis. Skewness (Sk) describes the asymmetry of the roughness amplitude distribution histogram, whereas kurtosis (Ku) describes the sharpness of the peak of the roughness amplitude distribution. The formula for calculating Sk and Ku can be seen in Equation 4.7 and 4.8 (Image Metrology, 2014):

$$Sk = \frac{1}{MNSq^3} \sum_{k=0}^{M-1} \sum_{l=0}^{N-1} [z(x_k, y_l)]^3$$

4.7

$$Ku = \frac{1}{MNSq^4} \sum_{k=0}^{M-1} \sum_{l=0}^{N-1} [z(x_k, y_l)]^4$$

4.8

If *Sk* is equal to 0, a symmetric height distribution is indicated like a Gaussian curve. If *Sk* less than 0, it can be a bearing surface with holes. If *Sk* is more than 0, it can be a flat surface with peaks. Values numerically greater than 1.0 may indicate extreme holes or peaks on the surface. For the Gaussian height distribution, *Ku* approaches 3.0. Smaller values indicate broader height distributions and vice versa for values greater than 3.0.

4.4. Depth and Volumetric Characterization

4.4.1. Depth characterization

As discussed in section 4.1, the ratio between the width of the channel and its depth affects the probability of spatial variability in bed shear stress, stream power, and bed material. Thus this research also examined the depth change along and across the channel. The depth profiles along and across the channel were extracted from segment A_1A_2, B_1B_2, and C_1C_2 (Figure 4.3).

Segment A_1A_2 represents the channel shape along the river. The depth along this segment is deeper in the river channel and becomes more shallow on the mouth bar. Segment B_1B_2 represents the channel shape restricted by the training dyke, while segment C_1C_2 is a representation of the channel shape within the unconstricted area (Figure 4.10).
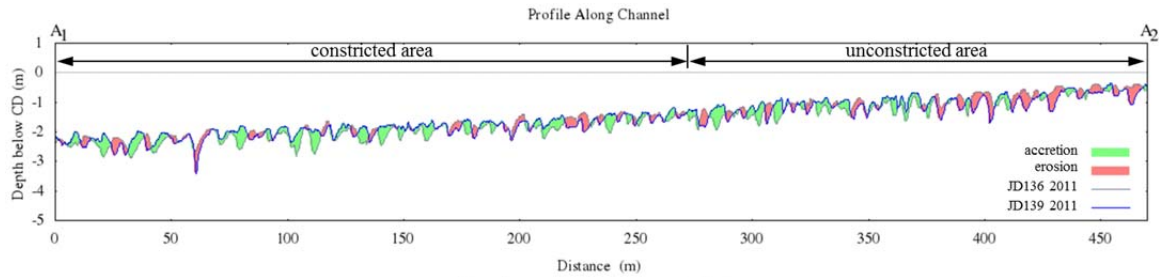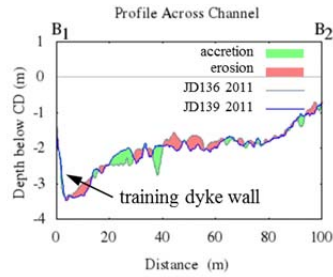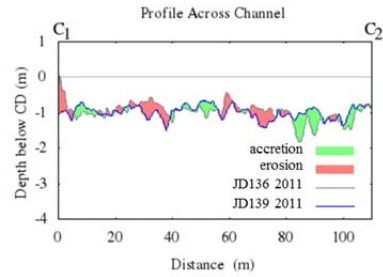
Figure 4.10: Depth profiles along the channel (a), across the channel within constricted area (b), and across the channel without constriction (c).

The depth change along and across the channel over time was calculated by subtracting the depths from one observation from the next for both depths along and across the channel. The difference in depth between two consecutive observations indicates how the channel was deepened or shallowed by the sediment over time. Figure 4.10 shows examples of the difference in depth along and across the channel between two consecutive observations. The red area represents erosion and the green area represents deposition. The depth analysis between two consecutive observations will be discussed in section 6.3.

4.4.2. Volumetric characterization

In order to qualitatively estimate the bedform migration on the delta top and to measure the sediment delivered to or removed from the delta top, the research used a volumetric characterization analysis. The volume between two consecutive observations is calculated by subtracting the depth of one terrain model from the depth of the subsequent terrain model.

The terrain model was built using a 0.25 m × 0.25 m grid cell. Each cell in a uniform grid has an elevation value that represents the average depth of the surface within the cell size. The volume of sediment can be calculated using formula 4.9. Positive quantities represent the volume gain (sediment deposited in the area) and negative quantities represent the volume loss (sediment removed from the area).

$$V_s = \sum_{x=x_{min}}^{x_{max}} \sum_{y=y_{min}}^{y_{max}} [z_2(x,y) - z_1(x,y)] \times \Delta A$$

$$4.9$$

where:

V_s = volume of sediment

x,y = horizontal coordinates of the grids cell

z_1 = depth of the first terrain model

z_2 = depth of the second terrain model

ΔA = area the grid cell

There are two areas for volumetric characterization, the delta top and the delta lip areas. The delta top area is approximately 67431 m^2 which includes the majority of the active mobile delta top. The boundary for the volumetric characterization on the delta top is set such that it excludes the edges of the delta. The delta lip area for volumetric characterization is approximately 62000 m^2 which is the off-delta extension of the area used for volumetric characterization on the delta top.

There are two parameters for volumetric analysis on the delta top: [1] the change index and [2] the mobility index. For the volumetric analysis on the delta lip, it also has two parameters: [1] the sediment flux index and [2] the mass wasting index. The illustration of these parameters can be seen in Figure 4.11.
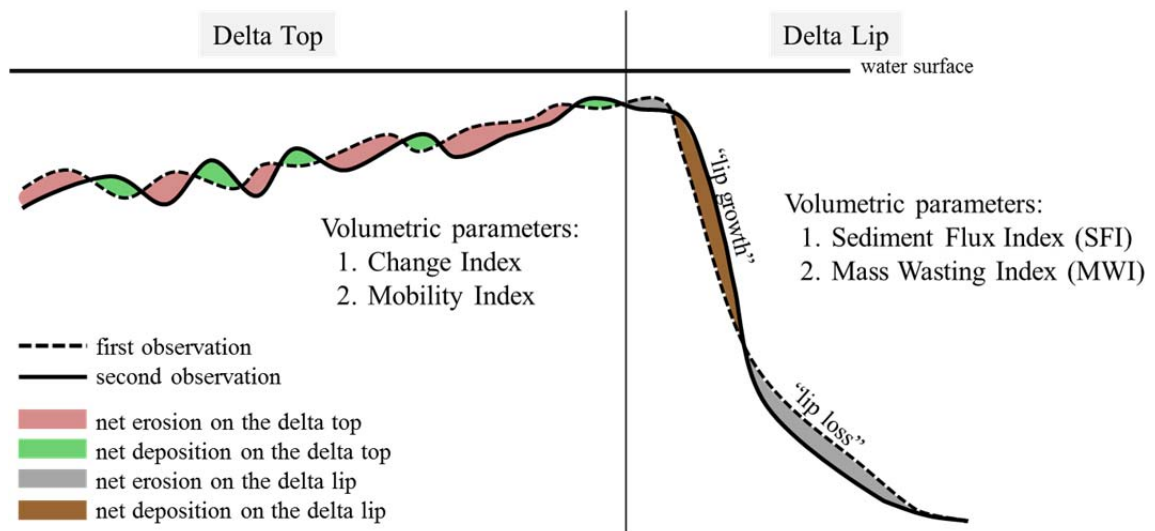
Figure 4.11: Volumetric parameterization for the delta top and delta lip area.

4.4.2.1. Volumetric characterization on the delta top

Two parameters which can be derived from volumetric characterization on the delta top:
[1] the change index and [2] the mobility index. The change index is basically the net volume. It describes how much was sediment deposited in or removed from the delta top. The mobility index is basically the volume range which is a qualitative measure of the bedform migration.

The change index is used as an indicator of the channel shape activity whether the long wavelength channel shape, in average, is static or deepened or shallowed as a response to the current flow through the channel. The change index is represented by the net of the sediment volume on the delta top which is calculated by adding the volume gain and the volume loss in the delta top area. The result of volumetric characterization on the delta top will be discussed in section 6.3.
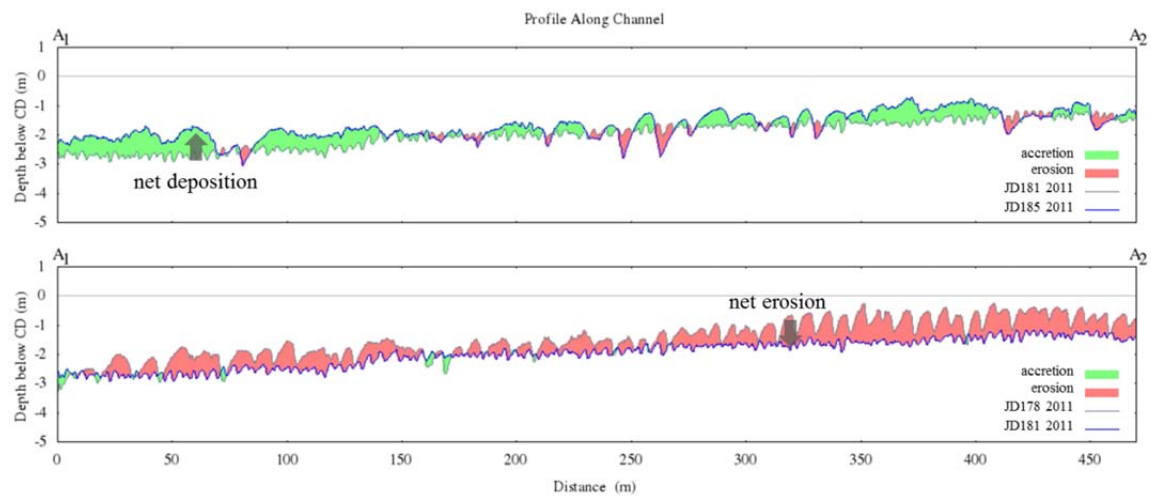
Figure 4.12: Change index shows how the channel got shallower (a) and deeper (b).

92

The second parameter of volumetric analysis is mobility index. The mobility index is basically the volume range. It is calculated by adding the absolute of volume gain and the absolute of volume loss in the area of interest. Although the delta top neither get shallower or deeper, if there is activity of the sediment on the delta top, the mobility index represents this activity. However, this approach is a qualitative measurement as the bedform moves more than half of a wavelength without any significant change in the net volume. Thus, the number of wavelengths of the bedform translation cannot be determined and the volume is really a measure of the mean bedform height. Figure 4.13 shows periods when there the change indexes are similar but they have completely different sediment activity in this area.

JD122 - JD118

Change Index = -1,934 m³
Mobility Index = 3,162 m³
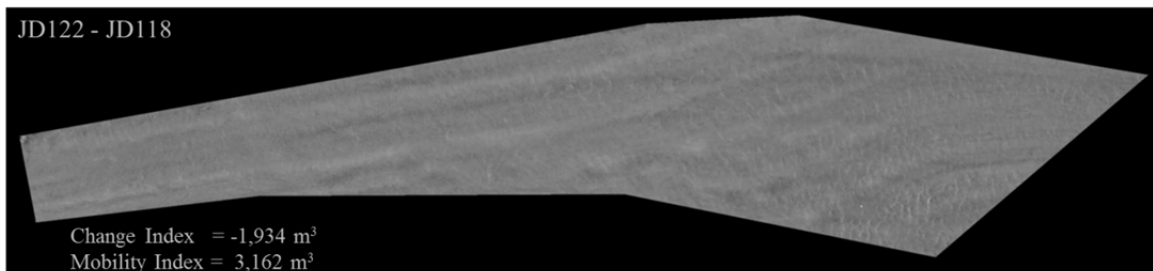
a. The difference terrain model between observation on JD118 and JD122 2011.

JD157 - JD153

Change Index = -1,838 m³
Mobility Index = 22,900 m³
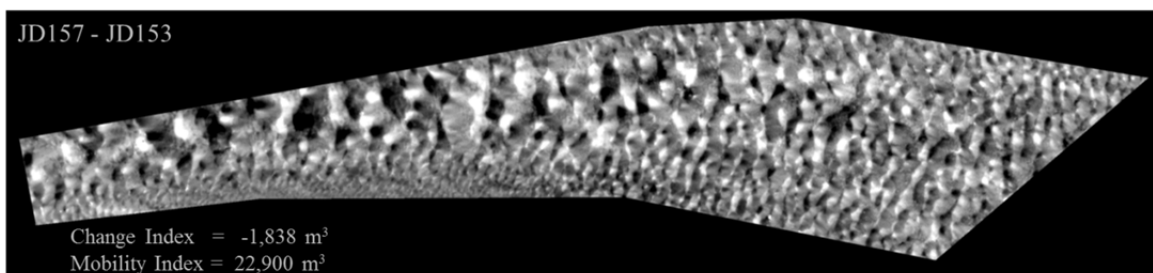
b. The difference terrain model between observation on JD157 and JD153 2011.

Figure 4.13: Difference terrain models with similar change index but completely difference in mobility index. The low sediment activity (a) and high sediment activity (b) on the delta top are represented by the mobility index.

93

Besides volumetric analysis on the delta top, the research has also undertaken volumetric analysis on the delta lip to examine the sediment activity in its vicinity. The volumetric parameters of the delta lip which were used in the research will be explained in the next section.

4.4.2.2. Volumetric characterization on the delta lip

There are two parameters for volumetric characterization on the delta lip: [1] the Sediment Flux Index (SFI) and [2] the Mass Wasting Index (MWI). The SFI is basically volume gain. It is used to investigate the off-delta lip transport (the sediment arrives in the delta lip). The MWI is used to represent the amount of sediment removed from the delta lip because of the slope failure. It is basically absolute volume loss.

The daily rate of sediment volume change was calculated by subtracting the depth of one terrain model from the depth of the terrain model of the next observation within the area of interest and dividing by the duration between those observations. The daily rate of volume gain represents the SFI of the off-delta lip and the daily rate of volume loss represents the MWI: the sediment moves downslope as landslides and/or turbidity currents. Figure 4.14 shows examples of SFI and MWI from difference terrain models.
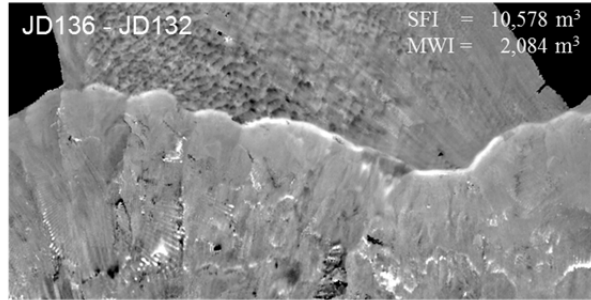
a. The difference terrain model of the delta lip between JD132 and JD136 2011.
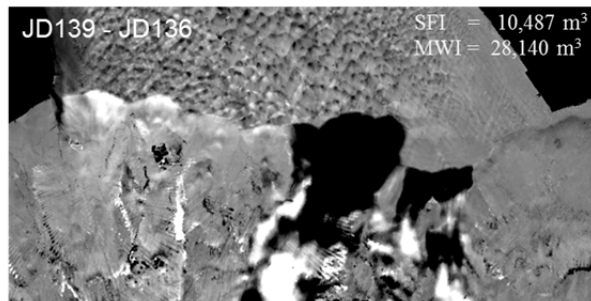
b. The difference terrain model of the delta lip between JD136 and JD139 2011.

Figure 4.14: The SFI and MWI from difference terrain models. The SFI is more dominant than the MWI (a). The MWI is more dominant than the SFI (b).

The SFI and MWI are conservative measures of the sediment transport process on the off-delta lip and slope because one process reduces the estimate for the other. The SFI is a conservative measure because there are some sediments collapsing from the area at the same time as there are sediments arriving. Conversely, the MWI is also a conservative measure because there are some sediments filling in the area at the same time as there are sediments collapsing.

The growth or retreat of the delta lip reflects the balance between the off-delta top sediment transport and the remobilization of that sediment flowing down slope due to

95

gravity. Hughes Clarke et al. (2012) have demonstrated that both are often active on the same day even though the collapses are quite discrete. Thus, if just the growth (excluding the collapse) is measured, it is a conservative estimate of the net daily off-delta lip sediment flux. This estimate is even more conservative as a significant fraction of the coarse silt and finer material would be moving as washload and thus, is not immediately deposited within the area used for the calculation which is approximately 50 to 100 m of the off-delta lip. Much of this finer material moves out further in the plume and is only deposited further down the fjord.

The SFI is a gradual process where the flux is related to the flow. In contrast, the MWI is an episodic process related to discrete mass wasting events. Thus, as the SFI and MWI are competing processes and the mass wasting is erratic, the shorter the time period between surveys, the more accurate (less under-estimated) the estimates of both MWI and SFI will be. Notably, the 2011 estimates which utilized 3to 4 day intervals are lower than the 2012 and 2013 estimates which using daily surveys.

This is best illustrated by looking at the total change over the 4 month period. If JD230 (the end of the observations in summer 2011) and JD118 (the beginning of the observation in summer 2011) are differenced, the apparent SFI and MWI respectively, averaged over the 112 days is only 312 m^3 per day and 982 m^3 per day. This reflects the net delta growth resulting from the continual interplay between deposition and onward remobilization. This is the process that controls the decadal scale delta growth as estimated by Hickin (1989).

The daily rate of sediment flux of the off-delta lip (SFI), and the daily rate of sediment removed because of the steep slope of the prodelta (MWI) will be discussed in section 6.4. A discussion of the relationship of these parameters with the flow regime will follow in section 6.5.2.

4.5. The Progradation and Retrogradation of the Delta Lip

Beside volumetric parametrization on the delta lip area, this research also investigated the growth and retreat of the lip of the delta. A horizontal displacement of the delta lip between two consecutive survey was used to monitor the progradation and retrogradation of the delta lip,

A rotated map of area B in Figure 4.3 is used to better illustrate the shape of the delta lip. The map is rotated 50° counterclockwise from the north direction. Figure 4.15 encodes the depth of the rotated map, focusing on depths between -1.0 m to 10.0 m (a positive depth is downward from Chart Datum).

In order to relate the evolving bedform fields on the delta top to the evolution of the delta lip shape, a 3.0 m depth contour referenced to Chart Datum was extracted from bathymetry data (blue line in Figure 4.15). This 3.0 m contour is used as a representation of the delta lip shape. The horizontal position variation of the delta lip between two consecutive measurements was examined to monitor the evolution of the delta lip over the course of the observations.

97
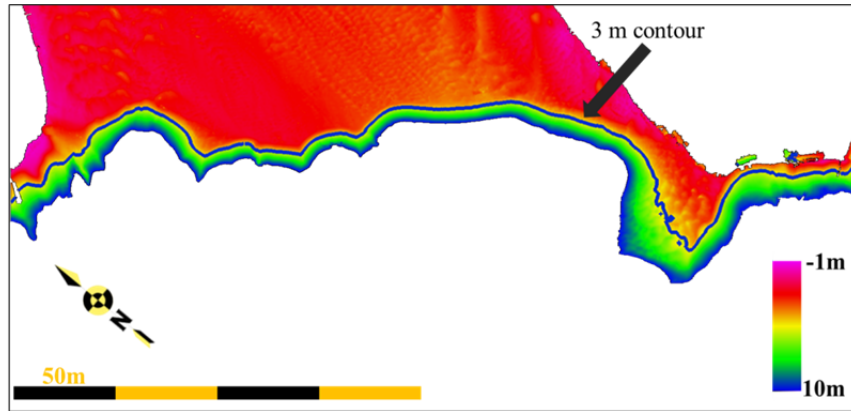
Figure 4.15: A depth color encoded of rotated map of area B. The 3 m contour (blue line) is used to investigate the progradation and retrogradation of the delta lip.

The horizontal position difference of the delta lip shape between two consecutive measurements was calculated by simply subtracting the y-rotated coordinates of one epoch from the y-rotated coordinates of the previous epoch. Figure 4.16 illustrates how to calculate the horizontal difference of the delta lip shape from two consecutive measurements. The red line represents the 3.0 m contour of the first measurement and the green line represents the 3.0 m contour of the second measurement (Figure 4.16a).

The horizontal difference (d_{21}) between two measurements is calculated by subtracting the y-rotated coordinate of the second measurement from the y-rotated coordinate of the first measurement ($y_1 - y_2$) at the same x rotated-coordinate ($x_1 = x_2$). A positive difference represents the delta lip progradation (green arrow in Figure 4.16b) and a negative difference represents the delta lip retrogradation (red arrow in Figure 4.16b). The evolution of horizontal displacement of the delta lip will be discussed in section 6.4.
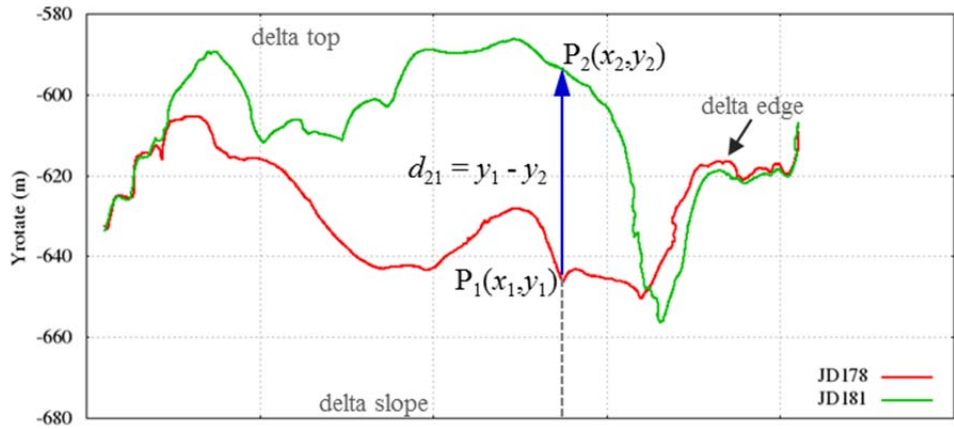
a. Top view of the delta lips
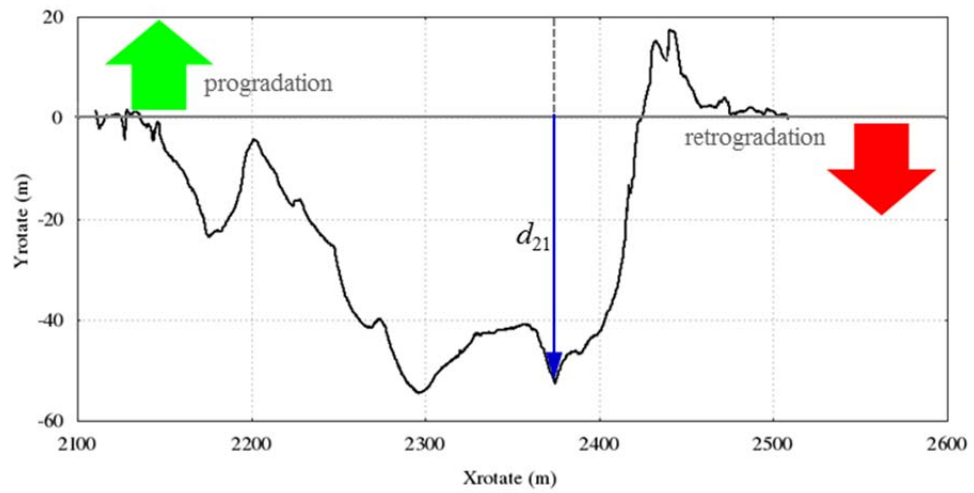
b. Horizontal difference of the delta lips

Figure 4.16: The horizontal difference of the delta lips between two consecutive measurements.

99

Chapter 5: Hydrodynamic Model of the Squamish River

The bedforms and the flow fields in the fluvial and estuarine system influence each other. The bedforms create complex flow fields, altering local velocities and flow resistance. On the other hand the flows transport sediment, modifying the presence of the bedform morphology [Clunie, 2012]. The flow fields are also affected by the morphological properties of the fluvial and estuarine system: depth, width, slope, and bottom roughness of a channel. The depth and the width of the channel at the river mouth depend on the water elevation (in this case strongly tidally modulated) and the discharge of the river. The composition of the sediment on the river floor influences the bedform roughness and reflects the available flow strength.
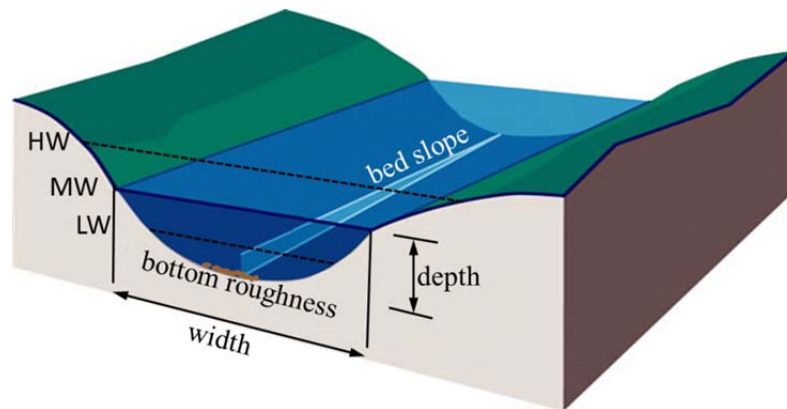
Figure 5.1: Variables which affect the flow fields in the fluvial and estuarine system.

All bathymetric surveying on the delta top had to take place at high tide as only then was there enough water to navigate. During high tide, current velocity is the lowest and does not represent the peak period of sediment movement. Thus the multibeam surveys only captured inherited bedforms, generated during low water at high current situations.

Ideally, to correlate the bedform migration and the flow conditions, a snapshot of the bedform has to be taken immediately after the sediment moves and the flow at this time has to be measured. However, this ideal situation cannot be easily achieved. Thus, a prediction of flow fields using a 3D hydrodynamic model was performed to investigate the correlation between the flow field and the available bathymetric data.

Hydrodynamic model helps to understand the flow field in the area of interest. Several previous studies have implemented of hydrodynamic model in an estuary [Church, 2014; Hu et al., 2009; Yang et al., 2014] to see how the flow interacts with sediment in the area. The study of Church is the only one that related the flow conditions to repetitive multibeam surveys. In Church (2014) case, the surveys were 6 months apart whereas this study uses surveys only a few days apart.

A hydrodynamic model is a tool that can describe or represent the motion of water. A hydrodynamic model solves a set of conservation equation that describes the motion of water. This set represents momentum, mass, and energy respectively. These equations are written in the co-ordinate frame of reference fixed to the rotating earth and are essentially Navier-Stokes equations [Kantha & Clayson, 2000].

The Navier-Stokes equations known as the momentum equations are derived from Newton's second law of motion applied to a small volume of fluid (fluid element). The forces due to gravitation buoyancy (Archimedean force due to density stratification) and the Coriolis (accelerations generated due to the non-inertial nature of the rotating co-ordinate frame) are included in the equations. An additional equation, known as the continuity equation, is required to ensure that mass is conserved [Kantha & Clayson, 2000].

Hydrodynamic models include the continuity of mass and energy conversion principle. As computers can only perform discrete calculations, the governing equations must be broken into small individual problems that can be solved on a computer [NOAA Office of Coast Survey, 2014]. The continuous mass of water is broken into discrete volumes so that the calculation of the model can be solved on a computer. In order to transform the continuous water into a discrete representation, the entire body of water within a model domain is divided into elements by creating a mesh that covers this area.

Two classes of mesh are common in hydrodynamic models: [1] structured grid approaches (primarily finite difference algorithms) and [2] unstructured grid approaches (including finite element and finite volume methods). Structured grid models tend to use quadrilateral grid cells that limit the grid's flexibility in resolving the complex shoreline. However, these grid models are straightforward and use efficient algorithms. Unstructured grid models have much more flexibility in their grid resolution by employing variable triangular elements, but tend to be more time consuming to run and more sensitive to numerical errors [NOAA Office of Coast Survey, 2014].

The model domain of this research includes the Squamish River and Howe Sound fjord (Figure 1.1). This covers a particularly large range of depth from less than 5.0 m on the delta to more than 200.0 m on the fjord. The transition between the two is extremely abrupt. Thus this research used an unstructured grid model with a finite-element method (triangular irregular mesh) to build the hydrodynamic model. The irregular mesh was used to accommodate the irregular shape of the model boundary as well as the rapidly changing depth (i.e. river mouth and delta edge).

The output of a hydrodynamic model has the ability to predict spatial and temporal water surface elevation, current velocity, temperature, and salinity. This research implemented the hydrodynamic model of Finite Volume Community Ocean Model (FVCOM) version 3.1.6 in barotropic mode to simulate the flow fields. A barotropic mode is used because the oceanographic samplings have confirmed that there is no salt-wedge penetration into the delta top during the observation period (section 3.4.4).

Two external forces were used in this model: [1] tide modulation and [2] river discharge. These are the dominant forces in this area. Waves and wind forces were not used as forcing conditions because the model domain is protected from open water. The steps involved in the implementation of the FVCOM model for this research will be described in the next sections.

5.1. Mesh Construction

FVCOM discretizes the continuity equation over an arbitrarily sized triangular mesh. The finite-volume approach is better suited to guarantee mass conservation in both the individual control element and the entire computational domain [Chen et al., 2011]. The model used a finite volume algorithm over the unstructured grids to provide the accurate fitting of the irregularity of coastline and the rapid change of depth within domain geometry.

The research used triangular irregular mesh to implement the FVCOM model. A triangular irregular mesh is essentially a triangular irregular network (TIN). Each element in this mesh comprises three nodal points with lines connecting them. In creating the mesh, the size and shape of the triangles can be selected to represent the shape and complexity of the terrain in the model domain. The more complex the terrain, the finer the mesh and the greater number of elements are used in the model. However, a mesh with too many elements can result in excessive calculation time [Boudreau et al., 2015].

The research used two primary data sources to create triangular mesh within the model domain. The first is a coastline of the area which resolved the fjords and islands inside the domain. The second is the best available bathymetry data inside the model domain. Using these primary data sources ensures that the effects on the tide from the changes in bathymetry are accurately reproduced.

The coastline within the model domain was collected by digitizing the boundary between land and water from satellite imagery provided by Digital Globe, GeoEye. This was done

using QGIS, a free and open source Geographic Information System software. The resolution of this imagery is sufficient to accurately represent the coastlines of the islands, the salt marshes, and the fjord walls within the model domain.

Bathymetry data used for creating the mesh were mainly obtained from the EM710 multibeam system. For the area that could not be surveyed by the Heron, the bathymetry data was collected using a low-cost single beam system mounted on the Boston-Whaler. The multibeam resolution roughly scales with depth (sounding resolution on the order of 1.7% of oblique range); the single beam and coastline data are much sparser in the shallow areas. The compilation of bathymetry data used to create the mesh is shown in Figure 5.3.
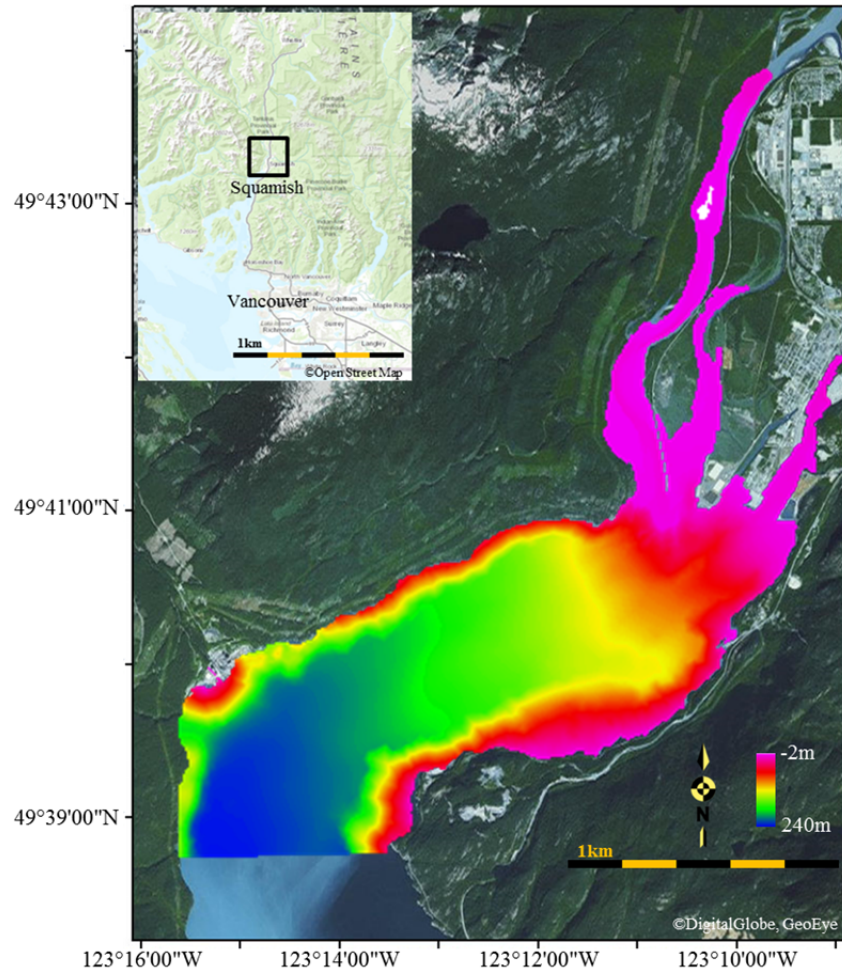
Figure 5.2: Compilation of bathymetry dataset to generate the mesh used for developing the

hydrodynamic model.

After compiling the coastline and the best available bathymetry data, the next step was

inputting these data into Resolute [Chaffey & Greenberg, 2003], a semi-automated

unstructured triangular mesh generating routine. Resolute subsamples the available high

resolution bathymetry to create an unstructured triangular mesh.

The output grid from Resolute had to be modified to fulfill the requirement of the

modelling software. The modifications include altering the location and density of some

nodes, removing unused nodes, reordering nodes and spatially averaging and smoothing

depths. Together with the chosen time step for model implementation, the resulting mesh

should meet the Courant-Friedrichs Lewy (CFL) stability criterion of the FVCOM model.

The CFL stability criterion is given in Equation 5.1 [Chen et al., 2011]:

$$\Delta t \leq \frac{\Delta L}{\sqrt{gD}}$$

5.1

where Δt is the time step, the computational length scale ΔL is the shortest edge of an

individual triangular grid element, g is gravity and D is the local depth. The CFL

condition used in this research is 1.5 with the time step for model implementation is 0.1 s.

The mesh modification may result in a difference between the depth of the mesh and the

real surface (terrain model built from observation data). To ensure the best depiction of

the delta top channel, an additional step was added to force back the depths so that the

depth of the mesh matches to the depth of the terrain model on the delta top. However, as

the mesh horizontal resolution (the mesh size) is much larger than the grid size of the

terrain model, the depth represented in the mesh is not as detailed as in the terrain model.

The size of the model mesh in this research varies between 13 m^2 and 215 m^2 whereas the

grid size of the terrain model is 0.25 × 0.25 m.

The grid resolution of the terrain model is much smaller than the mesh resolution of the

model. The model mesh resolution limits the resolution of the hydrodynamic model

output. The output of the model has a limitation in resolving small wavelength bedforms. This means the smallest model output may not be sufficient to capture the changing of short wavelength bedform. However, a roughness parameter in FVCOM can be adjusted and used to accommodate the roughness of the bedform. Figure 5.3 shows the difference in resolution between the mesh and the bedforms. It is clearly seen that bedforms on some parts have smaller wavelengths than the resolution of the model mesh.
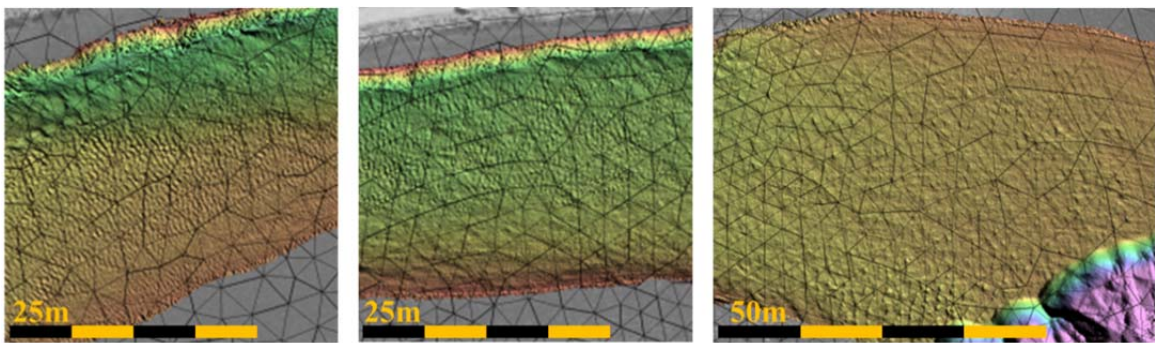
Figure 5.3: The difference in resolution between the mesh and terrain model of the observed depth.

The mesh was built with 14073 nodes (vertices of triangles) and 26498 triangles. The size of the mesh varies over the model domain which depends on shape and complexity of the bathymetry and coastline. The size of the mesh also depends on the area of interest where more details of simulated flow fields are desired. In this case, the size of the mesh used in the delta top area is smaller than the size of the mesh used in other area inside the model domain. The triangular irregular mesh used in this research can be seen in Figure 5.4.

Note the bathymetry of the delta top evolved over the run period of the model, but the grid used for the hydrodynamic model was not updated. This may affect the output of the

hydrodynamic model. Section 5.4 (model validation) will discuss the result of using a static bathymetry in the model development while in reality the bathymetry of the area is dynamic and changing.
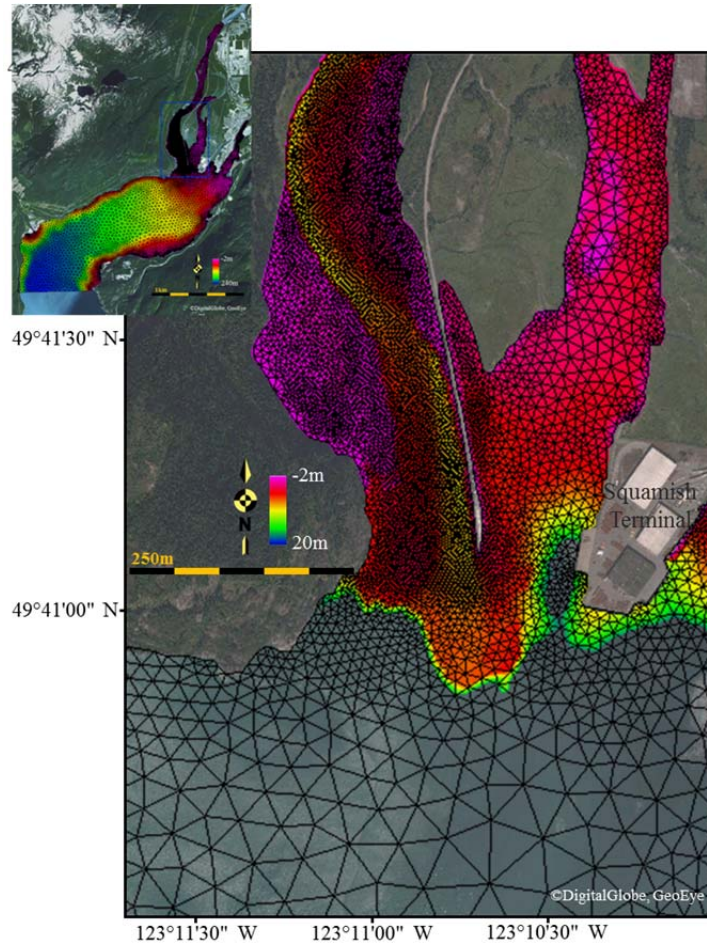
Figure 5.4: The difference in mesh resolution within the model domain. The delta top area has smaller mesh than the other area inside model domain.

5.2. Boundary and Initial Condition

A hydrodynamic model can take into account temporally and spatially varying forcing conditions criteria such as the tide or other boundary conditions including river discharge, temperature, salinity of the water column, pressure gradient, or surface heating [Ip & Lynch, 1995]. Changing any of these variables at the open boundary will affect the rest of the model depending on the governing equations.

Open boundary must be set using boundary conditions to give the model information on how to force the flow. In this case, the open boundary was forced using a river discharge and tide observation data to drive the model simulation. The open boundary for river forcing is located at one node in the northernmost area of the model domain boundary (Figure 5.5a). The tides forcing condition was used along the open boundaries located at Howe Sound fjord, about 5.0 km from Woodfibre. There are 22 nodes across the fjord that were used to force the model using tide observation (Figure 5.5b).
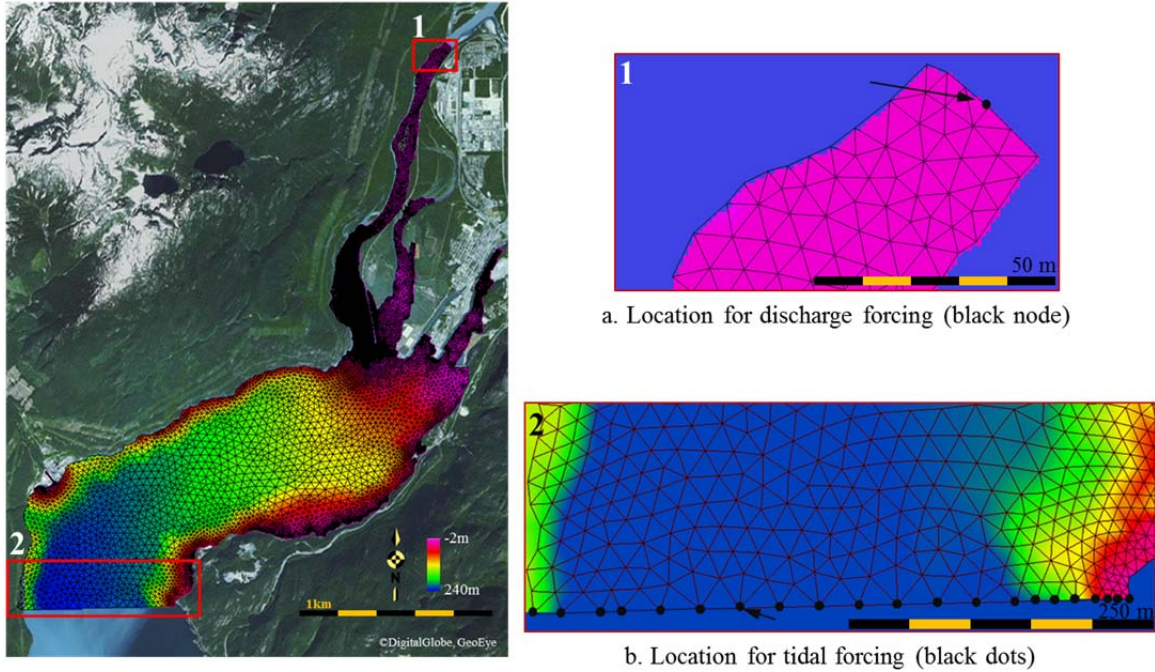
Figure 5.5: Open boundary conditions which were used in the research. The northernmost open
boundary is forced by river discharge (1) and southernmost open boundary is forced by tidal
modulation (2).

5.3. Implementation of FVCOM Model

The mesh and the open boundary conditions that had been prepared were implemented in
the FVCOM model [Chen, 2013] with initial conditions for simulation. FVCOM is an
open source, an unstructured-grid, free-surface, finite-volume, 3D primitive equation
community ocean model developed originally by Chen et al. (2003) at the University of
Massachusetts-Dartmouth and Woods Hole Oceanographic Institution (WHOI). The
model was chosen for this research due to its ability to handle areas with complex
coastlines and bathymetry.

FVCOM accommodates a variety of vertical layering coordinate solutions. A total of 20 sigma layers were used in vertical layering. The number of vertical layers in this model is constant throughout the domain, but the layer thickness varies depending on water depth and water level. The vertical resolution of the sigma layer is high near the surface and bottom.

FVCOM also provides an accurate simulation of the water transport flooding onto and draining out of the inter-tidal zone [Chen, 2013]. The research took advantages of this by implementing a wetting and drying condition in simulating the flow in the intertidal area. In order to filter the high frequency numerical noises due to the wave reflection, a sponge layer was introduced at the open boundary condition in the model implementation [Chen, 2013]. The sponge layer used in the model implementation consisted of 22 nodes with a friction coefficient increased from 0.001 to 0.05 at the open boundary over a distance of radius 500 m. The sponge layer only affects the numerical solution near the boundary with no influences on the interior solution [Chen, 2013].

The model was initiated with zero velocities and zero sea surface heights before it was run. In order to allow the model to adjust naturally with the boundary forcing conditions, the model was spun-up for five days. The water levels at the open boundary were ramped up from zero at the beginning of the simulation to full amplitude after twelve hours into the model run. The ramping up of open boundary water levels allowed the model to slowly adjust based on the water level and river discharge conditions.

FVCOM is able to take advantage of a Message Paring Interface (MPI) parallelization to maximize processing efficiency [Chen et al., 2011]. The model ran on 128 processors using the Atlantic Computational Excellence Network (ACEnet), a high performance computing network (ACENET, 2014). The model was run for 120 days during the summer of 2011, 10 days during the summers of 2012 and 2013.

The model output a series of netcdf (.nc) files that include water surface elevation, horizontal and vertical velocities at each level of each node and prescribed output time-step of the duration of the model run. Any of these variables can be extracted for a desired location, depth and time period within the model domain. Figure 5.7 illustrates the current magnitude extracted from 30 minutes of output of the hydrodynamic model in the year 2011.
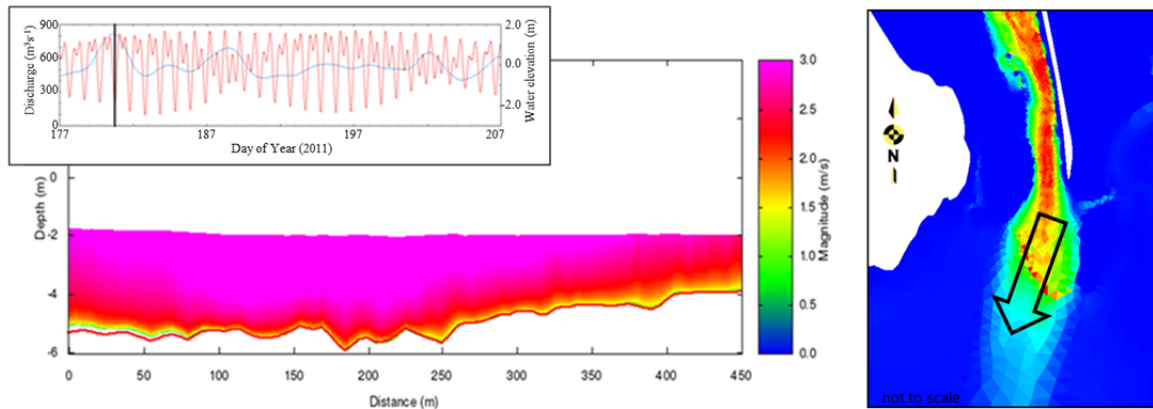
a. Current magnitude during low water and high discharge
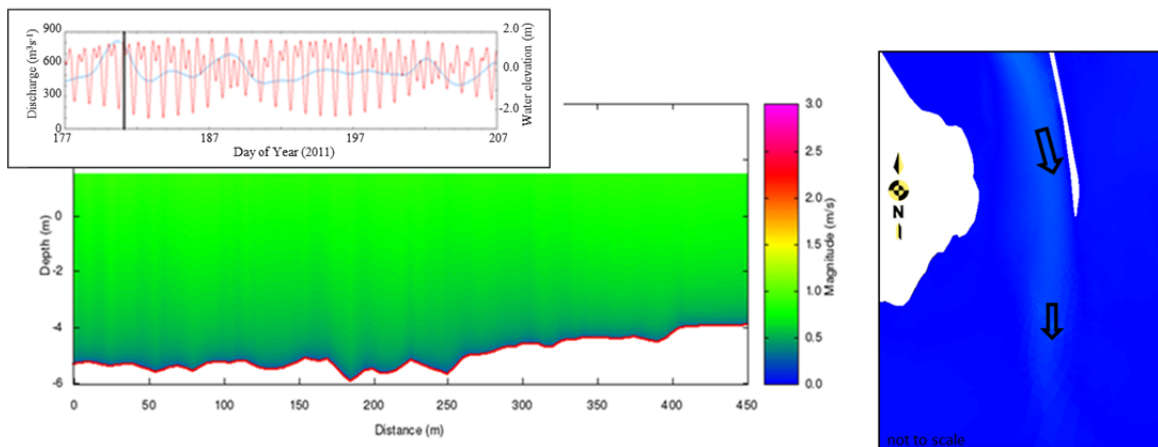
b. Current magnitude during high water and moderate discharge

Figure 5.6: Current magnitude extracted over the segment A_1A_2 from the hydrodynamic model.

5.4. Model Validation

The output of the hydrodynamic model should be validated to see how well it replicates the actual flow field. This is generally done by comparing model results to observations. The flow fields are the primary output from the model used for the analysis in this research. However, the research has limited observation data to calibrate the model output, as it was not possible to place a current observation instrument on the delta top

during the 4 month experimental period. Two attempts had been conducted for acquiring data for calibration without any success. In the first attempt, the ADCP was swept out by the current and during the second, the ADCP was exposed during the lowest water periods.

Nevertheless, the model should be validated. Thus, this research used small boat drift trajectories as a means of model validation. The trajectories of the small boat were collected during the lowest tide period. The boat was placed upstream to approximately 1000 m from the delta lip, the engine was turned off and the boat was allowed to drift with the current, thus acting as a Lagrangian drifter.

Three parameters that can be derived from this trajectory are the horizontal position, the vertical position and the speed of the boat while drifting. These parameters were derived from the position collected using a geodetic GPS mounted on the small boat. The PPP processing was accomplished to improve the GPS solutions. The boat trajectories, water surface elevation and current magnitude were the parameters used to validate the output of the model.

In order to compare model output to the boat trajectories, output from FVCOM's offline 3D Lagrangian particle tracking module was used in the research. 20 random particles were released at the position where the boat started to drift. These particles were created randomly inside a cylinder with 5 m diameter and 1 m height (Figure 5.7). The particles positions were calculated using currents from the model output. The trajectories of these particles were then compared with small boat trajectories.
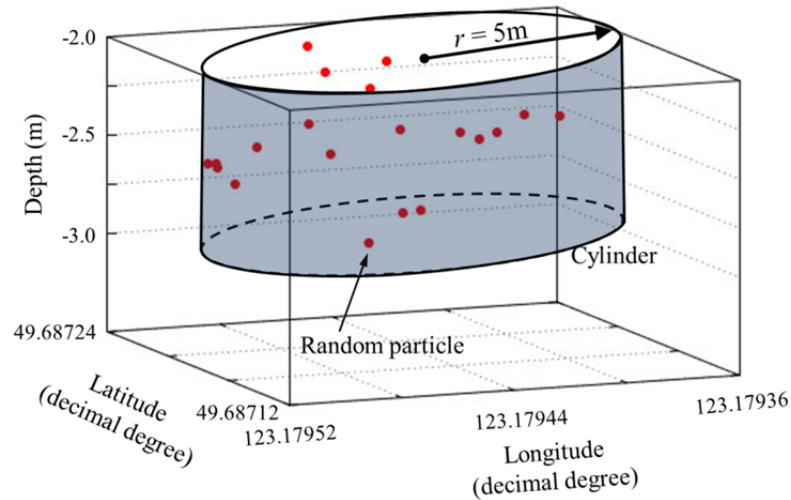
Figure 5.7: Random particles inside a cylinder with a 5.0 m radius and 1.0 m height. The red dots are random particles created using particle tracking software.

Two Lagrangian trajectories were used for comparison with the model output. Figure 5.8 shows the trajectories of the boat and the particles. The first and the second boat trajectories are shown in solid red and blue lines, respectively. The first and second particles' trajectories are shown in dashed red and blue lines, respectively

The difference in starting time between the first and the second Lagrangian trajectories of the small boat is 15 minutes. This is smaller than the time resolution of the model output (30 minutes). In order to validate the model, the particles' positions were interpolated based on the time of the small boat trajectories
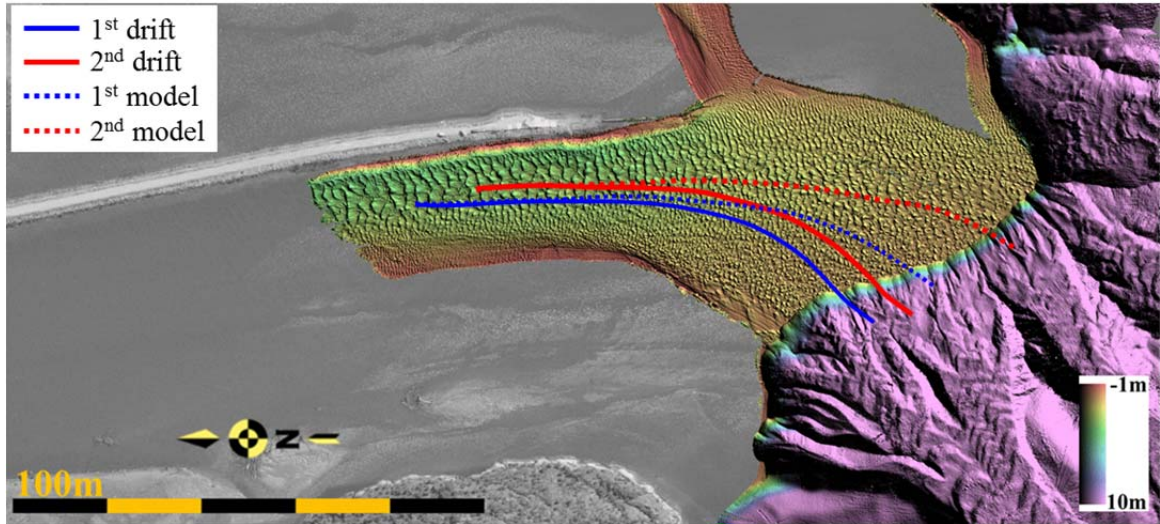
Figure 5.8: The Lagrangian drifts of the boat and the particles' trajectories. The solid lines represent the observations and the dashed lines represent particles' trajectories which were simulated using particle tracking software.

In order to compare the trajectories of the boat and the particles, both trajectories were sliced every 1.0 m in a cross flow direction. The comparison between these data pairs can be seen in Figure 5.9. The difference between the boat drift and particles track is less than 2.0 m within the area constricted by the training dyke. The difference increases gradually until about the delta edge and it is steady afterward. That gradual divergence represents trajectories that are just approximately 4° apart. Thus the velocity current azimuths clearly agree within that angle.

117
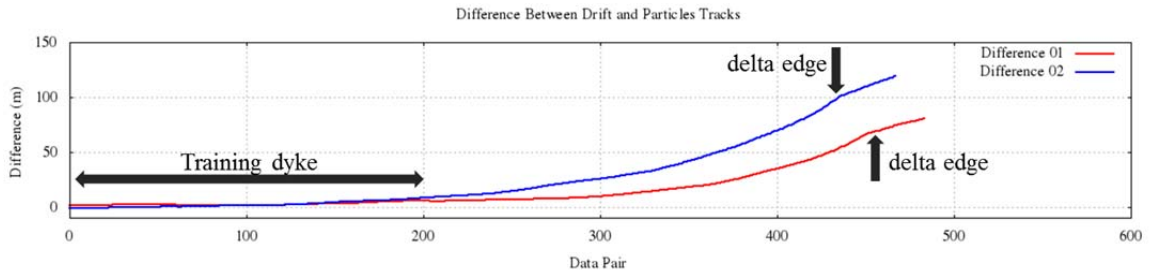
Figure 5.9: The difference between the drifts and particle trajectories.

The slight divergence between these trajectories is probably because when the data was collected, the bathymetry of delta top was actually different than the model. The model is very sensitive to the shape of the delta lip. Figure 5.10 shows the difference map between the bathymetry from the model and the bathymetry of the delta top when the observation was conducted.

118
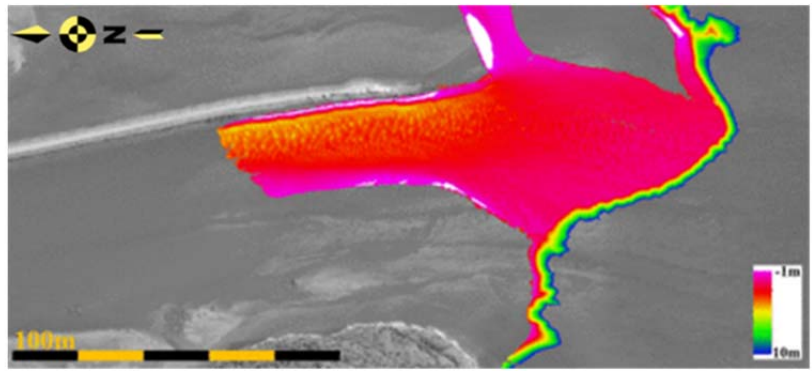
a. The terrain model built from multibeam survey at time of boat drift.
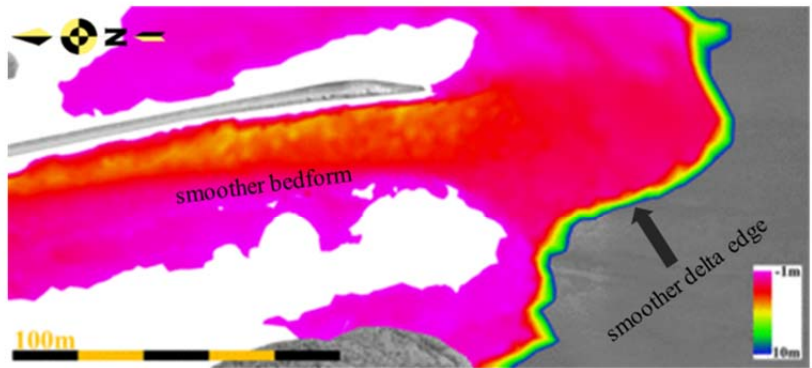
b. The terrain model used in the hydrodynamic model.
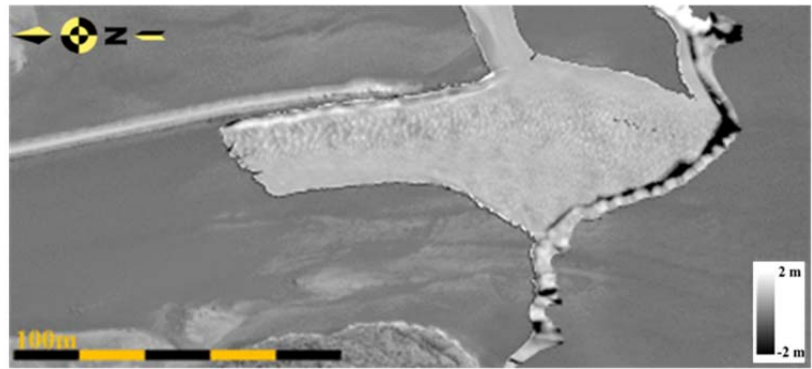
c. The difference between terrain model of the hydrodynamic model and the observation

Figure 5.10: Difference depth between the model and the observation.

The second parameter for the model validation is current magnitude. The speeds of the

boat when drifting were compared with the current magnitude extracted from the model

exactly on the boat trajectories. Figure 5.11 shows the current magnitude observation and

the model (top) and their difference (bottom). The average difference of current velocities

between the first trajectory and model is 0.122 ms^{-1}. The average difference between the

second trajectory and the model is 0.135 ms^{-1}.

Area A in Figure 5.11 shows the current magnitude of the model is about 0.5 ms^{-1}, slower

than the observation in the constricted area. The similar difference also occurs in the

vicinity of the delta lip (area B). These differences occur probably due to the difference in

topography between the model and the observation terrain model. The topography of the

model is smoother than the observation and the delta lip of the model is not as abrupt as

the observation. Another possibility is the extremely shallow water in the mouth bar (less

than 0.5 m) at lowest water. The model underestimates the drag coefficient, with dunes

that are more than 0.2 m in height, roughness elements are as much as 40% of the depth.
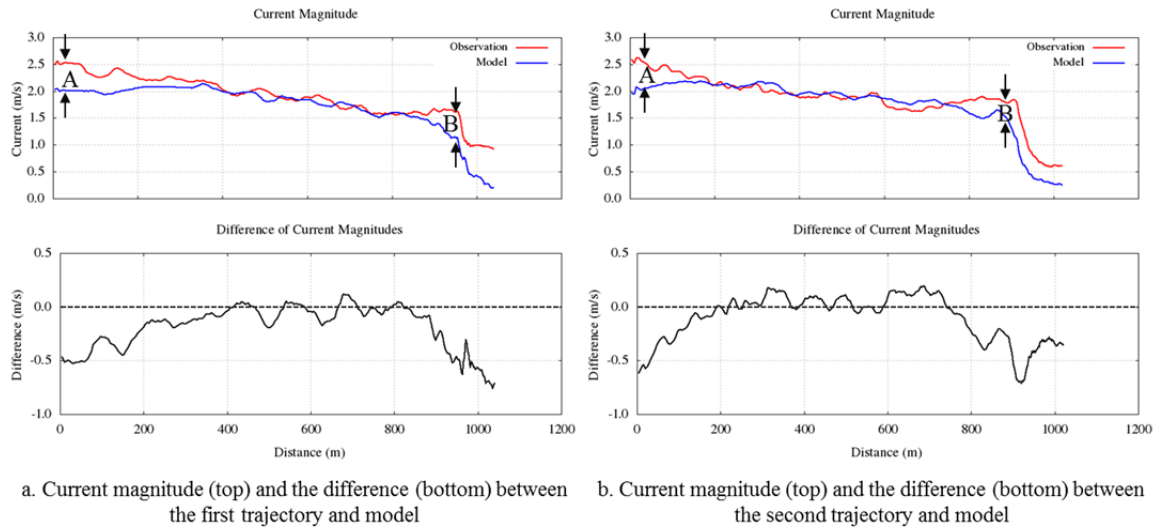
Figure 5.11: The difference of current magnitude derived from the observations and the model.

The third parameter used for validating the hydrodynamic model is water surface elevation. The observation of water surface elevation was calculated from vertical position of the boat trajectory, which is ellipsoid referenced. Then, it was corrected to the geoid (EGM 2008) and adjusted with vertical offset of the antenna and water surface. The comparison between water surface between model and observation along trajectories can be seen in Figure 5.12.

Figure 5.12 (top) shows the water elevation derived from the model and the observation along trajectories. The observed elevation trajectories are steeper than the modelled downstream water level elevation drop with an additional 10-20 cm of water level drop over the 1000 m long trajectory. This implies a greater hydraulic head than the model is predicting.

121

This steeper river-level drop implies that the roughness of the river channel must be greater than the value used in the model. The roughness parameter is a variable in FVCOM. By default a single value is used throughout the whole model domain. Most of the domain is deep and thus the seabed drag is relatively unimportant (the choice of eddy viscosity would be a far larger influence). In the river channel, however, where the flow at low tide is less than 3 m deep, the presence of the bedforms which have heights between 10 and 50 cm must have a significant influence on the form roughness.

The PPK derived river level slope is thus a useful indicator of the resulting drag of the river bed. While it would be possible to try different values of the roughness coefficient, because the amount of bed roughness is varying so strongly (the dunes are seen to grow and die in a matter of days), unless the roughness was allowed to be a time variable parameter, it is not clear what single value would be most appropriate for all water level conditions.

a. Water surface elevation (top) and the difference (bottom) between the first trajectory and model

b. Water surface elevation (top) and the difference (bottom) between the second trajectory and model
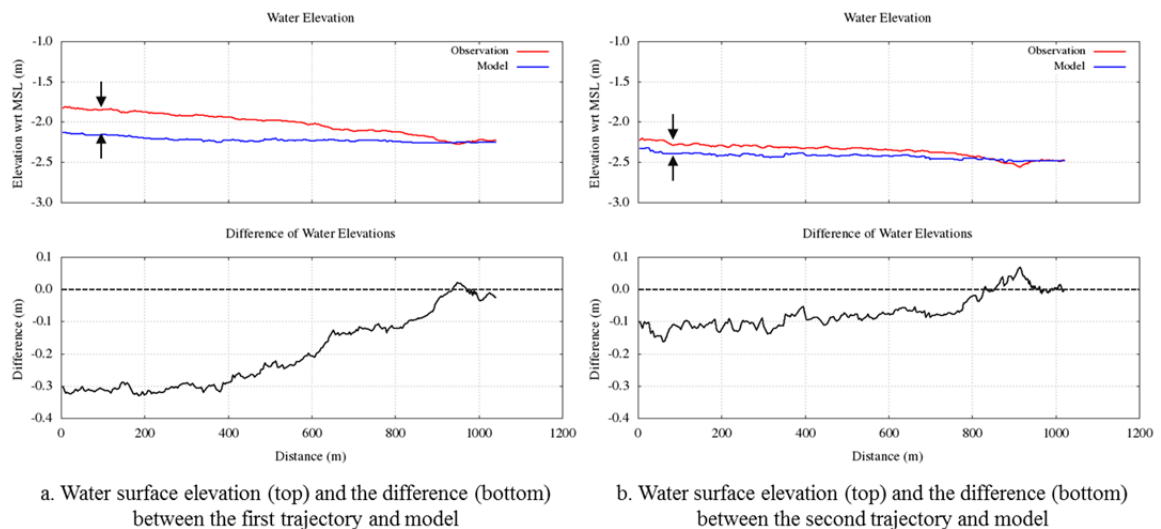
Figure 5.12: The difference of water surface elevation derived from first trajectory and the model.

122

The repetitive multibeam surveys clearly indicate that the sedimentary processes in the Squamish River are very active. The net result of the ongoing erosion and deposition is that shape of the delta top varies from day to day within the observation window (discussed in section 6.3). As stated previously, however, the model bathymetry was static. An additional concern is that the bathymetry used in the model was unavoidably smoothed. This results in differences of parameters which were used for validation between model and observation. However, the concern of this research is primarily on current magnitude in order to determine bed shear stress. As Figure 5.11 demonstrated there is good agreement between the model and the observation. Thus the model output is considerably adequate for describing the spatial and temporal flow field on the delta top.

Chapter 6: Delta Top Evolution

In this chapter, the various multibeam surveys are compared to determine the evolution of the short wavelength bedform roughness and long wavelength channel shape on the delta top as a function of hydrodynamic conditions. The methods used to quantify these evolutions are discussed in Chapter 4. The bedform characteristics and the shape of the channel from every epoch can then be compared with current velocities and Froude number derived from the hydrodynamic model, which is modulated with tide and river discharge (Chapter 5).

This research examines 30 epochs of the delta top multibeam data, which were collected every 3 to 4 days during a 4 month period in summer 2011. An additional 17 epochs from the daily multibeam surveys in summer 2012 and summer 2013 were also used. This chapter presents the observations and discussion relating the flow conditions to the evolution of both bedform characteristics and the channel shape on the delta top. At the end of this chapter, these are considered as causal factors associated with landslides and/or turbidity currents on the adjacent slope.

Herein, the epoch of every data acquisition is represented using a simple numbering system. The pattern of this numbering system is *YYEE*, where *YY* is the two end digits of the observation year and *EE* is the epoch sequence. For example, *1123* is the data for epoch number 23 in the year 2011. A complete list of each epoch and its corresponding Julian Date and Gregorian Date is given in Appendix C.

6.1. Bedform Roughness Evolution on the Delta Top

6.1.1. Summer 2011

The terrain models used to understand the evolution of the delta top start April 28, 2011 (JD118, epoch 1101) and continue until August 18, 2011 (JD230, epoch 1130). The tide modulation, the river discharge conditions, and the current magnitude within this time window are shown in Figures 6.1a, 6.1b, and 6.1c respectively. Vertical dashed lines in Figure 6.1 represent the epoch of the delta top morphological observations.
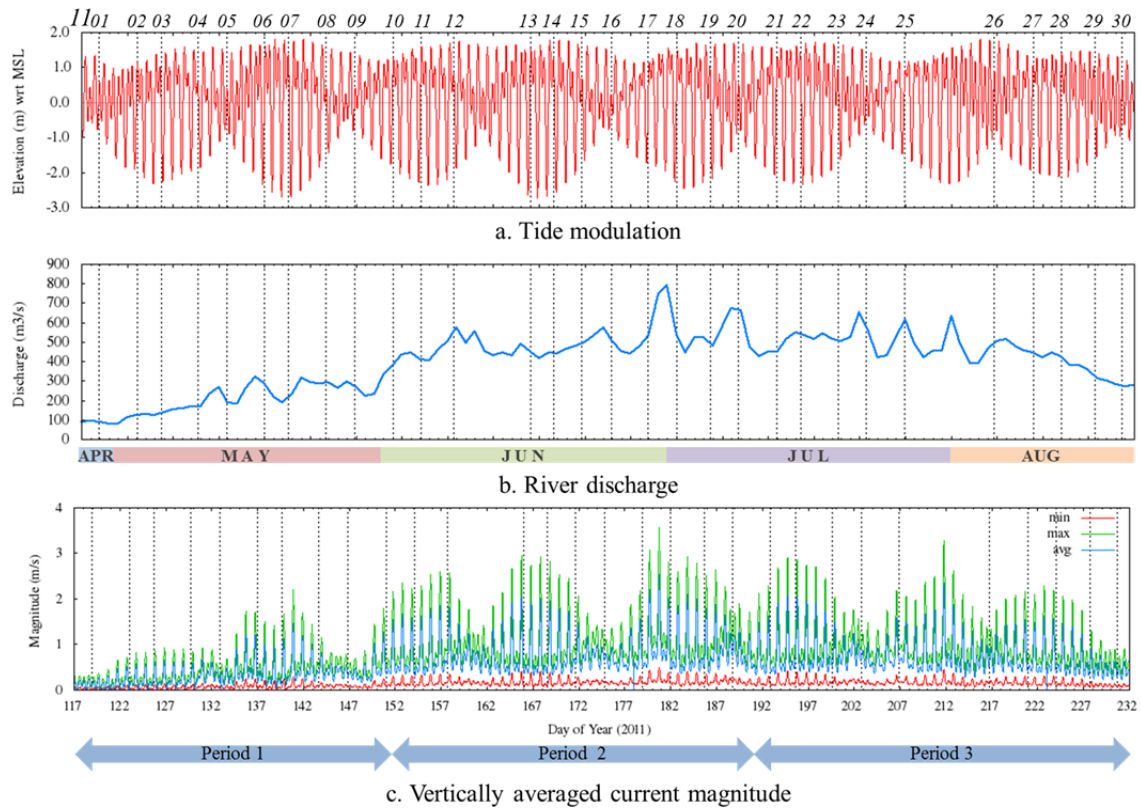
Figure 6.1: The tide observations (a), the river discharge measurements (b), current magnitude derived from the hydrodynamic model (c) during data acquisition in summer 2011 period. The minimum, maximum, and average of current magnitude was extracted from segment A_1A_2.

125

The river discharge was less than 100 m^3s^{-1} at the beginning of data acquisition. It began to rise when the snow melt freshet commenced. The steepest rise of the river discharge occurred at the end of May, and the river discharge continued to rise until the middle of June. After, it fluctuated with an average discharge of approximately 600 m^3s^{-1} until the beginning of August. The maximum discharge during this period was on June 29, 2011 (JD180, between epochs *1117* and *1118*), when the discharge peaked at more than 800 m^3s^{-1}. A gentle decrease in river discharge started at the beginning of August and continued until the end of the data acquisition.

There were 8 spring-neap cycles in this time window. The vertically averaged current magnitude was extracted from the hydrodynamic model along segment A_1A_2 (Figure 4.5) during the time of observation (Figure 6.1c). The spring-neap tide modulation is clearly controlling the peak current magnitude. The waxing and waning of the river discharge also affects the peak current magnitude and produces a significant superimposed variability.

The current magnitude maximum was in June and July, when a low water spring tide was combined with a high river discharge. These factors will affect the sedimentary processes in the area. As will be demonstrated in the next section, the interaction of the current fluctuations with the sediment on the riverbed leads to major variations in bedform characteristics. This chapter will quantify these changes and attempt to explain the relationship between the hydrodynamic regime and bed morphology on the delta top.

In order to better describe the evolution of the delta top, the observations from summer 2011 are divided into 3 periods with 10 observations in each period. The first period runs from April 28, 2011 (JD118, epoch *1101*) to May 30, 2011 (JD150, epoch *1110*), the second, from June 2, 2011 (JD153, epoch *1111*) to July 7, 2011 (JD188, epoch *1120*), and the third, from July 11, 2011 (JD192, epoch *1121*) to August 18, 2011 (JD230, epoch *1130*).

a. <u>The first period in summer 2011: April 28, 2011 - May 30, 2011</u>

For each period, a common presentation style is used. At the top of the figure, the sun-illuminated terrain models are followed by histograms of the dominant wavelength and histogram of the roughness amplitude for each epoch. The dominant wavelength distribution is derived from a 2D spectral analysis and the roughness amplitude distribution is calculated from a detrended terrain model, as explained in Chapter 4. On the lower half of the figure, the corresponding backscatter strength is shown. Accompanying these combined plots are corresponding plots of the wavelength, roughness amplitude, skewness, mean backscatter and its standard deviation, and the Froude number which is used as a representative of the flow regime in the delta top area.

Figure 6.2a shows that bedforms on epochs *1101* to *1105* are morphologically stable with a similar distribution of the dominant wavelength and the roughness amplitude. These bedforms have a peak of approximately 9.4 m in dominant wavelength. The standard deviation of the roughness amplitude distribution of these bedforms is approximately 0.06 m.
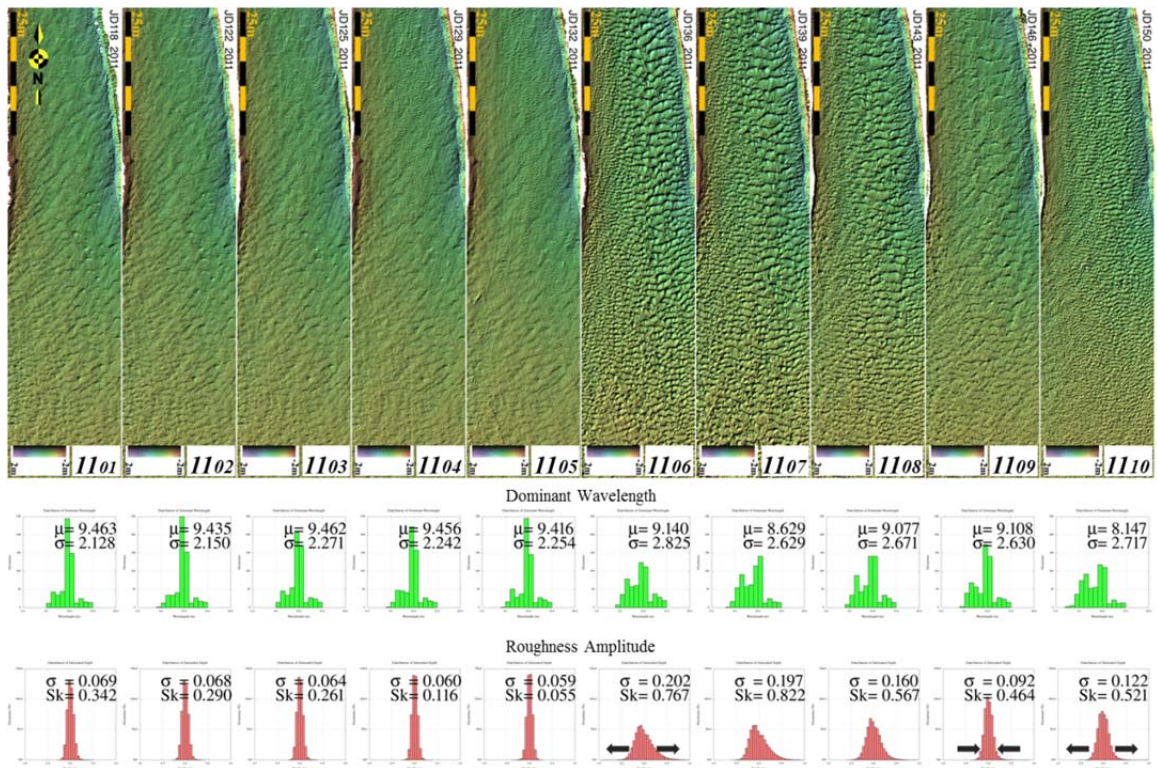
a. Bathymetric terrain models, dominant wavelength histograms and roughness amplitude histograms
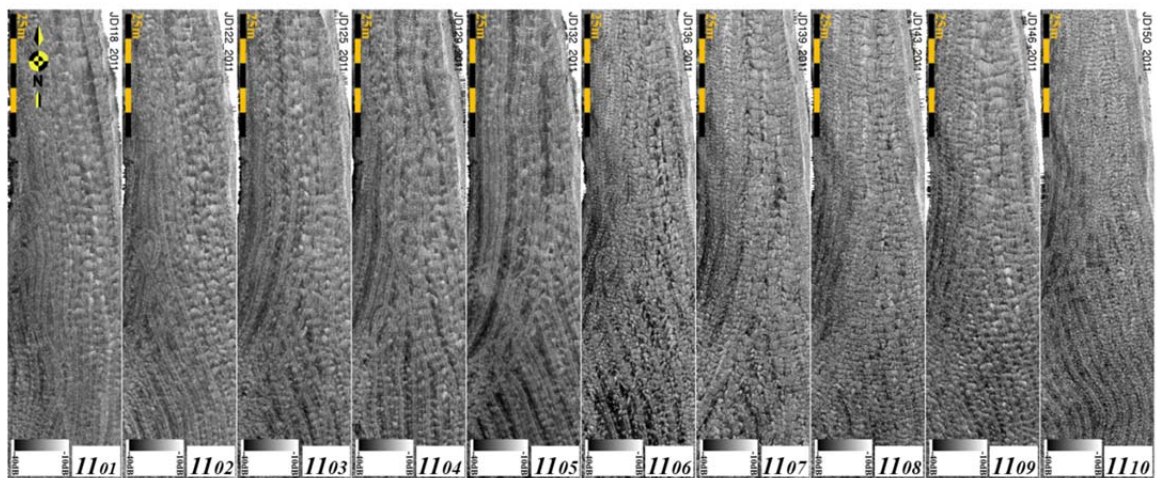
b. Backscatter maps

Figure 6.2: Sun-illuminated terrain models (top) and backscatter maps (bottom) of the first period in summer 2011.

The sediment distributions (based on backscatter intensity maps) during this period had not changed significantly (shown by the backscatter strength mean and standard deviation in Figure 6.3). The mean backscatter strength is approximately -26 dB and the standard deviation is approximately ±10 dB (the smallest of the year). The peak Froude numbers during this period were relatively low: less than 0.2 (see Figure 6.3).

The first changes of the year are seen after epoch *1105*. Bedforms on epoch *1106* started to develop when the river discharge increased and the tide was in its spring cycle (see Figure 6.1). The highest Froude numbers immediately prior to this epoch (the red arrow in Figure 6.3) is obviously larger than *1101* to *1105*. Corresponding with the increase in Froude number is an increase in the standard deviation in the roughness amplitude (approximately 0.2 m). The increase in the standard deviation can be seen in Figure 6.2a.

The mean and standard deviation of the backscatter strength of the bedforms on epoch *1106* also increases. At the same time that the Froude number and the amplitude increase, the skewness also increases (Figure 6.3). Epochs *1106*, *1107*, and *1108* have a similar roughness morphology and an analogous dominant wavelength distribution which is broader than that of epochs *1101* to *1105* (Figure 6.2a).

Figure 6.3: Wavelength, roughness amplitude, skewness, mean and standard deviation of backscatter, and Froude number on segment A_1A_2 within the first period in summer 2011. The red arrow is pointing to the highest Froude number immediately prior to epoch *1106*.

As the flow decreased after *1108*, there is a reduction in the roughness amplitude and a return to a more peaked dominant wavelength distribution on epoch *1109*. Qualitatively, the terrain exhibits only a degraded remnant of the preexisting bedform pattern. When the Froude number peaked up again by epoch *1110*, the standard deviation of roughness amplitude distribution expanded again and the dominant wavelength had a broader distribution.

The focus of this work is on the peak Froude number that was present during the last lower low water before the multibeam survey. This is assumed to be the last period of high bed shear stress when the Froude number was most elevated and this is responsible for the preserved bedforms. Notice that when the Froude number is more than 0.2, the roughness amplitude distribution starts to spread out and when the Froude number is less than 0.2, the roughness of the bedform is relatively subdued (Figure 6.3).

In order to demonstrate the bedform characteristics over longer wavelengths, 1D power spectra are extracted from the depths along segment A_1A_2 for each epoch (Figure 6.4). Bedforms of epochs *1101* to *1105* have similar power spectra with a slow rise in power spectrum with increasing wavelength. The slope average of these spectra is -1.450 dBm (decibel meter) for wavelengths less than 10 m and -0.344 dBm for wavelengths more than 10 m. The abrupt change in spectra between epochs *1105* and *1106* is represented by the red arrow shown in Figure 6.4.
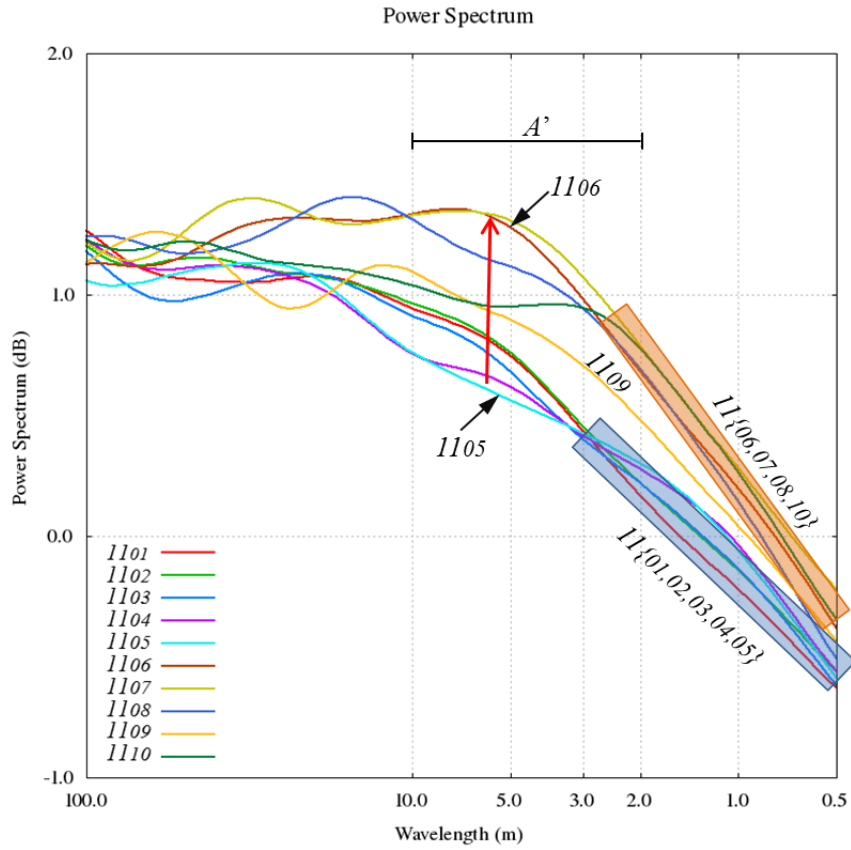
Figure 6.4: 1D power spectra of segment A_1A_2 within the first period in summer 2011. The red arrow indicates the increasing power spectra between epochs *1105* and *1106*. A' is the range of wavelength in which a relict relief occurs.

Based on Figure 6.4, bedforms on epochs *1106*, *1107*, *1108*, and *1110* have significantly more energy than those of epochs *1101* to *1105* in all available wavelengths and notably have a steeper rise in power spectra. For wavelengths less than 5.0 m, the average slope is -2.280 dBm and for wavelengths more than 5.0 m, the slope of the power spectra is 0.171 dBm (relatively flat). The energy was reduced on epoch *1109* but, before the bedform population completely degraded, the current increased again resulting in a higher Froude

132

number and thus, epoch *1110* reestablished a 1D spectra similar to that of epoch *1108*. It appears to take more than one low water to wipe out the "relict" relief which occurs at longer wavelengths (*A'* in Figure 6.4).

b. <u>The second period in summer 2011: June 2, 2011 – July 7, 2011</u>

The daily average of the river discharge in the second period was more than 600 m^3s^{-1}: thus, it was significantly bigger than that of the first period in 2011. Qualitatively, by looking at the sun-illuminated terrain models and the backscatter maps in Figure 6.5, the evolution of the bedforms in this period was more active than in the first period.

The combined plots in Figure 6.5 exhibit the enormous change of the bedforms during this period. The bedform on epoch *1111* evolved from epoch *1110* through expansion in roughness distribution and increasing Froude number (from 0.35 to 0.45 see Figure 6.6). Epochs *1111* and *1112* have a similar dominant wavelength and the last peak of Froude numbers before those epochs are nearly identical.

There is more than an 8 day gap (Figure 6.6) between epochs *1112* and *1113*, thus the bedform's transition within this gap cannot be analyzed. The last peak Froude numbers before epochs *1113* and *1114* are the highest seen so far in this year and are greater than 0.55 (the red arrows in Figure 6.6). The roughness distribution on epochs *1113* and *1114* are narrower than epochs *1111* and *1112* and the dominant wavelength on epochs *1113* and *1114* distributes evenly.
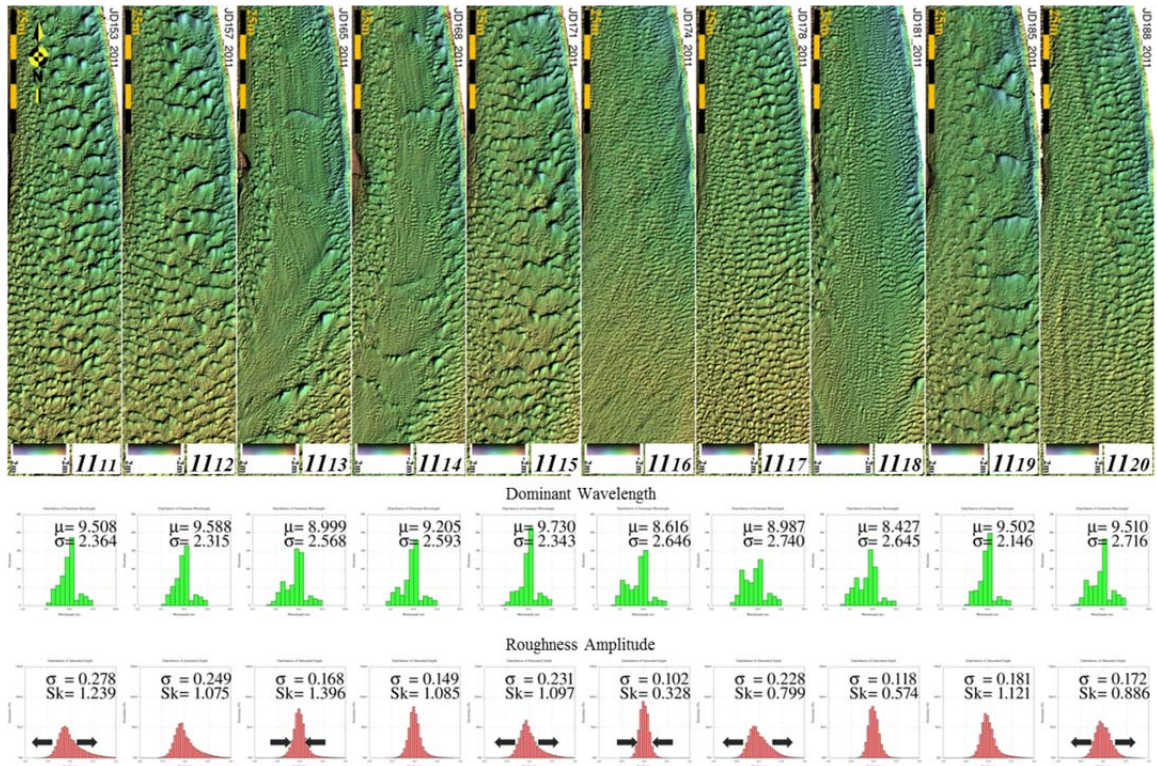
133

Dominant Wavelength

μ= 9.508 σ= 2.364	μ= 9.588 σ= 2.315	μ= 8.999 σ= 2.568	μ= 9.205 σ= 2.593	μ= 9.730 σ= 2.343	μ= 8.616 σ= 2.646	μ= 8.987 σ= 2.740	μ= 8.427 σ= 2.645	μ= 9.502 σ= 2.146	μ= 9.510 σ= 2.716

Roughness Amplitude

σ = 0.278 Sk= 1.239	σ = 0.249 Sk= 1.075	σ = 0.168 Sk= 1.396	σ = 0.149 Sk= 1.085	σ = 0.231 Sk= 1.097	σ = 0.102 Sk= 0.328	σ = 0.228 Sk= 0.799	σ = 0.118 Sk= 0.574	σ = 0.181 Sk= 1.121	σ = 0.172 Sk= 0.886

a. Bathymetric terrain models, dominant wavelength histograms and roughness amplitude histograms
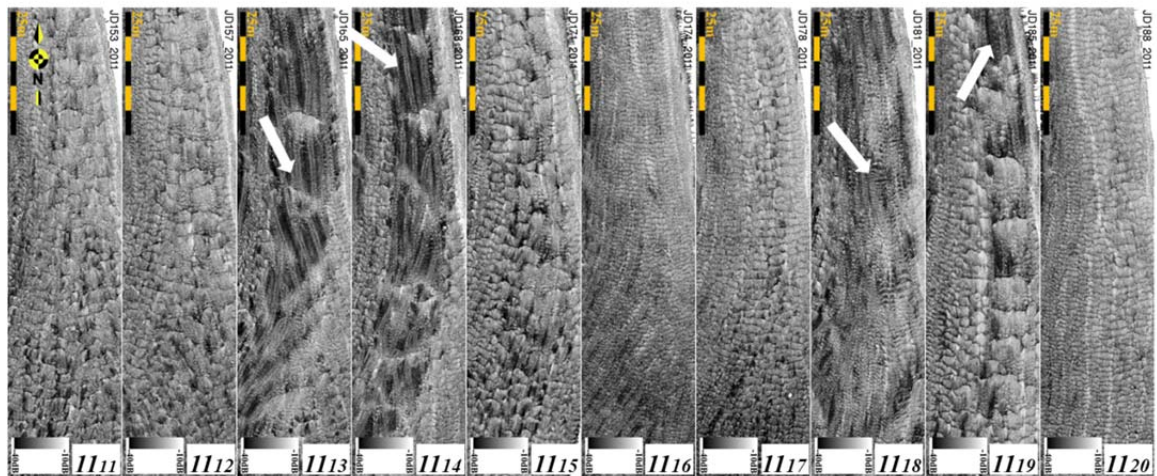
b. Backscatter maps

Figure 6.5: Sun-illuminated terrain models (top) and backscatter maps (bottom) of the second period in summer 2011. The white arrows are pointing at the backscatter patchiness.
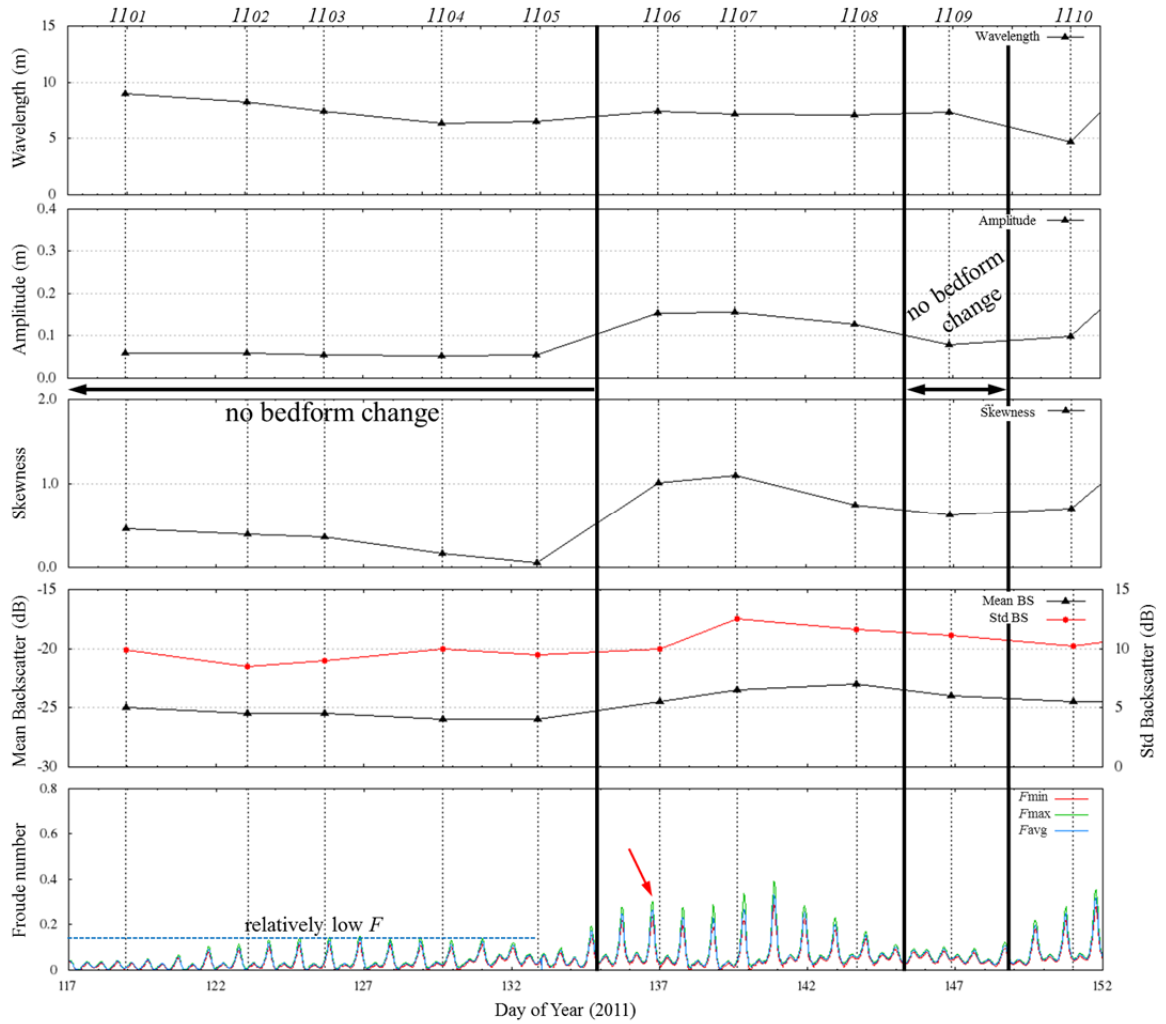
134
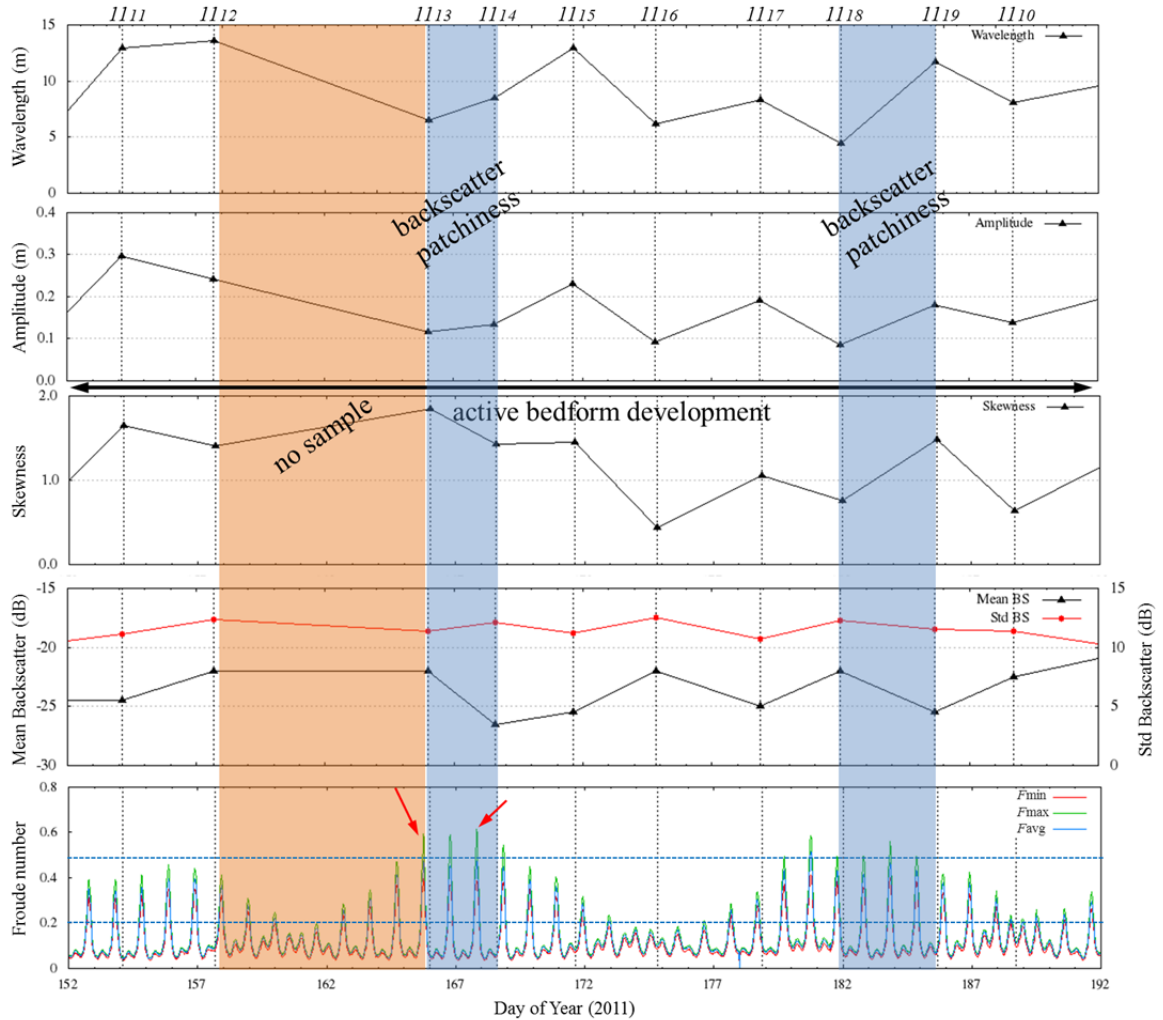
Figure 6.6: Wavelength, roughness amplitude, skewness, mean and standard deviation of backscatter, and Froude number on segment A_1A_2 within the second period in summer 2011. The red arrows represent the highest Froude number seen so far in this year. The shaded blue areas are the time when the backscatter patchiness occur during the second period in summer 2011.

Qualitatively, looking at the terrain model during epoch 1113 to 1114, the flanks of the channel during epochs 1113 to 1114 are similar to epochs 1111 and 1112, yet the centre of the channel has become smooth. At the same time during this transition, a marked change

135

in the backscatter now appears for the first time. There is a notable backscatter patchiness, which occurs on epochs *1113* and *1114* (white arrows Figure 6.5b). Based on the relationship between mean backscatter and mean grain size of the sediment sample (Figure 3.16), the darker color in the backscatter map represents the finer sediment and vice versa.

At first glance, this might seem counterintuitive. The observed mean grainsize appears to get smaller during the highest current speeds. One possible explanation for this is that, at these higher flow speeds, during the low water flow peak, there was much more sand in suspension moving as washload. As the backscatter, however, is only observed when the current speed has dropped (at high tide), then this washload is abruptly dropped out of suspension and drapes the seafloor that has previously been planated by the washout phase of the peak flow. Only by sampling the seabed during these washout conditions, both at high and low water could such a hypothesis be tested.

After *1114*, as the peak ebb flow slows, the bedforms gradually return to the previous population (*1115*), similar to those of epochs *1111* and *1112*. The lower Froude number immediately before epoch *1116* is reflected in a smaller roughness amplitude distribution, which is now similar to those of epochs *1101* to *1105*, but with a different dominant wavelength distribution. As the spring cycle grows again by *1117*, the bedform roughness increases and a broader range of principal wavelengths reappears.

A particularly unusual event happens between epochs *1117* and *1118,* reflected in the flow and bedforms. As with *1113* and *1114*, although the Froude number before epoch

1118 was high (more than 0.55), it has a similar shape of the dominant wavelength distribution and roughness amplitude distribution as on epoch *1116*, which has a notably lower flow stage. As will be discussed later, a major alteration to the downstream delta has taken place immediately before this event.

The high Froude number before epoch *1119* generated a bedform population with roughness amplitude distribution similar to those of epochs *1113* and *1114*. As the flow stage descends again to *1120*, the standard deviation of roughness distribution decreases and the standard deviation of the dominant wavelength distribution increases (Figure 6.5).

Distinct low backscatter zones, with along channel dimensions of more than 50 m, appeared on epochs *1113*, *1114*, *1118*, and *1119* (Figure 6.5b). The patches are spaced according to the location of the longest wavelength bedforms. This patchiness is quite distinctive, occurring uniquely just after peaks in Froude number greater than 0.5. The patchiness can be identified by a drop in mean backscatter (Figure 6.6).

Although bedforms *1116* and *1118* show similarity in the roughness amplitude and wavelength distributions, based on qualitatively looking at the backscatter map, the sediment distributions on these epochs are completely different. The change in sediment distribution (based on backscatter strength distribution) between epochs *1112-1113*, *1114-1115*, *1117-1118*, and *1119-1120* corresponds to when the flow passed up or down through Froude number of approximately 0.55.

The 1D power spectra of the bedforms within this period can be seen in Figure 6.7. All the 1D spectra exhibit almost identical trends for wavelengths less than 3.0 m, with the average slope of -2.673 dBm. The shapes of the 1D spectra vary significantly between wavelengths of 5.0 m to 100.0 m. There seems to be a progressive extension of the spectral slope at the same gradient as the longer wavelength roughness grows.

Figure 6.7: 1D power spectra segment A_1A_2 of the second period in summer 2011. The blue arrows represent a dropping of power spectra and the red arrow represents an increasing of power spectra. The wavelengths less than 3.0 m which have a similarity in power slope are inside a blue shaded area.

c. The third period in summer 2011: July 11, 2011 - August 18, 2011

The observations from the preceding two periods have shown correlated parameters that indicate distinct bedform population characteristics. In the third period, four

138

characteristics are recognized both in morphology and backscatter strength. Concerning the topography, the following groupings are identified. Bedforms on epochs *1121*, *1122*, and *1123* have a similar wavelength distribution and roughness amplitude (Figure 6.8). Epochs *1124*, *1126*, and *1129* share the same shape of dominant wavelength distributions and they have similar roughness amplitudes. The wavelength distributions and roughness amplitudes on epochs *1125*, *1127*, and *1128* appear to be very similar. Lastly, the dominant wavelength distribution and the roughness amplitude on epoch *1130* are similar to those of epochs *1101* to *1105* (Figure 6.2).

Concerning the backscatter, the aforementioned groupings also exhibit distinct backscatter patchiness. The long wavelength backscatter patchiness (more than 50.0 m), similar to *1113*, *1114*, *1118*, and *1119*, does not occur in this period. Clear patchiness is, however, seen at shorter wavelengths (approximately 20 m), again related to the corresponding spacing of discrete large bedforms when they are present. These occur on epochs *1121*, *1122*, and *1123*, which are similar to those of epochs *1111*, *1112*, and *1115*.

Shorter backscatter patchiness (less than 10 m) similar to those of epochs *1116*, *1117*, and *1120* took place as the dominant wavelength was getting shorter (*1125*, *1127*, and *1128*). For all the characteristic clusters, the mean and standard deviation of backscatter strength does not vary significantly over this period (Figure 6.9). None of the groupings exhibit the drop in mean and increase in standard deviation seen in epochs *1113*, *1114*, *1118*, and *1119*.
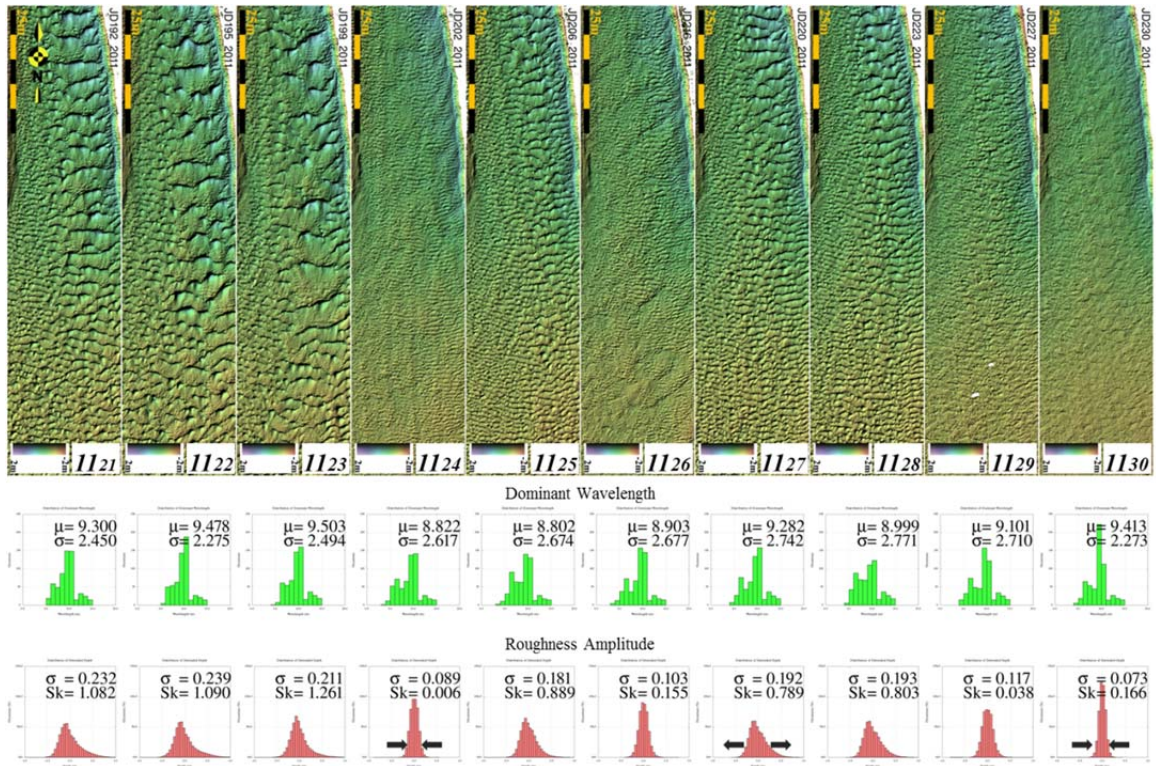
Dominant Wavelength

| $\mu= 9.300$ $\sigma= 2.450$ | $\mu= 9.478$ $\sigma= 2.275$ | $\mu= 9.503$ $\sigma= 2.494$ | $\mu= 8.822$ $\sigma= 2.617$ | $\mu= 8.802$ $\sigma= 2.674$ | $\mu= 8.903$ $\sigma= 2.677$ | $\mu= 9.282$ $\sigma= 2.742$ | $\mu= 8.999$ $\sigma= 2.771$ | $\mu= 9.101$ $\sigma= 2.710$ | $\mu= 9.413$ $\sigma= 2.273$ |

Roughness Amplitude

| $\sigma = 0.232$ Sk= 1.082 | $\sigma = 0.239$ Sk= 1.090 | $\sigma = 0.211$ Sk= 1.261 | $\sigma = 0.089$ Sk= 0.006 | $\sigma = 0.181$ Sk= 0.889 | $\sigma = 0.103$ Sk= 0.155 | $\sigma = 0.192$ Sk= 0.789 | $\sigma = 0.193$ Sk= 0.803 | $\sigma = 0.117$ Sk= 0.038 | $\sigma = 0.073$ Sk= 0.166 |

a. Bathymetric terrain models, dominant wavelength histograms and roughness amplitude histograms
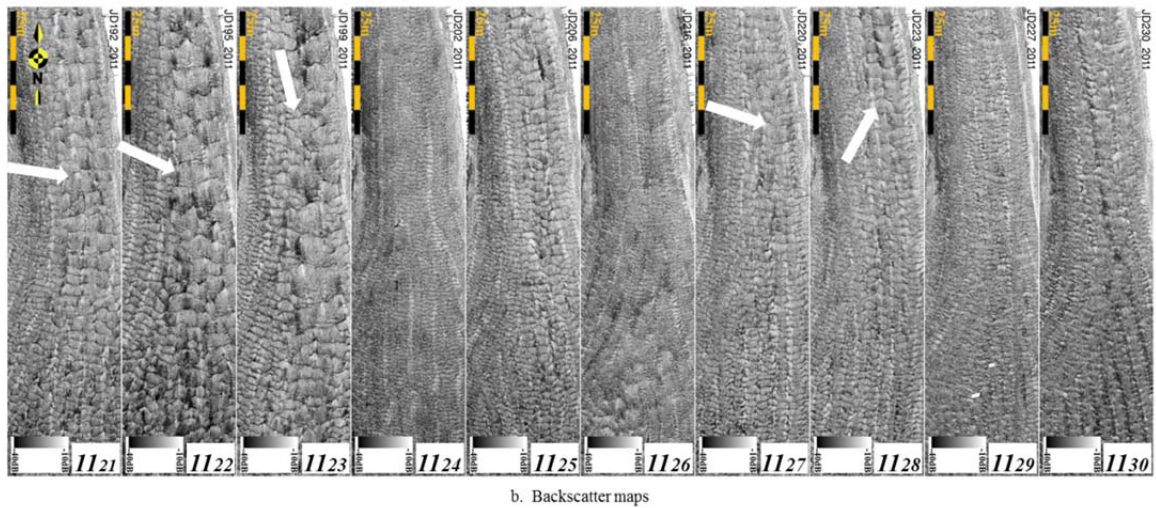
b. Backscatter maps

Figure 6.8: Sun-illuminated terrain models (top) and backscatter maps (bottom) of the third period in summer 2011. The white lines are pointing at the backscatter patchiness.

140
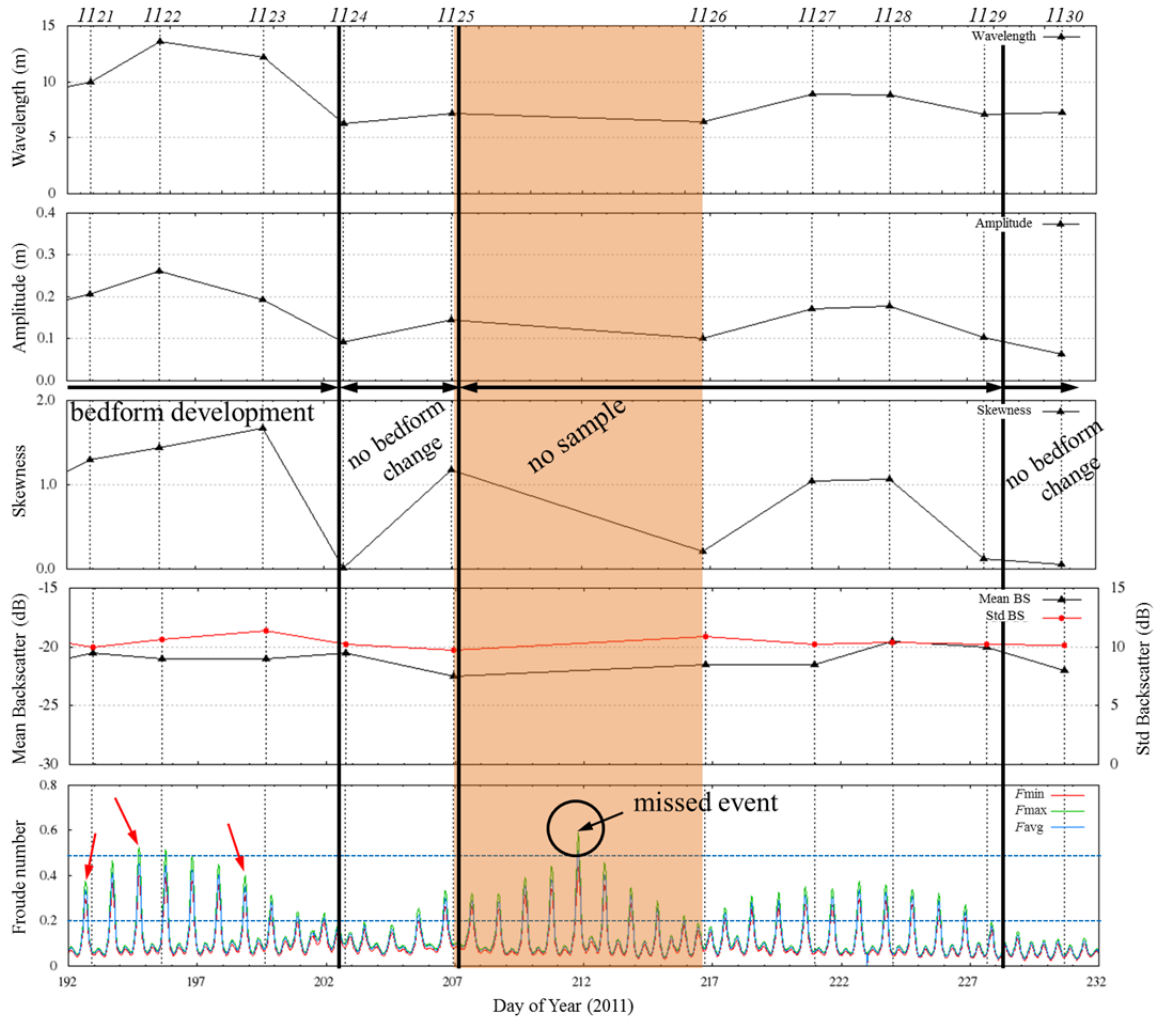
Figure 6.9: Wavelength, roughness amplitude, skewness, mean and standard deviation of backscatter, and Froude number on segment A_1A_2 within the third period in summer 2011. The red arrows represent the Froude number higher than 0.4.

Figure 6.9 compares the variations of these bedforms with the flow regime. The four characteristic morphologies correspond to distinct Froude numbers. The maximum Froude numbers before epochs 1121, 1122, and 1123 (red arrows) are slightly above 0.4. The lower flow regimes, with Froude numbers of approximately 0.2, occurred on epochs

1124, *1126*, and *1129*. Epoch *1125*, *1127*, and *1128* resulted from identical flow stages with the peak Froude numbers at about 0.3 just before data acquisitions. At the final survey (epoch *1130*), the flow dropped to a lower flow regime with a Froude number of less than 0.2.

The 1D power spectra of the third period show that bedforms on epochs *1121* to *1129* have almost identical power for wavelengths less than 3.0 m, with the slope -2.210 dBm (Figure 6.10). The variation begins at wavelengths that are more than 3 m. Epochs *1121*, *1122*, *1123*, *1125*, *1127*, and *1128* all show a similar spectral slope trend but include a variable amount of extension of the slope to longer wavelengths (more than 10.0 m).

Epochs *1124* and *1126* have a similar power spectral slope for wavelengths from 3 m to 10 m, which is approximately -0.271 dBm, but epoch *1126* has more energy than to that of epoch *1124*. *1130* stands out, as the power spectra decreased significantly from epoch *1129* to *1130*. The power spectra of epoch *1130* is similar to epochs *1101* to *1105* at the beginning of the summer 2011 period with a slowly rising slope (-1.432 dBm).
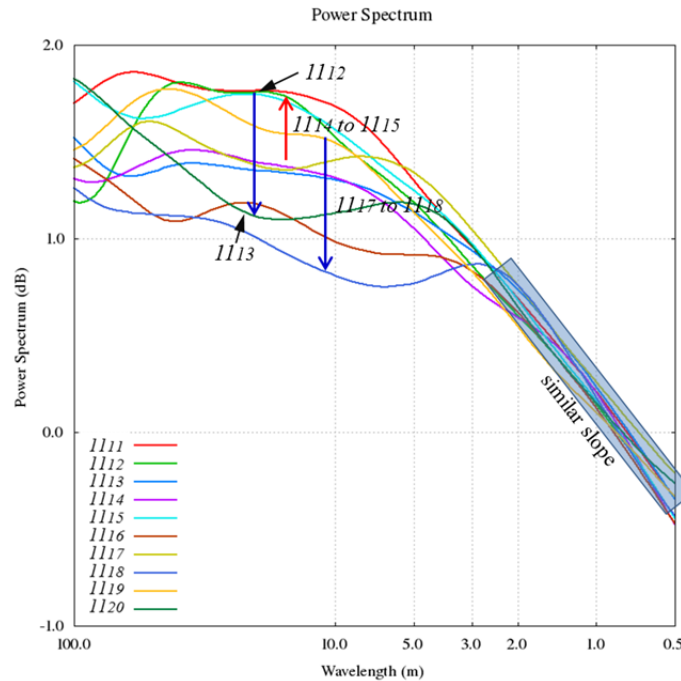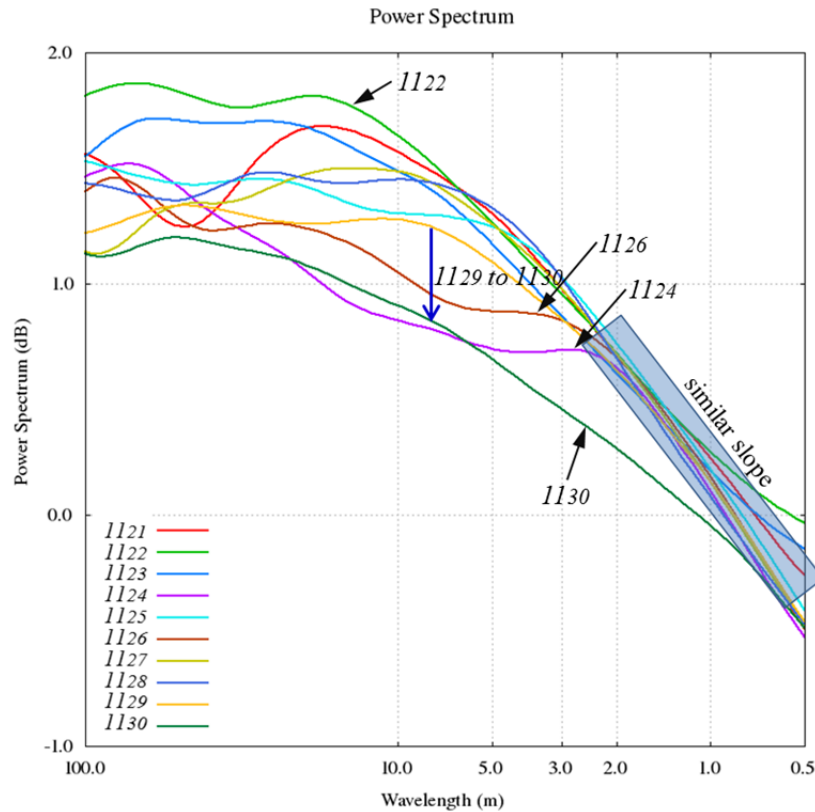
Figure 6.10: 1D power spectra segment A_1A_2 of the third period in summer 2011. The blue arrow represents a dropping of power spectra. The wavelengths less than 3.0 m which have a similarity in power slope are inside a blue shaded area.

In summary, combining the three periods, the short wavelength bedform characteristics changed dramatically during the spring-neap cycle within the 4 month period in summer 2011. However, as bedform morphological characteristic changed daily but was only sampled every 3 to 4 days, it is hard to see a good correlation with the flow conditions. Thus, to get better insight into the bedform's evolution, daily surveys in 2012 and 2013 were conducted in the same area (Figure 4.5). The next section will discuss the higher temporal resolution of bedform evolution seen in those years.

143

6.1.2. Summer 2012

In this period, the observation was focused on daily surveys during a progressive transition from neap to spring tide cycle. The daily average of the river discharge was relatively constant and high, at about 550 m^3s^{-1}. The tide modulation and the river discharge during this period are presented in Figure 6.11a and Figure 6.11b, respectively. The current magnitude extracted from the model is shown in Figure 6.11c. It is obvious that the current magnitudes fluctuate according to the tide modulation.
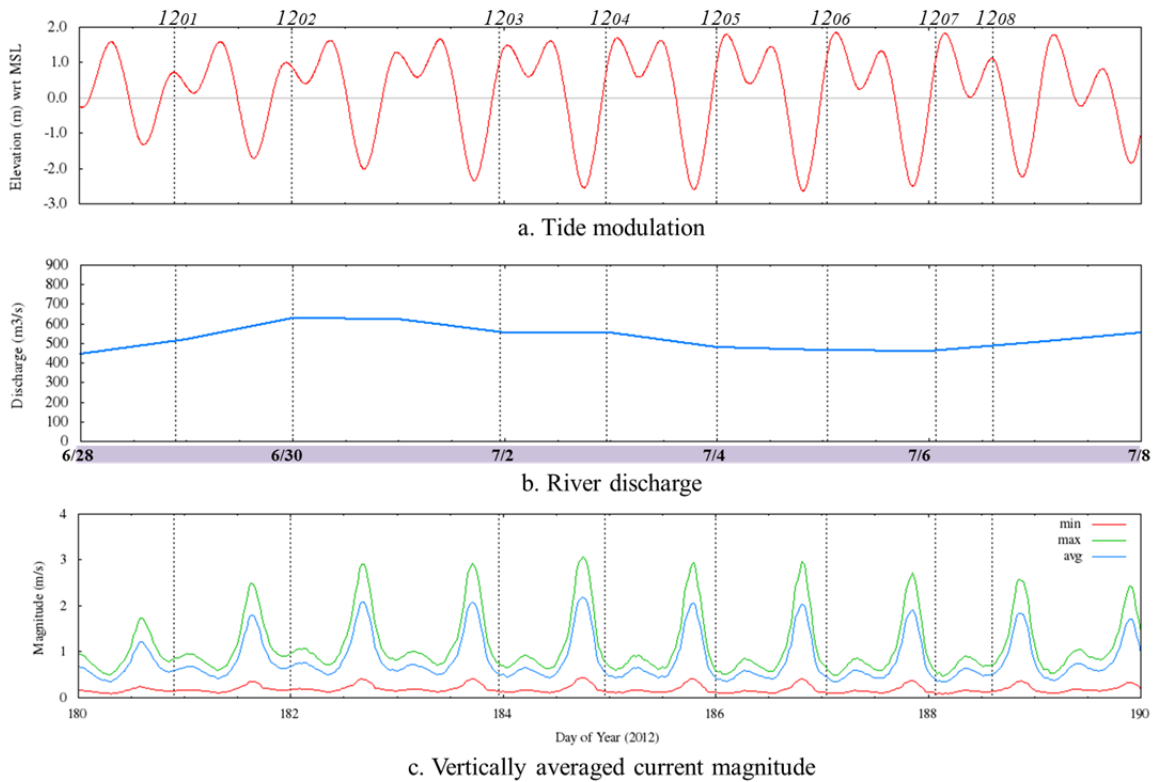
Figure 6.11: The tide observations (a), the river discharge measurements (b), and the current magnitude derived from the hydrodynamic model (c) during data acquisition in 2012. The minimum, maximum, and average of current magnitude was extracted from segment A_1A_2.

Figure 6.12a shows bathymetry terrain models during this period. The bedform on epoch *1201* has a similar type of dominant wavelength distribution and roughness distribution to those of epoch *1116* (see Figure 6.5). The standard deviation of roughness amplitude and dominant wavelength distribution on epoch *1201* is the smallest during the summer 2012 period. As the flow increased, longer wavelengths started to appear (epoch *1202*). The bedform population on this epoch has a similar dominant wavelength and roughness amplitude distributions to those of epoch *1111*.

The mean dominant wavelength is increasing from that on epoch *1203* to epoch *1206*. These bedforms are very similar to that on epoch *1114* (Figure 6.5). During epoch *1203* to epoch *1206*, the standard deviations of roughness amplitude are fluctuated between 0.179 and 0.213 m. Bedform on epochs *1207* and *1208* are very similar. These last two epochs share nearly identical dominant wavelength and roughness distributions (inside the shaded area in Figure 6.12). This is because these bedforms were observed between two high water and high low water without an intervening lowest low water. During the period without a Froude number peak, the bedform population is almost static.

The long wavelength (more than 50.0 m) backscatter patchiness, similar to those of epochs *1113*, *1114, 1118*, and *1119* shown in Figure 6.5, can be seen during epochs *1203*, *1204* and *1205* (white arrows in Figure 6.12). Approximately 20.0 m long backscatter patchiness also appears on epoch *1206*. Shorter backscatter patchiness (less than 10.0 m) appears on epochs *1207* and *1208*.
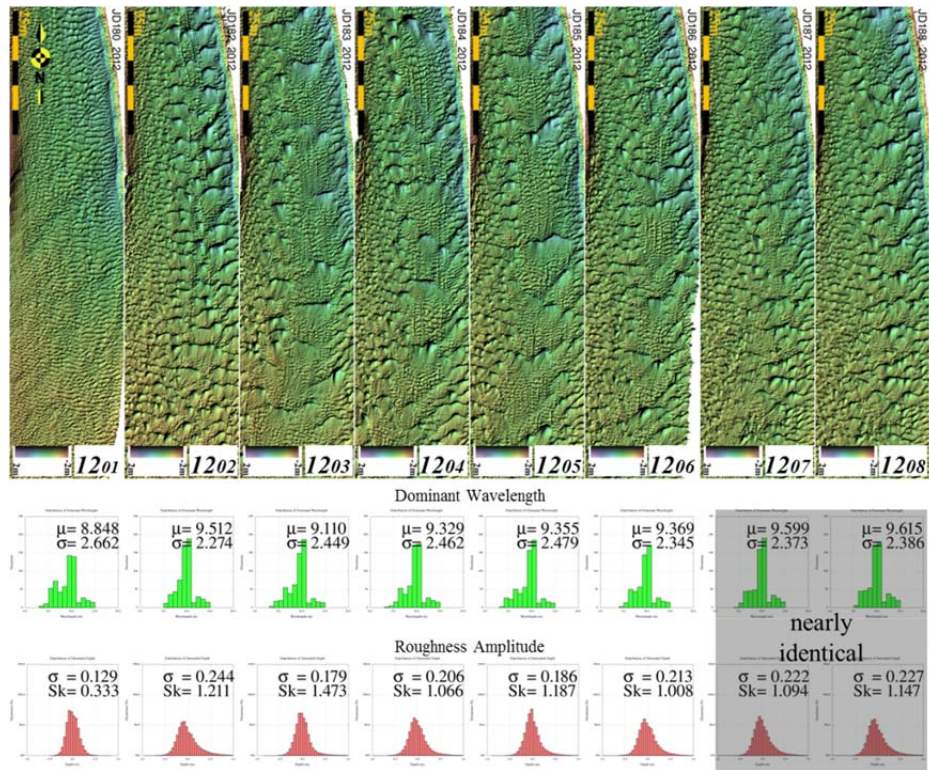
a. Bathymetric terrain models, dominant wavelength histograms and roughness amplitude histograms
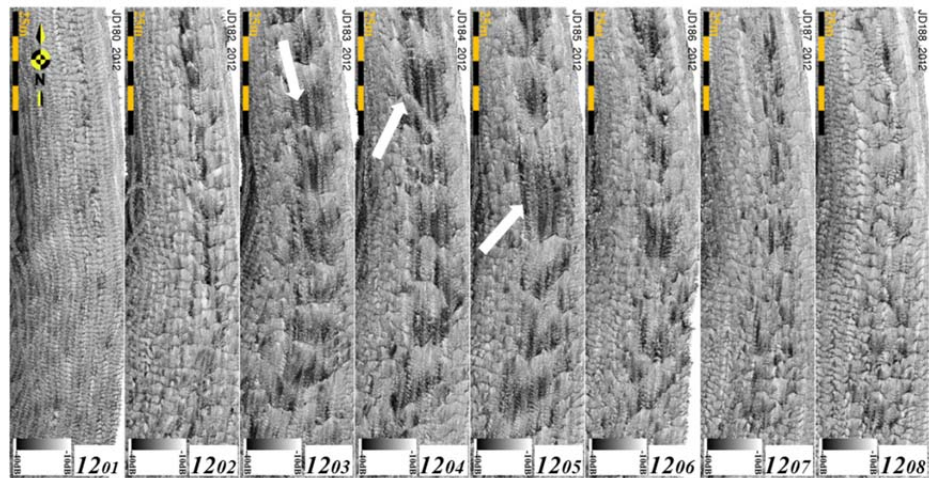
b. Backscatter maps

Figure 6.12: Sun-illuminated terrain models (top) and backscatter maps (bottom) in summer 2012 period.

The difference in dominant wavelength and roughness amplitude distributions from epochs *1201* to *1202* and epochs *1206* to *1207* relates to differences in backscatter images. This means that, during these epochs, the distribution of the sediment changed parallel with the changing of the bedforms roughness and wavelength. The peak Froude number during this period was never below 0.2 (Figure 6.13). The Froude numbers on epochs *1203*, *1204*, *1205*, and *1206* exceed 0.5, reflected in long wavelength backscatter patchiness. These bedforms are reminiscent of those on epochs *1113*, *1114*, *1118*, and *1119* (Figure 6.5), which happened when the Froude number was more than 0.5.

Skewness on this period increases as the Froude number gets bigger (epoch *1201* to *1203*). When the Froude number was more than 0.5, the skewness decreases (epoch *1204*) and stays constant until epoch *1207* (Figure 6.13).

Figure 6.13: Wavelength, roughness amplitude, skewness, mean and standard deviation of backscatter, and Froude number on segment A_1A_2 during summer 2012 period. The red arrows represent the Froude number higher than 0.55.

The 1D power spectra from summer 2012, are presented in Figure 6.14. Unlike the 1D power spectra of the summer 2011 period, there is significant power spectra variation for wavelengths less than 1.0 m. Looking qualitatively at the terrain models, the reason for this short wavelength variability is not obvious. One possibility is the increased near

nadir sounding noise due to degrading bottom detection performance in 2012. For

wavelengths between 1.5 m to 4.0 m, these bedforms share the same trend of power

spectra, with the average slope is -2.374 dBm. A significant change in slope of the power

spectra happened when the wavelength was more than 4 m. As the Froude number grows

from 0.2 to 0.5, the 1D spectra slope grows to longer wavelengths. Bedform *1204* shows

the greatest extension of the spectral slope trend towards longer wavelengths.

Figure 6.14: 1D power spectra of segment A_1A_2 in summer 2012. The red arrow represents an

increasing of power spectra.

6.1.3. Summer 2013

The daily experiment was repeated in 2013 at a different river discharge. River discharge during this period was relatively stable with an average slightly below 400 m^{3}s^{-1}, notably less than was what observed in 2012 (Figure 6.15b). During this period, the delta top was observed from the end of spring tide until the middle of the next spring tide (Figure 6.15a). The current amplitude derived from hydrodynamic model increases significantly when the tide was its approaching springs cycle (Figure 6.15c).
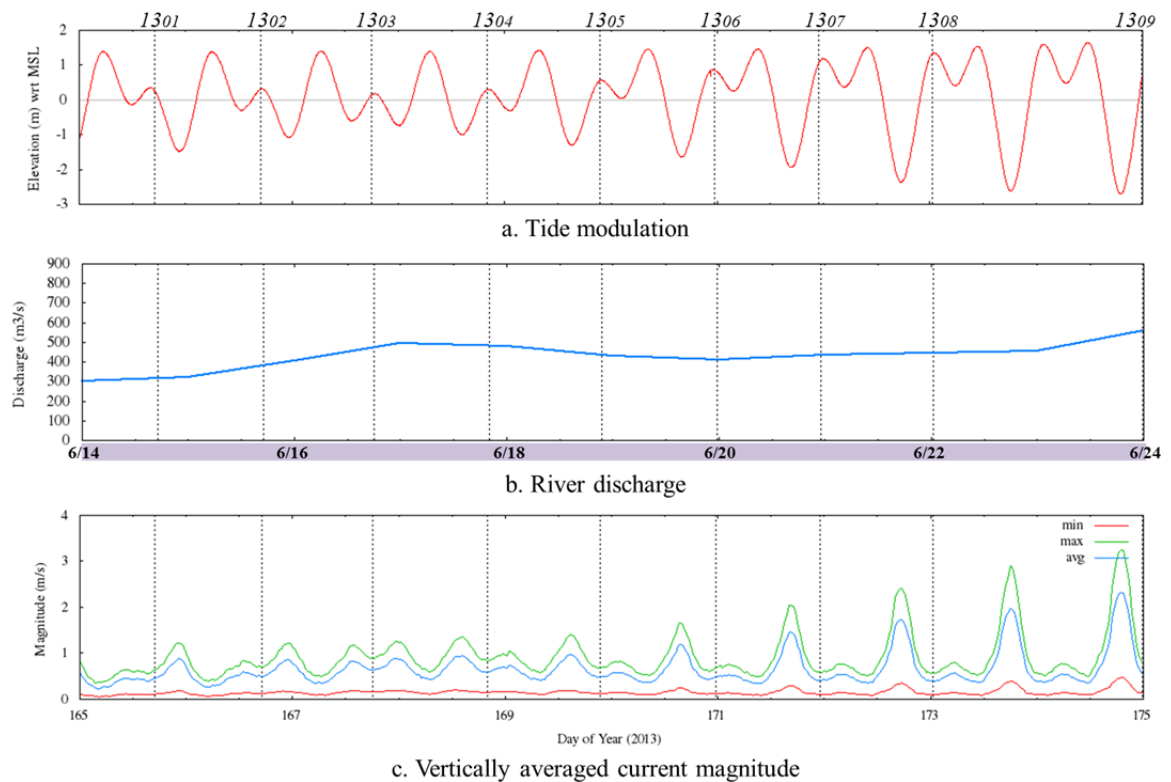
Figure 6.15: The tide observations (a), the river discharge measurements (b), and the current

magnitude derived from the hydrodynamic model (c) during data acquisition in 2013.

Bedforms from epochs *1301* to *1304* are all subdued, although overprinted by an along

track refraction artifact (Figure 6.16a). These bedforms have similar distributions of

dominant wavelength and roughness amplitude to epochs *1101* to *1105* (Figure 6.2). The

bedforms started to develop on epoch *1305* as the current magnitude increased. Figure

6.16 shows there is a significant change in roughness distribution from bedforms on

epochs *1307* to *1308*. The roughness distribution started to spread as the flow increased

(epochs *1308* and *1309*).

Based on the backscatter maps (Figure 6.16b), there is no significant change in the

sediment distribution. The mean and standard deviation of backscatter strength during the

summer 2013 period is relatively stable (Figure 6.17). Notice the western parts have low

backscatter intensity on epochs *1301* to *1308*. This was uniquely seen in 2013 and is

believed to be a result of a change in the western channel boundary since 2012. The

region of low backscatter decrease from epochs *1305* to *1309* at which point it has almost

disappeared. This may be a result of moderate flow regime (the Froude number is more

than 0.7), which arises just before epoch *1309* (see Figure 6.17c).
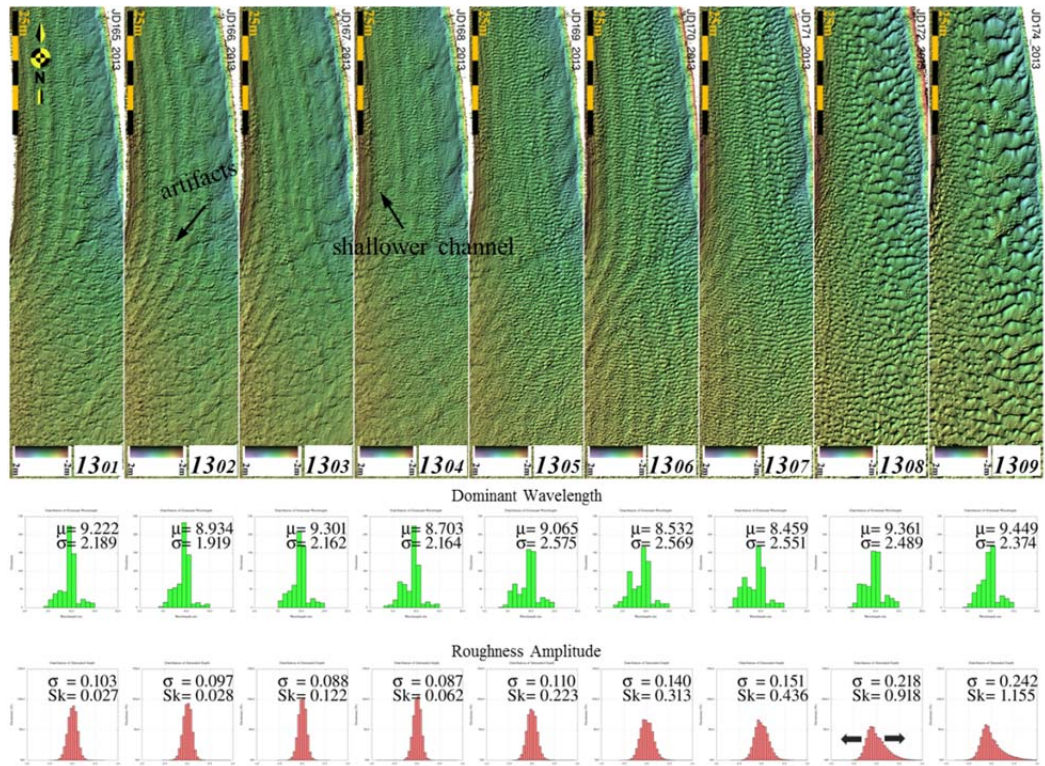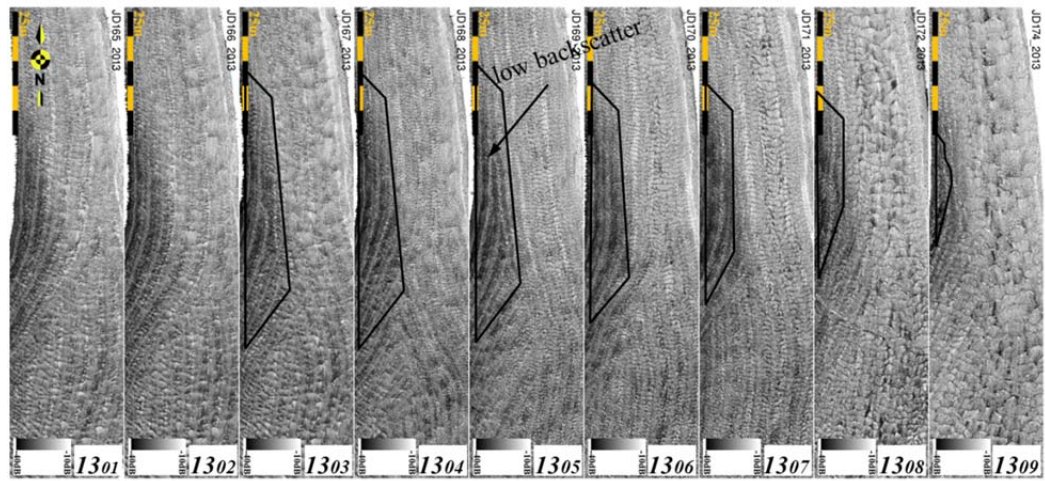
Figure 6.16: Sun-illuminated terrain models (top) and backscatter maps (bottom) in summer 2013 period.

The correlation among the roughness amplitude, the wavelength and the skewness with Froude number can be visually seen in Figure 6.17. The discussion of this correlation will be reviewed in section 6.5. Based on Figure 6.17, the bedform started to develop when the Froude number was more than 0.25.
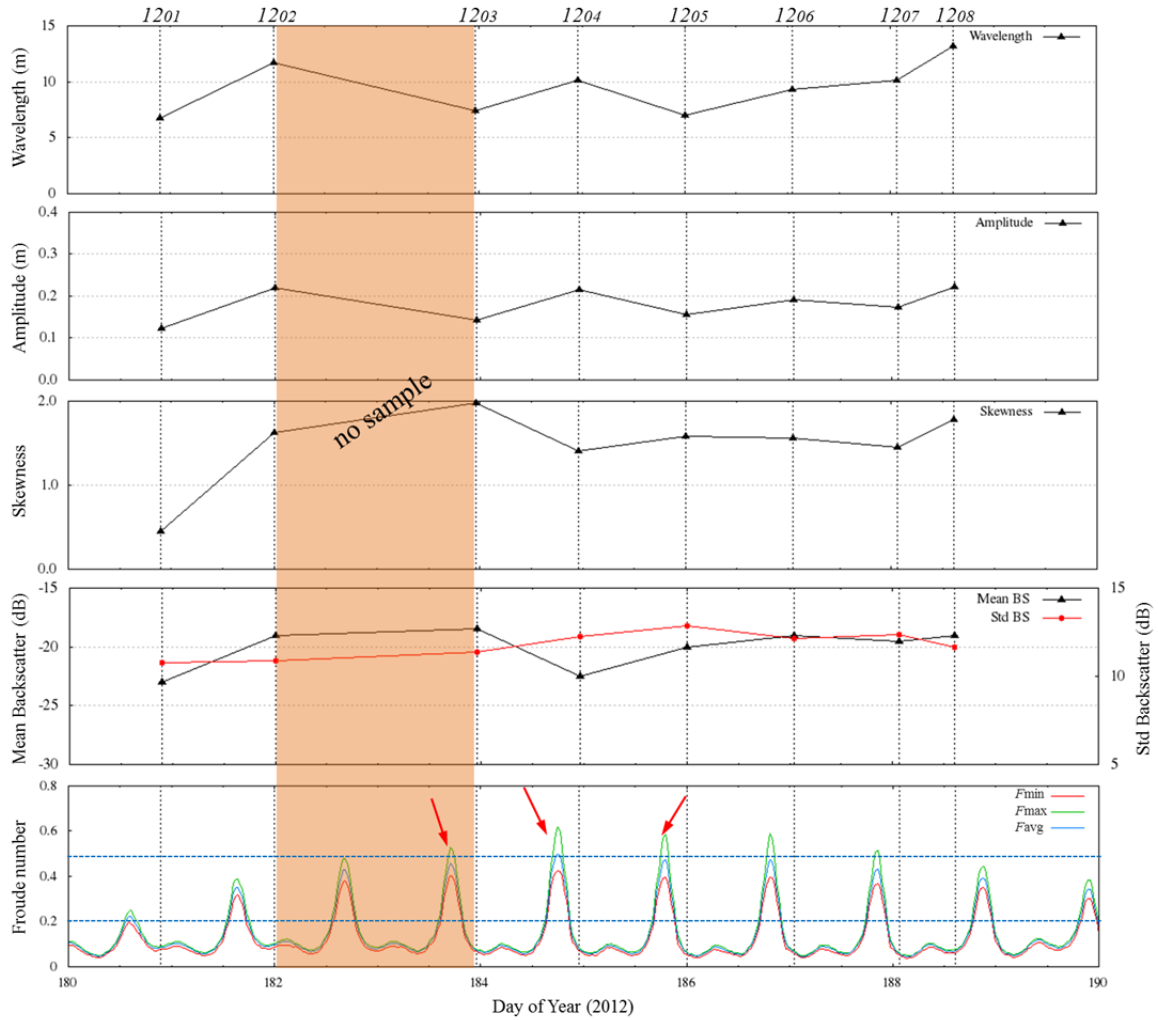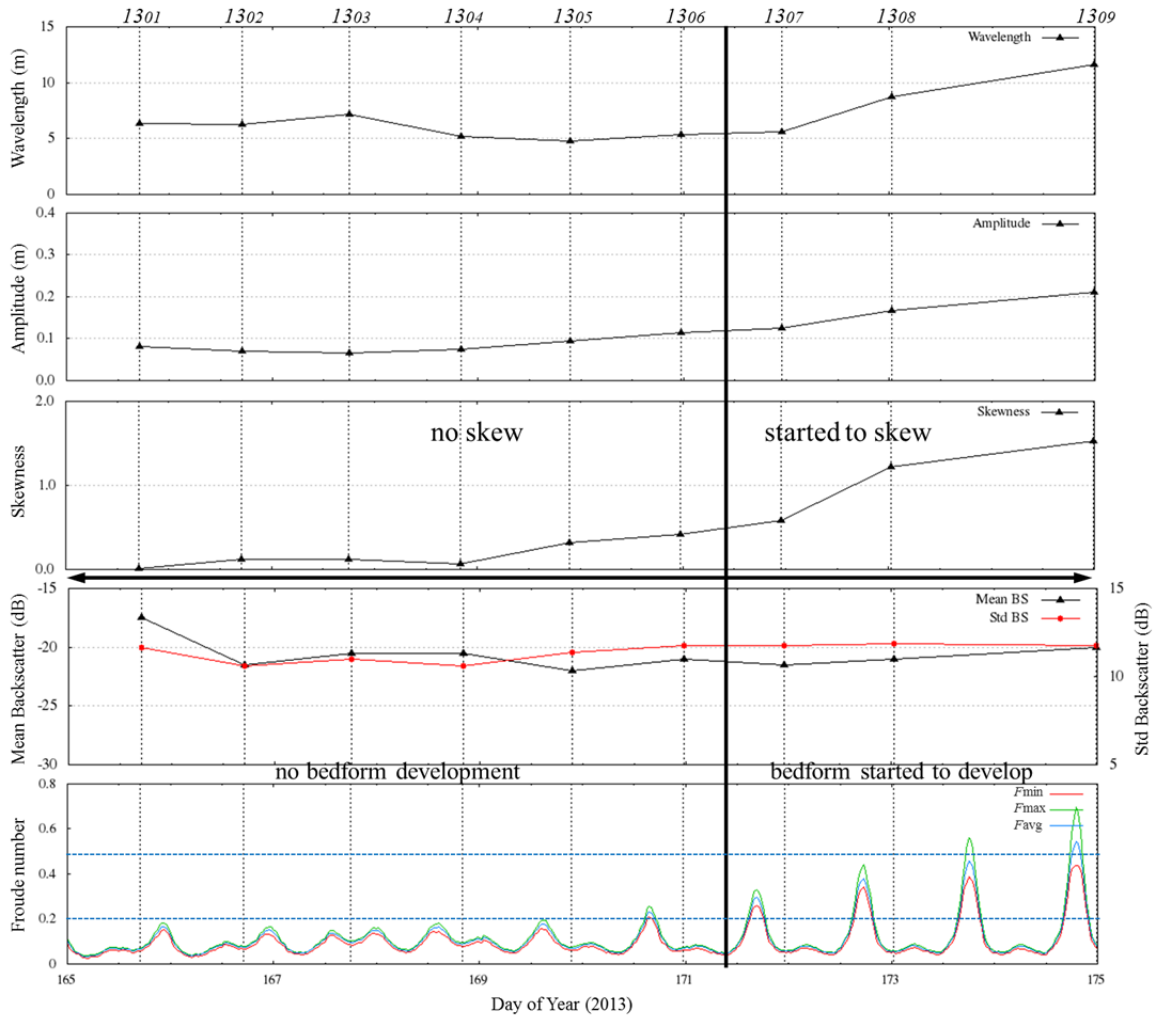

Figure 6.17: Wavelength, roughness amplitude, skewness, mean and standard deviation of backscatter, and Froude number on segment A_1A_2 during summer 2013 period. The upper dashed blue line in the Froude number graph represents the value of 0.5 while lower dashed blue line is Froude number of 0.2.

153

In the summer 2013 period, all bedforms exhibit similar trend of 1D power spectrum variation for wavelengths of less than 1 m with the slope is -2.652 dBm (Figure 6.18). The power spectra of epochs *1301* and *1302* are similar to those of epochs *1101* to *1105* with characteristic slow rise in power spectrum (-1.505 dBm) as the wavelength is getting longer. As the roughness increases, the spectral slope steepens and the trend extends to longer wavelength.

Power spectra of epochs *1301* to *1307* show almost identical trend for wavelengths of 7.5 m to 50 m. The power increased significantly from epochs *1307* to *1308* at about 10 m wavelength, as the peak Froude number increased significantly (more than 0.4). Notice that the power spectra trends on epochs *1305*, *1306*, and *1307* have relatively flat slope within 2 m to 7.5 m wavelength, similar to those of epochs *1124* and *1126*. The power spectra show increasing inflection from epochs *1304* to *1309* as larger wavelength bedforms appear (Figure 6.18). This may evolve as the Froude number was getting higher from epochs *1304* to *1309*. The maximum of 1D power spectra from this period is on epoch *1309* with the Froude number is more than 0.7.
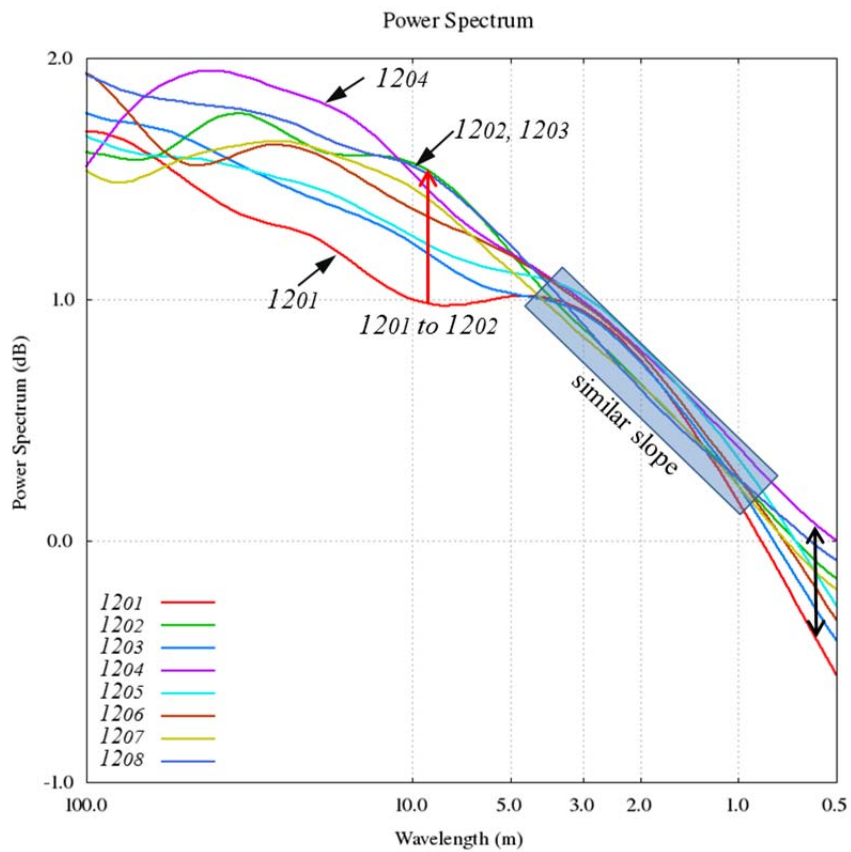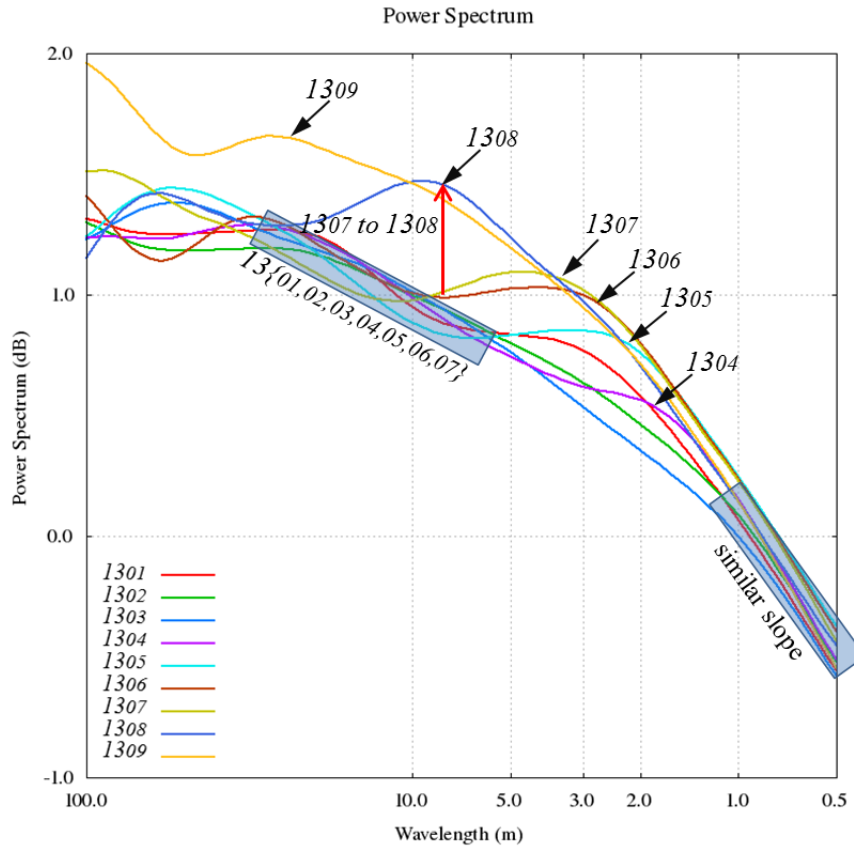
Figure 6.18: 1D power spectra of segment A_1A_2 in summer 2013. The red line represents an increasing of power spectra.

6.2. Depth Variability Analysis

As well as short wavelength bedform variability (explained in previous section), this research also covers long wavelength variations in the channel shape, resulting from the hydrodynamic regime. Depth variability, along and across the channel, was used to represent the dynamics of the long wavelength channel shape.

Figure 6.19 shows the along and across segments for depth analysis. Segment A_1A_2 is used to examine the long wavelength channel evolution in the direction of the flow. This segment was previously used to analyze the 1D roughness. Segments B_1B_2 and C_1C_2 were used to monitor the evolution of the width to depth channel ratio (as discussed in section 4.4). Cross section B_1B_2 was chosen to represent the constricted area that is located between the training dyke and the western inter tidal shoal. Cross section C_1C_2 lies on the area with no constriction. The average inter-epoch erosion and deposition are the focus of this section.
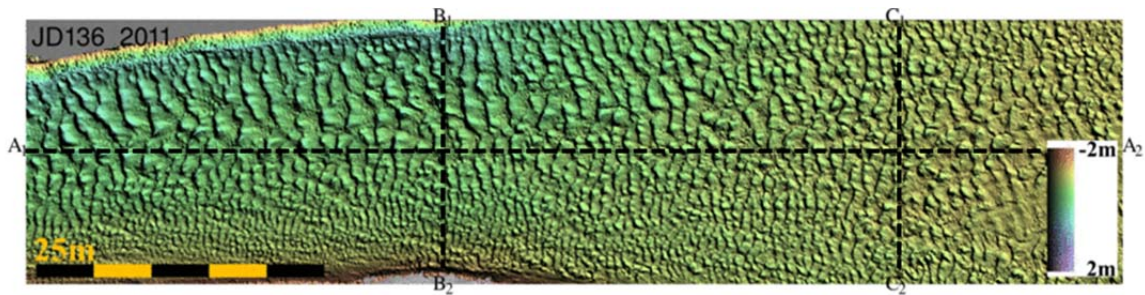
Figure 6.19: Segment A_1A_2, B_1B_2 and C_1C_2 for long wavelength analysis.

6.2.1. Depth analysis along the channel

The depth along the channel can be used as a means of visualizing inter-epoch erosion and deposition in this area. Figure 6.20 shows the variability of depth along the channel during the summer 2011. Generally, the depth along this channel did not change very much; the depth trend is similar within this period, which become more shallow from within the constriction zone toward the mouth bar (A_2).

The amount of depth variability, however, changes between these periods. The first period exhibits the smallest depth deviation. The greatest variability is in the second period, and variability decreases in the third period although it remains more pronounced than during the beginning of the year (Figure 6.20). The variability is reflected in the roughness amplitude histograms shown in Figure 6.2, 6.5 and 6.8.
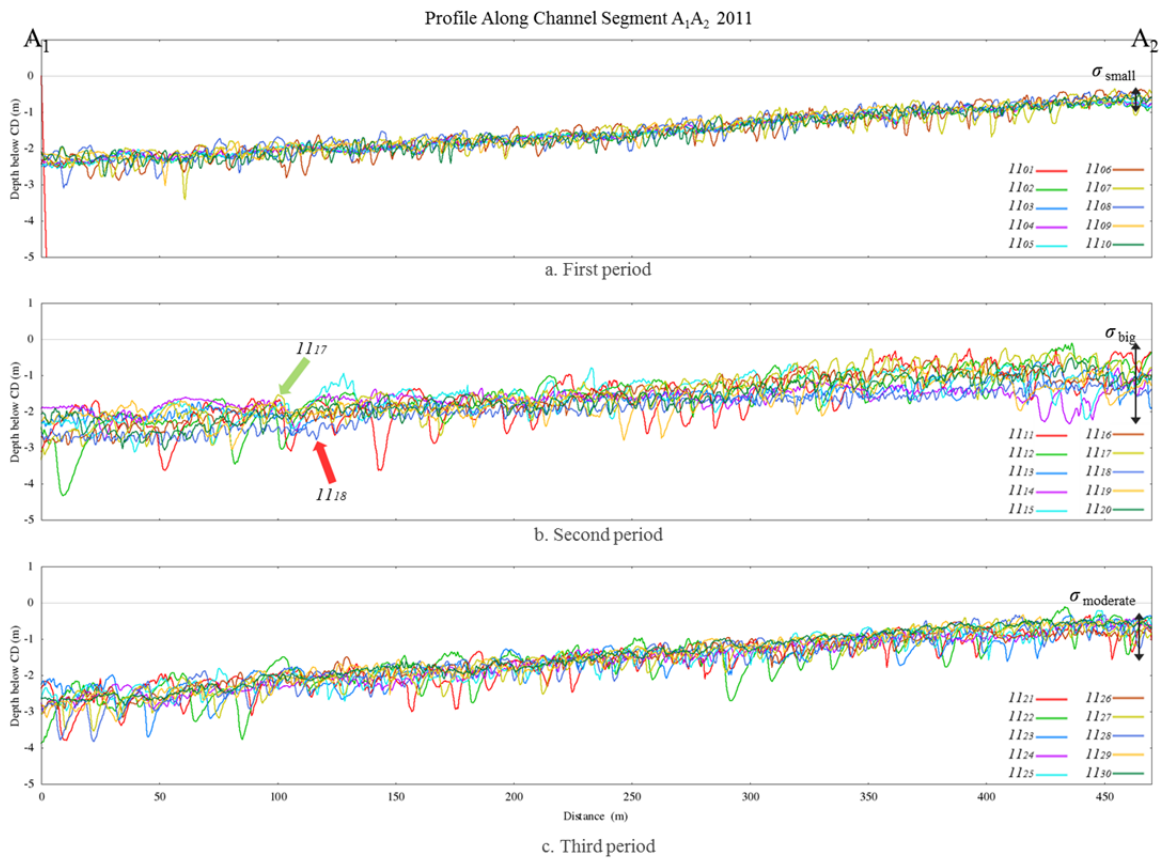
Figure 6.20: Depth profile along channel during summer 2011.

The single greatest epoch to epoch variability occurred in the second period when the depth along this channel systematically dropped 1.0 m deeper within less than 3 days (*1117* to *1118*). On the next epoch (*1119*), the inverse trend was seen whereby depth now decreased systematically because it filled up with sediments. This specific event will be discussed in section 6.5.

The depth variability during the summer 2012 period (Figure 6.21) was relatively high, comparable to the third period of 2011. The largest variability occurred between epoch *1203* and *1204*.
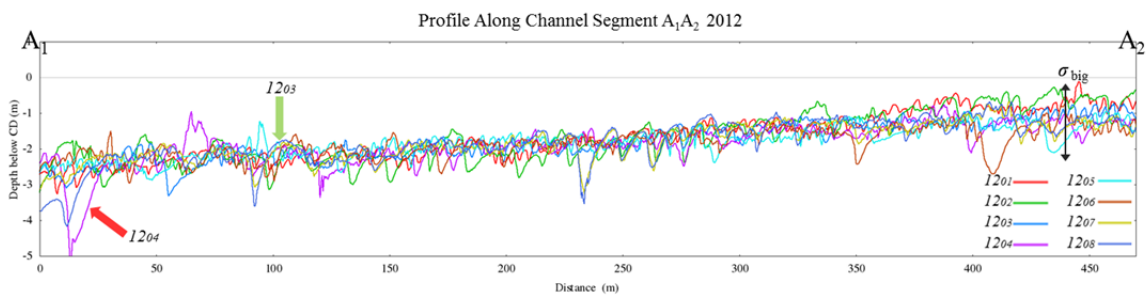
Figure 6.21: Depth profile along channel during summer 2012.

During the summer 2013 period, the depth variability along segment A_1A_2 was relatively small (Figure 6.22) similar to the first period in 2011. This is as expected, because during this time the river discharge was lower than 2012.
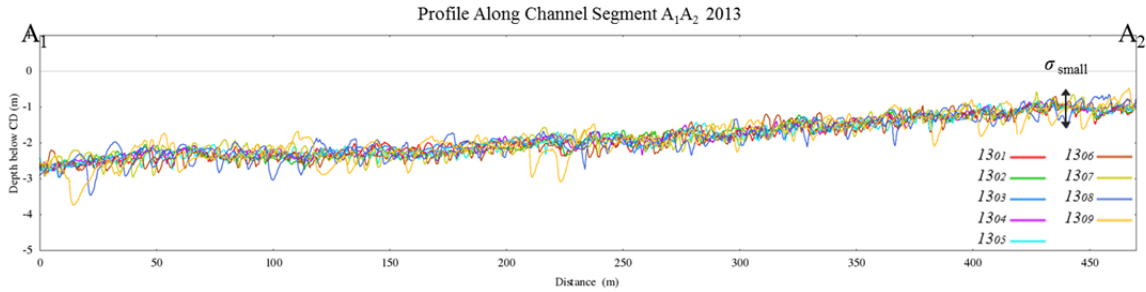
Figure 6.22: Depth profile along channel during summer 2013.

6.2.2. Depth analysis across channel

Figure 6.23 shows that the depth profiles across channel during the first period in summer 2011 do not have a significant variation in segments B_1B_2 and C_1C_2. The biggest depth variation during this period occurred between epochs *1106* and *1107*. Within the second period, depths have large deviation for both segments. The channel became significantly shallower from epoch *1112* to *1116*, on some parts the accretion was up to 1.0 m.

Again reflecting the largest epoch to epoch event, between epoch *1117* and *1118*, the average erosion was approximately 1.0 m and within a short time (between *1118* and *1119*) the riverbed accreted back to the previous level. This phenomenon will be discussed later in section 6.5.

A moderate depth variation across channel is displayed within the third period of summer 2011 (Figure 6.23c). Notice that in segment B_1B_2 and C_1C_2, the depth change rapidly from epoch *1121* to *1123*, although the wavelength and the roughness amplitude distributions are similar. This is because the segment was located at the edge of a big

159

bedform. This illustrates the potential for aliasing when using a single section to represent a surface.

Dashed lines in Figure 6.23 are the average depth during each period. The averaged depth of segment B_1B_2 changed significantly from one to the next period. The depth close to B_2 was curled up early in the year 2011; by the end of summer 2011 it was shallower toward the intertidal bar. This implies that the channel has spread out over the summer. For segment C_1C_2 the depth average in the third period is shallower than the first and the second period.
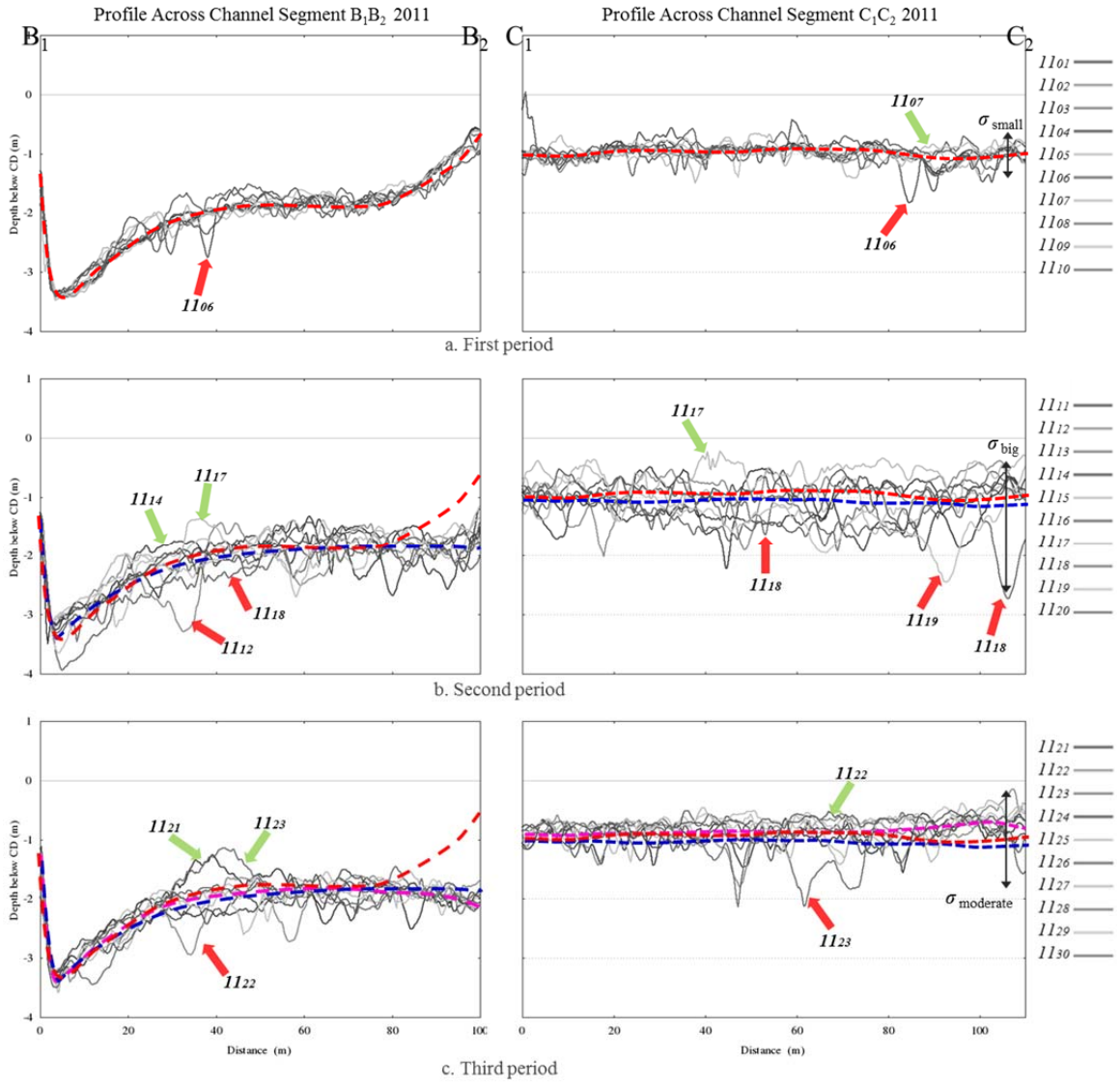
Figure 6.23: Depth profile across channel summer 2011. The dashed red lines, the dashed red lines, and dashed magenta lines represent the average depth across the channel of the first, the second, and the third period, respectively.

Similar morphology is seen in the 2012 time series. Figure 6.24 shows that a comparable event to epochs *1117* and *1118* was also happened between epochs *1203* to *1204*. Notice that the shape of the channel (dashed lines), both from segment B_1B_2 and C_1C_2, has evolved since the third period of summer 2011. The depth on segment B_1B_2 curled up again toward intertidal bar and the depth on segment C_1C_2 was not flat anymore. There is a deeper part close to C_2 on this segment implying that the channel migrated westward from 2011 to 2012.
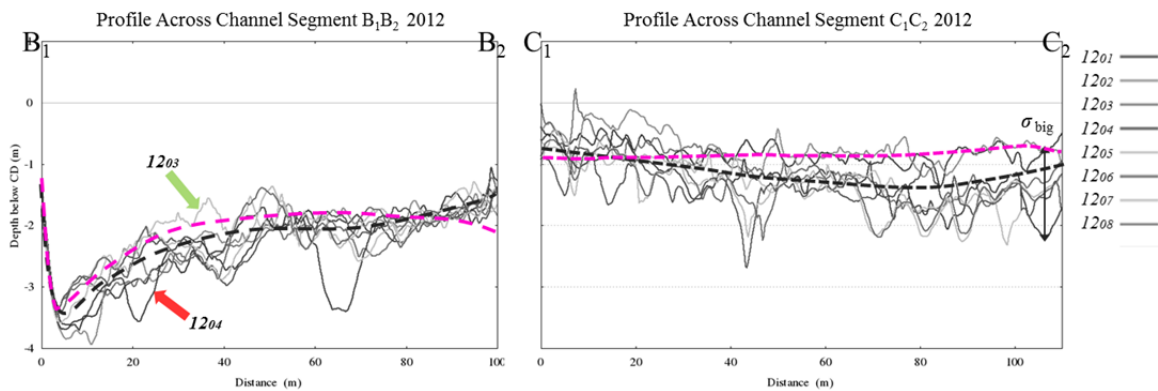
Figure 6.24: Depth profile across channel summer 2012. The dashed magenta lines represent the average depth across the channel of the third period of the summer 2011 and the dashed black lines represent the average depth across the channel of the summer 2012 period.

As can be seen in Figure 6.25, the depth variation across channel in the year 2013 is relatively small. However, the depth deviation across channel on segment C_1C_2 between epochs *1308* and *1309* was relatively high. The across shape of the channel has also evolved from the previous year. Notice that on the area close to B_2, the depth is shallower than 2012 and the depth close to C_2 is deeper than 2012 implying the channel's thalweg

162

narrowed in the constrained section but moved further toward west side in the unconstrained section. This is believed to be the reason for the low backscatter region seen in Figure 6.16. A better day to day image about the difference on the depth along channel and across channel can be seen in Appendix B.
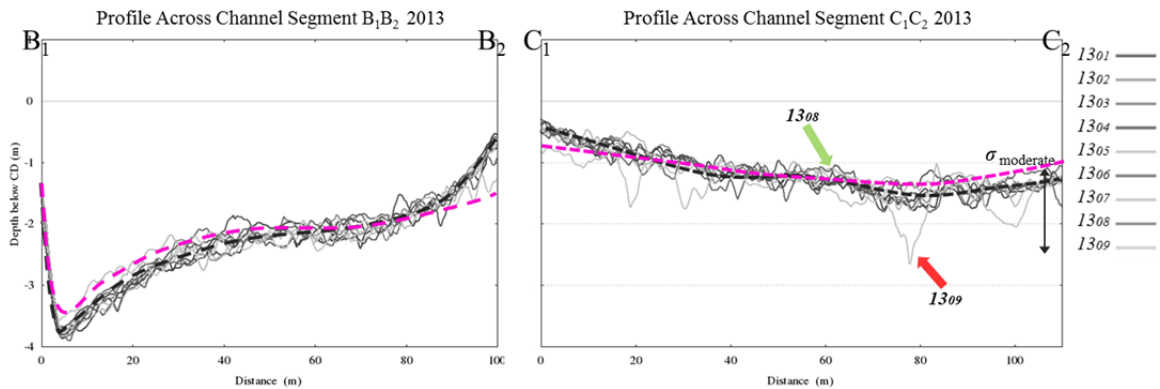
Figure 6.25: Depth profile across channel summer 2013. The dashed magenta lines represent the average depth across the channel of the summer 2012 period and the dashed black lines represent the average depth across the channel of the summer 2013 period.

6.3. Volumetric Analysis

The volumetric analysis on the delta top was represented using the mobility and change indexes (described in section 4.4). The mobility index (the range including both total sediment erosion and deposition) represents a measure of the translation of morphology. The change index (the net erosion and deposition) measures the contribution (positive or negative) of the channel floor to the off-delta transport.

163

It is important to recognize that the net change is a minimum estimate as there would be flux through the area (from upstream) that leaves without record. The translation is a qualitative measure of the through flux which is probably a higher contributor to the off-delta flux. Unfortunately, as the range of erosion and deposition depends on bedform height (and migration rate which cannot be quantified) that through flux cannot be precisely quantified, thus it is only a qualitative measurement.

For 2011, the range of erosion and deposition between each epoch grew from the spring to a peak in mid-summer and then died away (Figure 6.26). The red arrow in Figure 6.26a shows a net volume of more than 30000 m^3 sediments was removed from the delta top in the big event between epochs 11_{17} (JD178) and 11_{18} (JD181). As this research did not have daily record during this period, it cannot thus be determined whether the 30000 m^3 of sediment suddenly removed in a short time or gradually removed within three days.

Within just 3 days after epoch 11_{18}, this area was covered by more than 10000 m^3 of sediments (green arrow). This means during these epochs (11_{18} and 11_{19}) approximately 3000 m^3 of sediment per day was delivered to this area from upstream. The activity of sediment during these epochs (between epoch 11_{18} and 11_{19}) was very intense due to relatively high flow regime (more than 0.55 of Froude number) (Figure 6.26b).
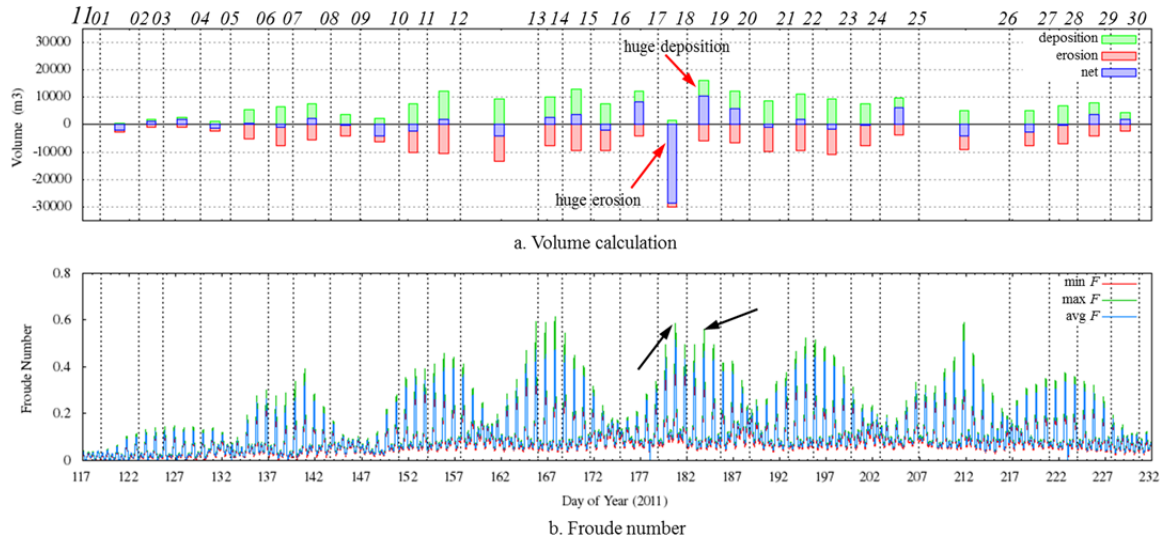
Figure 6.26: The volume calculation (a) and the Froude number (b) of the summer 2011 period. The black arrows represent the maximum Froude numbers during the period when the sediment activity was high (the red arrows).

Figure 6.27 shows that the typical erosion/deposition range during summer 2012 period is comparable to mid-summer 2011. The volume range is similar during this period, except between epochs 12_{07} and 12_{08} because they are not separated by a lower low water. Between epochs 12_{02} (earlier JD182) and 12_{03} (late JD183) there is a notably net negative volume. More than 15000 m^3 of sediment were removed between these epochs. An event similar to the event between epochs 11_{17}-11_{18} in 2011 was suspected as a trigger for this loss. This corresponds to the most active prodelta activity on JD182 in summer 2012 (Hughes Clarke et al., 2014, Fig 22.2)
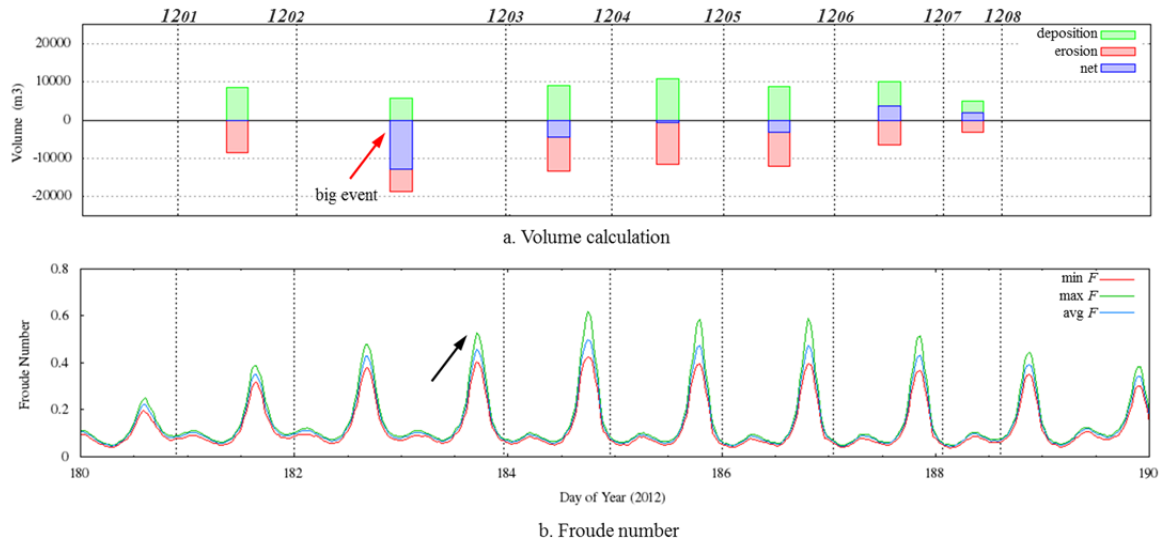
Figure 6.27: The volume calculation (a) and the Froude number (b) of the summer 2012 period. The black arrow represents the maximum Froude number between epochs *1202* and *1203* when the change index was high (the red arrow).

The range of erosion and deposition (mobility index) in summer 2013 (Figure 6.28) is graphically much lower than 2012 (Figure 6.27) and similar to spring 2011 (Figure 6.26). Generally, there was little observable change (the bedform was relatively inactive) between epochs *1301* and *1307*. However, approximately 10000 m^3 of sediment were removed from this area between epochs *1307*-*1308* and epochs *1308*-*1309* when the Froude number gradually increased.
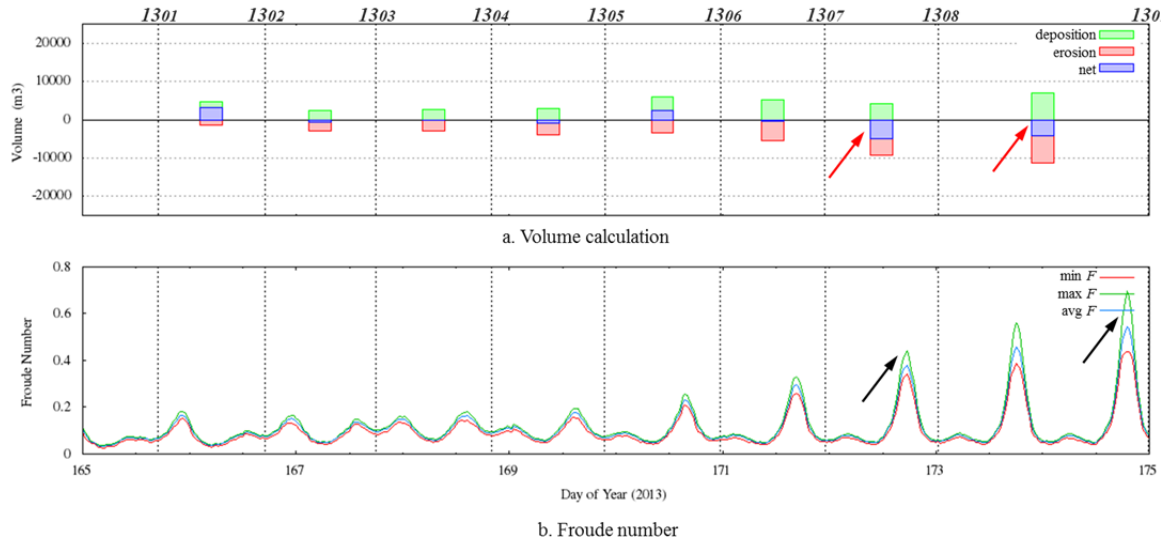
Figure 6.28: The volume calculation (a) and the Froude number (b) of the summer 2013 period. The black arrows represent the maximum Froude numbers when the change index started to increase (the red arrows).

The erosion and deposition range is a relative indicator of the bedload flux. When the range of erosion and deposition peaks the off-delta transport should be highest. The correlation between that flux and the associated delta lip evolution will be discussed in next section.

6.4. The Evolution of the Delta Lip

As discussed in section 4.5, the outline of the delta lip and its volumetric growth are used as a means of monitoring the progressive evolution of the delta lip morphology. The delta lip is presented at the time when the delta top was surveyed; it was surveyed only every 3

to 4 days during the summer 2011 period. As a result the daily rate of volumetric change has to be assumed as constant from day to day.

6.4.1. The evolution of the delta lip in summer 2011

The progressive change of horizontal displacements of the delta lip during summer 2011 is shown in Figure 6.29. During the first period, the delta lip was relatively stable at the outermost extent. The delta was prograding approximately 5 m on western parts of the delta lip over this period (green arrows in Figure 6.29a). Between epochs *1101* and *1105* (14 day duration), the delta lip gained an average of 1111 m^3 of sediment per day (Table 6.1). Between epochs *1105* and *1106*, the SFI increased to 2564 m^3 per day. There was one major collapse with more than 10700 m^3 of the sediment removed from the delta lip per day between epochs *1106* and *1107*. After this collapse the delta lip was relatively stable from epoch *1107* to epoch *1110* with an average flux of 1293 m^3 per day.
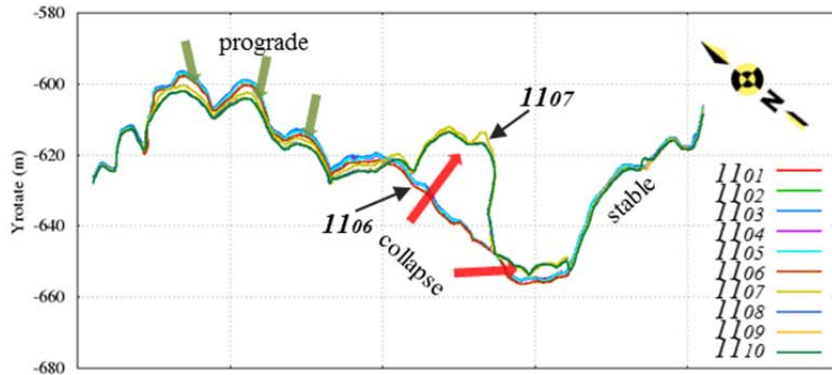
a. Evolution of the delta lip in the first period of summer 2011.
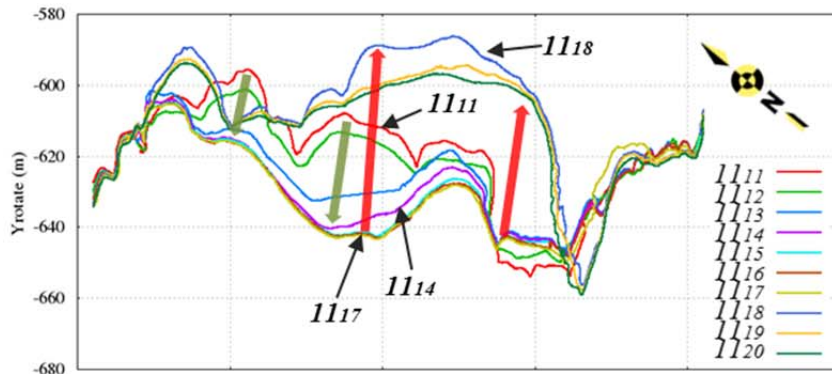
b. Evolution of the delta lip in the second period of summer 2011.
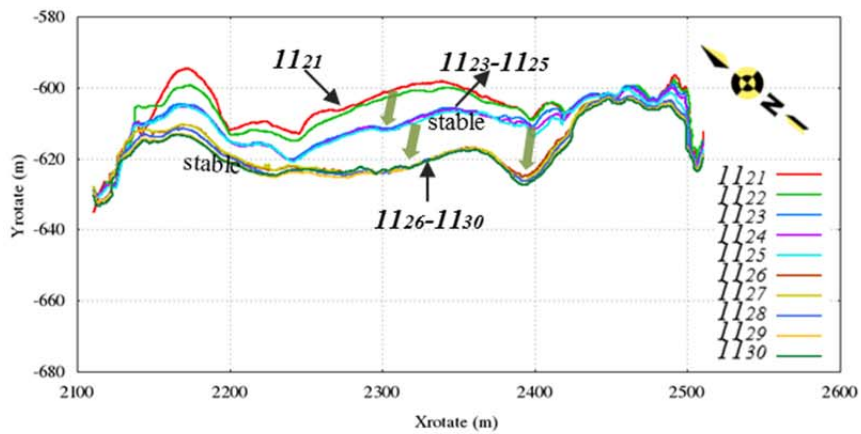
c. Evolution of the delta lip in the third period of summer 2011.

Figure 6.29: The delta lip shape evolution of the summer 2011 period. The red arrows represent the retrogradation of the delta lip and the green arrows represent the progradation of the delta lip.

169

Table 6.1: Volumetric analysis of the delta lip area in summer 2011.

Epoch		Julian Date (decimal day)		Duration (decimal day)	Volume (m³)		Daily Volume (m³/day)	
from	to	from	to	(days)	gain	loss	SFI	MWI
1101	*1102*	118.938	123.063	4.125	4734	-3445	1148	-835
1102	*1103*	123.063	125.667	2.604	3425	-4727	1315	-1815
1103	*1104*	125.667	129.660	3.993	4461	-2817	1117	-705
1104	*1105*	129.660	132.875	3.215	2782	-2726	865	-848
1105	*1106*	132.875	137.000	4.125	10578	-2084	2564	-505
1106	*1107*	137.000	139.625	2.625	10487	-28140	3995	-10720
1107	*1108*	139.625	143.667	4.042	9113	-4135	2255	-1023
1108	*1109*	143.667	146.875	3.208	2402	-5382	749	-1678
1109	*1110*	146.875	151.000	4.125	3614	-4323	876	-1048
1110	*1111*	151.000	154.104	3.104	16348	-24703	5266	-7958
1111	*1112*	154.104	157.667	3.562	26480	-12814	7433	-3597
1112	*1113*	157.667	166.000	8.333	32694	-18103	3923	-2172
1113	*1114*	166.000	168.583	2.583	24807	-5930	9603	-2295
1114	*1115*	168.583	171.625	3.042	14064	-4942	4624	-1625
1115	*1116*	171.625	174.833	3.208	6844	-5001	2133	-1559
1116	*1117*	174.833	178.875	4.042	12635	-6402	3126	-1584
1117	*1118*	178.875	182.000	3.125	12095	-180326	3870	-57704
1118	*1119*	182.000	185.667	3.667	33996	-33793	9272	-9216
1119	*1120*	185.667	188.708	3.042	39490	-2880	12983	-947
1120	*1121*	188.708	192.896	4.188	13959	-71562	3333	-17089
1121	*1122*	192.896	195.604	2.708	19877	-8477	7339	-3130
1122	*1123*	195.604	199.625	4.021	32893	-6061	8181	-1507
1123	*1124*	199.625	202.750	3.125	8530	-6438	2730	-2060
1124	*1125*	202.750	206.938	4.188	14376	-19910	3433	-4755
1125	*1126*	206.938	216.708	9.771	47976	-11819	4910	-1210
1126	*1127*	216.708	220.958	4.250	7698	-12456	1811	-2931
1127	*1128*	220.958	224.000	3.042	10178	-11560	3346	-3801
1128	*1129*	224.000	227.646	3.646	10935	-5879	2999	-1613
1129	*1130*	227.646	230.667	3.021	7833	-4031	2593	-1334

The delta lip was much more active within the second period of summer 2011 (Figure 6.29). The centre part of the delta lip prograded approximately 5 m between epochs 11_{11} (JD153) and 11_{12} (JD157). The SFI between these epochs was more than 7400 m^3 per day. Between epochs 11_{12} (JD157) and 11_{13} (JD165), the centre part of the delta lip grew gradually about 2 m per day with an average flux of more than 3900 m^3 per day. Between epochs 11_{13} (JD165) and 11_{14} (JD168), the delta lip prograded by more than 5 m; the SFI was approximately 9600 m^3 per day. Overall, more than 30 m of the centre part of the delta lip advanced within just 15 days (epoch 11_{11} to epoch 11_{14}). Note that epochs 11_{13} and 11_{14} are the first epochs with major long wavelength patchiness on their backscatter image (recall Figure 6.5b).

An enormous collapse event occurred between epochs 11_{17} and 11_{18}, which was the largest observed collapse of the year. More than 150000 m^3 of sediment were removed from the delta front and the lip retreated by more than 50 m between these epochs (Hughes Clarke et al., 2012). The rate sediment loss between these epochs was 57704 m^3 per day. The peak Froude number before epoch 11_{18} was more than 0.55. During this period, the bedform morphology also evolved significantly (section 6.1). This event can be associated with increased long wavelength backscatter patchiness as shown in Figure 6.5b. It is this period in which the major net delta channel floor erosion occurs (to be discussed in section 6.5).

Between epochs 1118 and 1119, the delta lip prograded approximately 5 m within just 4 days. This very active progradation was accompanied with a relatively high Froude number (more than 0.55) between these epochs. During the same period, the delta top rapidly accreted again, regaining 30% of the lost volume (section 6.3) and the rate of the volume gains on the delta lip was approximately 9300 m^3 per day. A significant SFI occurred between epochs 1119 and 1120 with the average flux being approximately 13000 m^3 per day. This is the highest rate of volume gain in the summer 2011.

Relatively intense activity of the delta lip occurred during the third period of summer 2011. There was a significant delta lip failure between epochs 1120 and 1121. The MWI between these epochs was 17089 m^3 per day. This is interesting, because between these epochs, there was neither a surge in the river discharge nor a low spring tide condition. This collapse appears to be the result of a geometrically protruding part of the lip that was unsupported and left behind from the previous collapse.

From 1121 (JD192) to epoch 1125 (JD206), the delta lip advanced more than 10 m with an average daily volume gain of more than 5400 m^3 per day. Between a period of 10 days (the period between epochs 1125 (JD206) and 1126 (JD216)), the delta lip prograded by more than 12 m, with an average daily sediment volume gain of more than 4900 m^3. Overall, during the 38 days between epochs 1121 (JD192) and 1130 (JD230)), the delta lip grew by more than 20 m with the SFI being more than 4100 m^3 per day.

6.4.2. The evolution of the delta lip in summer 2012

Looking at the whole summer 2011, based on the horizontal displacement, the shape of the delta lip dynamically grew and retreated. The off-delta fluxes also clearly fluctuated from 1100 m^3 per day at the beginning of the observation time to a peak of approximately 13000 m^3 per day in the mid-summer. The sediment moved on the adjacent slope also varied with the range from 2840 m^3 per day to 12575 m^3 per day.

There was a significant difference between the delta lip shapes in 2012 and the delta lip shapes in the previous year (Figure 6.30). The eastern part that existed in 2011 (dashed line) completely disappeared in 2012. Within just one week of observation, the centre part of the delta lip prograded by more than 20 m (green arrow) and the delta lip gained sediment at the rate of approximately 11550 m^3 per day. The maximum daily flux occurred between epochs *1203* and *1205* with the average being 15734 m^3 per day.

The western and centre parts of the delta lip retreated by more than 10 m between epochs *1201* and *1202* (blue arrows in Figure 6.30) with approximately 9400 m^3 of sediment was removed from the delta lip area per day. The western part of the delta lip retrograded by more than 15 m (red arrow) during the period from epochs *1202* to *1203*. The daily rate of volume loss between these epochs was 12575 m^3 per day (Table 6.2). The location of retrogradation (area A in Figure 6.30) was the origin of activity turbidity currents as identified by Hughes Clarke et al. (2014).
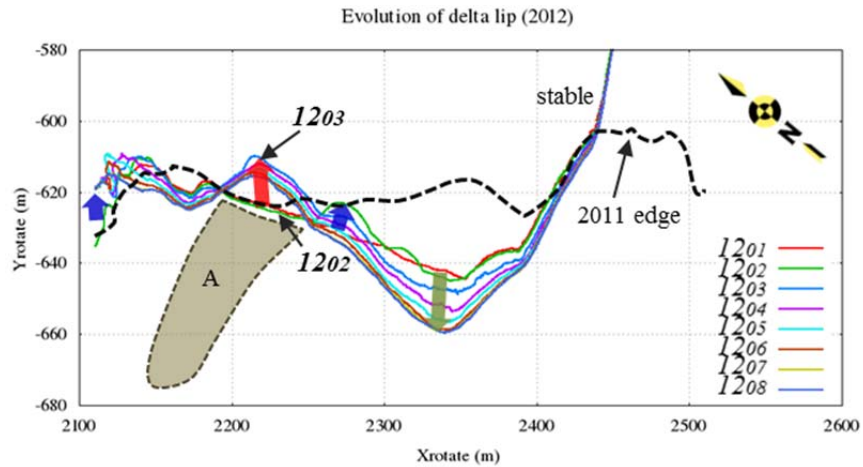
Figure 6.30: The delta lip shape evolution of the summer 2012 period. The blue arrows represent a relatively small retrogradation, the red arrow represents the retrogradation when big event occurred, and green arrow represents the progradation. The area A is the location turbidity currents as identified by Hughes Clarke, et al. (2014).

Table 6.2: Volumetric analysis of the delta lip area in summer 2012.

Epoch		Julian Date (decimal day)		Duration (decimal day)	Volume (m³)		Daily Volume (m³/day)	
from	to	from	to	(days)	gain	loss	SFI	MWI
1201	*1202*	180.896	182.000	1.104	13858	-10371	12551	-9393
1202	*1203*	182.000	183.958	1.958	16500	-24627	8426	-12575
1203	*1204*	183.958	184.958	1.000	15925	-12907	15925	-12907
1204	*1205*	184.958	186.000	1.042	16190	-5603	15542	-5379
1205	*1206*	186.000	187.042	1.042	11081	-5142	10638	-4936
1206	*1207*	187.042	188.063	1.021	10857	-2899	10635	-2840
1207	*1208*	188.063	188.604	0.542	3874	-2883	7152	-5322

6.4.3. The evolution of the delta lip in summer 2013

The evolution of the delta lip horizontal displacement in summer 2013 was slower than in summer 2012. The slower evolution (Figure 6.31) reflects the lower discharge and low erosion/deposition rates. During this period the delta lip shape did not change very much. No solitary collapses were seen during this period. However, compared with 2012, the centre and eastern part of the delta lip grew by more than 40 m (green arrow) and the western part of the delta lip retreated by more than 20 m (red arrows).
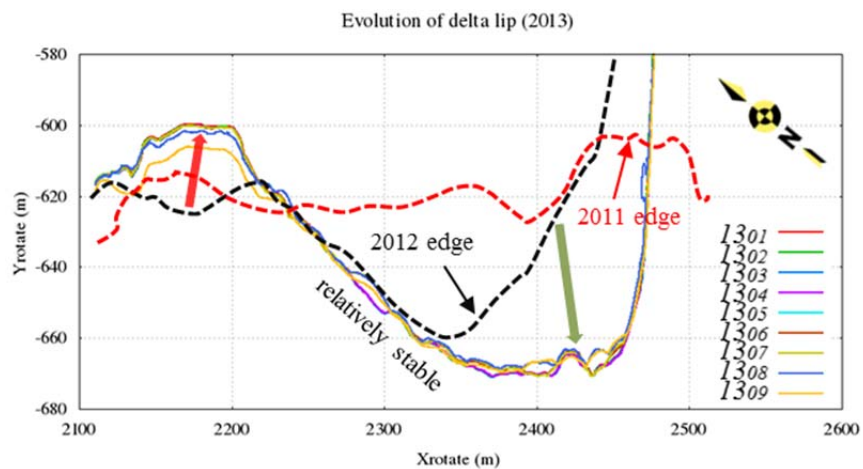
Figure 6.31: The delta lip shape evolution of the summer 2013 period. The dashed red line and dashed black line represent the shape of the delta lip at the end of the summer 2011 and summer 2012 observations, respectively.

The average rate of sediment volume gain of the off-delta lip during the summer 2013 period was approximately 3800 m^3 per day. The SFI was relatively stable, with average being approximately 2550 m^3 per day, from epoch *1301* to epoch *1307*. The maximum rate of SFI during this period occurred between epochs *1308* and *1309*, with average flux of 9316 m^3 per day (Table 6.3). The MWI gradually increased from *1301* to epoch *1307* with the average being approximately 2300 m^3 per day. The highest rate of sediment moves downslope occurred between epoch *1307* and *1308* (6981 m^3 per day).

Table 6.3: Volume calculation of the delta lip in summer 2013.

Epoch		Julian Date (decimal day)		Duration (decimal day)	Volume (m^3)		Daily Volume (m^3/day)	
from	to	from	to	(days)	gain	loss	SFI	MWI
1301	*1302*	165.708	166.708	1.000	2695	-1349	2695	-1349
1302	*1303*	166.708	167.750	1.042	2452	-2002	2354	-1922
1303	*1304*	167.750	168.833	1.083	2107	-2715	1945	-2506
1304	*1305*	168.833	169.896	1.063	4073	-3622	3833	-3409
1305	*1306*	169.896	170.979	1.083	2271	-948	2096	-875
1306	*1307*	170.979	171.958	0.979	2366	-828	2416	-846
1307	*1308*	171.958	173.021	1.063	6392	-7417	6016	-6981
1308	*1309*	173.021	174.990	1.969	18340	-8395	9316	-4264

6.5. Discussion

6.5.1. Relationship between bedform characteristics and flow regime

The prediction of equilibrium hydraulic conditions in sand-bed channels requires knowledge of flow resistance and bed material transport [Bennett, 1997]. Bedforms are a key component of flow resistance in rivers, which can be partitioned between sediment size and form resistance. In sand-bedded rivers, form resistance is primarily generated by bedforms [Venditti, 2013].

The Squamish River is composed of mixed-size gravel and coarse sand on the river channel while on the edge of the delta is dominated by finer sand. To relate the flow regime to the bedforms is a very complicated problem because the bedforms respond at different rates, depending both on the rate of sediment transport and on the amount of sediment contained in a bedform.

In flows where the sediment transport rate is large and bedforms are small, bedforms respond so rapidly that they reflect the current flow conditions within as little as a few minutes. Where the volume of sediment contained in a bedform is larger, or where the sediment transport rate is lower, bedforms respond more slowly and may only reflect the flow conditions of an entire tide cycle (Rubin & McCulloch, 1980).

This research used the peak Froude number derived from hydrodynamic model at the lower low water immediately preceding the survey as a representative of the flow condition and attempted to relate this with the bedform morphological characteristics. The relationships between short wavelength bedform characteristics (wavelength,

amplitude, and skewness) and the maximum Froude number immediately prior to each

epoch, are presented in Figure 6.32, 6.33 and 6.34.

In the relationship between peak Froude numbers and wavelengths, epochs *1113, 1114,*

and *1118* are outliers (Figure 6.32). These epochs also become outliers in the relationship

between peak Froude numbers and roughness amplitudes (Figure 6.33). If those samples

are excluded, the correlation is much stronger. However, the skewness has a strong and

positive correlation with the peak Froude numbers even with inserting epochs *1113, 1114,*

and *1118* data (Figure 6.34).
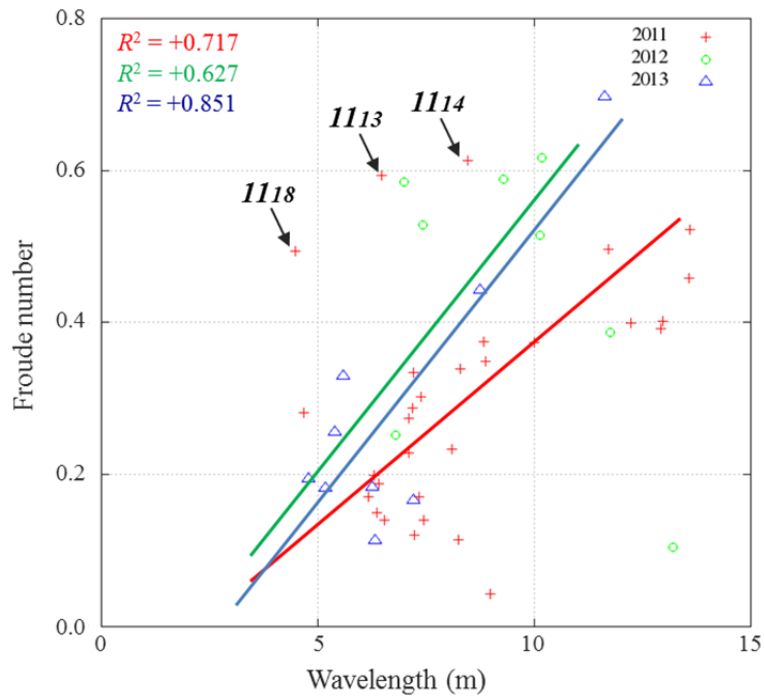
Figure 6.32: The relationship between the Froude number and the wavelength of the bedform. The red, green and blue represent the trends of the relationship of the summer 2011, 2012, and 2013 periods, respectively.

178
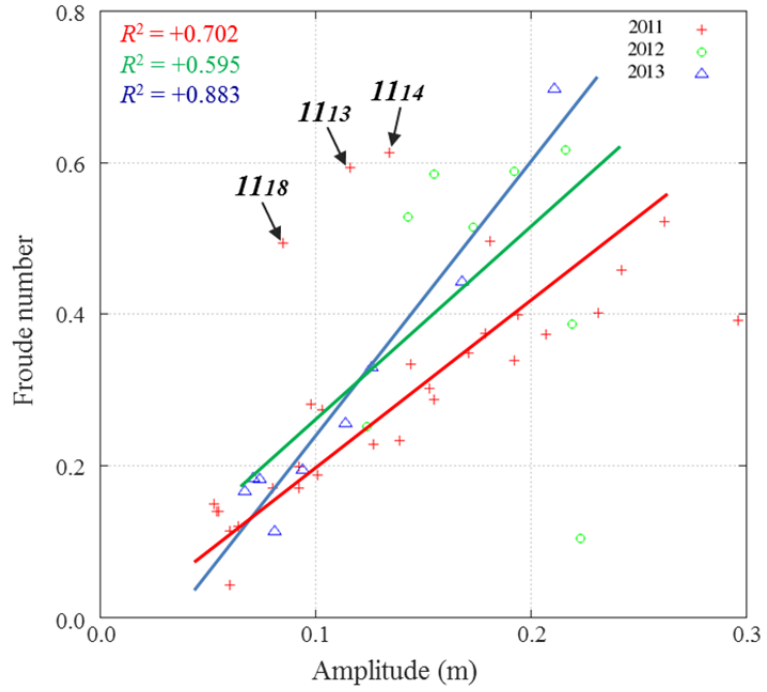
Figure 6.33: The relationship between the Froude number and roughness amplitude.
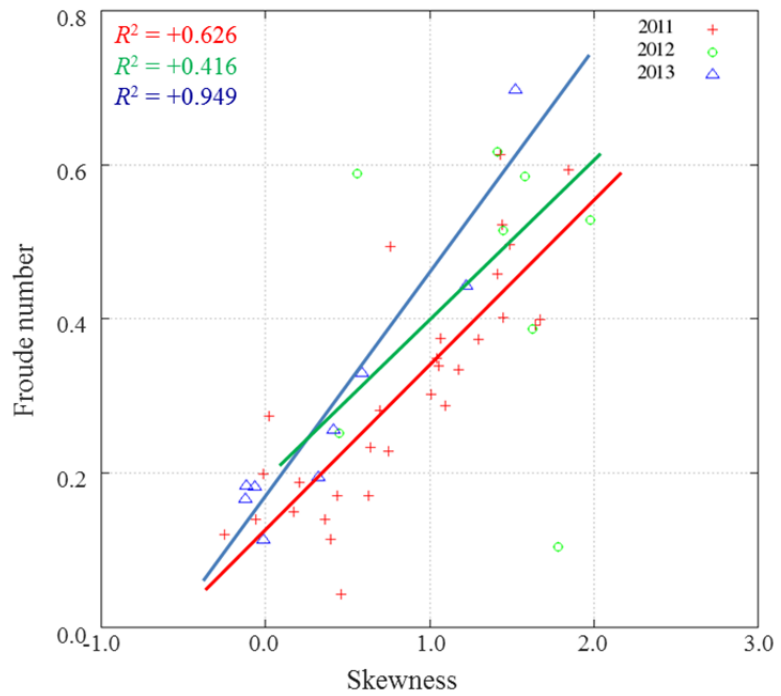
Figure 6.34: The relationship between the Froude number and skewness.

179

Other than epochs *1113*, *1114*, and *1118*, Froude numbers range from 0.2 to 0.5, and as

expected from Simons & Richardson (1966), bedform wavelength and amplitude increase

as the Froude number increases. When the Froude number is more than 0.5, the

wavelength and the amplitude decrease. According to Cheel (2005), this can be

categorized as a washout bedform which starts at about Froude number 0.54. In this case,

the long wavelength backscatter patchiness appears at the same time when the

wavelength and amplitude drop.

More qualitatively, visual patchiness of epochs *1113*, *1114*, and *1118* (Figure 6.5) shows

that only the centre of the channel floor has been washed out but the dunes are still well

developed on the sides. Those locations are actually distinct with lower Froude number

(0.2 - 0.3) population.

There are a variety of bedforms that develop under certain hydraulic condition in the

Squamish River within the observation time. In order to characterize the type of the

bedforms, this research uses the 1D power spectra trend. Based on the spectra trend,

bedforms in the delta top can be categorized into 5 types: type 0, A, B, C, and D. The

nomenclature of this categorization follows the nomenclature used by Cheel (2005)

which he based on Simons & Richardson's research (1966) (Figure 4.2).

Figure 6.35 illustrates that bedform type 0 occurs when the power spectrum has a characteristic low spectral slope (about -1.500 dBm) up to 15.0 m wavelength, then is relatively flat up to 100 m. Type A has a significantly higher spectral slope (-2.230 dBm) from wavelengths 0.5 to 3.0 m, then its spectral power gradually increases to longer wavelengths. Type B has the same steep slope from 0.5 to approximately 7.5 m, and then the slope is relatively flat to longer wavelengths. Type C has power spectra trend with characteristic steep slope up to 10.0 m and relatively flat on the wavelengths of more than 10.0 m. The power spectra trend of bedfrom type D is similar to those of type A or B (solid red lines in Figure 6.35).
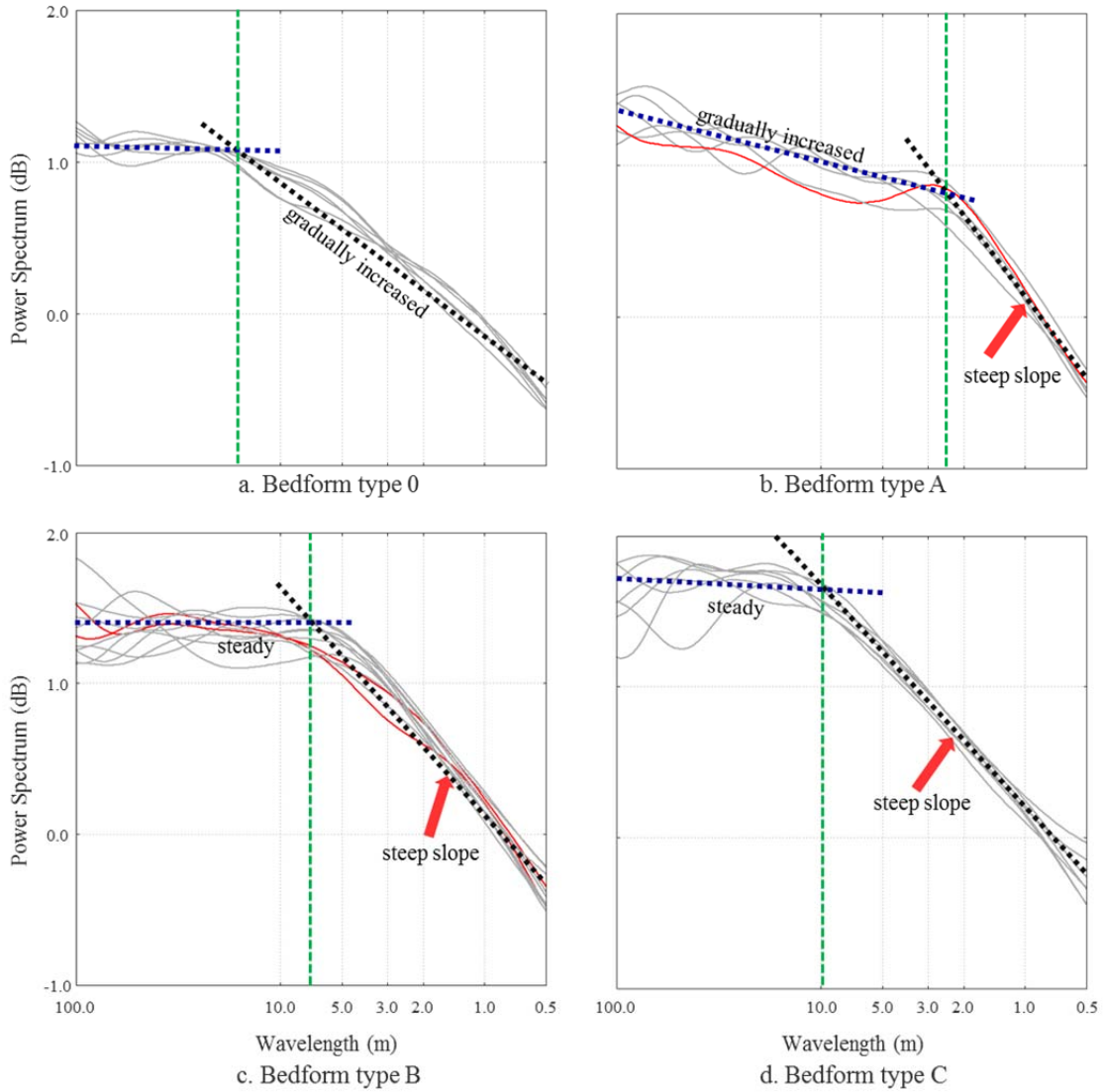
Figure 6.35: Bedform classification based on its power spectrum. Bedform type D is represented by solid red lines. The green dashed lines show the wavelength at the intersection between the steep slope and the flat slope of the power spectra trend.

As the power spectra of bed type D is almost identical to those of type A or B, there should be a method to discriminate this bedform from type A or B. The bedform Type D only occurs when the Froude number is more than 0.5 and fortunately, a distinct long wavelength signature (patchiness) appears on backscatter maps. This signature can be used as additional information to discriminate bedforms at this stage from bedforms with lower Froude number (bedform type A or B).

For each of the epochs, the 1D spectra was examined and assigned to one of the 5 classes. The relation between the types of the bedforms and the peak Froude numbers shown in Figure 6.36 is very strong. As it was explained before, epochs *1113*, *1114*, and *1118* are the anomaly. The 1D power spectra of these bedforms are similar to that of bedform type A or type B, but their peak Froude numbers are relatively high. The long wavelengths of these bedforms are removed and the amplitudes are reduced within this relatively high flow regime. This results in the simple relationship breaks down above Froude number 0.55 (epochs *1113* and *1114* inside shadowed area in Figure 6.36).

The major event between epochs *1117* and *1118* also departs from the relationship at lower Froude number (approximately 0.5). Thus it would appear that based on simple morphological character alone, flow regime above 0.55 cannot be detected. Therefore the backscatter patchiness can be used as additional information to distinguish bedforms on epochs *1113*, *1114*, and *1118* from that on the lower Froude number.
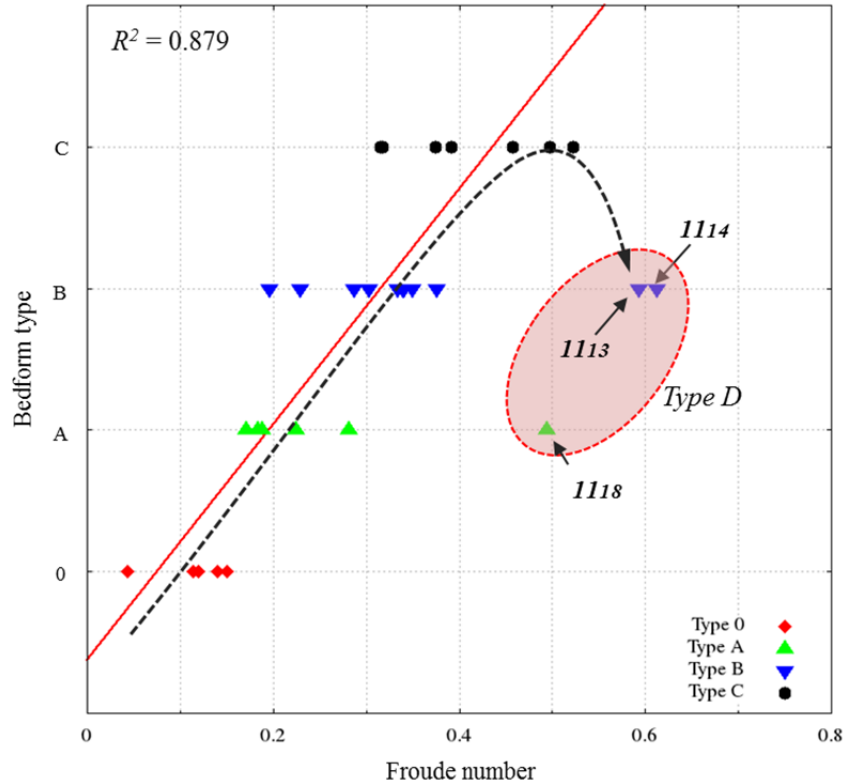
Figure 6.36: The relationship between type of power spectrum and Froude number. The red line represents the linear trend of the relationship. The black line illustrates the relation breaks down to the type D (inside the shaded area) because of the high Froude number (above 0.55) or the major event on the delta lip (between epochs 1117 and 1118).

To illustrate this proposed classification, terrain models and backscatter mosaics are presented as representatives of each type of bedform in the Squamish River (Figure 6.37). The short wavelength patchiness (less than 20 m) seen in type 0 and type A (Figure 6.37b) is a relict remnant of bedforms developed under type B or type C during previous higher flow events. These bedforms are degraded and thus do not have high relief (less than 20.0 m wavelength) but they are not completely smoothed out.

184

a. Bathymetric terrain models   b. Backscatter maps
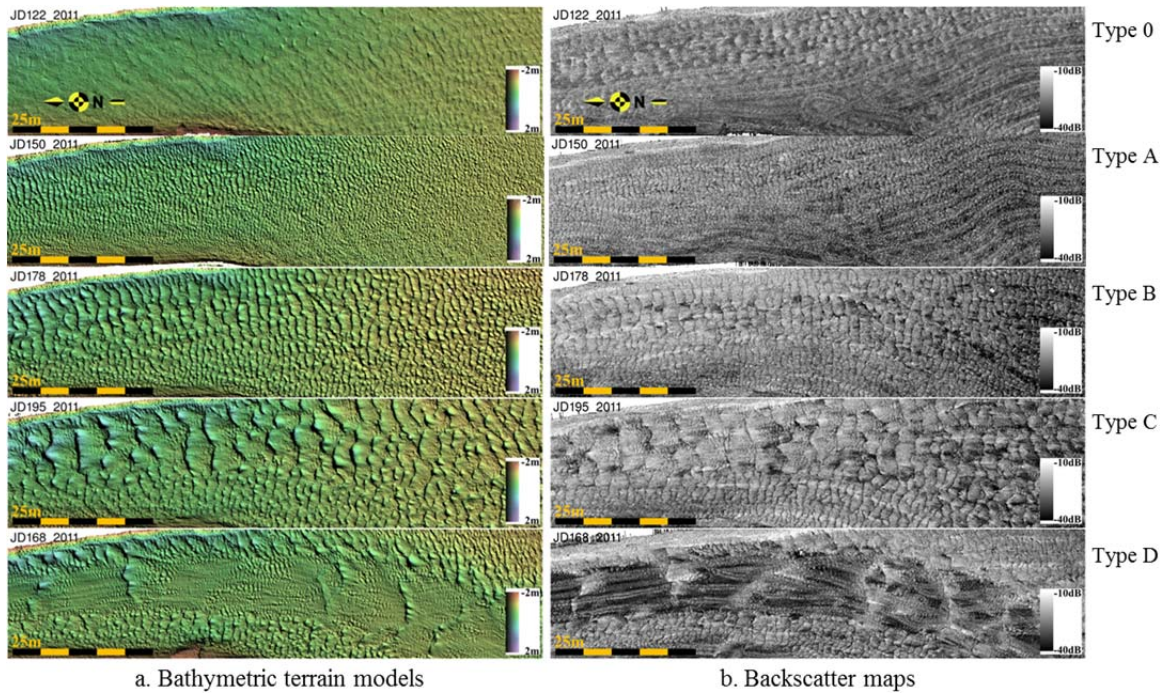
Figure 6.37: Representatives of bedforms classification.

6.5.2. Relationship between the dynamic of the delta lip and the flow regime

The preceding section has emphasized the effect of the flow regime on the bedform driven by bedload transport on the delta top. This section examines the relation between the flow conditions (represented by a Froude number) and the dynamics of the delta lip over time. The dynamics of the delta lip are represented by using the difference of 3.0 m contour positions from one epoch to the next epoch as well as the daily rate of volume gains and losses on the delta lip.

6.5.2.1. <u>Summer 2011 period</u>

In the summer 2011 period, there were three significant delta lip failures. The first event occurred between epochs 1106 and 1107, the second was between 1117 and 1118, and the third was between 1120 and 1121 (red arrows in Figure 6.38a). The delta lip retrograded more than 30 m and when each of these events occurred, between 28000 m^3 to 180000 m^3 of sediment was removed from the delta lip (shadowed area in Table 6.1).

The first event occurred between epochs 1106 and 1107, when more than 30 m of the centre part of the delta lip collapsed (Figure 6.39). This event happened at the lowest low spring tide and the river discharge was approximately 200 m^{3}s^{-1}. The last peak Froude number during this period was less than 0.4. Table 6.1 shows that the rate of the delta lip volume loss was more than 10700 m^3 per day.
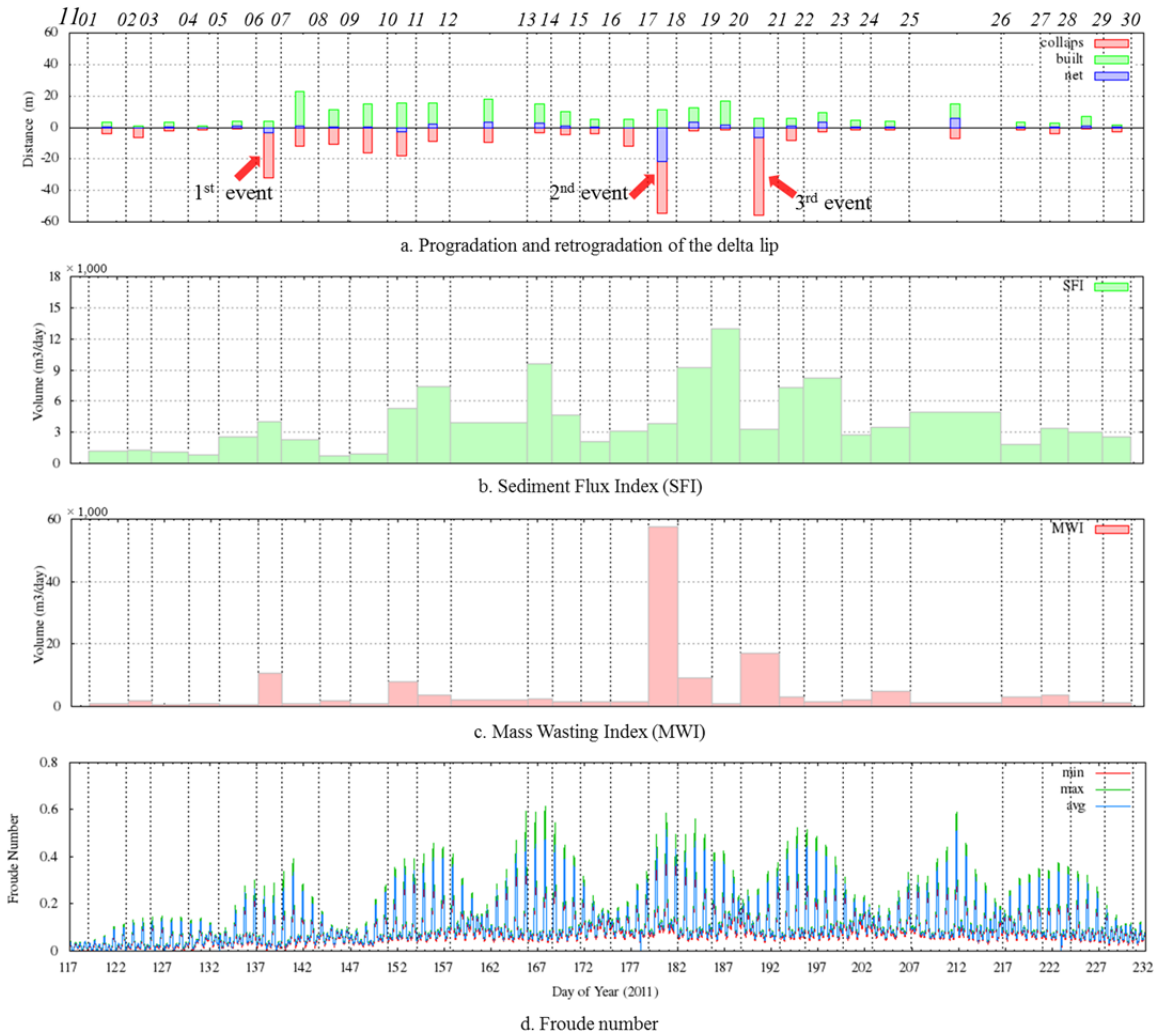
Figure 6.38: The progradation and retrogradation of the delta lip (a), the Sediment Flux Index (b), the Mass Wasting Index (c), and related Froude number (d) in summer 2011. The red arrows are pointing at the major events in the summer period of 2011.

187

a. Delta lip terrain model on epoch 1106 b. Delta lip terrain model on epoch 1107
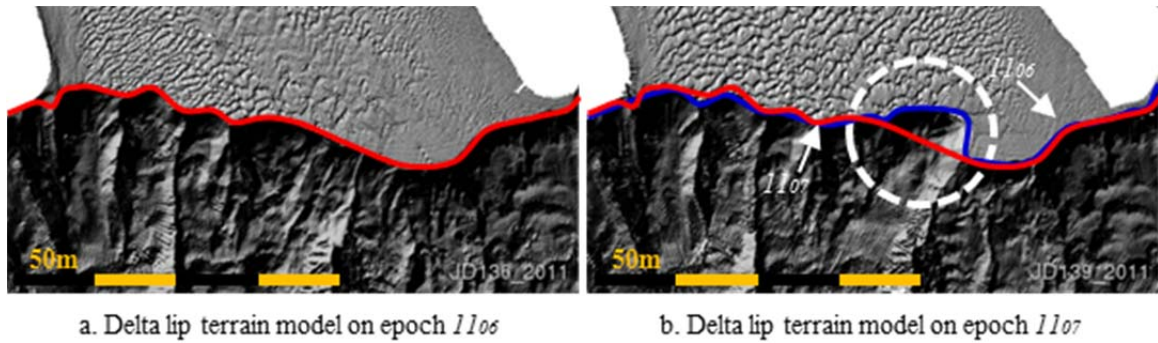
Figure 6.39: Terrain models of the delta lips before (a) and after (b) the first major delta lip failure in 2011. The red line and the blue line represent the shape of the delta lip on epoch 1106 and 1107, respectively. More than 30 m of the centre part of the delta lip collapse between these epochs (inside dashed white line).

More than 28100 m^3 of sediment was removed from the delta lip because of this event. However, some parts of the delta lip grew and between these epochs the SFI rate was approximately 4000 m^3 per day. This relatively high sediment flux off the delta lip arrived as a response to an increase of the flow regime between these epochs.

The range of erosion and deposition on the delta top was more than 10000 m^3 while the net volume was less than 500 m^3 (Figure 6.26). Relatively moderate sediment mobility happened during this time; however, the channel was neither deepened nor shallowed because of this event. The depth profiles along segment A_1A_2 on epoch 1107 (Figure 6.40) show that the sediment activity during this period was predominantly a result of migration by filling troughs (green area) and eroding crests (red area) from the previous bedform.
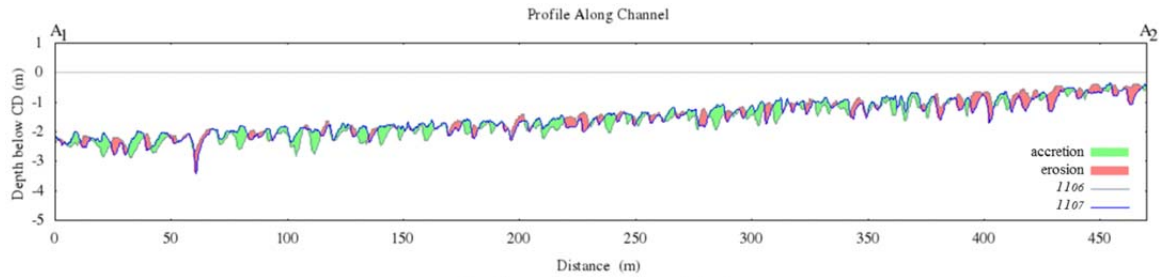
188

a. Depth profile on segment A_1A_2
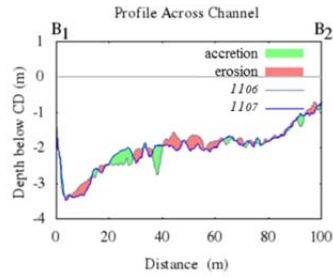
b. Depth profile on segment B_1B_2
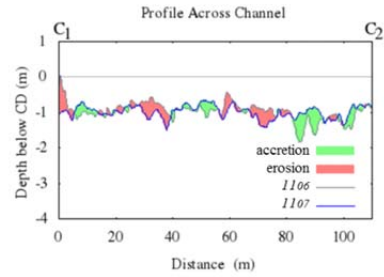
c. Depth profile on segment C_1C_2

Figure 6.40: Depth profile along (a) and across (b, c) the channel between epochs *1106* and *1107*.

The second big collapse in 2011 occurred between epochs *1117* and *1118*. During this period, the river discharge was at the highest (approximately 800 m^3s^{-1}) and the tide approached springs. Figure 6.41 shows that more than 50 m of the delta lip retrograded between these epochs. Almost all parts of the delta lip collapsed (more than 10000 m^2), only a small part in the eastern side stayed (Figure 6.41).

a. Delta lip terrain model on epoch 11_{17} b. Delta lip terrain model on epoch 11_{18}
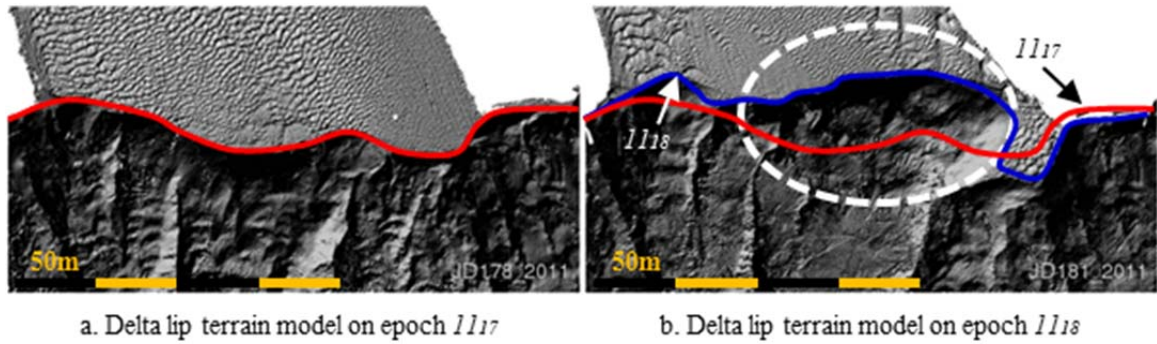
Figure 6.41:Terrain models of the delta lips before (a) and after (b) the second major delta lip failure in 2011. The red line and the blue line represent the shape of the delta lip on epoch 11_{17} and 11_{18}, respectively. More than 30 m of the centre part of the delta lip collapse between these epochs (inside dashed white line).

The second major event also resulted in more than 180000 m^3 of sediment being removed from the delta lip. The MWI between these epochs was the highest in the summer 2011 period with an average of 57704 m^3 per day. The average sediment flux was more than 3800 m^3 per day. This demonstrates that, despite the loss, some sediment was deposited during this time. Figure 6.39 shows that the eastern part of the delta lip grew between these epochs.

The peak Froude number between epochs 11_{17} and 11_{18} was relatively high, at more than 0.5. The volume range on the delta top shows that enormous sediment activity occurred between these epochs. The net volume displayed in Figure 6.26 also shows that a significant amount of sediment was removed from the channel. The depth profiles both along and across the channel (Figure 6.42) display the significant effect of a high flow

190

regime combined with the delta lip failure on the long wavelength channel shape of the delta top.

Figure 6.42 indicates that the depths along and across the channel on epoch *1117* were eroded by the flow (red area) and approximately 1.0 m of sediment layer was washed away from the delta top. This results in a deeper depth on epoch *1118* and decreases the width to depth ratio. This presumably was in response to the river surge and allowed a greater discharge rate. Whether the flow cut the channel and then the lip collapsed or the collapse happened and then the channel deepened cannot be determined. According to Rubin and McCulloch (1980), this bedform morphology can be categorized as a washout bedform.

a. Depth profile on segment A_1A_2

b. Depth profile on segment B_1B_2

c. Depth profile on segment C_1C_2
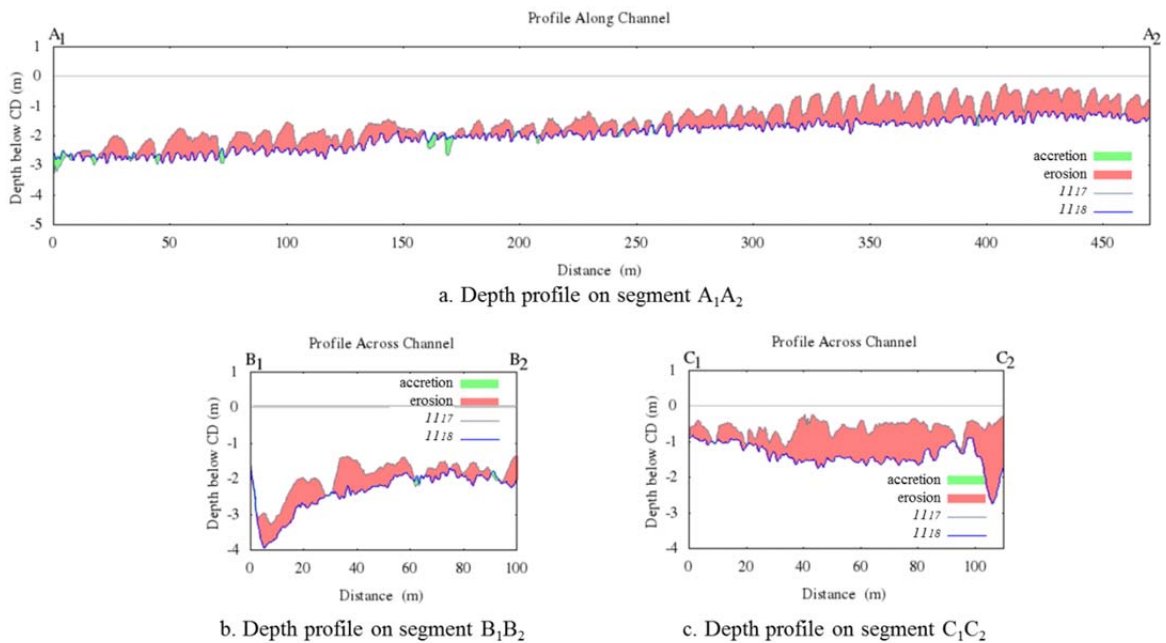
Figure 6.42: Depth profile along (a) and across (b, c) the channel between epochs *1117* and *1118*.

The red area shows the depth was shallowed by approximately 1.0 m.

191

The third major delta failure in 2011 occurred between epochs *1120* and *1121* (Figure 6.38). The lip of the delta retreated by more than 50 m on the eastern part (Figure 6.43). During this time, the flow regime was relatively low (the Froude number was less than 0.3). In a lower flow regime, resistance to flow is large and sediment transport is small [Simons & Richardson, 1966].

Nevertheless, a major delta lip failure still occurred during this period. The failure was on the part which remained during the second collapse (Figure 6.43). This delta lip failure occurred probably because of the instability of the eastern part of the delta edge as it exceeded its critical angle. Figure 6.43 shows the terrain models on the delta lip before and after the third major delta lip collapse of the summer 2011 period.

a. Delta lip terrain model on epoch *1120*   b. Delta lip terrain model on epoch *1121*
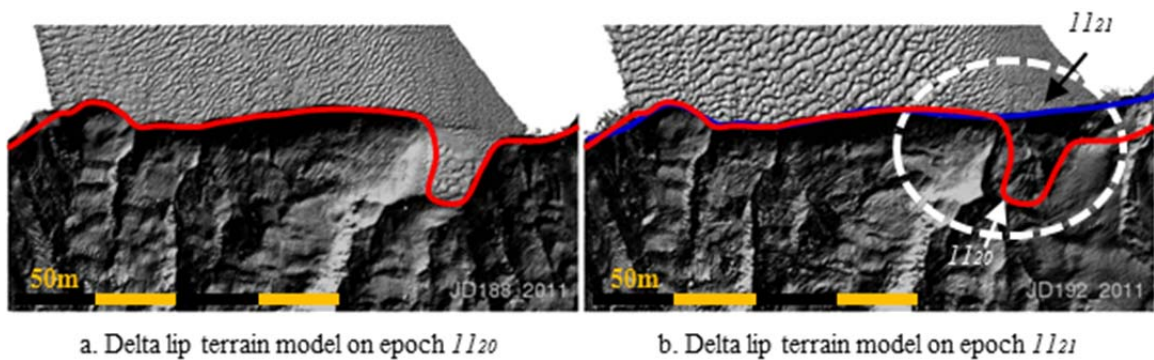
Figure 6.43: Terrain models of the delta lips before (a) and after (b) the third major delta lip failure in summer 2011.

Between epochs *1120* and *1121,* more than 71500 m^3 of sediment was removed from the delta lip. The SFI during this time was 3333 m^3 per day. This shows that there was sediment deposited on some parts of the delta lip. The change index of the sediment on the delta top was more than 15000 m^3 and the mobility index on the delta top was less than -2000 m^3. These (the change and mobility index) show that even though the sediment movement during this period was relatively high, there was no significant variation in the depth both along and across the channel between these epochs (Figure 6.44).

a. Depth profile on segment A_1A_2

b. Depth profile on segment B_1B_2

c. Depth profile on segment C_1C_2

Figure 6.44: Depth profile along (a) and across (b, c) the channel between epochs *1120* and *1121*.

6.5.2.2. <u>Summer 2012 period</u>

An event similar to those of summer 2011 also occurred during the summer 2012 period. Figure 6.45 shows that there was one major delta lip failure which occurred between epochs 1202 (JD182) and 1203 (JD183). The peak Froude number at this time was relatively high (approximately 0.5). The river discharge was approximately 600 m^3s^{-1} and the tide approached springs.

The western part of the delta lip retreated approximately 18 m between these epochs. The delta lip retrogradation was less than that of any of the three events in summer 2011. The rate of sediment volume loss between these epochs was approximately 12500 m^3 per day. This is less than the rate of volume loss either in the second or the third major collapse in 2011, but is greater than that of the first event in summer 2011. More than 24600 m^3 of sediment was removed from the delta lip. The MWI between these epochs was more than 12500 m^3 per day.

Figure 6.45b shows that in the summer of 2012, the daily sediment fluxes were notably higher than the peak of summer 2011. This apparent higher sediment discharge (SFI) reflects the fact that the surveys were performed on a daily basis instead of every 3 to 4 days. The more days between surveys, the more likely that the delta lip collapsed, removing evidence of deposition.
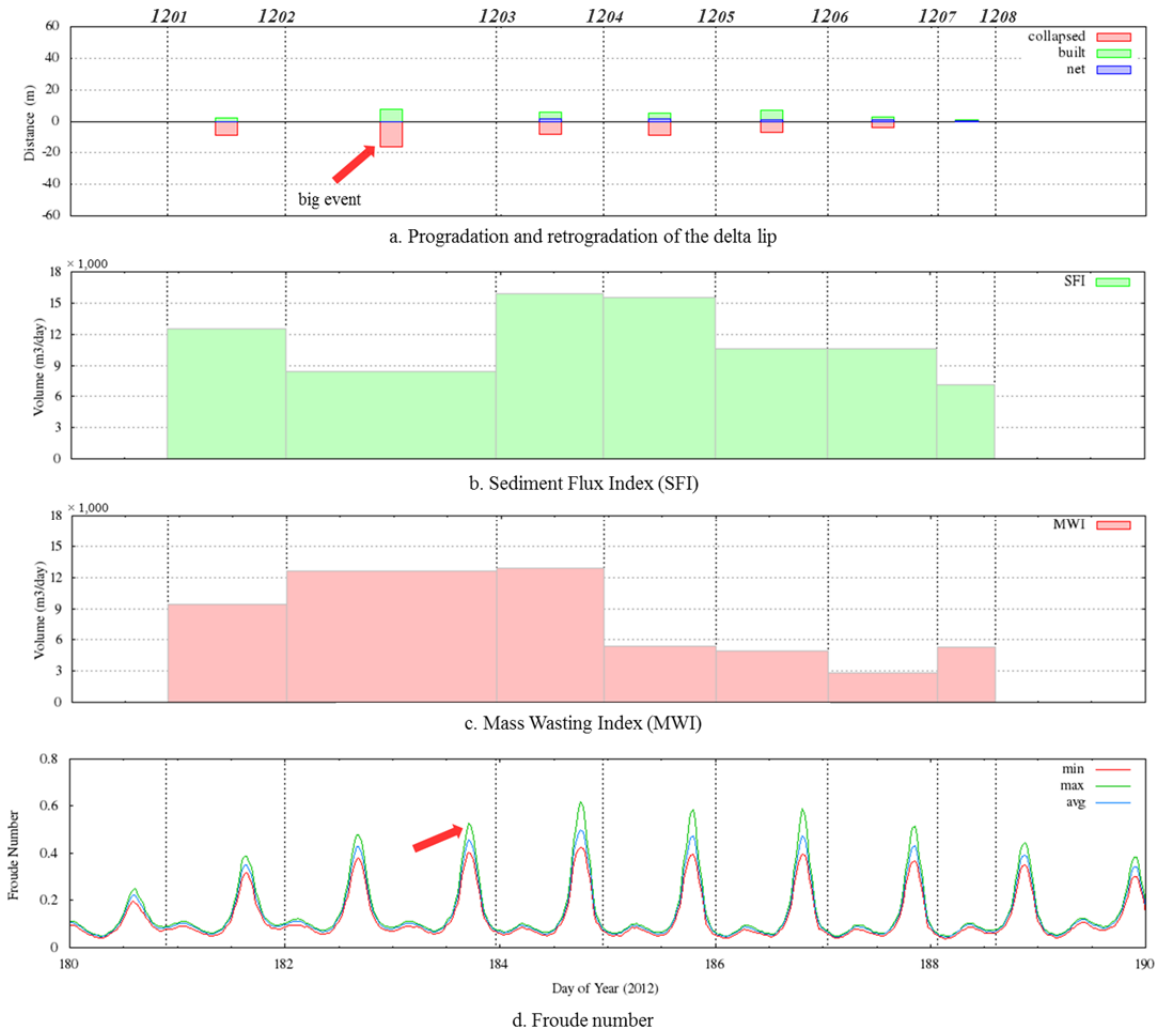
Figure 6.45: The progradation and retrogradation of the delta lip (a), the Sediment Flux Index (b), the

Mass Wasting Index (c), and related Froude number (d) in summer 2012.

The range of erosion and deposition on the delta top between these epochs (Figure 6.27) was relatively high (more than 25000 m^3). This shows that the activity of the sediment on the delta top during these epochs was relatively high. This event has a more significant effect on the depth in the unconstricted area (the mouth bar) than in the constricted area (Figure 6.46a).

Approximately 1.0 m of sediment was removed from the western part of the channel on the unconstricted area (Figure 6.46c). This suggests that the mouth bar was partially breached as a result of the peak flow. However, the peak flow upstream was not significant enough to deepen the constrained channel; the river discharge at this time was 600 m^{3}s^{-1}, compared to the higher flow of 800 m^{3}s^{-1} in the summer 2011 period.

a. Depth profile on segment A$_1$A$_2$

b. Depth profile on segment B$_1$B$_2$

c. Depth profile on segment C$_1$C$_2$
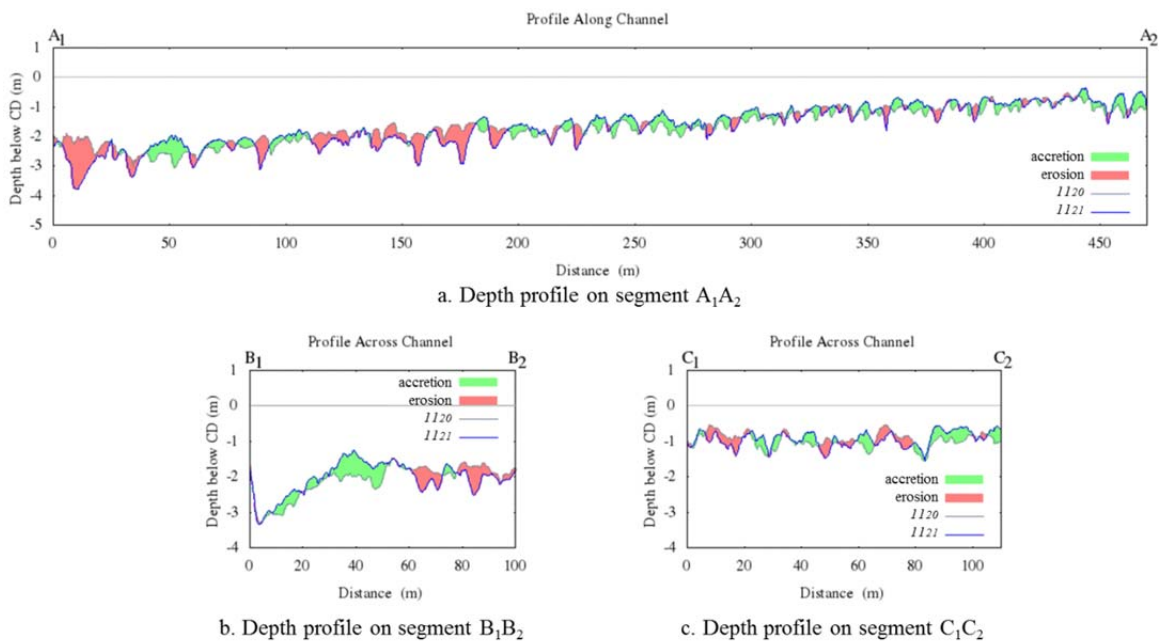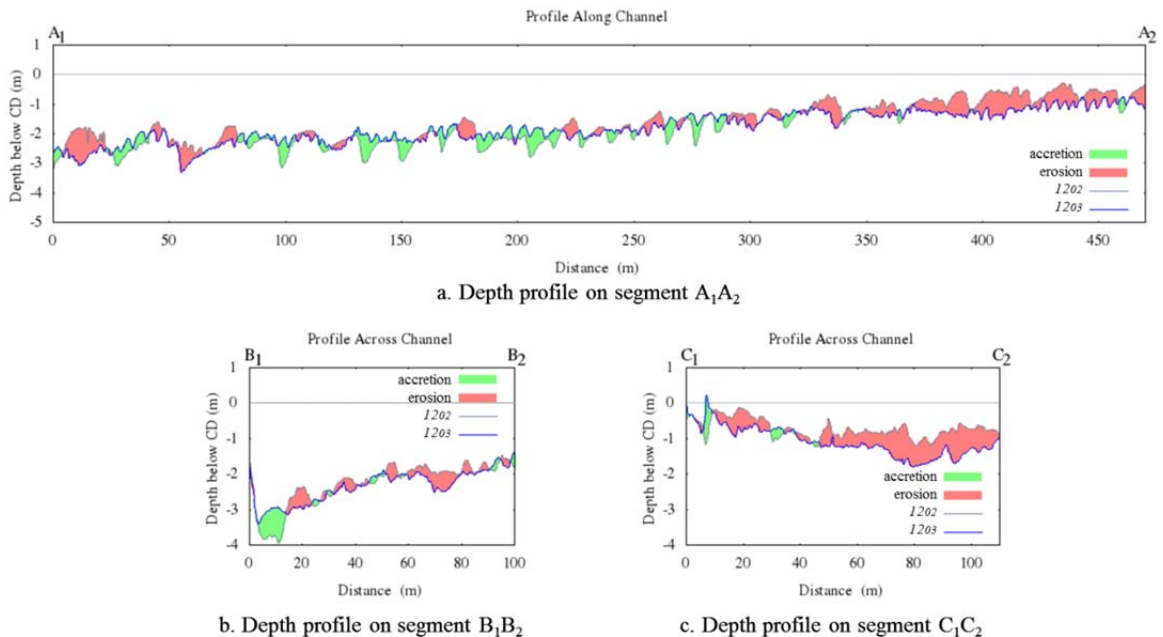
Figure 6.46: Depth profile along (a) and across (b, c) the channel between epochs *1202* and *1203*.

6.5.2.3. Summer 2013 period

Compared to the summer 2011 and 2012 periods, the delta lip in the summer 2013 period had less activity. However, the daily change of the volume gain and loss on the delta lip shows that day to day sediment activity in this area increased (Figure 6.47b and 6.47c) as the flow stage increased. This process can be seen in Figure 6.47, which shows the range of growth and retreat of the delta lip becoming more pronounced as the Froude number increases (red arrows in Figure 6.47).

During this period, the maximum delta lip progradation occurred when the Froude number was approximately 0.7 (between epochs 13_{08} and 13_{09}). According to Simons and Richardson (1966), a stream power of this magnitude is sufficient to cause channel instability and large changes in channel geometry.
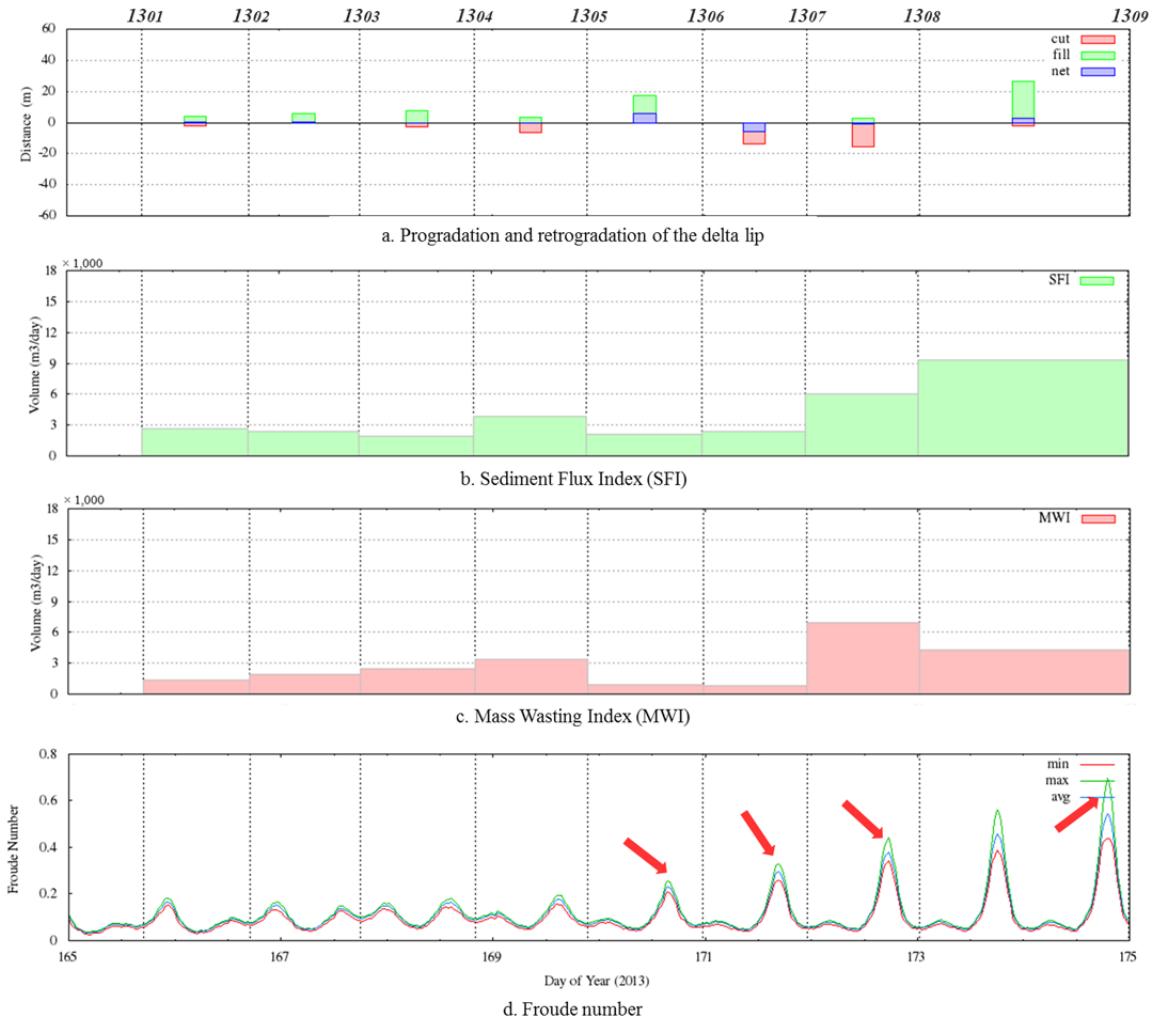
Figure 6.47: The progradation and retrogradation of the delta lip (a), the Sediment Flux Index (b), the Mass Wasting Index (c), and related Froude number (d) in summer 2013.

6.5.2.4. Response of the delta lip in wake of collapse

Notice that after each of the big delta failure events in 2011 and 2012, the delta lip prograded in the subsequent epoch (Figure 6.38 and 6.45). Between epochs 11_{18} and 11_{19}, the centre part of the delta lip grew by more than 10 m (Figure 6.48). Between

198

these epochs, the Froude number was still relatively high (approximately 0.5) and more than 10000 m^3 of sediment arrived on top of the delta top and covered this area within just 3 days.
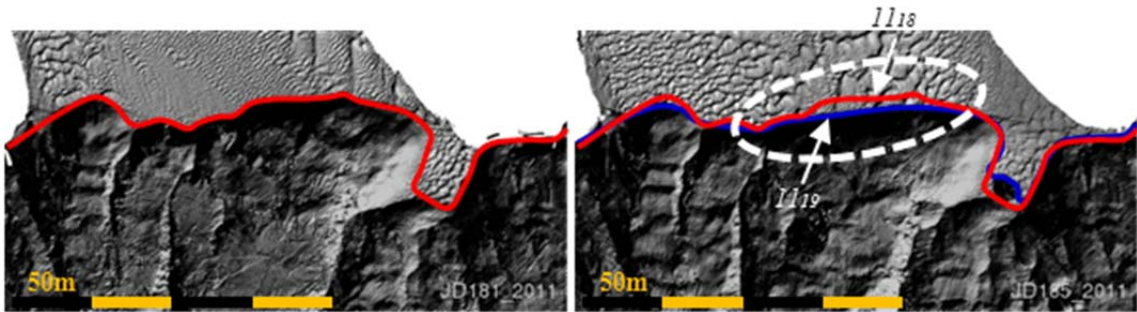
Figure 6.48: The growth of the delta lip between epochs 11_{18} and 11_{19}, after the major collapse between epochs 11_{17} and 11_{18},

Figure 6.49 shows depth profiles after the big event between epochs 11_{17} and 11_{18}. The depth of the delta top on epoch 11_{19} was shallower by approximately 0.75 m than on epoch 11_{18}. The sediment was deposited more in the constricted area than in unconstricted area (green area in Figure 6.49).
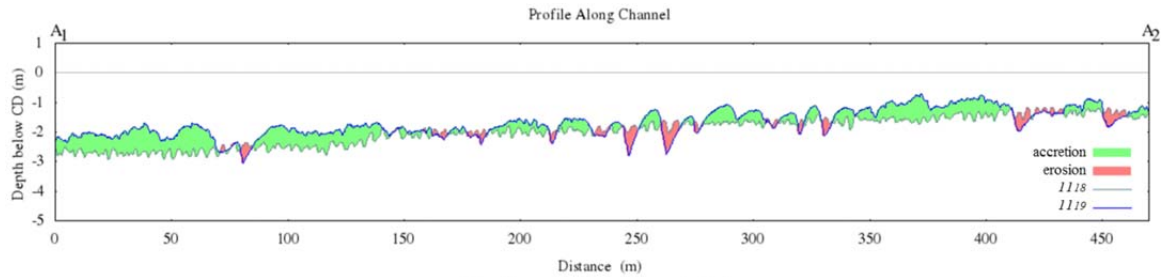
a. Depth profile on segment A_1A_2
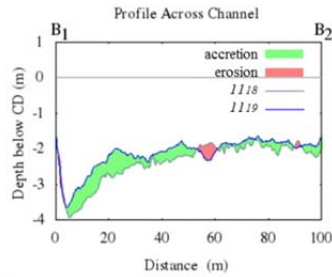
b. Depth profile on segment B_1B_2
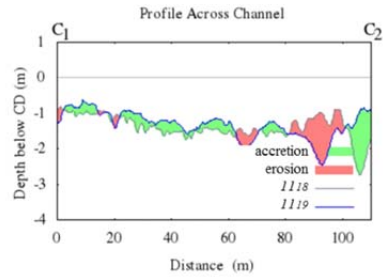
c. Depth profile on segment C_1C_2

Figure 6.49: Depth profile along (a) and across (b, c) the channel between epochs *1118* and *1119* in summer 2011.

The sediment activity on the delta lip was not as intense as on the delta top. Table 6.1 shows the SFI and MWI between these epochs (*1118* and *1119*) had a similar value (approximately 9200 m^3 per day). This implies that a less significant volume of sediment was deposited on the delta lip than on the delta top. Presumably the sediment flux was predominantly utilized upstream accreting the delta top and little made it to the lip.

6.5.2.1. <u>The relationship of the volumetric characterization with the flow regime</u>

It should be noted that the hydrodynamic model cannot perfectly describe the flow as the bathymetry was very different from one epoch to the next. The model assumes a fixed channel depth, yet in reality, during the largest velocity events, the mean channel depth both deepened and shoaled by up to 1 m. Given that the low tide channel is only approximately 1 m to 2 m deep, the Froude number will be affected profoundly.

The analysis of the relationship between the volumetric characterization and the flow regime was performed on the delta top and delta lip. The analysis on the delta top used the change index (the net volume) and mobility index (the range of volume). The duration of these volumetric parameters was from one epoch to the next. The volumetric parameters used on the delta lip are the SFI and MWI which represent the daily change of sediment volume gain and loss in the area.

a. <u>Volumetric analysis on the delta top.</u>

The relationship between the flow regime and how much sediment deposited and removed on the delta top can be examined by comparing the Froude number and the change index. Figure 6.50 shows that the change index varies within $\pm$ 10000 m^3 (shaded area). This indicates the channel shape is not static due to the variation of the flow regime.

When there were delta failure events (between epochs *1117 - 1118* and *1202 - 1203*) more than 10000 m^3 of sediment were removed from the area. These events occurred when the Froude number was about 0.5. There was, however, no obvious trend such as a greater

change at a higher Froude number. Note that the vertical positioning uncertainty (Chapter 3) contributes to noise in this signal. A 3.9 cm bias in tidal correction between epochs would result in approximately 2600 m^3 of apparent volume change.
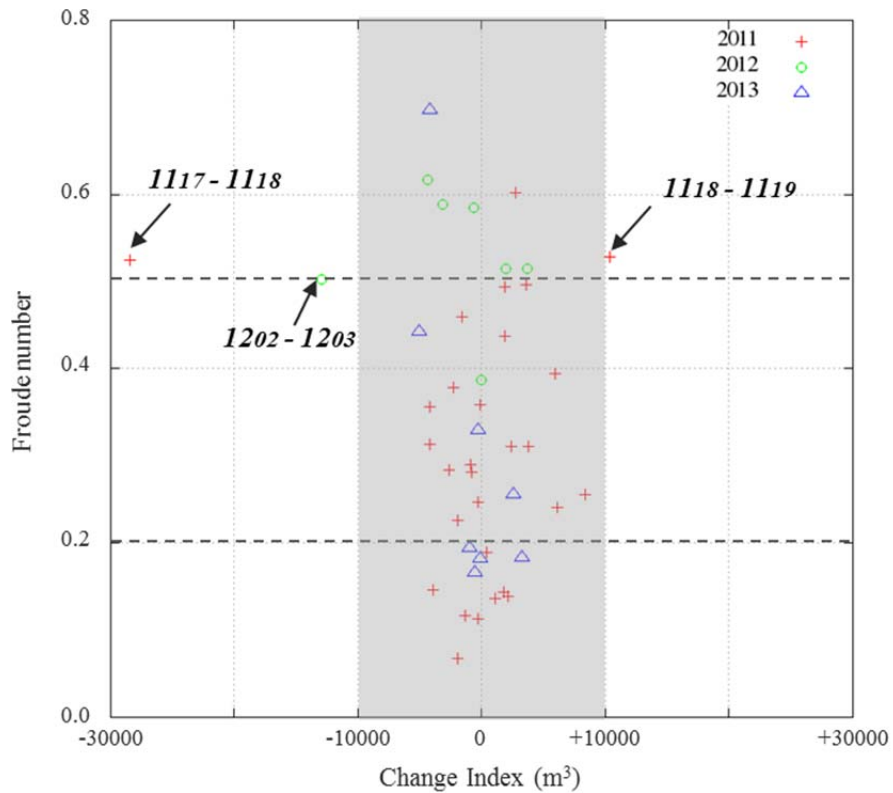
Figure 6.50: The relationship between the change index and the Froude number.

The relation between the mobility index and Froude number on the delta top shows that the sediments are more active when the Froude number is high (Figure 6.51). This correlation is much clearer. Notably, vertical positioning uncertainty does not effect this calculation as a bias just shifts the crossover between erosion and deposition, but without altering the range.
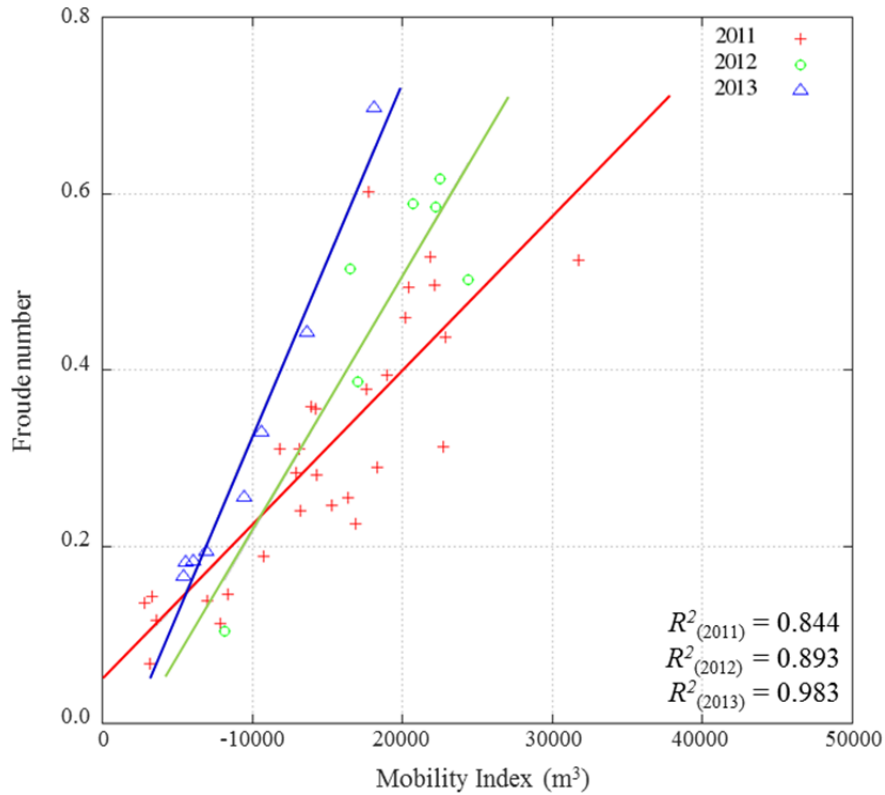
Figure 6.51: The relationship between the mobility index and the Froude number. The red, green, and blue lines represent the linear trends of the relationship between the mobility index and the Froude number in the summer 2011, 2012, and 2013, respectively.

b. Volumetric analysis on the delta lip.

The relationship between the flow regime and sediment flux in the off-delta lip was examined by comparing the Froude number and the SFI. The SFI is a conservative measure of the sediment flux. However, if the sediment were deposited and there was no collapsed at the delta lip, the SFI would be an excellent means for measuring the total sediment flux in this area.

The accumulation of the sediment on the off-delta lip causes the slope of the prodelta to become steeper and ultimately leads to a collapse. The SFI is a conservative measure as there are some sediments arriving on and collapsing from the area of interest at the same time. In the summer 2011 period, the surveys were performed every 3 to 4 days, whereas in the summer 2012 period was in daily basis. The average SFI of the summer 2012 was more than 12250 m^3 per day. This is much bigger than the average SFI of the second period of summer 2011 which was approximately 6300 m^3 per day, although these periods have a similar hydrodynamic condition.

The difference of the average SFI between the second period of summer 2011 and the summer 2012 period occurred because the duration between two consecutive epochs in the second period of summer 2011 is longer than of that in the summer 2012 period. As discussed in Chapter 4, as the inter-survey interval has a longer duration, the episodic and discrete nature of the MWI is hidden and, by averaging over several days, increasingly reduces the SFI estimate. Nevertheless. Figure 6.52 shows that the relationship between the SFI and the Froude number is positive and strong.
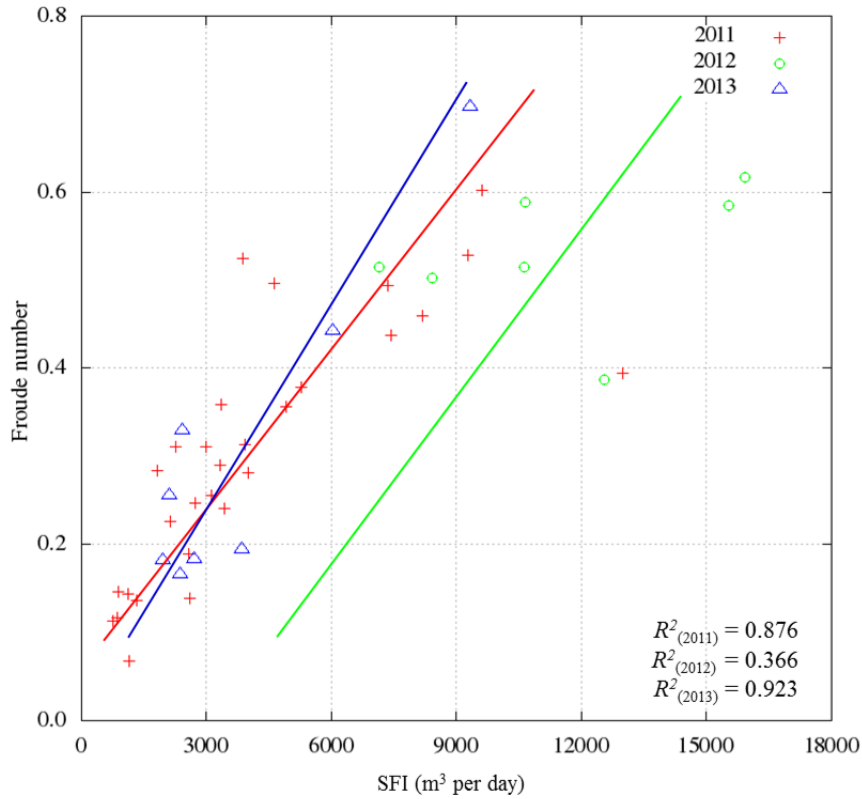
Figure 6.52: The relationship between the SFI and the Froude number.

As the sediment builds up just off the delta lip, this makes the slope of the prodelta

steeper and at some discrete point that causes the slope failure. When that occurs, the

sediment moves downslope and creates mass wasting events and/or turbidity currents.

The MWI represents this phenomenon. Again the MWI is a conservative measure as

there is simultaneous sediment deposition off the delta lip that partially refills the slump

scars left in the wake of a collapse of the prodelta slope. As the mass wasting is more

episodic, compared to the more continuous deposition resulting from the steady off delta

sediment transport, the MWI correlation with Froude number would not be expected to

be as good as with the SFI. The relationship between the MWI and Froude number is moderate for the summer 2011 and 2013 period, but is very weak in the summer 2012 period (Figure 6.53).
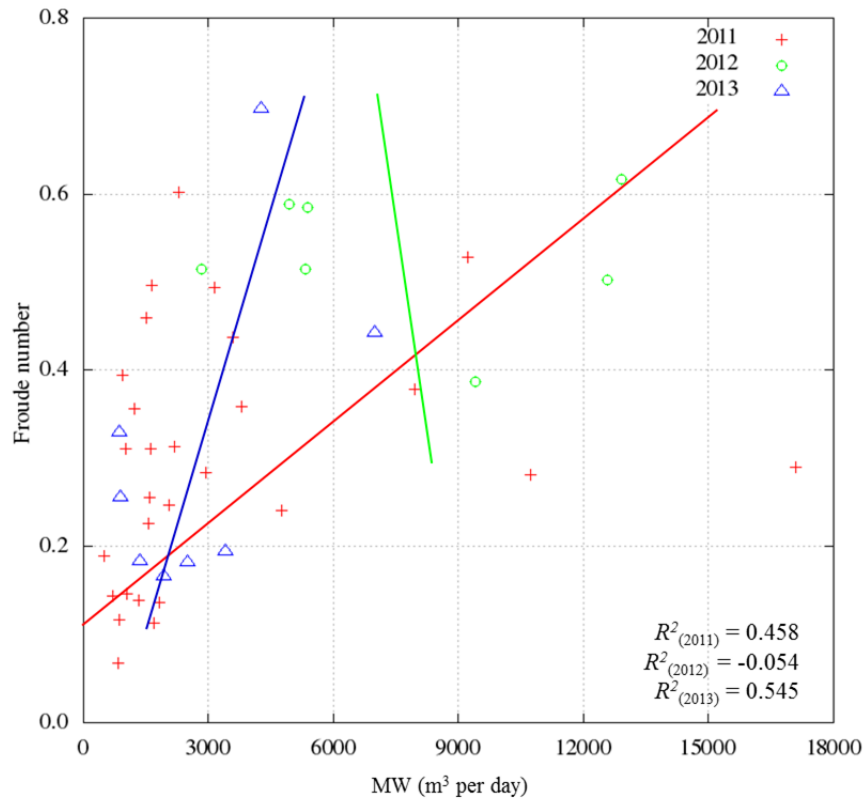
Figure 6.53: The relationship between volumetric parameters of the off-delta lip and the Froude number.

To summarize, a relatively high Froude number (above 0.5) was not necessary for delta lip failure to occur. Some delta lip failures happened when the Froude number was lower than 0.5. During the event between epochs *1106* and *1107*, even though the Froude number was less than 0.4, the delta lip retrograde was more than 30 m. Similarly, between epochs *1120* and *1121*, the delta lip retrograded significantly (more than 50 m),

206

yet the Froude number was less than 0.3. However, if the discrete retrograde events are excluded, the delta lip displacement (Figure 6.38, 6.45, and 6.47) and the volume range (mobility index) on the delta top (Figure 6.26, 6.27, and 6.28) grows when the Froude number increases.

6.5.3. Hypothesized extrapolation of flow regime

As the hydrodynamic model has demonstrated, the flow fields on the delta top are driven by a combination of the tide modulation and the river discharge. The prime drivers appear to be the spring/neap modulation, the seasonal waxing and waning of the river discharge, and the superimposed short-lived surges. As the Froude number is used to parameterize the flow regime in this area, knowing the relation among the Froude number, tides modulation and river discharge can be used to predict when this area is most likely to be in a high flow regime.

Of particular interest would be to examine the conditions might exist when the Froude number is beyond critical and the off-delta sediment fluxes would be at a maximum. Given that the major events appear to be associated with washout conditions, could the flow go even higher and become supercritical? Under such a regime, the off-delta sediment transport could be quite different (presumably much higher) reflecting a supercritical regime. The Froude number as a function of the tide modulation is displayed in Figure 6.54.
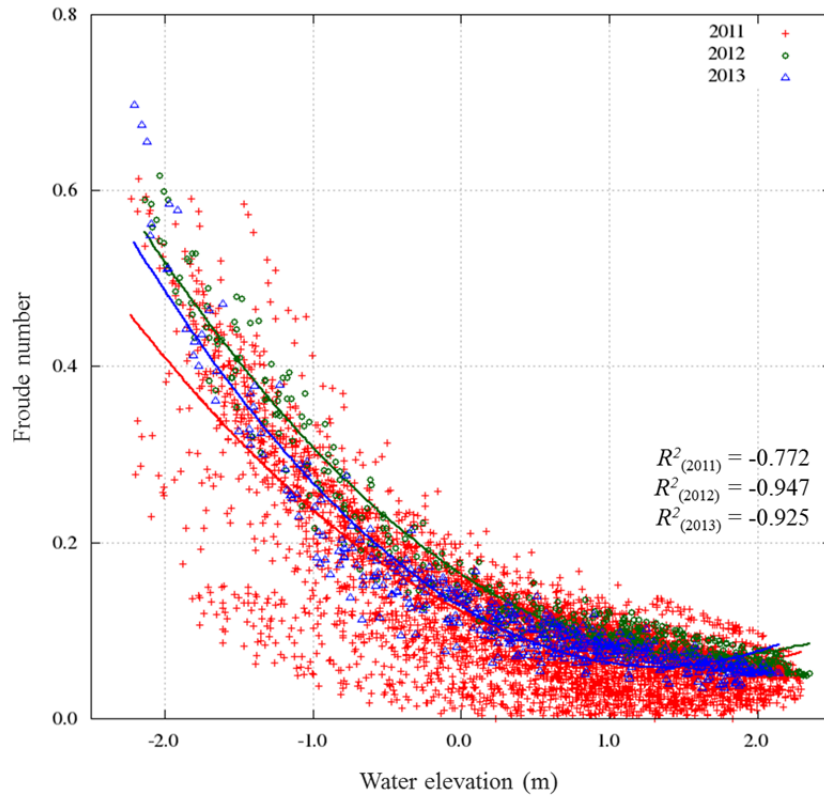
Figure 6.54: The correlation between the tide modulation and Froude number. The red, green, and blue lines represent the second order trend of the relationship between the Froude number and the tide observations in the summer 2011, 2012, and 2013 periods, respectively.

The maximum Froude number during the observation in 2011, 2012, and 2013 is more than 0.6. The relation between the tide and the Froude number, as expected, is negative and very strong. The relationship is second order, as the channel cross section decreases non-linearly with tide height. It means high Froude number results during low water and vice versa.

The relationship between water level and Froude number varies from year to year. The correlation between these parameters in the summer of 2011 is relatively low compared with the summers of 2012 and 2013. This is because the river discharge, as a third component also played a role in this situation and it was highly variable during this period. Whereas in the year 2012 and 2013, the river discharges varied less during time of observation.

Unlike a river without tidal influence in which the flow is approximately constant, the currents here are strongly modulated by the tide, in particular the bed shear stress peaks at low water. During the summer the river discharge is high and the flow never reverses. The bedform populations therefore are predominantly influenced by the combined ebb peak and river current.

During slower current condition, such as during neap tides, the bedforms are essentially static. Figure 6.55 shows the river discharge and the Froude number relationship. The interesting point to notice is the maximum river discharges in high water have lower Froude numbers than the moderate discharge in low water. Thus the lowest low spring tide combined with the river surge may create very sensitive peak current conditions.
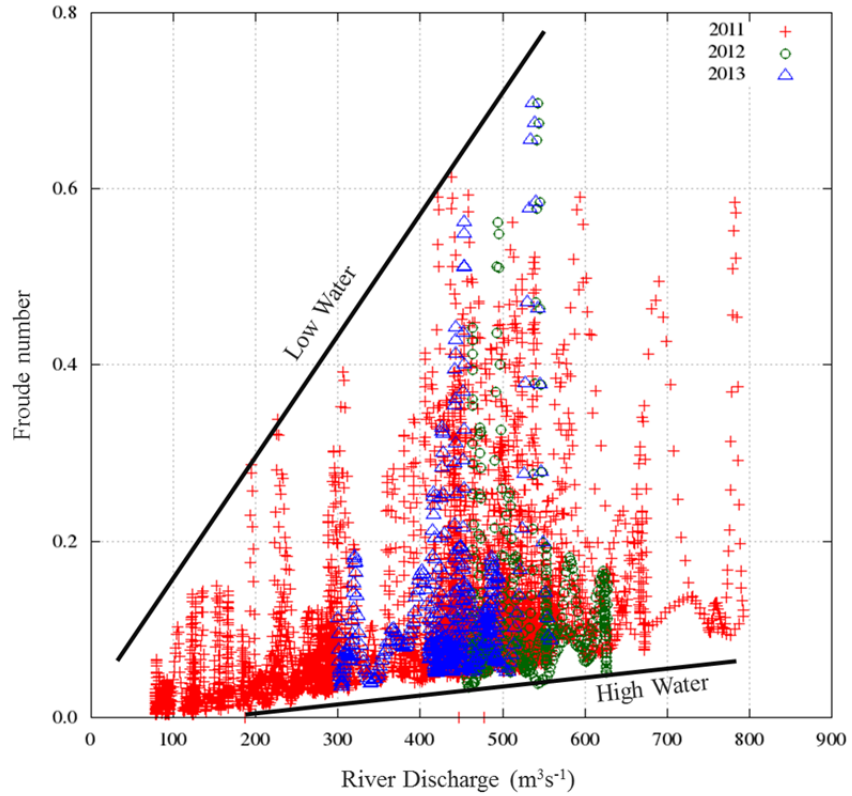
Figure 6.55: The relationship between the river discharge and Froude number.

To usefully predict the trend of the flow regime in the area, a relationship of tidal height, river discharge, and the Froude number needs to be examined simultaneously. In order to investigate at what discharge the river section might go supercritical, the relationship among these parameters was analyzed.

The relationship between Froude number from the model, the tidal elevation (τ) and river discharge (δ) observation can be seen in Figure 6.56 and this can be represented with the empirical Equation 6.1:

$$F = -0.0181 + 0.0003\,\delta - 0.0246\,\tau - 2.9e\text{-}08\,\delta^2 - 0.0001\,\delta\tau + 0.0288\,\tau^2 \qquad 6.1$$
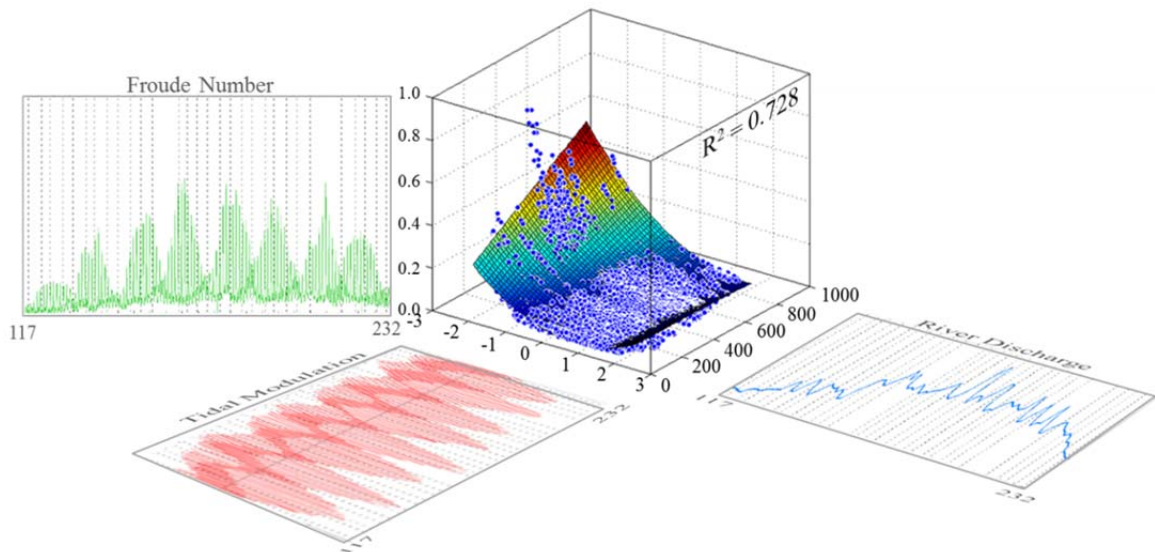
Figure 6.56: Illustration of the relationship among tidal elevation, river discharge, and current velocity at profile A_1A_2.

The relationship between the Froude number and the tidal modulation and river discharge as the two parameters which are responsible in controlling the flow regime in this area is strong (R^2 is 0.728). For a given discharge, the flow velocity and the water elevation follows a second order trend. As the discharge grows, the trend steepens and rises. According to Simons & Richardson (1966), the critical condition to get a washout bedform is when the Froude number is 1.0. During the lowest low water spring, the water depth is less than 0.6 m on the vicinity of the mouth bar area, to get a supercritical bedform condition, the river discharge must exceed 1300 m^3s^{-1}.

Note, however, the example of 11_{17} to 11_{18} this was the highest discharge peak and when it happened the flow appears to have cut a deeper channel, thereby allowing reduced flow velocity and hence lower Froude number. Would a higher surge simply cut a deeper channel?

All three years of experimentation have focused on summer when a sustained high discharge is guaranteed due to snow melt. Under those conditions, surges of up to 800 m^3s^{-1} can occur. However outside the summer period, short duration surges of even higher magnitude exist in winter and autumn periods as recorded by Environment Canada (Figure 6.57). While of shorter duration, the estimated Froude number indicate that a very different (presumably much more) sediment flux should exist. This could have the most dramatic effect on the delta lip. Thus this event may be disproportionately important in triggering large turbidity current. Thus, the next project should consider this phenomenon as well.
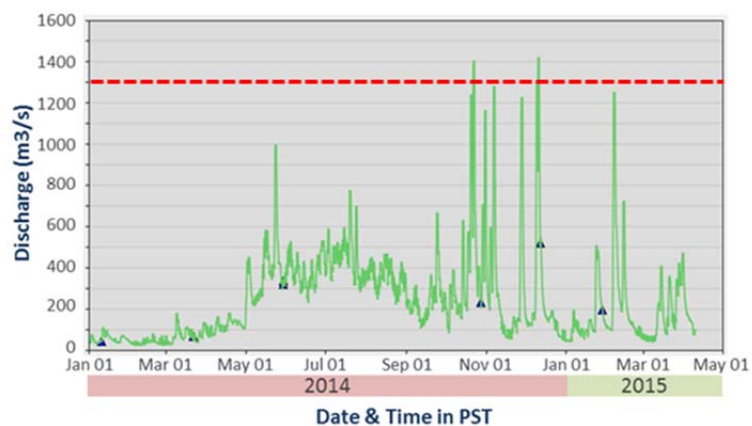
Figure 6.57: The daily average of the Squamish River discharge in 2014 and 2015. The red dashed line represents the river discharge at 1300 ms^{-1}.

212

Chapter 7: Conclusion

7.1. Conclusion

This project was an attempt to take advantage of the latest accuracy and resolution in seabed mapping and combine it with a detailed hydrodynamic model to address a specific sediment transport issue. This is the first project of which the author is aware, that involved such dense observations. The objective of this research is to understand the mechanism of the delta top sediment transport which leads to mass wasting. This is achieved by means of combining repetitive multibeam survey and hydrodynamic modelling. This research shows that repetitive multibeam surveys can be used to provide snapshots of the bedform morphology on the delta top as well as delta lip evolution. Those snapshots can provide insight into recent flow regime and associated sediment fluxes.

Through surveys every 3 to 4 days during a 4 month period in summer of 2011 and daily surveys in summer 2012 and summer 2013, the terrain models constructed from multibeam data show the bedforms in the Squamish River evolved significantly during each survey period in a manner that can be quantitatively correlated with the hydrodynamic conditions. The evolutions of the bedforms which can be captured by the repetitive mutibeam surveys are shown to reflect the flow regime during low and high river discharge and neap-spring tide modulation.

In order to improve the understanding of the change in bedform morphology, this research developed a hydrodynamic model which provides continuously varying flow conditions in this area. A validation of the model was performed in this research to assess the usefulness of the model output. As difficulties were encountered in attempting to measure the current in this area, Lagrangian trajectories from the Boston-Whaler were used in this research as a means to validate the model.

The validation of the output with the small boat trajectories showed a reasonable result. There are relatively small variations between the model outputs and the observations. These variations are the result of the smoothed and outdated bathymetry used in the model and unknown drag coefficient of the small boat. This research used current magnitudes from the model output to represent the hydrodynamic conditions in this area. The output from the model is used to calculate the Froude number which is used as a means of describing flow regime in this area. The flow regime in this area is well correlated with the tide modulation. The variation of the river discharge also plays a part in governing the flow regime, yet its effect is much smaller than that of the tide.

A 2D spectral analysis tool was developed in this research to parameterize bedform characterization, but it has a spatial limitation in solving long wavelength morphology as it depends on the size of the window used for analysis. Thus this research also takes advantage of 1D spectral analysis to examine longer wavelength. Based on 1D spectral analysis the bedform on the delta top of Squamish River can be categorized into 5 types. This categorization is based on Cheel (2005) after the Simons and Richardson (1966)

model: type 0, A, B, and C. The high stage (D) does not appear distinct based on these parameters.

The riverbed starts from type 0 as a lower plane bed with Froude number less than 0.2. When the Froude number is more than 0.2, the bedform on this area starts to develop as a type A passing through small to progressively longer dunes by Froude number 0.5 as type B and C. When the Froude number is more than 0.55, the bedform population starts to show the characteristic of washout. This generates relief that is not distinct from type A or type B as the roughness is being removed.

The washout characteristic, however, can be identified through the patchiness observed in the backscatter data. A quite distinct patchiness only appears when Froude number is more than 0.5. This is believed to correlate with state of washout conditions and it can be used to unambiguously distinguish bedform type D from type A or type B. In this case the pattern on the backscatter is clearly changed as a function of bed shear stress. At lower Froude number, beside the patchiness at spacing of crest to trough, there is little difference in the mean backscatter strength and standard deviation to distinguish these flow stages.

This research also found that the failure and progradation of the delta lip cannot be simply correlated with the high river discharge and low spring. The observations indicate that the time of collapse is only expected to be secondarily related to the day to day discharge as this is dominated by discrete slope events and the state of the slope prior to the next collapse.

The SFI and Mobility Index both show a clear correlation with the flow regime in this sand-bed river mouth. The relationship, however, between both change index and mass wasting index with the hydrodynamic regime is not so clear. While the MWI has a poorer correlation with flow regime, the larger mass wasting events were found to have a preference for the spring tide periods.

This research could potentially alter the way scientists and engineers monitor sediment transport in river mouths. In the future, for the case of estuarine environments that are similar to the conditions at Squamish, the correlations revealed by this research could be used to indirectly infer the sediment transport conditions (sediment flux, likelihood of mass wasting) by looking at the characteristics of the bedform, population. Once the correlations are confirmed locally, a surveyor could undertake this analysis by merely running a single line along the center of the active channel. From a 1D power spectra of the resulting profile, the type of the bedform can be determined. Based on this, the current sediment flux rate can be empirically determined.

7.2. Suggestions for Future Research Directions

The hydrodynamic model constructed as part of this research is a robust means of depicting the flow field in this area. A barotropic model was used to reduce the computational load, because in the summer, the delta top was purely fresh water. However, to improve the model capability, a baroclinic model can be developed to give better flow fields predictions, as it considers temperature and salinity data in their

calculation. This will probably not produce significantly different result on the delta top, but would profoundly change the predicted characteristic of the hypopycnal plume off the delta lip that may feed turbidity currents on the delta slope.

Again to ease computational load, a single realization of the delta top bathymetry was used. However, as the delta lip and the depth of this area vary significantly during the summer period, the other thing to be considered in developing the hydrodynamic model is using an accurate temporally evolving bathymetry model which represents the actual depth and the shape of the delta lip. Epochs 1117 and epoch 1108 in 2011 were a good example of that feedback. A model that allowed the terrain to change would be a potential future research project.

Another limitation of the flow modelling is that just a single value (the default) roughness parameter was used. The water surface height measurements, that were used to assess the model, indicate that for the peak flow period, the delta top roughness was probably underestimated. Using different roughness parameter values thus may improve the model-observation agreements.

An added complication, however, is that this thesis has demonstrated that the bedform population is strongly correlated with the flow regime. As the bedforms represent the form roughness component of the total roughness, variations in the bedform height probably indicate a significant variation in the total roughness. Thus future modeling might consider utilizing a roughness parameter that varies as a function of the local (nodal) flow conditions.

As long term seabed mounted current measurement is not feasible in this area, releasing buoys and tracking their trajectories can be performed as an alternative solution to get the current data for model calibration. As the model has indicated that lower low water conditions are the most critical, small boat based combined multibeam and ADCP measurement may provide insight over a single tidal cycle.

Although the correlation between backscatter strength and grain-size is moderately related, this correlation is not simple. This research utilized only limited bed load sediment samples. In order to see a valid relation, it is recommended that future programs obtain at least 3 grab samples during each delta top survey as the bedform might change completely on the next day. However, it is challenging to do a survey, process it, and sample it on the same vessel.

Of particular interest would be to understand the sediment composition responsible for the long wavelength patchiness when the Froude number is more than 0.5. The inter day terrain models differences at the delta lip indicate the most intense deposition immediately off the lip. A future project should address the abrupt deceleration of the flow at this location. Further research is clearly required into the interacting effect of sediment flux feeding the delta lip and intermittent small scale collapses.

Bibliography

ACENET. [2014]. Retrieved December 11, 2015, from http://www.ace-net.ca/

Allen, J.R.L. [1982], Sedimentary Structures: Their Character and Physical Basis,
Elsevier, New York, NY.

Applanix - A Trimble Company. [2014]. Retrieved December 11, 2015, from
http://www.applanix.com/

Beaudoin, J. [2012]. *R / V Hugh R . Sharp Multibeam Echosounder System Review
Multibeam Advisory Committee Sea Acceptance Team*. Retrieved from
http://mac.unols.org/sites/mac.unols.org/files/20121031_Hugh_R_Sharp_SAT_repo
rt-final.pdf

Bell, L. M. [1975]. Factors Influencing The Sedimentary Environments of The Squamish
River Delta in Southwestern British Columbia. *ProQuest Dissertations and Theses*.
Retrieved from http://search.proquest.com/docview/302823274?accountid=14611

Bennett, J. P. [1997]. Resistance, sediment transport, and bedform geometry relationships
in sandbed channels. In *Proceedings of the US Geological Survey (USGS) sediment,
workshop* [Vol. 47]. Retrieved from
http://water.usgs.gov/osw/techniques/workshop/bennett.html

Blott, S. J., & Pye, K. [2001]. Technical Communication Gradistat : a Grain Size
Distribution and Statistics Package for the Analysis of Unconsolidated Sediments,
1248, 1237–1248.

Boudreau, P., Cantin, J., Bouchard, A., Fortin, P., Fiset, J., Fortin, N., … Morin, G. [2015]. Development of an experimental 2D hydrodynamic model of Lake Champlain using existing bathymetric data (Task 1-2).

Brucker, S., Hughes Clarke, J., Beaudoin, J., Lessels, C., Czotter, K., Loschiavo, R., … Hill, P. . [2007]. Monitoring flood-related change in bathymetry and sediment distribution over the Squamish Delta, Howe Sound, British Columbia. *U.S. Hydrographic Conference*, [1], 1–16.

Buckley, J. R. [1977]. *The Currents , Winds and Tides Of Northern Howe Sound*. Unversity of British Columbia.

C&C Technologies. [2014]. Retrieved December 11, 2015, from http://www.cctechnol.com/

Cazenave, P. W., Lambkin, D. O., & Dix, J. K. [2008]. Quantitative bedform analysis using decimetre resolution swath bathymetry, 1–12.

Chaffey, J. D., & Greenberg, D. A. [2003]. resolute: A Semi-Automated Finite Element Mesh Generation Routine. *Can. Tech. Rep. Hydrogr. Ocean Sci*.

Cheel, R. J. [2005]. Bedforms and stratification under unidirectional flows. *Introduction to Clastic Sedimentology*, 126.

Chen, C. [2013]. FVCOM-An unstructured grid Finite-Volume Community Ocean Model Critical Issues in Coastal Ocean Modeling Irregular geometry Steep topography Intertidal wetlands.

Chen, C., Beardsley, R. C., Cowles, G., Qi, J., Lai, Z., Gao, G., … Lin, H. [2011]. An unstructured-grid, finite-volume community ocean model fvcom user manual (3rd edition). Massachusetts: Massachusetts Institute of Technology Cambridge.

Church, I. [2014]. *Modelling the Estuarine Circulation of the Port of Saint John: Applications in Hydrographic Surveying*.

Clunie, T. M. [2012]. *Flow over fluvial bedforms*. The University of Auckland. Retrieved from http://researchspace.auckland.ac.nz/handle/2292/13073

Duffy, G. P., & Hughes-Clarke, J. E. [2005]. Application of spatial cross correlation to detection of migration of submarine sand dunes. *Journal of Geophysical Research: Earth Surface*, *110*[4], 1–11. http://doi.org/10.1029/2004JF000192

Friele, P. A., Ekes, C., & Hickin, E. J. [2000]. Evolution of Cheekye fan, Squamish, British Columbia: Holocene sedimentation and implications for hazard assessment. *Canadian Journal of Earth Sciences*, *36*[12], 2023–2031.

Gibson, J. W., & Hickin, E. J. [1997]. Inter- and supratidal sedimentology of a fjord-head estuary, south-western British Columbia. *Sedimentology*, *44*[6], 1031–1051. http://doi.org/10.1046/j.1365-3091.1997.d01-60.x

Hammerstad, E. [2000]. Backscattering and seabed image reflectivity. *EM Technical Note*.

Hickin, E. J. [1978]. Mean flow structure in meanders of the Squamish River, British Columbia. *Canadian Journal of Earth Sciences*, *15*[Hickin 1977], 1833–1849. http://doi.org/10.1139/e78-191

Hickin, E. J. [1989]. Contemporary Squamish River sediment flux to Howe Sound, British Columbia. *Canadian Journal of Earth Sciences*, *26*[10], 1953–1963.

Hoskin Scientific:US BMH-60 Bed-Material Samplers. [2012]. Retrieved April 2, 2016, from http://www.hoskin.ca/catalog/index.php?main_page=product_info&products_id=2045

Hu, K., Ding, P., Wang, Z., & Yang, S. [2009]. A 2D/3D hydrodynamic and sediment transport model for the Yangtze. *Journal of Marine Systems*, *77*[1-2], 114–136. http://doi.org/10.1016/j.jmarsys.2008.11.014

Hughes Clarke, J. E. [2003]. Dynamic Motion Residuals in Swath Sonar Data : Ironing out the Creases. *International Hydrographic Review*, *4*, 6–23.

Hughes Clarke, J. E. [2012]. Optimal use of multibeam technology in the study of shelf morphodynamics. *International Association of Sedimentologists*.

Hughes Clarke, J. E., & Brucker, S. [2009]. Monitoring morphological evolution of fjord deltas in temperate and Arctic regions. *International Conference on Seafloor Mapping for Geohazard Assessment. Lerici, Italy May2009*, *7*[May], 147–150.

Hughes Clarke, J. E. [2010]. Multibeam motion compensation: course notes. Geodesy and Geomatics Eng. University of New Brunswick.

Hughes Clarke, J. E., Brucker, S., Muggah, J., Church, I., & Cartwright, D. [2011]. Assessing the practical limits of change detection using repetitive multibeam surveying : The 2011 Squamish Delta program. Fredericton, Canada: Ocean Mapping Group, University of New Brunswick.

Hughes Clarke, J. E., Brucker, S., Muggah, J., Church, I., Cartwright, D., Kuus, P., … Eisan, B. [2012]. The Squamish ProDelta: monitoring active landslides and turbidity currents. In *Canadian Hydrographic Conference* [p. 15].

Hughes Clarke, J. E., Brucker, S., Muggah, J., Hamilton, T., Cartwright, D., Church, I., … Kuus, P. [2012]. Temporal progression and spatial extent of mass wasting events on the Squamish prodelta slope. In *11th International Symposium on Landslides, Conference Proceedings, Banff, June 2012* [Vol. 122].

Hughes Clarke, J. E., Marques, C. R. V., & Pratomo, D. [2014]. Imaging Active Mass-Wasting and Sediment Flows on a Fjord Delta, Squamish, British Columbia. In *Springer Internaitonal Publishing* [pp. 249–260]. Springer. http://doi.org/10.1007/978-3-319-02904-7

Hughes Clarke, J. E. [2015]. Swathed. Geodesy and Geomatics Eng. University of New Brunswick.

Ip, J. T. C., & Lynch, D. R. [1995]. Comprehensive coastal circulation simulation using finite elements: nonlinear prognostic time-stepping model QUODDY3 users manual. *Rep.No.NML95-1, Thayer School of Engineering, Dartmouth College, Hanover, New Hampshire, USA*.

Irizarry, R. A, & Bravo, H. C. [2010]. Smoothing, 1–39.

Kantha, L. H., & Clayson, C. A. [2000]. *Numerical models of oceans and oceanic processes* [Vol. 66]. Academic press.

Kostaschuk, R., & Best, J. [2005]. Response of sand dunes to variations in tidal flow: Fraser Estuary, Canada. *Journal of Geophysical Research: Earth Surface*, *110*, 1–11. http://doi.org/10.1029/2004JF000176

Lefebvre, A. [2009]. A new system for seafloor characterisation: BRAD, the Benthic Roughness Acoustic Device. *Underwater Acoustic Measurements: Technology and Results*, 1–8. Retrieved from http://promitheas.iacm.forth.gr/UAM_Proceedings/uam2009/19-3.pdf

Lefebvre, A., & Lyons, A. P. [2011]. Quantification of roughness for seabed characterisation. *Underwater Acoustic Measurements Conference*, 8.

223

Lemke, K. A. [2015]. 3. Stream Sediment. Retrieved December 11, 2015, from

http://www4.uwsp.edu/geo/faculty/lemke/geomorphology/lectures/03_stream_sedim

ent.html

Mayer, L. A., Lee, Y. C., Hughes Clarke, J. E., Wells, D. E., & Coleman, D. J. [1991].

Analysis of Multibeam Sonar Data for the Characterization of Seafloor Habitats.

Source, 153. Retrieved from http://hidrografica.tripod.com/Analysis_MB_

SeafloorHabitats.pdf

Medialdea, T., Somoza, L., Leon, R., Farran, M., Ercilla, G., Maestro, A., … Alonso, B.

[2008]. Multibeam backscatter as a tool for sea-floor characterization and

identification of oil spills in the Galicia Bank. *Marine Geology*, *249*[1-2], 93–107.

http://doi.org/10.1016/j.margeo.2007.09.007

Metrology, I. [2014]. Roughness Parameters. Retrieved August 10, 2015, from

http://www.imagemet.com/WebHelp6/Default.htm#RoughnessParameters/Roughne

ss_Parameters.htm#Roughness_Average

Mitchell, N. C., & Hughes Clarke, J. E. [1994]. Classification of seafloor geology using

multibeam sonar data from the Scotian Shelf. *Marine Geology*, *121*, 143–160.

http://doi.org/10.1016/0025-3227(94)90027-2

Nittrouer, J. A., Allison, M. A., & Campanella, R. [2008]. Bedform transport rates for the

lowermost Mississippi River, *113*[April], 1–16. http://doi.org/10.1029/

2007JF000795

NOAA Office of Coast Survey. [2014]. How Hydrodynamic Models Are Used. Retrieved

January 30, 2016, from http://www.nauticalcharts.noaa.gov/csdl/learn_models.html

Nyander, A., Addison, P., Mcewan, I., & Pender, G. [2003]. Analysis of River Bed Surface Roughnesses Using 2D Wavelet Transform-Based Methods. *The Arabian Journal for Science and Engineering*, *28*[1C], 107–121.

Pfannkuch, H. O., & Rick Paulson. [n.d.]. Grain Size Distribution. Retrieved April 1, 2016, from http://faculty.njcu.edu/wmontgomery/Coastal_Zone/Grain Size Distribution.htm

Poppe, L. J., Eliason, A. H., Fredericks, J. J., Rendigs R. R., Blackwood, P. C. [2000]. Chapter 1: Grain-Size Analysis of Marine Sediments: Methodology and Data Processing. Retrieved April 1, 2016, from http://pubs.usgs.gov/of/2000/of00-358/text/chapter1.htm

Preston, J. M., Christney, A. C., Bloomer, S. F., & Beaudet, I. L. [2001]. Seabed classification of multibeam sonar images. *MTS/IEEE Oceans 2001. An Ocean Odyssey. Conference Proceedings (IEEE Cat. No.01CH37295)*, *4*, 2616–2623. http://doi.org/10.1109/OCEANS.2001.968411

Prior, D. B., & Bornhold, B. D. [1984]. Geomorphology of slope instability features; Squamish Harbour, Howe Sound, British Columbia. *Geological Survey of Canada, Open File Report*.

Rodriguez, G. [2001]. Smoothing and Non-Parametric Regression, 1–12.

Rubin, D. M., & McCulloch, D. S. [1980]. Single and superimposed bedforms: a synthesis of San Francisco Bay and flume observations, *26*, 207–231.

Simons, D. B., & Richardson, E. V. [1966]. Resistance to flow in alluvial channels. *Physiographic and Hydraulic Studies of Rivers, Geological Survey Professional Paper 422-J*.

Singh, A., Lanzoni, S., Wilcock, P. R., & Foufoula-Georgiou, E. [2011]. Multiscale

    statistical characterization of migrating bed forms in gravel and sand bed rivers.

    Water Resour. Res., *47*[December], W12526.

    http://doi.org/10.1029/2010WR010122

Squamish Estuary Management Plan. [1981].

Squamish Estuary Management Plan. [1999].

Taylor, K.. [2012]. MVP Profiles - Squamish River. Retrieved June 12, 2013, from

    http://www.omg.unb.ca/Projects/SQ_2011_html/pages/MVP_SQ_html/MVP_Squa

    mish.html

Tides, Currents, and Water Levels - Fisheries and Oceans Canada. [2008]. Retrieved May

    7, 2014, from http://www.waterlevels.gc.ca/

van Rijn, L. C. [1985]. Sediment transport, part III: bed forms and alluvial roughness,

    110[12], 1733–1754.

Venditti, J. G. [2013]. Bedforms in Sand-Bedded Rivers. In *Treatise on Geomorphology*

    [Vol. 9, pp. 137–162]. Elsevier Ltd. http://doi.org/10.1016/B978-0-12-374739-

    6.00235-9

Water Office - Environment Canada. [2011]. Retrieved May 7, 2014, from

    https://wateroffice.ec.gc.ca/

Yang, Z., Wang, T., Voisin, N., & Copping, A. [2014]. Estuarine response to river flow

    and sea-level rise under future climate change and human development. *Estuarine,*

    Coastal and Shelf Science, *156*. http://doi.org/http://dx.doi.org/10.1016/

    j.ecss.2014.08.015

XTide: Harmonic tide clock and tide predictor. (2010). Retrieved June 12, 2014, from

http://www.flaterco.com/xtide/files.html

http://www.ngs.noaa.gov

Appendix A

Grain-size analysis of sediment samples collected in the summer 2012 and the corresponding backscatter map (available in CD).

Appendix B

Depth profiles along and across the channel (available in CD).

Appendix C

List of epochs and their corresponding Julian Date

C.1. List of epochs in the summer of 2011

Epoch	Julian Date 2011	Julian Date (exact time)			Gregorian Date (2011)
		day	hour	minute	
1101	118	118	22	30	April 28
1102	122	123	01	30	May 2
1103	125	125	16	00	May 5
1104	129	129	15	50	May 9
1105	132	132	21	00	May 12
1106	136	137	00	00	May 16
1107	139	139	15	00	May 19
1108	143	143	16	00	May 23
1109	146	146	21	00	May 26
1110	150	151	00	00	May 30
1111	153	154	02	30	June 2
1112	157	157	16	00	June 6
1113	165	166	00	00	June 14
1114	168	168	14	00	June 17
1115	171	171	15	00	June 20
1116	174	174	20	00	June 23
1117	178	178	21	00	June 27
1118	181	182	00	00	June 30
1119	185	185	16	00	July 4
1120	188	188	17	00	July 7
1121	192	192	21	30	July 11
1122	195	195	14	30	July 14
1123	199	199	15	00	July 18
1124	202	202	18	00	July 21
1125	206	206	22	30	July 25

Epoch	Julian Date 2011	Julian Date (exact time)			Gregorian Date (2011)
		day	hour	minute	
1126	216	216	17	00	August 4
1127	220	220	23	00	August 8
1128	223	224	00	00	August 11
1129	227	227	15	30	August 15
1130	230	230	16	00	August 18

C.2. List of epochs in the summer of 2012

Epoch	Julian Date 2011	Julian Date (exact time)			Gregorian Date (2011)
		day	hour	minute	
1201	180	180	21	30	June 28
1202	182	182	00	00	June 30
1203	183	183	23	00	July 1
1204	184	184	23	00	July 2
1205	185	186	00	00	July 3
1206	186	187	01	00	July 4
1207	187	188	01	30	July 5
1208	188	188	14	30	July 6

C.3. List of epochs in the summer of 2013

Epoch	Julian Date 2011	Julian Date (exact time)			Gregorian Date (2011)
		day	hour	minute	
1301	165	165	17	00	June 14
1302	166	166	17	00	June 15
1303	167	167	18	00	June 16
1304	168	168	20	00	June 17
1305	169	169	21	30	June 18
1306	170	170	23	30	June 19
1307	171	171	23	00	June 20
1308	172	173	00	30	June 21
1309	174	174	23	45	June 23

Curriculum Vitae

Candidate's full name: Danar Guruh Pratomo

Universities attended:

2010-2016   Ph.D., Geodesy & Geomatics Eng., University of New Brunswick

2005-2007   MScE., Geodesy & Geomatics Eng., Institut Teknologi Bandung, Indonesia

1998-2003   BScE., Geodesy Eng., Institut Teknologi Bandung, Indonesia

Publications:

Hughes Clarke, J.E., Marques, C.R., **Pratomo, D.G.**, 2014, Imaging Active Mass-Wasting and Sediment Flows on a Fjord Delta, Squamish, British Columbia: in S. Krastel et al. (eds.), Submarine Mass Movements and Their Consequences, Advances in Natural and Technological Hazards Research, 37, p.249-260, DOI 10.1007/978-3-319-00972-8 22.

Hughes Clarke, J.E., Brucker, S., Muggah, J., Church, I., Cartwright, D., Kuus, P., Hamilton, T., **Pratomo D.G.,** Eisan, B., 2012, The Squamish ProDelta: Monitoring Active Landslides and Turbidity Currents: Canadian Hydrographic Conference 2012, Proceedings, 15pp.

Conference Presentations:

Pratomo, D.G., Hughes Clarke, J. E., 2015, Understanding Sediment Flux Through Delta-top Channels Using Repetitive Multibeam and Hydrodynamic Modeling, American Geophysical Union Joint Assembly 2015, Montreal - Canada.

Hughes Clarke, J. E., **Pratomo, D. G.**, Marques, C. R., 2012, Monitoring the Onset, Propagation, Associated Bedform Migration, and Wake of Active Turbidity Currents on the Squamish Prodelta Slope. American Geophysical Union, Fall Meeting 2012, San Francisco.